STUDIES OF NEBULAE EJECTED FROM MASSIVE STARS BASED ON OBSERVATIONS WITH THE HERSCHEL SPACE OBSERVATORY

CHLOI VAMVATIRA-NAKOU

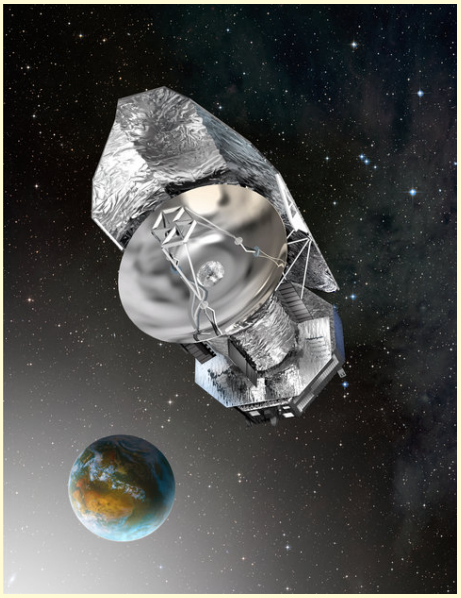

STUDIES OF NEBULAE EJECTED FROM MASSIVE STARS BASED ON OBSERVATIONS WITH THE HERSCHEL SPACE OBSERVATORY

CHLOI VAMVATIRA-NAKOU

PhD thesis in Science
Department of Astrophysics, Geophysics
and Oceanography
Faculty of Science
University of Liège, Belgium

August 2015

SUPERVISOR:
Dr. Damien Hutsemékers

MEMBERS OF THE JURY:
Prof. Jean Surdej (ULg) - president,
Dr. Nick Cox (IRAP), Dr. Martin Groenewegen (ROB), Prof. Pierre Magain (ULg),
Dr. Yäel Nazé (ULg), Prof. Gregor Rauw (ULg), Dr. Pierre Royer (KUL)

Chloi Vamvatira-Nakou: *Studies of nebulae ejected from massive stars based on observations with the Herschel Space Observatory*

Cover image: Artist concept of the Herschel spacecraft – ESA

The work presented in this thesis was done thanks to the financial support from the Belgian Federal Science Policy Office via the PRODEX Programme of ESA. It is based on observations made by *Herschel*, an ESA space observatory with science instruments provided by European-led Principal Investigator consortia and with important participation from NASA.
This document was typed in LaTeX using the *ClassicThesis* package.

στους γονείς μου

ACKNOWLEDGMENTS

I wish to thank my PhD supervisor Dr. Damien Hutsemékers for having given me the opportunity to work in such an interesting field with new data and for his valuable help during the years of this work towards the completeness of this thesis.

I thank all the members of the jury for accepting to be part of it. Moreover, I wish to thank Dr. Pierre Royer for the hours spent to explain me how the infrared instruments onboard Herschel work, for his valuable help with the data reduction and for his suggestions for the data analysis and interpretation, Dr. Martin Groenewegen for having given me the opportunity to be part of the MESS collaboration and for his valuable suggestions during this work, Dr. Yäel Nazé for helping me with the data analysis and for her comments and suggestions that greatly improved my work and this manuscript, Prof. Gregor Rauw, the leader of the group where I belonged during this work, for all his help, Prof. Pierre Magain for the deconvolution that he performed for one of the studied targets and for his valuable help with all the PhD formalities and Dr. Nick Cox for providing the maps of the studied nebulae and for all his suggestions that improved the studies presented in this thesis. I wish to thank Prof. Jean Surdej for accepting to be the president of the jury.

Many thanks to all the MESS collaborators. It was my pleasure to be part of this team. I thank especially Prof. Michael Barlow for his valuable suggestions, Prof. Christoffel Waelkens for encouraging me with his kind comments, Dr. Katrina Exter for helping me with the data reduction and Dr. Djazia Ladjal for the valuable discussions.

Special thanks goes to Sandrine Sohy and Alain Detal for always being there willing to help me with all the software and hardware problems I faced during the years of this work. I wish to thank all people working in the Herschel Helpdesk for their quick and precise answers to all the tickets I have sent for problems with the HIPE package. A big thank to Denise Caro, Sylvia Grandjean, Angela della Vecchia and Mélanie Gardier for their help with the administration procedures and formalities.

I thank the colleagues of the department for making the institute such a friendly place to work. I thank all my friends, new and old ones, here in Belgium and abroad, for the happy moments that we have spent together.

Last but not least, I wish to thank my family in Greece, my brother and my parents, for their support during all these years of my PhD. Thanks to my parents who have never forced me to do anything I have followed my dream to study astrophysics.

ABSTRACT

This PhD thesis is devoted to the study of the nebulae ejected by the luminous blue variable (LBV) stars WRAY 15-751 and AG Car as well as by the Wolf-Rayet star WR 124. It is based on new infrared data taken by the Herschel Space Observatory. These data were complemented by optical data as well as by archived infrared observations.

In the first chapter, a general introduction to the subject is given along with a description of the methods used for the data analysis. The three following chapters contain the study of each one of the three nebulae separately. This led to the determination of the physical parameters of the dust and gas components, with the aim to shed a new light on the mass-loss history of the central stars.

In particular, the new Herschel infrared images provide a detailed mapping of the nebular dust distribution and of the circumstellar environment at different scales, revealing multiple shells and cavities linked to previous mass-loss events. Moreover, the combination of Herschel photometric results along with archival data was used to model dust with the help of a two-dimensional publicly available radiative transfer code. This model provided us with the dust mass, temperature and composition.

The Herschel infrared spectra of all nebulae revealed forbidden nebular emission lines coming not only from an ionized gas region but also from a region where the gas is neutral. Based on the emission line flux measurements, the gas mass and the abundance ratios were estimated. These results, combined with the theoretical models of stellar evolution, were then used to constrain the evolutionary stage of the star at which each nebula was ejected.

This study underlines the importance of the Herschel infrared observations for these nebulae. Thanks to them, a better understanding of these objects has been achieved. In particular, a second bigger and fainter dust shell was discovered around WRAY 15-751. In addition, all nebulae were found lying in empty cavities, probably formed during a previous evolutionary phase of their central star. The dust models indicated the necessity to include large grains in all nebulae to reproduce the data. This study showed that for the LBV WRAY 15-751, with an initial mass of 40 $M_{\odot}$, the nebular ejection took place during a red supergiant phase, while for the LBV AG Car, with an initial stellar mass of 55 $M_{\odot}$, the ejection happened during a cool LBV phase. For the nebula M1-67 around the star WR 124, with an initial mass of 60 $M_{\odot}$, the ejection also took place during a LBV phase. These results are in agreement with the current evolutionary models with little stellar rotation.

RÉSUMÉ

Cette thèse de doctorat est dédiée à l'étude des nébuleuses ejectées par les étoiles variables lumineuses bleues (LBV) WRAY 15-751 et AG Car, ainsi que par l'étoile Wolf-Rayet WR 124. Elle est basée sur des nouvelles données infrarouges obtenues par l'Observatoire Spatial Herschel, complétées par des données optiques et infrarouges archivées.

Dans le premier chapitre, une introduction générale est donnée avec une description des méthodes utilisées pour l'analyse des données. Les trois chapitres suivants se rapportent à l'étude individuelle de chacune des nébuleuses. Les analyses conduisent à la détermination des paramètres physiques de la poussière et du gaz qui composent les nébuleuses, ce qui nous éclaire sur l'historique de la perte de masse par les étoiles centrales.

Ainsi, les images fournies par Herschel fournissent une cartographie précise de la poussière, et révèlent l'environnement circumstellaire à différentes échelles, mettant en évidence la présence de cavités dues à des éjections plus anciennes. De plus, en combinant les résultats photométriques obtenus avec Herschel avec les données archivées, un modèle de la poussière a été élaboré en utilisant un code de transfert radiatif bidimensionnel disponible publiquement. Cette modélisation nous a fourni la masse, la température et la composition de la poussière.

Les spectres infrarouges de toutes les nébuleuses ont révélé des raies en émission interdites ne venant pas seulement de la région du gaz ionisé mais aussi d'une région où le gaz est neutre. Sur base des mesures de flux des raies en émission, la masse du gaz et les rapports des abondances ont été estimés. Ces résultats, couplés aux modèles théoriques d'évolution stellaire, ont été utilisés pour contraindre le stade évolutif de l'étoile au moment où la nébuleuse a été éjectée.

Cette étude souligne l'importance des observations de ces nébuleuses réalisées avec Herschel. Grâce à elles, une meilleure compréhension de ces objets a été obtenue. Notamment, une seconde nébuleuse de poussière, plus large et plus faible a été découverte autour de WRAY 15-751. Toutes les nébuleuses ont été observées dans des cavités vides, probablement formées pendant une phase évolutive précédente des étoiles centrales. Les modèles d'émission de la poussière ont indiqué la nécessité d'inclure des gros grains pour reproduire les données. Notre étude a montré que pour la LBV WRAY 15-751, avec une masse initiale de 40 $M_{\odot}$, l'éjection de la nébuleuse a eu lieu pendant la phase de supergéante rouge, tandis que pour la LBV AG Car, avec une masse initiale de 55 $M_{\odot}$, l'éjection s'est passée pendant la

phase LBV froide. Pour la nébuleuse M1-67 autour l'étoile WR 124, avec une masse initiale de 60 $M_{\odot}$, l'éjection a aussi eu lieu pendant la phase LBV. Ces résultats sont en accord avec les modèles actuels d'évolution stellaire incluant peu de rotation stellaire.

CONTENTS

LIST OF FIGURES

LIST OF TABLES

ACRONYMS

AGB Asymptotic Giant Branch

BB Black Body

BSG Blue Super Giant

CCD Charge-Coupled Device

ESA European Space Agency

ESO European Southern Observatory

FIR Far-InfraRed

FUV Far-UltraViolet

FWHM Full Width at Half Maximum

HIFI Heterodyne Instrument for the Far Infrared

HIPE Herschel Interactive Processing Environment

HR Hertzsprung-Russell

HST Hubble Space Telescope

IRAF Image Reduction and Analysis Facility

IRAS Infrared Astronomical Satellite

ISO Infrared Space Observatory

LBV Luminous Blue Variable

LMC Large Magellanic Cloud

MADmap Microwave Anisotropy Dataset mapper

MESS Mass-loss of Evolved StarS

NTT New Technology Telescope

OD Observational Day

obsID observation Identification Number

PA Position Angle

PACS Photodetector Array Camera and Spectrometer

PAH Polycyclic Aromatic Hydrocarbon

PDR Photodissociation Region

PN Planetary Nebula

PSF Point Spread Function

RSG Red Super Giant

RSRF Relative Spectral Response Function

SED Spectral Energy Distribution

SN SuperNova

SPIRE Spectral and Photometric Imaging Receiver

STSDAS Space Telescope Science Data Analysis System

WR Wolf-Rayet

YHG Yellow Hyper Giant

YSG Yellow Super Giant

ZAMS Zero Age Main Sequence

Part I

INTRODUCTION, DATA AND METHODS

1

INTRODUCTION

In the first part of this introductory chapter, the group of the massive evolved star is presented and more particularly the subgroups of Luminous Blue Variable (LBV) and Wolf-Rayet (WR) stars, since two of the three nebulae analyzed in this study are located around a LBV star and the third one surrounds a WR star. The basic characteristics and physical properties of these stars are given, followed by an overview of open questions concerning these stellar evolutionary stages.

In the second part, our scientific project that is based on *Herschel* data is presented. Firstly, the *Herschel* guaranteed time key programme Mass-loss of Evolved StarS (MESS) is described and secondly our project that is more specifically dedicated to the study of massive evolved stars is presented.

In the third part, the infrared and optical photometric and spectroscopic observations of the nebulae together with the reduction procedures are presented. The *Herschel* Space Observatory mission is described along with two of the three onboard instruments which were used for the infrared observations, followed by a presentation of the observing modes and the data reduction steps for the infrared imaging and spectroscopy of the three nebulae discussed in this study. In addition, the optical instruments used for the imaging of the nebulae are presented along with their specific data reduction procedures.

In the last part, the methods used for data analysis are presented. Since this study is based on infrared and optical observations, the data gives information on the dust and the gas that together form the nebulae. The dust nebula modeling is discussed first. The publicly available radiative transfer code 2-Dust used for the dust modeling is presented. After, the tools for the analysis of the ionized gas emission are presented, followed by the tools for the analysis of the neutral gas emission. Finally, a description of the method to constrain the evolutionary path of the central star and the epoch at which the nebula was ejected is given. It is based on the available information obtained from the data analysis and on the current theoretical models of stellar evolution.

1.1 MASSIVE STARS

A star is considered to be massive when it has an initial mass higher than about 8 $M_\odot$ at a solar metallicity. At the Zero Age Main Sequence (ZAMS), it is an O-type or B-type star and, depending on its initial mass and rotation, it can end its life as Red Super Giant (RSG), Yellow Hyper Giant (YHG), LBV or WR star (Groh et al. 2013 [43]) that are all core-collapse SuperNova (SN) progenitors.

Massive stars are rare in the Universe in comparison to the number of stars with lower masses, because of the steepness of the initial mass function that describes the rate of star formation as a function the stellar mass (Salpeter 1955 [122]; Miller & Scalo 1979 [93]; Chabrier 2003 [13]) and because of their short lifetime of some million years. However, despite their rarity, massive stars have a crucial role in astrophysics and their study is extremely important.

Massive stars are important sources of chemical enrichment of the interstellar medium because only in their cores the temperature and pressure reach values high enough for the carbon fusion to begin. Moreover, important amount of dust that contributes significantly to the enrichment of the interstellar medium with metals is produced not only during SN explosions but also during LBV eruptions, where large dust grains can be formed (Kochanek 2011 [69], 2014 [70]). This enriched material is then spread into the interstellar medium in the form of gas and dust through strong stellar winds, through episodes of extreme mass-loss at the late stages of their evolution and through the powerful SN explosions at the very end of their lifetime.

In addition, massive stars largely contribute to the total radiation of their host galaxies, to the ionization of their surrounding interstellar medium by ultra-violet photons and to the infrared emission through the heating of the dust. Furthermore, massive stars interact with the interstellar medium. Their strong stellar winds, which inject huge amounts of mechanical energy into the interstellar medium, can form wind-blown bubbles, while episodes of extreme mass-loss, like the outbursts during a LBV phase, can form nebulae around the stars. Depending on the stellar motion, these bubbles and nebulae can form bow shocks. Consequently, the study of the circumstellar environments is crucial for understanding the mass-loss history and the evolution of massive stars.

In this thesis, the study of three nebulae, two around LBVs and one around a WR star, is presented. The main aim is to shed light on the formation process of the nebulae as well as on the mass-loss history and the evolutionary stage of the central star at that time. This is achieved by precisely calculating the parameters of the gas (density, abundances, mass) and the dust (temperature, mass, composition) components of the nebulae based on new sensitive infrared data combined with archival data and optical observations.

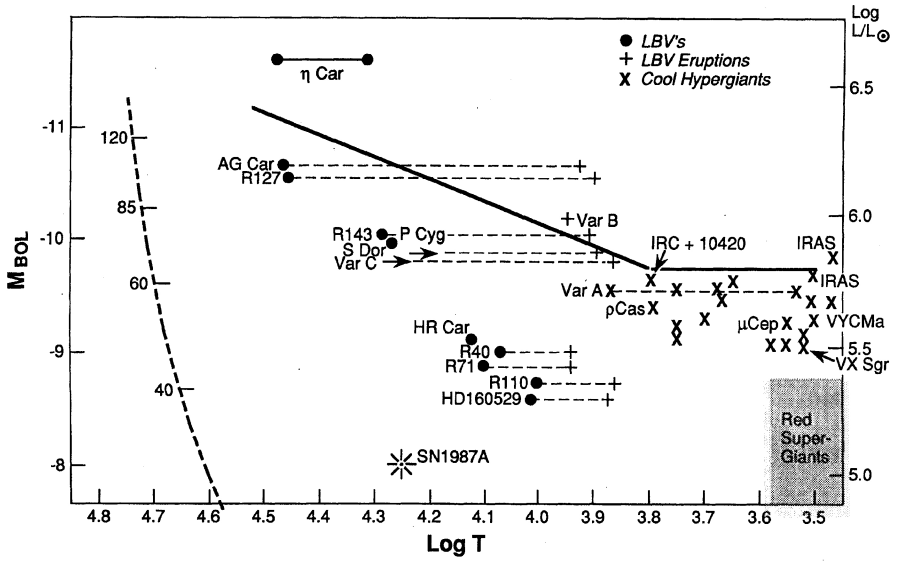

Figure 1.1: The location of the most luminous stars in the HR diagram. The dashed lines represent the transition of the LBV stars from the quiescence, the minimum hot phase, to the eruption, the maximum cool phase. Luminous cool hypergiants are also plotted. The solid line represents the empirical upper luminosity limit. Image reproduced from Humphreys and Davidson (1994 [117]).

1.1.1 *Luminous blue variables*

Conti (1984 [19]) used the term "luminous blue variable" LBV for the first time to refer to hot luminous massive variable stars that are evolved but are not WR stars. According to current evolutionary scenarios (Maeder & Meynet 2010 [79]), LBV represent a short stage ($\sim 10^4 - 10^5$ yr) in the evolutionary path of an early-type O star with initial mass $\geqslant 30\ M_\odot$ that evolves to a WR star by losing a significant fraction of its initial mass. The mass is lost through the stellar wind and through episodes of extreme mass-loss during an intermediate phase of the star, like the LBV outbursts. The number of stellar objects that have been confirmed to be LBV stars is quite small in the Milky Way and the nearby galaxies. This is explained by the short duration of this evolutionary phase. The most well known galactic LBV stars are η Carinae and P Cygni.

These unstable transition objects, also known as S Doradus variable stars, are located in the upper left part of the Hertzsprung-Russell (HR) diagram, although some of them undergo occasional excursions to the right during their outbursts (Fig. 1.1). They have the following characteristics: a) high luminosity, $\sim 10^6\ L_\odot$, close to the Eddington limit (Maeder & Conti 1994 [78]; Humphreys & Davidson 1994 [117]) which is an upper limit of the luminosity to mass ratio in the HR diagram, and some times above the Humphreys-Davidson limit (Humphreys and Davidson 1979 [57]) that is the limit above which

a massive star becomes unstable and high mass-loss episodes take place (Fig. 1.1); b) high mass-loss rates, from $\sim 10^{-5}$ to 10^{-4} $M_\odot$ yr^{-1} (Humphreys & Davidson 1994 [117]; Smith et al. 2004 [135]; Groh et al. 2009 [41]); and c) photometric variability, with amplitudes from $\sim$ 0.1 mag that correspond to small oscillations up to $\geqslant$ 2 mag that correspond to giant LBV eruptions, like P Cygni in the 17th century and η Carinae in the 19th century. The smaller variations may be superposed to the larger ones.

Eruptions of $1-2$ mag, in the visual, with a timescale of $10-40$ yr, detected as a visual brightening due to the maximum luminosity shift from the ultra-violet to visual wavelengths (Humphreys & Davidson 1994 [117]; Smith 2014 [134]), constitute the so-called S Dor phase of a LBV star (van Genderen [159]). During the quiescent or minimum (i.e., minimum V brightness) hot phase, LBVs have temperatures from 12 000 to 30 000 K, with the hottest being the most luminous. In this case they display spectra of hot supergiants or Of/WN9 stars, depending on their luminosity (Humphreys & Davidson 1994 [117]; Smith et al. 2004 [135]; Smith 2014 [134]). In the maximum, cool phase, they all have temperatures of $\sim 7000-8000$ K and display spectra of a cool supergiant of A or F spectral type (Humphreys & Davidson 1994 [117]; Smith 2014 [134]). The S-Dor variations occur at constant luminosity (Humphreys & Davidson 1994 [117]) although Groh et al. (2009 [41]) reported variations in the bolometric luminosity of the LBV star AG Car.

Many LBV stars are surrounded by circumstellar nebulae that are formed from material ejected during previous eruption events rather than from a continuous stellar wind (Hutsemékers 1994 [59]; Nota et al. 1995 [103]; Smith 2014 [134]). Nota et al. (1995 [103]) classified morphologically the LBV nebulae into three main groups: a) shell nebulae, the majority; b) filamentary nebulae, like the one around the LBV HR Car; and c) peculiar morphologies like the case of P Cyg. Dust has been detected in many LBV nebulae (McGregor et al. 1988 [88]; Hutsemékers 1997 [60]). The study of these circumstellar nebulae provides the total amount of the ejected mass during an eruption (Smith 2014 [134]) and the stellar surface abundances at the time of the ejection (Smith 1997 [130]).

1.1.2 *Wolf-Rayet stars*

WR stars are characterized by strong broad emission lines in the optical region due to stellar winds. They are named after the astronomers Wolf and Rayet (1867 [171]) who reported the discovery of three stars with broad emission lines in the constellation of Cygni. They are divided into two groups: a) the WN subtypes that show strong lines of He and N; and b) the WC and WO subtypes that show strong He, C, and O in their spectra (Crowther 2007 [21]). The WN stars show the

products of the CNO hydrogen burning cycle at their surface, while the WC stars show the products of triple-α helium burning reactions (Maeder and Conti 1994 [78]; Crowther 2007 [21]).

WR stars represent an intermediate phase in the late evolution of O-type massive stars with an initial mass $\geqslant$ 30 $M_\odot$ (Maeder & Meynet 2010 [79]). The initial star loses a significant fraction of its mass through the stellar wind and/or through episodes of extreme mass-loss during an intermediate evolutionary phase, a RSG or LBV phase. The outer layers are removed, revealing the products of hydrogen burning, and subsequently helium burning at the stellar surface, leaving a bare core that becomes a WR. The lower limit for the initial stellar mass is not as robust for a WR belonging to a close binary system (Crowther 2007 [21]). In such cases the H-rich envelope is lost through a Roche-lobe overflow. The luminosity of WR stars is $\sim 10^5 - 10^6$ $L_\odot$, their temperature is about 35 000 – 85 000 K, and they have mass-loss rates between $\sim 10^{-5}$ to 10^{-4} $M_\odot$ yr^{-1} (Crowther 2007 [21]).

Marston (1997 [85]) observed that one third of the galactic WR stars have an associated nebula in the optical. Different types of morphologies have been observed around galactic WR stars by Chu et al. (1983 [15]) who divided them into categories according to their formation mechanism: wind-blown bubbles, stellar ejecta and HII regions. A similar percentage of the WR stars in the Magellanic Clouds are surrounded by ring nebulae, either formed from stellar ejecta or from swept-up interstellar material (Dopita et al. 1994 [25]). The ring nebulae around WR stars are thought to represent material that has been ejected in a previous evolutionary phase of the star, a LBV or a RSG phase (Crowther 2007 [21]). The chemical abundances in the WR nebulae are similar to the abundance in the LBV nebulae (Smith 1997 [130]). Moreover, cold dust has been detected in WR nebulae (Marston 1991 [83]; Mathis et al. 1992 [87]) as it is the case of LBV nebulae. The study of WR nebulae provides information on the previous evolutionary stages of the WR stars and their mass-loss history.

1.1.3 *Open issues on the massive star evolution*

Despite the huge progress of observational studies that has been made in the last years at all wavelengths and the theoretical studies based on sophisticated models, there are still questions on all the stages of the evolution of massive stars that need to be tackled.

In particular, the current models of stellar evolution do not include any eruption events. That makes the predicted post-main-sequence evolutionary paths very uncertain. The role of rotation in the evolution of those stars is not yet perfectly understood. Also, the dependence of the evolution on the metallicity is a very important aspect that requires more observational data to be better understood. The

cause of clumpiness in massive stellar winds that led to re-estimate the mass-loss rates downwards is still uncertain. The mechanism at the origin of the formation of nebulae around massive star needs to be unveiled. The role of the dust in these circumstellar environments is extremely important but the mechanisms of its formation during LBV eruptions and SN explosions are not clearly known.

For the LBV stars, it is still unclear what is the cause of the violent eruptions and what mechanism can explain them. This is very important for understanding why nebulae around LBV are observed to have different morphologies. Also, the role of these LBV eruptions in the evolution of the star is not entirely known. Important parameters, such as the total mass lost during a LBV outburst, the LBV lifetime and the mass-loss rate need to be precisely constrained from the observations and then explained by theoretical models.

For the WR stars, it is very important to obtain accurate stellar physical parameters for a bigger sample of all types in order to constrain their evolution towards the end points of massive stellar evolution and better understand the link between them and the SN explosions. The similarities between nebula around WR stars and nebulae around LBV stars need to be studied in detail to establish more firmly the connection between these two evolutionary stages.

1.2 OUR PROJECT WITH HERSCHEL

1.2.1 *The Herschel MESS guaranteed time key programme*

The *Herschel* infrared observations of the nebulae were carried out mainly in the framework of the *Herschel* MESS[1] guaranteed time key programme with Dr. Martin Groenewegen as principal investigator. The observing list of this programme contains 128 objects with a total duration of 330 hours of observations. The *Herschel* onboard instruments Photodetector Array Camera and Spectrometer (PACS) and Spectral and Photometric Imaging Receiver (SPIRE) were used for these observations. The corresponding proposal was a joint effort by Belgium (PACS), Austria (PACS), Heidelberg-Germany (PACS), SPIRE SAG-6 group, the Herschel Science Centre, and Mission Scientists.

The aim of the MESS programme was the study of the circumstellar environment in post-main-sequence objects of various masses: low- and intermediate-mass objects (Asymptotic Giant Branch (AGB), post-AGB, Planetary Nebula (PN)), high-mass stars (RSG, WR, LBV), and SN. More precisely, by searching for single or multiple shells around a representative sample of evolved stars with the help of infrared imaging, it aims to study the mass-loss history of these stars and their interaction with the interstellar medium. It aims also to study the dust and gas chemistry in the circumstellar environment of these ob-

1 http://www.univie.ac.at/space/MESS/

Object	Type	PACS imag.	PACS spectr.	SPIRE imag.	SPIRE spectr.
AG Car	LBV	MESS	MESS	-	MESS
HR Car	LBV	MESS	GT2	-	-
WRAY 15-751	LBV	MESS	*	-	-
G79.29+0.46	LBV	MESS	GT2	-	-
He 3-519	LBV?	MESS	-	-	-
HD 168625	LBV?	MESS	MESS	-	-
M1-67	WR	MESS	GT1	MESS	MESS
NGC 6888	WR	MESS	-	-	-
NGC 6164/5	Of?p	GT1	GT2	-	-

Notes. * Observed during the calibration phase of the instrument

Table 1.1: List of objects of our project dedicated to the study of circumstellar environments of massive evolved stars. The object studied in this thesis are in blue.

jects with the help of infrared spectroscopic observations. A detailed description of the MESS key programme is given in Groenewegen et al. (2011 [39]) where the target selection and the observing strategy are presented along with results obtained during *Herschel*'s science demonstration phase. First results and an updated status were later presented in Groenewegen et al. (2011 [40]).

1.2.2 *Massive evolved stars study*

In the framework of the MESS programme, our project is dedicated to the circumstellar environments of massive evolved stars, LBVs and WR stars (Vamvatira-Nakou et al. 2011 [155]), aiming at studying in detail the gas and the dust physical properties.

Herschel data consist of flux-calibrated images and flux-calibrated spectra, mostly taken with the PACS instrument (see Table 1.1). In our analysis, they were combined with older infrared data as well as with archival radio and optical observations. The images taken in different wavebands provide detailed information on the dust content of the nebulae (grain size and structure, total mass, temperature). The spectra on the other hand enable us to determine the properties of the gas component (density, temperature, abundances). Overall, this project aims at studying and understanding the mass-loss history of these stars.

The objects that have been observed as part of the MESS programme by Dr. Damien Hutsemékers, Dr. Pierre Royer and Prof. Gregor Rauw are the LBVs AG Car, HR Car, WRA 15-751 and G79.29+0.46, the candidate LBVs He 3-519 and HD 168625 and the WR nebulae M 1-67 and NGC 6888. The target list was complemented with the nebula NGC 6164/5 around the peculiar Of?p star HD 148937 observed after the

acceptance of two guaranteed time (GT) proposals for the first and the second in-flight Announcement of Opportunity (AO1 and AO2) with Dr. Pierre Royer as principal investigator. This target list consists of a representative sample of nebulae with various morphologies around LBV and WR stars of different luminosities. It is presented in Table 1.1 along with the instrument used and the corresponding programme (MESS, GT1 or GT2). Images of some of these targets are given in Fig. 1.2, Fig. 1.3[2] and Fig. 1.4[3].

This thesis focuses on three nebulae; the nebula around the LBV star WRAY 15-751 (Chap. 2), the nebula around the LBV star AG Car (Chap. 3) and the nebula M1-67 around the star WR 124 (Chap. 4).

1.3 OBSERVATIONS

1.3.1 *Infrared Herschel observations*

The *Herschel* Space Observatory[4] (Pilbratt et al. 2010 [113]) is a mission of the European Space Agency (ESA). It was launched on 14 May 2009, on an Ariane 5 ECA rocket that was shared with *Planck*, another mission of ESA, from Kourou, French Guyana. It then reached its operational orbit around the 2nd Lagrangian Point of the Earth-Sun system located 1.5 million km from Earth. *Herschel* carried the largest telescope ever flown in space, with a primary mirror diameter of 3.5 m (Fig. 1.5). It is the first space observatory dedicated to observe the full far-infrared and submillimetre waveband (55-670 μm). The scientific observations started in autumn 2009 and ended on 29 April 2013 when *Herschel* ran out of helium.

Three instrument were onboard *Herschel*; PACS (Poglitsch et al. 2010 [115]), SPIRE (Griffin et al. [38]) and the Heterodyne Instrument for the Far Infrared (HIFI) (de Graauw et al. 2010 [23]). In this thesis, only data taken with PACS and SPIRE, each one of them composed of a photometer and a spectrometer, are analyzed and discussed.

The PACS imaging dual-band photometer consists of two filled bolometer arrays, one of 64×32 pixels (blue channel) and another of 32×16 pixels (red channel), that allow the simultaneous imaging in two bands: 60-85 μm (blue filter) or 85-130 μm (green filter) and 130-210 μm (red filter).

The observing mode that was used for all the nebulae is the 'scan map' mode at which the telescope slews at constant speed (the medium speed of 20″/s in this case) along parallel lines to cover the required area of the sky. For each nebula two orthogonal scan

2 Images presented in the poster presentation by Vamvatira-Nakou et al. in the conference "The Universe Explored by Herschel" held in ESA/ESTEC, Noordwijk, on 15-18 October 2013 (http://www.cosmos.esa.int/web/herschel/the-universe-explored-by-herschel).

3 Image presented in Vamvatira-Nakou et al. (2011 [155]).

4 http://www.cosmos.esa.int/web/herschel

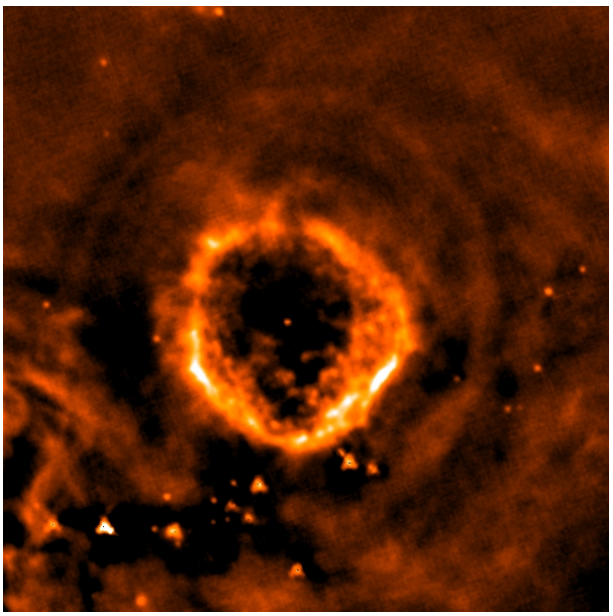

Figure 1.2: The PACS 70 μm image of the LBV star G79.29+0.46 is a characteristic case of multiple shells detection around the central star. The size of the image is 10′×10′. North is up and east is to the left. The 'highpassFilter' task was used to produce the image (see Sect. 1.3).

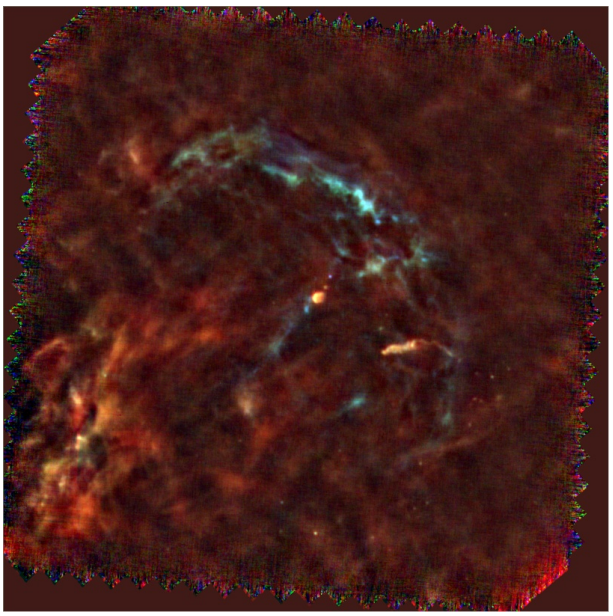

Figure 1.3: Three-color (70 μm in blue, 100 μm in green, and 160 μm in red) PACS image of the nebula NGC 6888 around the star WR 136. The size of the image is 27′×27′. North is up and east is to the left. The 'highpassFilter' task was used to produce each one of the three images (see Sect. 1.3).

maps were obtained with an angle of 90° between them. The final

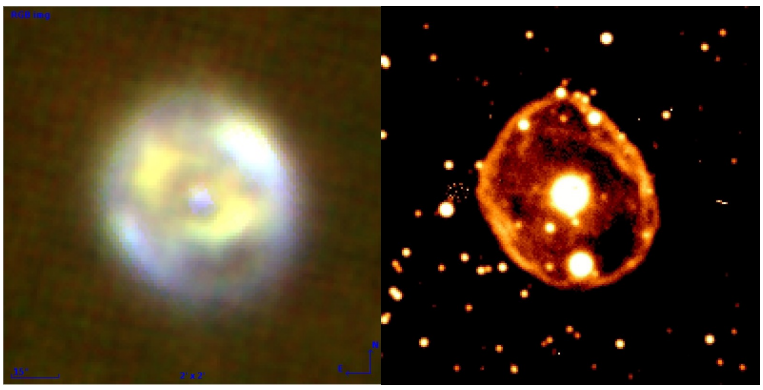

Figure 1.4: The nebulae around the LBV candidate He 3-519. *Left*: morphology in the IR (RGB image with R being the PACS 100 µm image, G the PACS 70 µm image and B the Spitzer 24 µm image). The 'highpassFilter' task was used to produce the images (see Sect. 1.3). *Right*: Hα image obtained with the 3.6m telescope at ESO, La Silla, Chile. The dimensions of both images are 2×2 arcmin. North is up and east is to the left.

PACS imaging data sets consists of maps at 70, 100 and 160 µm. For the data reduction, the Herschel Interactive Processing Environment (HIPE) (Ott 2010 [108]), specifically designed for the *Herschel* data, was used.

The 'highpassFilter' task detailed in Groenewegen et al. (2011 [39]) was used to produce the final images of WRAY 15-751 (see Sect. 2.2). To investigate fainter nebular emission at large scales, a second independent data reduction was performed using the Microwave Anisotropy Dataset mapper (MADmap) algorithm (Cantalupo et al. 2010 [10]) provided in HIPE. This is an optimal algorithm for map making, designed to remove the uncorrelated (1/f) noise from bolometer time ordered data based on matrix inversion, so that the final maps have no banding or striping effects. That helps the detection of possible faint emission.

For the data of AG Car and M1-67 (see Sect. 3.2 and Sect. 4.2, respectively), after the reduction up to level 1, using HIPE, the Scanamorphos software (Roussel 2013 [119]) was used to further reduce and combine the data to produce the final images. This, new at that time, software contains an optimal algorithm for map reconstruction from scan observations made with bolometer arrays and especially *Herschel* data. It was designed to remove the low-frequency noise without depending on any noise model but using the redundancy in the observations. It preserves the flux and can restore point sources and extended structures with scales just below the map size.

For the nebula around WRAY 15-751, deconvolution was applied to the three PACS images produced with the 'highpassFilter' task to better reveal the morphology of the inner nebula, using the Point Spread Function (PSF) of Vesta and the MCS deconvolution method

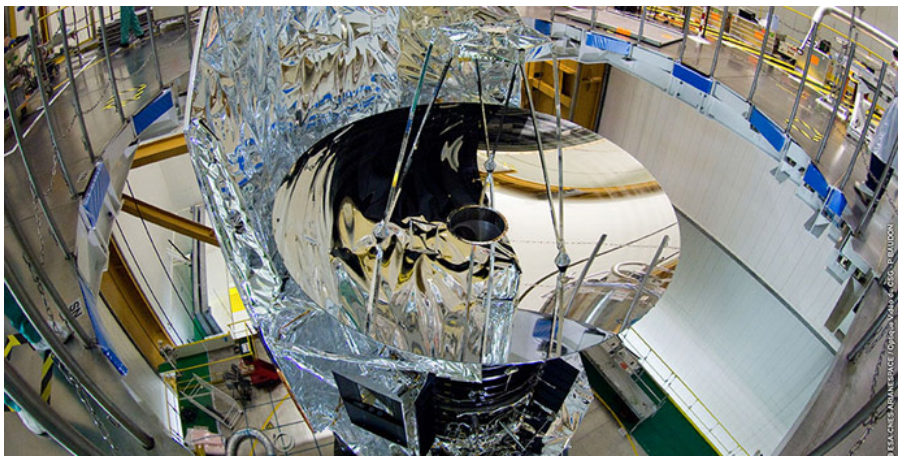

Figure 1.5: The Herschel Space Telescope. ESA-CNES-Arianespace / Optique Vidéo du CSG - P Baudon.

(Magain et al. 1998 [80]). It was performed only on this nebula because it is the smaller one. From its convolution with the PACS PSF a difference can result in the observed morphology with respect to the real nebular morphology. The *Herschel* PACS PSF Full Width at Half Maximum (FWHM)s are 5.2″, 7.7″ and 12″ at 70 μm, 100 μm and 160 μm, respectively. The MCS method has the advantage of not violating the sampling theorem. Each image is not deconvolved by the total PSF, which leads to an infinite resolution, but with a partial PSF chosen to respect the desired resolution of the final deconvolved image. After the deconvolution with the corresponding PSF, the final spatial resolution was twice as good as the initial one.

The PACS integral-field spectrometer is composed of two Ge:Ga photoconductors arrays with 16×25 pixels. It covers the wavelength range from 52 μm to 220 μm in two channels that operate simultaneously in the blue, 52-98 μm band (second order: B2A 52-73 μm and B2B 70-105 μm, third order: B3A 52-73 μm), and the red, 102-220 μm band (first order: R1A 133-220 μm and R1B 102-203 μm). It provides simultaneous imaging of a $47'' \times 47''$ field of view that is resolved in 5×5 square spatial pixels (i.e., spaxels). An image slicer employing reflective optics is used to re-arrange the two-dimensional field-of-view along a 1×25 pixels entrance slit for the gratings. Its resolving power is $\lambda/\delta\lambda \sim 940 - 5500$, depending on the wavelength.

The 'Spectral Energy Distribution (SED)' observing mode that provides a complete coverage between 52 and 220 μm was used for the observations of WRAY 15-751 and AG Car. For the nebula M1-67, the 'chopped line scan' mode was used in which, instead of having a complete coverage, the observations are done in specific, previously chosen, short wavebands between 52 μm and 220 μm where it is possible to detect a nebular emission line. The data reduction was performed using HIPE and following the standard reduction steps, in particular

Object	PACS imag.	PACS spectr.	SPIRE imag.	SPIRE spectr.
WRAY 15-751	scan map	SED	-	-
AG Car	scan map	SED	-	spectro point$^{\alpha}$
M1-67	scan map	chop. line scan	large map	spectro point$^{\alpha}$

Notes. $^{(\alpha)}$ These observations were not used in this study (see Sect. 3.5 and Sect. 4.5)

Table 1.2: Observing modes of the three nebulae studied in this thesis.

the subtraction of the background spectrum obtained through chopping and nodding.

The SPIRE imaging three-band photometer is composed of three photometer bolometer arrays that allow the simultaneous imaging at 250, 350 and 500 μm. Only the nebula M1-67 was observed with this instrument. The observing mode used was the 'large map', in which the telescope also slews at constant speed (the nominal speed of 30″/s in this case) along parallel lines so as to scan the required sky area. To obtain two orthogonal scans during a single observation, the cross scan pointing mode was selected. These data were retrieved from the archive, processed up to level 2. The surface brightness of the three maps was then transformed from Jy/sr to Jy/pixel, with the help of HIPE, to further analyze the data.

The SPIRE Fourier Transform spectrometer consists of two bolometer detector arrays that operate simultaneously at 194-313 μm and 303-671 μm respectively. The spectral resolution is variable, $\lambda/\delta\lambda \sim 40 - 1000$ at 250 μm. The 'single pointing' observing mode was used to observe AG Car and M1-67. These observations were not used in this study because the target flux cannot be recovered with certainty, due to the chosen observing mode and the detector geometry with respect to the nebular geometry (see Sect. 3.5 and Sect. 4.5).

Table 1.2 summarizes the observing modes, both the photometric and the spectroscopic ones, that were used for each one of the three nebulae studied in this thesis.

1.3.2 *Optical observations*

The optical observations were carried out using the 3.6-m telescope at the European Southern Observatory (ESO), La Silla, Chile[5], by Dr. Damien Hutsemékers between 1994 and 1995. This telescope is located at an altitude of 2400 meters above sea level. The EFOSC1 camera was used for these observations. For each one of the nebulae,

5 https://www.eso.org/sci/facilities/lasilla/telescopes/3p6.html

a series of short and long exposures, whose duration depends on the object, were secured in a Hα+[NII] filter (λ_c = 6560.5Å; FWHM = 62.2Å), and in a continuum filter just redward (λ_c = 6644.7Å; FWHM = 61.0Å). The frames were bias-corrected and flat-fielded. An example image obtained with this optical instrument is given in Fig. 1.4

1.4 DATA ANALYSIS METHODS

1.4.1 *Dust nebula modeling*

The *Herschel* infrared images of the three nebulae give information on the distribution of the dust in these circumstelllar environments. The aperture photometry, performed using HIPE, provides the nebular fluxes at the different observed wavelengths. This nebular SED enables us to model the dust, hence to calculate its mass, temperature and composition. To complement the infrared photometric datasets with nebular fluxes at other wavelengths, infrared data obtained during previous space missions were taken from the NASA/IPAC Infrared Science Archive[6] and from the literature.

1.4.1.1 *The 2-Dust code*

The publicly available two-dimensional radiative transfer code 2-Dust (Ueta and Meixner 2003 [152]) was used to model the dust nebulae of the three targets. This code solves the radiative transfer equations in a two-dimensional polar grid by considering a three-dimensional radiation field. It can be supplied with various grain size distributions and optical properties as well as complex axisymmetric density distributions. Its advantage, apart from the two-dimensionality, is that it uses the geometry constraints from the infrared images of the nebulae and specifically the inner nebular radius.

In this code, spherical polar coordinates are used for the grid points with the assumption of axial symmetry. The profile of the dust density is a two-dimensional function $\rho(r,\Theta)$. Symmetry with respect to the equatorial plane is also assumed. The grid consists of radial zones. At each position (r,Θ), the directions are defined by two angles, θ and ϕ. The specific intensity, $I_\nu(r,\Theta;\theta,\phi)$, is calculated using the solution of the radiative transer equation

$$I_\nu(r,\Theta;\theta,\phi) = \int_{(r,\Theta)}^{(r_0,\Theta_0)} S_\nu(r',\Theta';\theta,\phi) e^{-\tau_\nu(r',\Theta')} d\tau_\nu \ , \qquad (1.1)$$

where S_ν is the source function and τ_ν is the optical depth. The line integration is done from the point (r,Θ) to the point (r_0,Θ_0) which is the end of the shell. After the end of the line integration, the mean specific intensity is computed and then the local temperature of dust grains is derived assuming radiative equilibrium. The

6 http://irsa.ipac.caltech.edu/

2-Dust code uses the iterative method described in Collison and Fix (1991 [18]) to constrain the fields of radiation and temperature with self-consistency.

Practically, it is first necessary to consider the morphology of the nebula revealed through the infrared PACS so as to choose the best geometric parameters for the axisymmetric dust density distribution model. The 2-Dust code uses a normalized density distribution function (Meixner et al. 2002 [89]) that is based on a layered shell model,

$$\rho(R,\theta) = \left(\frac{R}{R_{min}}\right)^{-B\left\{1+C\sin^F\theta\left[e^{-(R/R_{sw})^D}/e^{-(R_{min}/R_{sw})^D}\right]\right\}} \times\left\{1+A(1-\cos\theta)^F\left[e^{-(R/R_{sw})^E}/e^{-(R_{min}/R_{sw})^E}\right]\right\}, \quad (1.2)$$

where $\rho(R,\theta)$ is the dust mass density at radius R and latitude θ, R_{min} is the inner radius of the shell, and R_{sw} is the superwind radius that defines the boundary between the spherical wind and the axisymmetric superwind. The first term represents the radial profile of the spherical wind; the parameters A-F define the density profile; the radial factor B can also be a function of the latitude through the elongation parameter C; A is the equatorial enhancement parameter; the parameter F defines the flatness of the shell; and D and E are the symmetry transition parameters that describe the abruptness of the geometrical transition in the shell. By comparing the PACS images to the synthetic ones, produced by 2-Dust and convolved with the PACS PSF, the dust nebula geometrical parameters can be defined.

After constraining the nebular geometry, the dust infrared SED is modeled, using as additional input the stellar parameters that are taken from literature for the specific object under scrutiny. All the input parameters can be divided into three groups related to: a) the computational grid; b) the central star and its dust shell; and c) the dust grains. The 2-Dust code uses the Mie theory to calculate the cross-sections of the absorption and the scattering of the dust grains for a given size distribution and optical properties of the dust grains. The size distribution for the dust grains of Mathis et al. (1977 [86]) was assumed for all nebulae: $n(a) \propto a^{-3.5}$ with $a_{min} < a < a_{max}$, a being the grain radius. For the dust composition, previous studies were considered if available, but in any case various compositions were tested to obtain the best fit of the SED. The optical properties of the dust grains for each composition were taken from literature. By varying a_{min} (or a_{max}), which controls the 20μm/100μm flux density ratio, and the opacity, which controls the strength of the emission, we can adjust the model to the data.

The output files contains the values of the derredened stellar intensity, the dust shell intensity, the specific intensity and temperature for each grid point and for each wavelength. Also, the mass of the dust nebula is calculated along with its temperature. Some of the outputs

can then be imported into auxiliary programs of this code to produce a SED as well as two-dimensional projected surface brightness and optical depth maps at given wavelengths. These final synthetic surface brightness maps of the nebulae were convolved with the corresponding PACS PSF and compared with the observed images.

1.4.1.2 *The black body fit*

The infrared SED is also fitted with a modified Black Body (BB) curve that is given by

$$F_\nu \propto B_\nu(T_d)\nu^\beta \ , \tag{1.3}$$

where F_ν is the flux at a given frequency ν, B_ν is the Planck function, T_d is the dust temperature and β is a factor linked to the dust composition. This fit gives directly the dust temperature for an adopted β factor.

In this model, to calculate the dust mass, the following equation is used

$$M_{dust} = \frac{F_\nu \ D^2}{B_\nu \left(T_d\right) \ \kappa_\nu} \ , \tag{1.4}$$

where κ_ν is the mass absorption coefficient, i.e. the absorption cross section per unit mass, and D is the distance to the nebula (Hildebrand 1983 [51]). This method widely used in the literature is considered here for a consistency check of the 2-Dust results.

1.4.2 *Ionized gas analysis*

Nebular forbidden emission lines of [NII], [NIII], [OI], [OIII], and [CII] are detected in the PACS infrared spectra of the three studied nebulae. More precisely, the lines: [OI] λλ 63, 146 μm, [NII] λλ 122, 205 μm, and [CII] λ 158 μm are detected in all the three spectra, while the lines: [NIII] λ 57 μm and [OIII] λ 88 μm are detected only in the spectra of WRAY 15-751 and M1-67, indicating higher ionization states. The integrated line fluxes, F, over the 25 spaxels of the spectroscopic detector, measured using the Image Reduction and Analysis Facility (IRAF) (Tody 1986 [149], 1993 [150]), are used to calculate the ionized gas properties.

1.4.2.1 *Electron density*

The [NII] 122/205 μm ratio is an electron density, n_e, diagnostic in the infrared waveband at low density, $1\ cm^{-3} \leqslant n_e \leqslant 10^3\ cm^{-3}$ (Rubin et al. 1994 [121]). Since these two lines are detected in all nebulae, this ratio is used for the electron density calculation. The electron temperature, T_e, assumed to be constant throughout the nebula, was either taken from the literature or estimated considering the observed

level of excitation and the available values for other nebulae of this type.

The task 'temden' of the package *nebular* of the IRAF/Space Telescope Science Data Analysis System (STSDAS) environment (Shaw & Dufour 1995 [125]) was used for the electron density calculations. This algorithm makes use of the fact that the nebular cooling-rate is dominated by ions that in majority have either p^2, p^3 or p^4 ground-state electron configurations, which have five low-lying levels. The main physical assumption is that only these five levels are considered to calculate the emission line spectrum.

1.4.2.2 *Abundance ratios N/O and N/H*

When the lines [NIII] 57 µm and [OIII] 88 µm are detected in the PACS spectrum of the nebula, the N/O abundance number ratio can be estimated by

$$\frac{N}{O} = \frac{\langle N^{++}\rangle}{\langle O^{++}\rangle} = \frac{F_{[NIII]57}/\varepsilon_{[NIII]57}}{F_{[OIII]88}/\varepsilon_{[OIII]88}}\,, \tag{1.5}$$

where F is the flux and ε is the volume emissivity of a given emission line. The emissivities are calculated with the task 'ionic' of the package *nebular*, using the adopted value for the electron temperature and the calculated value for the electron density.

The N/H abundance number ratio can be estimated when the lines of [NII] at 122 µm and 205 µm are detected, with the use of the Hα 6562.8 Å flux, obtained from the optical observation analysis. If the line [NIII] 57 µm is detected it is also considered. The following equation is used

$$\frac{N}{H} = \frac{\langle N^{+}\rangle + \langle N^{++}\rangle}{\langle H^{+}\rangle}\,. \tag{1.6}$$

To calculate the Hβ flux from the dereddened Hα flux, the equation

$$F_0(H\alpha)/F_0(H\beta) = j_{H\alpha}/j_{H\beta} = \alpha^{eff}_{H\alpha}\lambda_{H\beta}/\alpha^{eff}_{H\beta}\lambda_{H\alpha}\,, \tag{1.7}$$

is used, where j is the emission coefficient, λ is the wavelength and $\alpha^{eff} = (4\pi j)/(n_e n_p h\nu)$ is the effective recombination coefficient of the respective line of hydrogen, with n_e being the electron density, n_p the proton density, h the Plank's constant and ν the frequency. Assuming a case-B recombination[7], the following equations of Draine (2011 [27]) are used

$$\alpha^{eff}_{H\alpha} = 1.17\times10^{-13}T_4^{(-0.942-0.031\ln T_4)}\ cm^3s^{-1}\,, \tag{1.8}$$

7 The case-B recombination, where the ionizing photons emitted during the recombination process are reabsorbed, with the probability to escape being very small, is an excellent approximation for the photoionized nebulae around O and B stars while the case-A, where every ionizing photo escapes, is a very good approximation for shock-heated regions where the density of neutral hydrogen is very small and the temperature very high (Draine 2011 [27]).

$$\alpha_{H\beta}^{eff} = 3.03 \times 10^{-14} T_4^{(-0.874-0.058 \ln T_4)} \text{ cm}^3 \text{s}^{-1} , \quad (1.9)$$

where $T_4 = T_e/(10^4 \text{ K})$. The flux ratios, $F/F_0(H\beta)$ are then calculated for each one of the detected infrared lines of nitrogen. The ionic abundances N^+/H^+ and N^{++}/H^+ are then derived using the task 'ionic' of the package *nebular*. Their sum gives the N/H abundance number ratio.

1.4.2.3 *Ionizing flux*

Since optical Hα observations are available for all the nebulae, the number of hydrogen ionizing photons per unit time and the Strömgren radius are calculated for each one of them. For the nebulae with radio observations available in the literature, these parameters are calculated based also on the radio flux and are then compared to the results derived from the Hα emission analysis. The equations used are given below.

The radius of the Strömgren sphere, R_S, in pc is given by (see Sect. A.1, A.2)

$$R_S = 3.17 \left(\frac{x_e}{\epsilon}\right)^{1/3} \left(\frac{n_e}{100}\right)^{-2/3} T_4^{(0.272+0.007 \ln T_4)} \left(\frac{Q_0}{10^{49}}\right)^{1/3} , \quad (1.10)$$

where the rate of emission of hydrogen-ionizing photons, Q_0, (in photons s^{-1}) using the Hα flux is given by

$$Q_{0(H\alpha)} = 8.59 \times 10^{55} T_4^{(0.126+0.01 \ln T_4)} D^2 F_0(H_\alpha) ; \quad (1.11)$$

when using the radio flux it is given by

$$Q_{0(\text{radio})} = 8.72 \times 10^{43} T_4^{(-0.466-0.0208 \ln T_4)} \left(\frac{\nu}{4.9}\right)^{0.1} x_e^{-1} D^2 S_\nu , \quad (1.12)$$

where $x_e = n_e/n_p$ is the ratio of the electron to the proton density, ϵ is the filling factor, $T_4 = T_e/(10^4 \text{ K})$, ν is the radio frequency in GHz, D is the distance of the nebula in kpc, $F_0(H\alpha)$ is the Hα flux in ergs cm^{-2} s^{-1}, and S_ν is the radio flux in mJy.

1.4.2.4 *Mass of the ionized gas*

An estimate of the ionized gas mass is made from the Hα and the radio emissions, when available. The equations that are analytically derived in Sect. A.1 and A.2 are used for this calculation.

For a spherical nebula the ionized mass in solar masses, taking into account the Hα emission, is given by

$$M_{i(H\alpha)}^{\text{sphere}} = 57.9 \frac{1 + 4y_+}{\sqrt{1 + y_+}} T_4^{(0.471+0.015 \ln T_4)} \epsilon^{1/2} \theta^{3/2} D^{5/2} F_0^{1/2}(H\alpha) , \quad (1.13)$$

where θ is the angular radius of the nebula ($R = \theta D$) in arcsec and $n_{H^+} = n_p$, n_{He^+}, and $n_{He^{++}}$ are the number densities of the ionized hydrogen, ionized helium, and doubly ionized helium, respectively. Assuming $n_{He^{++}} = 0$ and denoting $y_+ = n_{He^+}/n_{H^+}$, we have $x_e = n_e/n_p \simeq 1 + n_{He^+}/n_{H^+} = 1 + y_+$ and $\mu_+ \simeq 1 + 4\, n_{He^+}/n_{H^+} = 1 + 4y_+$.

Considering now the radio flux and using the same formalism as above, the mass of a spherical nebula in solar masses is given by

$$M^{\text{sphere}}_{i(\text{radio})} = 5.82 \times 10^{-5} \frac{1 + 4y_+}{1 + y_+} T_4^{0.175} \left(\frac{\nu}{4.9}\right)^{0.05} \epsilon^{1/2} \theta^{3/2} D^{5/2} S_\nu^{1/2} \,. \tag{1.14}$$

1.4.3 *Neutral gas analysis*

A Photodissociation Region (PDR) is a region where the gas is neutral and the Far-UltraViolet (FUV) photons (with $h\nu < 13.6$ eV) play a significant role in the chemistry and the heating. Among the most important coolants in a PDR are the fine structure emission lines [OI] 63, 146 µm and [CII] 158 µm (Hollenbach & Tielens 1997 [54]). The first detection of a PDR in a nebula around a LBV was made by Umana et al. (2009 [153]), through the presence of fine structure lines in their Spitzer study of the nebula that surrounds HR Car. A PDR was later found in the nebula around the LBV candidate HD 168625 (Umana et al. 2010 [154]), this time through the detection of spectral features that indicate the presence of Polycyclic Aromatic Hydrocarbon (PAH)s.

The three lines, [OI] 63, 146 µm and [CII] 158 µm, are detected in all the three PACS nebular spectra. This detection may indicate the presence of a PDR in the nebulae. On the other hand, a shock, which is the result of the interaction between the fast stellar wind and the slow expanding remnant of a previous evolutionary phase, could also photodissociate molecules and result in [OI] and [CII] emission. The flux ratios of [OI] 63 µm/[OI] 146 µm and [OI] 63 µm/[CII] 158 µm can be used to exclude one of these two possible scenarios, considering the PDR models predictions of Kaufman et al. (1999 [67]). Moreover, the ratio [OI] 63 µm/[CII] 158 µm is a diagnostic between PDR and shock. In PDRs, this ratio is < 10 (Tielens and Hollenbach 1985 [147]), while in shocks, it is $\gtrsim 10$ (Hollenbach and McKee 1989 [53], Castro-Carrizo et al. 2001 [12]). The conclusion for all the three nebulae is that a PDR, and not a shock, is responsible for the [OI] and [CII] emission.

The physical conditions in the PDR can be determined using these three infrared fine structure lines. But firstly, any possible contribution of the ionized gas to the observed line intensities must be determined and subtracted. The lines [OI] 63, 146 µm arise exclusively from the PDR (Malhotra et al 2001. [81]) because neutral oxygen can be found only in neutral regions, as its ionization potential (13.62 eV) is very close to the ionization potential of hydrogen. On the contrary, carbon, which is the fourth-most abundant element, has an ionization

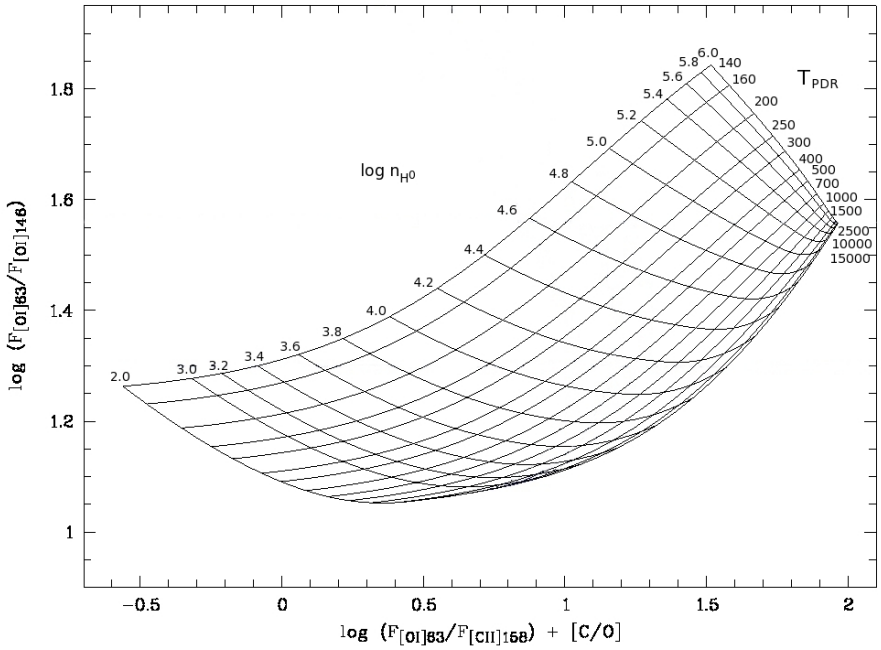

Figure 1.6: Temperature-density PDR diagnostic diagram. The grid of flux ratios $F_{[OI]63}/F_{[OI]146}$ versus $F_{[OI]63}/F^{PDR}_{[CII]158}$ was calculated by solving the level population equations for a range of temperatures and densities. $F_{[OI]63}/F^{PDR}_{[CII]158}$ is normalized to the solar abundance $(C/O)_{\odot} = 0.5$ so that $[C/O] \equiv \log(C/O) - \log(C/O)_{\odot}$.

potential (11.26 eV) lower than that of hydrogen. Consequently, C^+ can be found in both PDRs and HII regions. Therefore, the line [CII] 158 μm may arise from the HII region of the nebula and/or from the associated PDR (Heiles 1994 [50]). In the following we describe a method based on the *Herschel* data to disentangle the contribution of each one of the two regions to the flux of the line [CII] 158 μm and at the same time estimate the C/O abundance ratio of the nebula.

Measurements of the flux of the line [NII] 122 μm can give an estimate of the contribution of the HII region to the flux of [CII] 158 μm line, $F^{HII}_{[CII]158}$, because the line [NII] 122 μm arises exclusively in the ionized gas regions. We define

$$F^{HII}_{[CII]158} = \alpha F_{[CII]158} \, , \tag{1.15}$$

where $F_{[CII]158}$ is the total flux of the [CII] 158 μm line measured on the PACS spectrum and α is a factor that needs to be determined. The ratio of fractional ionization is given by

$$\frac{\langle C^+ \rangle}{\langle N^+ \rangle} = \frac{F^{HII}_{[CII]158}/\varepsilon_{[CII]158}}{F_{[NII]122}/\varepsilon_{[NII]122}} \, . \tag{1.16}$$

Assuming $\langle C^+ \rangle / \langle N^+ \rangle = C/N$ we have

$$\frac{F^{HII}_{[CII]158}}{F_{[NII]122}} = \frac{\varepsilon_{[CII]158}}{\varepsilon_{[NII]122}} \frac{C}{N} \, , \tag{1.17}$$

where the emissivities are calculated using the task 'ionic' of package *nebular*. If the N/O abundance ratio has been calculated or is known from the literature, then

$$\frac{C}{O} = \frac{C}{N}\frac{N}{O} \,. \tag{1.18}$$

The theoretical $F_{[OI]63}/F_{[OI]146}$ ratio against the $F_{[OI]63}/F^{PDR}_{[CII]158}$ ratio normalized to the solar $(C/O)_{\odot} = 0.5$ abundance ratio (Fig. 1.6), is then plotted following a similar study by Liu et al. (2001 [76]). To calculate the populations of the fine-structure levels of C^+ and O^0, the two- and three-level atom equilibrium equations were solved, respectively, considering that collisions with atomic hydrogen dominate in the PDR (Draine 2011 [27]). The radiative transition probabilities, A_{ij}, for the [CII] and [OI] fine-structure lines and the electron collision strengths, Ω_{ij}, were taken from Draine (2011 [27]). The collisional rate coefficients for the fine-structure excitation by hydrogen for [CII] and [OI] were taken from Barinovs et al. (2005 [2]) and from Abrahamsson et al. (2007 [1]), respectively. A simple analytic extrapolation was made for temperatures higher than those given in these two references[8]. Furthermore, pressure equilibrium between the HII region and the PDR was assumed (Tielens 2005 [146])

$$n_{H^0} k T_{PDR} \simeq 2 n_e k T_e \,, \tag{1.19}$$

where n_{H^0} is the atomic hydrogen number density and T_{PDR} is the temperature of the PDR. This relation is used to define a locus of possible values in the diagram of Fig. 1.6.

Using this diagnostic diagram along with the constraints from Eq. 1.19 and the observed line ration $F_{[OI]63}/F_{[OI]146}$, the value of $\log(F_{[OI]63}/\ F^{PDR}_{[CII]158})$ + [C/O] is determined. The values of α and C/O are then calculated using Eq. 1.15, Eq. 1.17 and Eq. 1.18.

The structure of a PDR is described by the incident FUV radiation field, G_0, along with the hydrogen density, n_{H^0}. Expressed in terms of the average interstellar radiation field that corresponds to an unidirectional radiation field of 1.6×10^{-3} erg cm^{-2} s^{-1}, G_0 is given by (Tielens 2005 [146])

$$G_0 = 625 \frac{L_\star \chi}{4\pi R^2} \,, \tag{1.20}$$

where $L_\star$ is the stellar luminosity, χ is the fraction of this luminosity above 6 eV, and R is the distance from the star.

The dust absorbs and re-emits the FUV radiation in the Far-InfraRed (FIR). Consequently, the dust temperature, T_{dust}, can be estimated as-

8 The difference between the diagram in the study of Liu et al. (2001 [76]) and Fig. 1.6 is due to the use of updated collision coefficients. We also consider a wider range of density and temperature values.

suming radiative equilibrium. In the case of silicates (i.e., $\beta = 2$) the dust temperature is given by (Tielens 2005 [146])

$$T_{dust} = 50 \left(\frac{1\mu m}{a} \right)^{0.06} \left(\frac{G_0}{10^4} \right)^{1/6} K \quad \text{for } T_{dust} < 250 \text{ K} . \qquad (1.21)$$

To verify the consistency of the PDR analysis with the results of the dust nebula analysis, the calculations of the dust temperature were also performed using this equation.

1.4.4 *The stellar evolutionary phase at the time of the nebular ejection*

The results of the analysis of the *Herschel* infrared imaging and spectroscopic data for the three nebulae can be used to constrain the evolutionary phase of the central star at the time when the ejection of the nebula took place. For this purpose we used the theoretical evolutionary models of Ekström et al. (2012 [29]), which are the Geneva models for initial stellar masses between 0.8 and 120 $M_\odot$ with solar metallicity available through an interactive webpage[9].

By choosing the initial stellar mass, metallicity and rotation rate, the code computes the theoretical evolution of various stellar parameters among which the luminosity, temperature, mass-loss rate and abundances. The observational data provides the mass-loss rate of the central star at the time of the nebular ejection, along with abundance ratios (N/H, N/O and C/O) that are assumed to be the surface abundances at the time of the ejection. These results are used to constrain the possible theoretical evolutionary paths and find the phase during which the nebular ejection occured.

9 http://obswww.unige.ch/Recherche/evoldb/index/

Part II

NEBULAE

2

THE NEBULA AROUND THE LBV STAR WRAY 15-751

The first object chosen to be part of this study is the LBV star WRAY 15-751 and its circumstellar environment. Previous studies revealed that this massive evolved star is surrounded by a nebula composed of dust and gas. Though this nebula has been previously observed in the infrared waveband, the analysis of the new high-resolution infrared *Herschel* data gave us more detail on the structure and the composition of the nebula and allowed us to calculate the basic properties of the dust and the gas component of the nebula with precision. Moreover, thanks to the large field-of-view of these observations we have been able to look for the possible presence of multiple shells and/or cavities in the circumstellar environment of this LBV star. These new data finally helped us to estimate at which time of the stellar evolution the nebula was ejected from the star.

This analysis was published in *Astronomy & Astrophysics* (2013 A&A, 557, A20), and the article is reproduced in the following pages. It is organized as follows. After the introduction to this chapter, where previous studies of this object related to our analysis are presented, the *Herschel* infrared imaging and spectroscopic observations along with the optical imaging observations are presented. The description of the nebular morphology revealed through the imaging follows. Apart from the well known nebula that surrounds WRAY 15-751, a second bigger but fainter nebula is detected for the first time in the infrared images. The spectrum of the nebula is then presented, followed by the analysis of the dust continuum emission and the analysis of the emission line spectrum.

The analysis of our observations and the discussion of the corresponding results led to the following basic conclusions of the study of the nebula around WRAY 15-751. The main inner nebula consists of mildly enriched material. It is composed of dust and ionized gas that are mixed together and are surrounded by a thin region where the gas is neutral. The presence of multiple shells around the central star shows that the mass-loss was a series of episodes of extreme mass-loss. Our results point to a nebular ejection during a RSG phase of a star of about 40 $M_{\odot}$ with little rotation.

HERSCHEL IMAGING AND SPECTROSCOPY OF THE NEBULA AROUND THE LUMINOUS BLUE VARIABLE STAR WRAY 15-751

Vamvatira-Nakou, C., Hutsemékers, D., Royer, P., Nazé, Y., Magain, P., Exter, K., Waelkens, C., and Groenewegen, M. A. T.

Abstract

We have obtained far-infrared *Herschel* PACS imaging and spectroscopic observations of the nebular environment of the luminous blue variable (LBV) WRAY 15-751. The far-infrared images clearly show that the main, dusty nebula is a shell of radius 0.5 pc and width 0.35 pc extending outside the Hα nebula. Furthermore, these images reveal a second, bigger and fainter dust nebula that is observed for the first time. Both nebulae lie in an empty cavity, very likely the remnant of the O-star wind bubble formed when the star was on the main sequence. The kinematic ages of the nebulae are calculated to be about 2×10^4 and 8×10^4 years, and we estimated that each nebula contains ~ 0.05 $M_\odot$ of dust. Modeling of the inner nebula indicates a Fe-rich dust. The far-infrared spectrum of the main nebula revealed forbidden emission lines coming from ionized and neutral gas. Our study shows that the main nebula consists of a shell of ionized gas surrounded by a thin photodissociation region illuminated by an "average" early-B star. We derive the abundance ratios N/O = 1.0 ± 0.4 and C/O = 0.4 ± 0.2, which indicate a mild N/O enrichment. From both the ionized and neutral gas components we estimate that the inner shell contains 1.7 ± 0.6 $M_\odot$ of gas. Assuming a similar dust-to-gas ratio for the outer nebula, the total mass ejected by WRAY 15-751 amounts to 4 ± 2 $M_\odot$. The measured abundances, masses and kinematic ages of the nebulae were used to constrain the evolution of the star and the epoch at which the nebulae were ejected. Our results point to an ejection of the nebulae during the red super-giant (RSG) evolutionary phase of an ~ 40 $M_\odot$ star. The multiple shells around the star suggest that the mass-loss was not a continuous ejection but rather a series of episodes of extreme mass-loss. Our measurements are compatible with the recent evolutionary tracks computed for an ~ 40 $M_\odot$ star with little rotation. They support the O–BSG–RSG–YSG–LBV filiation and the idea that high-luminosity and low-luminosity LBVs follow different evolutionary paths.

2.1 INTRODUCTION

LBVs, or S Doradus variables, represent a short stage ($\sim 10^4 - 10^5$ yr) in the evolution of massive stars with initial mass $\geqslant 30$ $M_\odot$ (Maeder

& Meynet 2010 [79]). They are located in the upper left part of the HR diagram, although some of them undergo occasional excursions to the right of the HR diagram. Their main characteristics are a) photometric variability, from giant eruptions, $\geqslant 2$ mag, to small oscillations, ~ 0.1 mag; b) high luminosity, $\sim 10^6$ $L_\odot$; and c) high mass-loss rates, $\sim 10^{-5} - 10^{-4}$ $M_\odot$ yr^{-1} (Humphreys & Davidson 1994 [117]).

According to current evolutionary scenarios (Maeder & Meynet 2010 [79]), an early-type O star evolves into a WR star by losing a significant fraction of its initial mass. Progressively, the outer layers of the star are removed, revealing a "bare core" that becomes a WR star. One way to lose mass is through stellar winds. However, in the past few years the mass-loss rates of O stars have been revised downward by up to one order of magnitude (Fullerton et al. 2006 [32]) and more often by a factor of a few (Bouret et al. 2005 [8]; Puls et al. 2008 [116]), highlighting the key role played by episodes of extreme mass-loss in an intermediate evolutionary phase (LBV or red supergiant phase).

Most LBVs are surrounded by ejected nebulae (Hutsemékers 1994 [59]; Nota et al. 1995 [103]). The HII nebulae have diameters of $0.5 - 2$ pc, expansion velocities of a few tens of km s^{-1}, and dynamical ages of 3×10^3 to 5×10^4 yr. Their morphologies are usually axisymmetric, from mildly to extremely bipolar or elliptical. Previous infrared and millimeter studies of LBV nebulae have revealed not only dust but also molecular gas (CO) (McGregor et al. 1988 [88]; Hutsemékers 1997 [60]; Nota et al. 2002 [105]).

There are many questions about the detailed evolution of these massive stars. For instance, we still do not know when and how the nebulae are ejected, what causes the strong mass-loss phases and what leads to the giant eruptions observed in some of them. Also, important quantities such as the nebular mass and the gas composition (CNO abundances) are very uncertain.

WRAY 15-751 (= Hen 3-591 = IRAS 11065-6026) was first considered to be a possible WR star by Henize (Roberts 1962 [118]) because of a perceptibly widened Hα emission line. Carlson and Henize (1979 [11]) included it in their sample of southern peculiar emission-line stars and classified it as a Bep star on the basis of the strong [FeII] emission lines characterizing its spectrum. Based on a photometric and spectroscopic study in the optical, Hu et al. (1990 [55]) concluded that WRAY 15-751 is a variable star with spectral type O9.5. After estimating its distance ($r > 5$ kpc) and temperature ($T_{eff} = 30000$ K), these authors calculated a lower limit of $\log L/L_\odot$ equal to 5.7. By plotting these data in an evolutionary diagram, they revealed that WRAY 15-751 is located in the region of LBV stars, with a lower limit on the initial mass of approximately $50 M_\odot$. De Winter et al. (1992 [24]) made an extensive comparative study of the optical and ultraviolet characteristic of this star with those of the LBVs AG Car and HR Car. They concluded that WRAY 15-751 was a LBV in a phase of qui-

escence surrounded by a cold dusty circumstellar shell with strong emission in the FIR, like HR Car.

Based on the available photometry, Sterken et al. (2008 [142]) showed that WRAY 15-751 exhibits strong variability, confirming that the star belongs to the S Dor class. Its variations have an amplitude of about two magnitudes in V and a cycle length of several decades, similar to the observed variations of AG Car. The star moved from V $\simeq$ 12.5 and $T_{eff} \simeq$ 30000 K in 1989, to V $\simeq$ 10.5 and $T_{eff} \simeq$ 9000 K in 2008.

Hutsemékers and Van Drom (1991 [61]) studied WRAY 15-751 with optical photometric and spectroscopic data. They found that the star is surrounded by a ring nebula of ionized gas with a diameter of about 22″. The nebula appeared non-uniform in brightness and is apparently not detached from the central star. This fact led them to conclude that the nebula might arise from a continuous mass-loss instead of from a sudden outburst. Based on their spectral analysis, they also suggested that the nebula is expanding almost symmetrically at 26 km s^{-1}.

The first infrared study of the nebula around WRAY 15-751 was made by Voors et al. (2000 [164]). By modeling ground-based infrared images taken at about 10 μm and Infrared Space Observatory (ISO) spectroscopic observations, they derived some properties of the circumstellar dust around the star: the distribution of emission is roughly spherical, the dust shell is detached and slightly elongated; there is neutral gas outside the dust shell and ionized gas only in the inner part of it; the dust shell contains on the average large grains and a minor population of warm very small grains.

Weis (2000 [165]) made a detailed kinematic and morphological study of the nebula and found that, in addition to a nearly spherical shell, it also displays a bipolar-like structure (caps). Duncan and White (2002 [28]) studied this nebula at radio wavelengths (3 and 6 cm) and confirmed the almost attached nebula surrounding the central star. Moreover, the subtraction of the central star as a point source revealed a two-component inner structure, which was interpreted by the authors as a disk or torus, suggesting a possible mass transfer from a companion star.

Van Genderen et al. (1992 [161]) calculated a lower limit of $4-5$ kpc for the distance to WRAY 15-751, based on the photometry of field stars. This value agrees with the suggestion of Hu et al. (1990 [55]). Hutsemékers and Van Drom (1991 [61]) found a larger distance of 7 kpc, determined from the kinematics of the [NII] lines. Pasquali et al. (2006 [111]) adopted a distance of 6 ± 1 kpc in their study of the birth-cluster of WRAY 15-751 based on the radial velocity of the star and its surrounding HII region. In this study we adopt a distance of 6 ± 1 kpc, which encompasses all measurements.

We analyze the images and the spectrum of the WRAY 15-751 nebula taken by PACS (Poglitsch et al. 2010 [115]), one of the three instruments onboard the *Herschel* Space Observatory (Pilbratt et al. 2010 [113]). The paper is organized as follows. The observations and the data reduction are presented in Sect. 2.2. In Sect. 2.3 a description of the nebula FIR morphology is given, while in Sect. 2.4 we give an overview of the spectrum. In Sect. 2.5 we model the dust continuum emission. The emission line spectrum is presented and analyzed in Sect. 2.6. A general discussion follows in Sect. 2.7 and conclusions appear in Sect. 2.8.

2.2 OBSERVATIONS AND DATA REDUCTION

2.2.1 *Infrared observations*

The infrared imaging and spectroscopic observations were carried out using PACS as part of the MESS Guaranteed Time Key Program (Groenewegen et al. 2011 [39]).

The imaging observations of the WRAY 15-751 nebula were carried out on January 2, 2010, which corresponds to the 233 Observational Day (OD) of *Herschel*. The scan map mode was used. In this observing mode, the telescope slews at constant speed (20″/s in our case) along parallel lines to cover the required area of the sky. For each filter, two orthogonal scan maps were obtained so that our final data set consists of maps at 70, 100 and 160 μm. The observation Identification Number (obsID)s of the four scans are 1342188849, 1342188850, 1342188851, and 1342188852. The duration of each one is 157 s.

The data reduction was performed using the HIPE (Ott 2010 [108]). The 'highpassFilter' task was used to produce the final images as detailed in Groenewegen et al. (2011 [39]). The images were oversampled by a factor of 3.2 with respect to the original pixel size, hence leading to pixel sizes in the final maps of 1″ in the blue (70, 100 μm) channel and 2″ in the red (160 μm) channel. Since the highpassFilter task filters out the largest structures, an independent data reduction was performed in all three wavelengths using the MADmap algorithm (Cantalupo et al. 2010 [10]) to investigate emission at large scales. This algorithm, also provided within HIPE, accounts for the significant detector drift.

Deconvolution was applied to the three PACS images, produced with the highpassFilter task, in an effort to better reveal the morphology of the inner nebula. For this purpose, the PSF of Vesta and the MCS deconvolution method (Magain et al. 1998 [80]) were used. The advantage of this method is that it does not violate the sampling theorem. Indeed, the image is not deconvolved by the total PSF, which leads to an infinite resolution, but the deconvolution makes use of a partial PSF chosen to respect the desired resolution of the final decon-

volved image. The *Herschel* PACS PSF FWHMs are 5.2″, 7.7″ and 12″ at 70 µm, 100 µm and 160 µm, respectively. After the deconvolution with the corresponding PSF, the final spatial resolution is twice as good as the initial one.

The spectrum of the WRAY 15-751 nebula was taken on November 26, 2009 (OD 196) during the calibration phase of the instrument. The PACS integral-field spectrometer covers the wavelength range from 52 µm to 220 µm in two channels that operate simultaneously in the blue, 52-98 µm band (second order: B2A 52-73 µm and B2B 70-105 µm, third order: B3A 52-73 µm), and the red, 102-220 µm band (first order: R1A 133-220 µm and R1B 102-203 µm). It has a resolving power of $\lambda/\delta\lambda \sim 940 - 5500$, depending on the wavelength. It provides simultaneous imaging of a $47'' \times 47''$ field of view, resolved in 5×5 square spatial pixels (i.e., spaxels). An image slicer employing reflective optics is used to re-arrange the two-dimensional field-of-view along a 1×25 pixels entrance slit for the gratings. We used the SED observing template, which provides a complete coverage between 52 and 220 µm. The two obsIDs of these observations are 1342187236 and 1342187237. The data reduction was also performed using HIPE, following the standard data reduction steps, in particular the subtraction of the background spectrum obtained through nodding.

2.2.2 *Visible observations*

The optical images of WRAY 15-751 and its nebula were obtained on March 14, 1994, with the 3.6-m telescope at the ESO, La Silla, Chile. The EFOSC1 camera was used in its coronographic mode: the 6″ circular coronographic mask was inserted in the aperture wheel and positioned on the central star, while the Lyot stop was inserted in the grism wheel (Melnick et al. 1989 [64]). A series of short (1s) and long (300s) exposures were secured in a Hα+[NII] filter (λ_c = 6560.5Å ; FWHM =62.2Å), and in a continuum filter just redward (λ_c = 6644.7Å; FWHM = 61.0Å). The Charge-Coupled Device (CCD) pixel size was 0.605″ on the sky. The night was photometric and the seeing around 1.6″. The frames were bias-corrected and flat-fielded. The continuum images were subtracted from the Hα+[NII] ones after correcting for the position offsets and for the different filter transmissions, using field stars. The resulting averaged images show more detail than those displayed in Hutsemékers and Van Drom (1991 [61]). They can be compared to those obtained at the ESO New Technology Telescope (NTT) with the STSci coronograph (Nota 1999 [100], Weis 2000 [165]).

2.3 MORPHOLOGY OF THE NEBULA

The images of the WRAY 15-751 nebula at the three PACS wavelengths, 70 µm, 100 µm and 160 µm, are illustrated in Fig. 3.1. Note that the

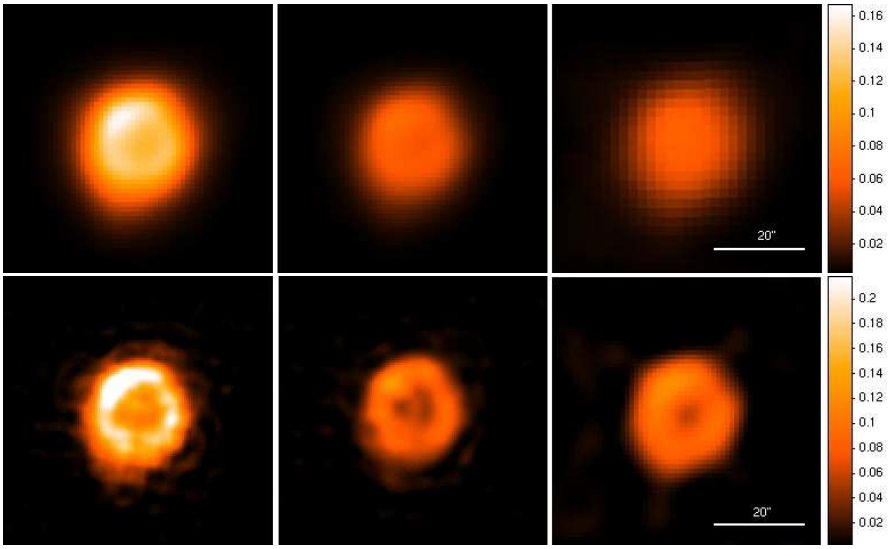

Figure 2.1: PACS images of the nebula around WRAY 15-751 at 70 μm, 100 μm and 160 μm, from left to right. *Top*: original images. *Bottom*: images deconvolved using the MCS method. The size of each image is 1′×1′. The scale on the right corresponds to the surface brightness (arbitrary units). North is up and east is to the left.

star is not visible at these wavelengths. While the ionized gas does not appear to be detached from the star (Hutsemékers and Van Drom 1991 [61]; Duncan and White 2002 [28]; Fig. 2.2), the dust emission seen in these images shows an almost symmetric ring-like morphology, as suggested by Voors et al. (2000 [164]) on the basis of mid-infrared imaging. This ring shape is more clearly seen at 70 μm, the wavelength at which the spatial resolution is the highest. The central part of the nebula is clearly fainter than the ring. The very inner nebula, which is unresolved in the optical but was detected at radio wavelengths by Duncan and White (2002 [28]), is not seen in the PACS images.

In the 70 μm deconvolved image, the ring extends up to ~ 18″ in radius with a width of ~ 12″. Adopting a distance of 6 kpc, these values corresponds to a nebular radius of about 0.5 pc and to a ring width of 0.35 pc. The surface brightness seems to be non-uniform, as the northeastern part of the nebula is brighter than the other parts. This asymmetry in the brightness distribution was also detected at optical and mid-infrared (Hutsemékers and Van Drom 1991 [61]; Voors et al. 2000 [164]).

Fig. 2.2 illustrates the nebula around WRAY 15-751 in the Hα+[NII] light. The nebula essentially appears disk-like with a circular rim 22″ in diameter, in agreement with the measurement of Hutsemékers and Van Drom (1991 [61]). It appears slightly elongated, with small caps (Weis 2000 [165]) along the main axis (Position Angle (PA) ~ 155°, east of north). The eastern part of the nebula is definitely brighter than

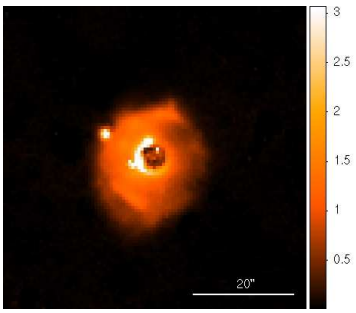

Figure 2.2: Hα+[NII] image of the nebula around WRAY 15-751. The size of the image is 1′ × 1′. The scale on the right corresponds to the surface brightness (arbitrary units). North is up and east is to the left. The central star is occulted by the coronograph spot.

the western one. A similar morphology is observed at radio wavelengths (Duncan and White 2002 [28]). No diffuse emission can be detected in the images obtained within the adjacent continuum filter. The Hα+[NII] rim, which corresponds to the ionized gas region, is inside the dust ring, which extends farther out.

In Fig. 2.3, we illustrate the large-scale infrared emission around WRAY 15-751, obtained after the reduction with the MADmap algorithm. A much larger, very faint ellipsoidal nebula can be seen circumscribing the WRAY 15-751 bright ring nebula. This outer nebula is detected at all three wavelengths but it is more clearly seen at 100 μm. Its size is roughly 2.1′ × 2.5′, which corresponds to a mean radius of 2 pc at a distance of 6 kpc. This nebula is elongated along the same PA as the Hα+[NII] inner shell (Fig. 2.2), supporting its physical association to WRAY 15-751. It is also interesting to note that it lies in a cavity, probably cleaned up prior to the ejection of the nebula. The radius of this empty cavity is about 4′, which corresponds to 7 pc at a distance of 6 kpc.

The kinematic age of the two nebulae can be estimated, assuming that the expansion velocity is the same in both cases. Hutsemékers and Van Drom (1991 [61]) measured the expansion velocity to be $v_{exp} \sim 26$ km s^{-1}. Adopting this value, the inner nebula, of radius $r = 0.5$ pc, has a kinematic age $t_{kin} = r/v_{exp}$ of 1.9×10^4 years, while the outer nebula, of mean radius 2 pc, has a kinematic age of 7.5×10^4 years.

To explore the environment of WRAY 15-751 in more detail, we considered the PACS observations of the field obtained in the framework of the *Herschel* Infrared Galactic Plane survey (Hi-GAL, Molinari et al. 2010 [96]). The observations, made immediately public for legacy, were retrieved from the archive processed up to level 2. The two orthogonal scans were added.

A two-color image is displayed in Fig. 2.4, illustrating the complex interstellar environment around WRAY 15-751. In particular, we can

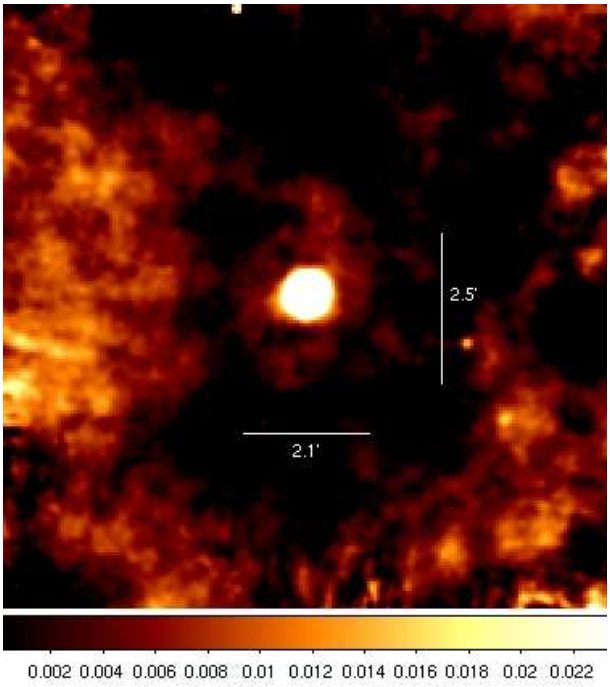

Figure 2.3: PACS 100 μm image of the nebula obtained using the MADmap reduction algorithm. The size of the image is 10′×10′. The scale on the bottom corresponds to the surface brightness (arbitrary units). North is up and east is to the left. A faint extended elliptical nebulosity is seen around the bright shell, the size of which is marked with the horizontal and vertical bars. Both appear located inside a cavity in the interstellar medium.

see a series of filaments that form a roughly circular structure around WRAY 15-751. We tentatively interpret this structure as the bubble formed by the O-star progenitor, although we cannot exclude a foreground/background structure. Velocity mapping would be needed to ascertain the physical association. WRAY 15-751 appears to be offset with respect to the bubble, possibly because of higher density material northwest of the star. The radius of this bubble is about 12′, which corresponds to 20 pc at 6 kpc.

2.4 SPECTRUM OF THE NEBULA: OVERVIEW

The footprint of the PACS spectral field-of-view on the image of the nebula at 70 μm is shown in Fig. 2.5. This figure allows us to identify which spaxel corresponds to which part of the nebula. It must be noted that the whole inner ring nebula is inside the spectral field of view although the center of the nebula is not exactly at the central spaxel (2,2).

The spectrum of the nebula, integrated over the nine central spaxels, is shown in Fig. 2.6. The shape of the continuum below 55 μm results from a yet-imperfect spectral response correction in this range.

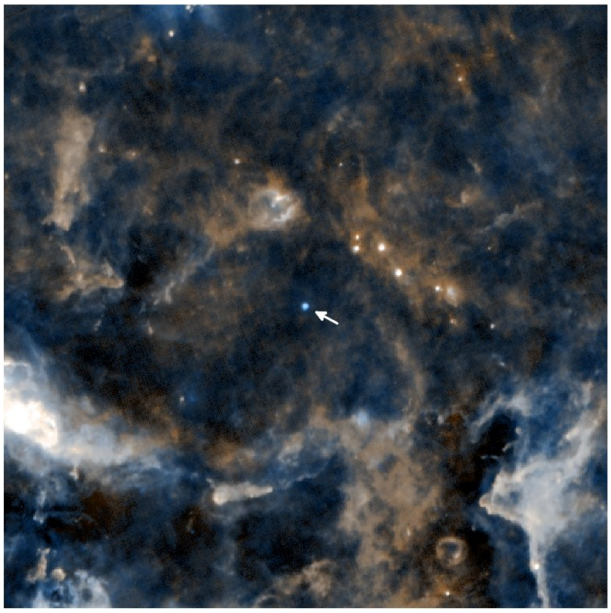

Figure 2.4: Two-color (70 μm in blue and 160 μm in red) image from the Hi-GAL survey of the complex environment of WRAY 15-751 (the blue spot at the center of the image marked with a white arrow). The size of the image is $1^\circ \times 1^\circ$. North is up and east is to the left. A bubble ~25′ in diameter and offset from the star is tentatively seen around WRAY 15-751.

Above 190 μm the continuum shape results from a light leak from the second diffraction order of the grating to the first one.

The following forbidden emission spectral lines are detected: [NIII] λ 57 μm, [OI] λλ 63, 146 μm, [OIII] λ 88 μm, [NII] λλ 122, 205 μm, and [CII] λ 158 μm. The highest ionization lines indicate an HII region around WRAY 15-751, while the lowest ionization lines reveal a PDR. Apart from these emission lines and the dust continuum, no other dust features have been detected. It should be noted that Voors et al. (2000 [164]) did not detect the [OI] λ 63 μm line on their ISO-LWS spectrum: only the lines [OIII] λ 88 μm and [NII] λ 122 μm were clearly visible.

2.5 DUST CONTINUUM EMISSION

Aperture photometry was performed on the PACS images and integrated flux densities derived for the bright nebular shell. Table 2.1 presents the *Herschel*-PACS flux density measurements, along with data taken from the archives of the Infrared Astronomical Satellite (IRAS) mission (Neugebauer et al. 1984 [99]), the ISO mission (Kessler et al. 1996 [68]) and the Infrared Astronomical Mission AKARI (Murakami et al. 2007 [98]). We did not include the IRAS observation at 100 μm because it is only an upper limit, and the AKARI observation

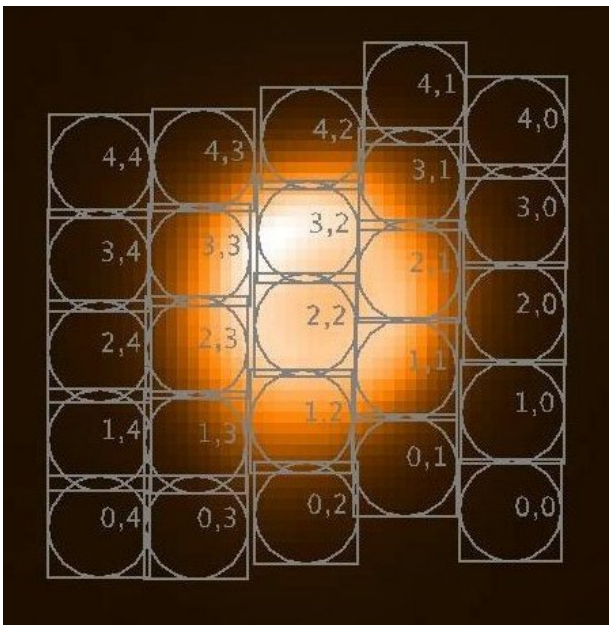

Figure 2.5: Footprint of the PACS spectral field of view on the image of the nebula at 70 μm. Each number pair is the label of a specific spaxel. The size of the image is $1' \times 1'$. North is up and east is to the left.

at 160 μm because of its low quality. Note that the beam size of the IRAS and AKARI observations is large enough to fully encompass the ring nebula.

Photometric color correction was applied to all flux densities derived from the data of these four space missions. This correction is needed to convert monochromatic flux densities that refer to a constant energy spectrum, to the true object SED flux densities at the photometric reference wavelengths of each instrument.

On the ISO-CAM image[1] the nebular flux density was measured through aperture photometry, subtracting the contribution from the central object. For the color correction of the IRAS data, we used the flux density ratios to derive the color temperature and then chose the corresponding color correction factor (Beichman et al. 1988 [4]). The ratio R (25,60) corresponds to a temperature of 190 K, while R (12,25) corresponds to 125 K. We decided to correct the flux density at 60 μm using the factor at 190 K. For the flux densities at 12 and 25 μm we calculated the corrections using both the low and the high temperatures and finally considered the average of the two corrected flux densities, the difference being accounted for in the errors. To estimate the color correction of AKARI FIS and IRC data, we fitted a BB to the two datasets independently, using the 25 μm IRAS observation because we

1 The 10.5 μm ISO-CAM image of the nebula is very similar to the ground-based mid-infrared images presented in Voors et al. (2000 [164]) but its spatial resolution is much lower.

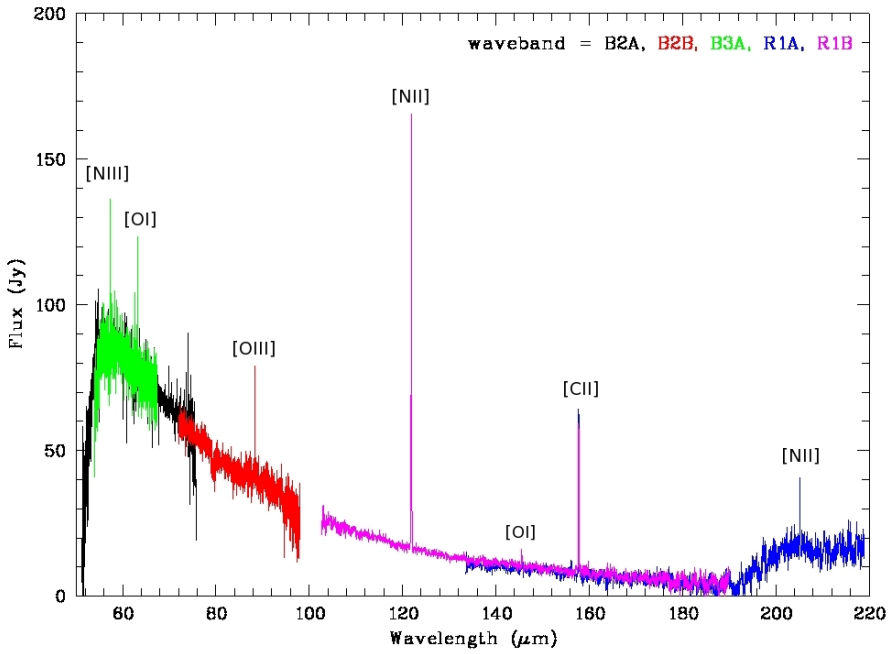

Figure 2.6: PACS spectrum of WRAY 15-751, integrated over the nine central spaxels. Indicated are the lines [NIII], [OI], [OIII], [NII] and [CII]. The continuum shape below 55 μm results from a yet-imperfect spectral response function correction, while above 190 μm it results from a light leak, from the second diffraction order of the grating in the first one. The different bands are indicated with different colors.

needed a measurement near the maximum of the curve. These fits led us to adopt the color correction factors that correspond to a temperature of 200 K for FIS (Yamamura et al. 2010 [173]) and 150 K for IRC data (Lorente et al. 2008 [77]). To color-correct the *Herschel*-PACS data, we fitted a BB, considering again the 25 μm IRAS observation. This fit gave a temperature of 200 K, therefore we adopted the corresponding correction factor (Müller et al. 2011 [144]). For the color correction of the ISO data we used the correction factors given in the corresponding handbooks (Blommaert et al. 2003 [6]; Laureijs et al. 2003 [73]). Finally, the mid-infrared flux density derived from ground-based imaging at ESO with the TIMMI instrument was taken from Voors et al. (2000 [164]).

All these measurements, presented in Table 2.1, were considered to model the dust continuum of the nebula, along with the PACS spectrum, integrated over the full field of view (25 spaxels) and the archived ISO-LWS spectrum discussed in Voors et al. (2000 [164]).

In Fig. 2.7, we show the infrared SED of WRAY 15-751 obtained at different epochs with the various instruments. Within the uncertainties, all these measurements agree excellently. First, the agreement between the PACS and ISO-LWS spectra obtained at different epochs,

Spacecraft-Instrument	Date	λ (μm)	F_ν (Jy)	Error (Jy)
IRAS	1983	12	14.54	0.75
		25	214	14
		60	112	12
ISO-CAM	1996	10.5	8.9	0.1
ISO-PHT	1996	25	150	40
		60	75	36
		105	29	4
AKARI-IRC	2007	9	3.32	0.03
		18	82.3	2.5
AKARI-FIS	2007	65	93.3	6.6
		90	41.4	2.7
		140	15.2	1.5
Herschel-PACS	2010	70	68.9	8.3
		100	31.7	5.6
		170	8.8	2.9
ground-based imaging				
TIMMI-ESO	1995	10	5.6	0.1

Table 2.1: Color-corrected nebular flux densities.

taking into account that at longer wavelengths the ISO PSF (100″ FWHM at 180 μm) becomes larger than the aperture (84″) so that some nebular flux is likely lost, while this is not the case with PACS (PSF of 14″ FWHM at 200 μm for a 47″ × 47″ aperture and a diameter of the nebula smaller than 40″). Second, the agreement between the spectra and the photometric data points, indicating that broad-band photometry is dominated by the dust continuum, and that the dust shell is well within the PACS spectroscopic field of view.

2.5.1 *Modeling the dust nebula*

To model and interpret the dust emission spectrum and the FIR images, we used the publicly available two-dimensional radiative transfer code 2-Dust (Ueta and Meixner 2003 [152]). 2-Dust is a versatile code that can be supplied with various grain size distributions and optical properties as well as complex axisymmetric density distributions.

Modeling the WRAY 15-751 dust nebula has previously been carried out by Voors et al. (2000 [164]) using IRAS and ISO near- to far-infrared spectroscopy, mid-infrared (10 μm) ground-based imaging and a one-dimensional radiative transfer code. Using the same data and adopting their input parameters for both the dust and the nebular properties, we derived quasi-identical results using 2-Dust (e.g. dust emission spectrum, temperature and mass). In the following, we use in addition the new PACS imaging and spectroscopic data, to-

gether with AKARI archive data to further constrain the dust shell properties.

Voors et al. (2000 [164]) showed that the discrepancy between their model and the data at ~10 μm (Fig. 2.7) is probably caused by a small amount of tiny, warm, out-of-equilibrium carbon grains in addition to silicates. These warm grains do not significantly contribute to the bulk of the dust mass at the origin of the emission at $\lambda > 20$ μm. Their mid-infrared image may thus not represent the main dust component. We then re-derived the inner radius of the dust shell using the PACS 70 μm image. We first assumed that the dust shell around WRAY 15-751 is spherically symmetric. This is a good proxy to the overall geometry and limits the number of free parameters. We also assumed that the dust density in the nebula runs as r^{-2}. By comparing the PACS images with the synthetic ones produced by 2-Dust and convolved with the PACS PSF (Fig. 2.8), we determined the inner radius of the dust shell, $r_{in} = 7''$. This agrees with the radius derived by Voors et al. (2000 [164]). We also adopted $r_{out} = 3 \times r_{in}$. At a distance of 6 kpc, this corresponds to $r_{in} = 0.20$ pc and $r_{out} = 0.60$ pc. These results are similar to the measurements discribed in Sect. 2.3, considering the errors.

Like other LBVs, WRAY 15-751 exhibits long-term strong photometric variations. Since the reaction (heating/cooling) of typical dust grains to luminosity changes is quasi-instantaneous (e.g. Bode and Evans 1979 [7]), the stellar parameters corresponding to the different epochs of observation must be considered. In a detailed study, Sterken et al. (2008 [142]) showed that the star was in a minimum (i.e., minimum V brightness), hot phase in 1989 and in a maximum, cooler phase in 2008. They suggested that WRAY 15-751 moved in the HR diagram from $\log L/L_\odot = 5.9 \pm 0.15$, $\log T_{eff} = 4.46 \pm 0.02$ in 1989 to $\log L/L_\odot = 5.4 \pm 0.15$, $\log T_{eff} = 3.92 \pm 0.02$ in 2008. By interpolating, we estimated $T_{eff} = 18000$ K in 1996, at the epoch of the ISO observations. A good fit of the ISOPHOT stellar spectrum at $\lambda < 5$ μm is obtained with $R_\star = 80 R_\odot$, which corresponds to a stellar luminosity $\log L/L_\odot = 5.8$. Unfortunately, the photometric measurements are very scarce before 1989. From the V light curve displayed by Sterken et al. (2008 [142]), the brightness of the star seems nevertheless similar in 1983, the epoch of the IRAS observations. We then adopted $T_{eff} = 18000$ K and $R_\star = 80 R_\odot$ as input for the 2-Dust modeling of both the IRAS and ISO data sets. At the epoch of the AKARI and *Herschel* observations in 2007-2010, the star is much cooler and apparently less luminous. This is quite surprising given the good agreement of the IRAS/ISO and the AKARI/*Herschel* spectroscopic and photometric data seen in Fig. 2.7. Although AKARI/*Herschel* flux densities might be marginally lower than the IRAS/ISO ones, this constitutes a strong constraint for the modeling since the nebula itself cannot have significantly changed between 1996 and 2007-2010. To

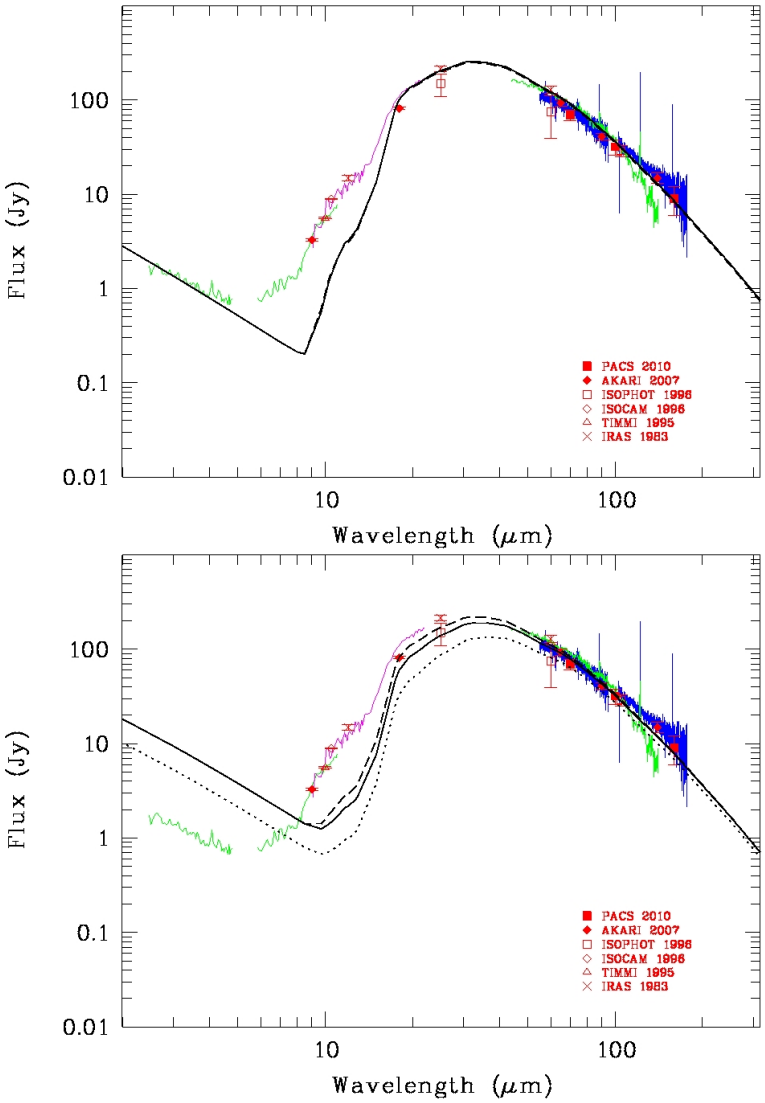

Figure 2.7: Infrared spectrum of WRAY 15-751 from data collected at different epochs: IRAS LRS from 8 to 22 μm (1983, magenta), ISOPHOT from 2.5 to 11 μm and ISO LWS from 45 to 140 μm (1996, green), *Herschel* PACS from 55 to 180 μm (2010, blue). The ISOPHOT data at $\lambda < 5$ μm are corrected for extinction using $E(B-V) = 1.8$. At $\lambda > 100$ μm, the flux density from ISO LWS is not reliable, the LWS aperture is too small for the ISO PSF. Color-corrected photometric measurements are superimposed (red symbols). The spectrum at $\lambda < 5$ μm comes from the central star, the bump at ~10 μm from silicates and very small out-of-equilibrium dust grains, and the spectrum at $\lambda > 20$ μm from the bulk of the dust shell. Results of the 2-Dust model fitting are illustrated. *Top*: best fits of the IRAS/ISO data assuming $R_\star/T_{eff}$ = 80/18000, a_{min}/a_{max} = 0.05/1.5 (solid line) and a_{min}/a_{max} = 0.2/0.5 (dashed line). *Bottom*: fits of the AKARI/*Herschel* data using the same dust shell properties but with $R_\star/T_{eff}$ = 320/9000. Results for a lower-luminosity star $R_\star/T_{eff}$ = 240/9000 and a_{min}/a_{max} = 0.2/0.5 are also displayed (dotted line).

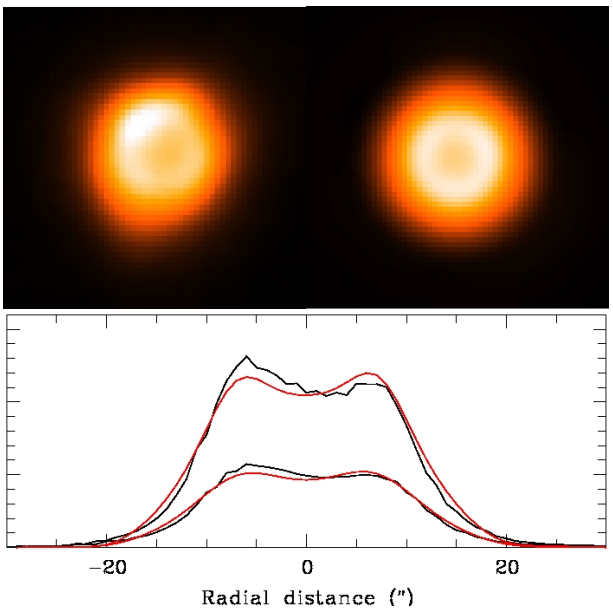

Figure 2.8: *Top left*: the $1' \times 1'$ image of the nebula around WRAY 15-751 observed with PACS at 70 µm. North is up and east to the left. *Top right*: the synthetic image computed with 2-Dust using $r_{in} = 7''$ and $r_{out} = 21''$ and convolved with the PACS PSF. *Bottom*: East-west cuts through the central part of the nebula, observed (black) and synthetic (red). The upper plots correspond to the 70 µm image, the lower ones to the 100 µm image.

model the 2007-2010 data, we considered two sets of stellar parameters: a constant-luminosity, low-temperature model with $T_{eff} = 9000$ K, $R_\star = 320 R_\odot$, and a low-luminosity, low-temperature one with $T_{eff} = 9000$ K, $R_\star = 240 R_\odot$ (i.e., $\log L/L_\odot = 5.5$) which better agrees with the most recent position of WRAY 15-751 in the HR diagram estimated by Sterken et al. (2008 [142]). Note that we neglected the delay in the response of the different parts of the dust shell to stellar changes, at most about four years in the observer frame for a shell radius of 0.6 pc. Such a delay will mostly smear out the effects of the stellar variations over some years.

Voors (1999 [163]) and Voors et al. (2000 [164]) found that the dust in the WRAY 15-751 nebula is dominated by amorphous silicates, with little contribution from crystalline species. They also obtained a best fit of the spectrum using pyroxenes and a 50/50 Fe to Mg abundance. We therefore started with a similar dust composition, using the optical constants given by Dorschner et al. (1995 [26]), extrapolated to a constant refraction index in the FUV. We assumed the size distribution for the dust grains of Mathis et al. (1997 [86], hereafter MRN): $n(a) \propto a^{-3.5}$ with $a_{min} < a < a_{max}$, a denoting the grain radius. By varying the opacity, which controls the strength of the emission, and a_{max} (or a_{min}), which controls the 20µm / 100µm flux density ratio, several good fits can be obtained (we did not at-

tempt to fit the 10 μm bump, which is due to out-of-equilibrium dust, only a minor contributor to the dust mass). Acceptable values of a_{max} range between 0.5 and 1.5 μm, confirming the presence of large ~ 1 μm dust grains in the nebula. In all cases the nebula is optically thin, the opacity is lower than 0.01 at 25 μm.

However, when a good fit of the IRAS/ISO data was obtained with the hot $R_\star/T_{eff} = 80/18000$ stellar parameters, we were unable to reproduce the AKARI/*Herschel* data using the same dust shell properties with the cooler star, even when using the constant luminosity 320/9000 model. A higher luminosity central star would be needed to compensate for the shift of stellar energy output from lower to higher wavelengths. We then tried to increase the near-infrared dust absorptivity by increasing the Fe to Mg ratio. Using the optical data of pyroxenes with a higher Fe to Mg ratio provided by Dorschner et al. (1995 [26]), the fit can be improved, but not sufficiently so. We then used the silicate dust with the highest available near-infrared absorptivity, i.e., the optical data given by Ossenkopf et al. (1992 [106]) for cold O-rich silicate with Fe inclusions (see also Fig. 7 of Dorschner et al. 1995 [26]), with an average bulk density $\rho = 3.5$ g cm^{-3}. Using a narrow range of dust radii, $a_{min} = 0.2 < a < a_{max} = 0.5$, we were finally able to fit both the IRAS/ISO data with the $R_\star/T_{eff} = 80/18000$ model and the AKARI/*Herschel* data with the $R_\star/T_{eff} = 320/9000$ model (Fig. 2.7). The observed dust emission cannot be reproduced when using the low-luminosity stellar parameters $R_\star/T_{eff} = 240/9000$ suggested by Sterken et al. (2008 [142]) for the 2007-2010 epoch.

In summary, the nebular dust emission can be reproduced for both the hot and cool stellar phases, assuming a constant stellar luminosity and Fe-rich dust grains. The adopted range of grain radii is unrealistically narrow, but numerical tests show that wider ranges can be considered if the near-infrared absorptivity is increased even more. As supported by the modeling, the fact that the dust emission does not significantly change from 1996 to 2010 suggests that stellar variations occur at essentially constant luminosity, as found in several LBVs (Wolf et al. 1981 [170]; Humphreys and Davidson 1994 [117]). Our results are not entirely incompatible with those of Sterken et al. (2008 [142]) since the uncertainties on the stellar luminosity are large and possibly underestimated, as quoted by the authors themselves. Our results demonstrate that the FIR dust emission from dust shells can be used to constrain the luminosity variations of the central star.

The mass and temperature of the dust shell we derive from the modeling depend little on the exact stellar parameters and dust sizes, provided that a good fit of the spectrum is obtained. We find that the total dust mass in the nebula is $M_{dust} = 4.5 \pm 0.5 \times 10^{-2}$ $M_\odot$ and that T_{dust} varies from 95 K at r_{in} to 66 K at r_{out}. The quoted uncertainty of M_{dust} only accounts for the dispersion of the values obtained with different models and is therefore underestimated. Our value of M_{dust}

is higher than the one derived by Voors et al. (2000 [164]) mainly because we used a larger distance to WRAY 15-751.

It is interesting to compare these estimates with those determined using empirical methods. Indeed, M_{dust} can be derived using

$$M_{dust} = \frac{F_\nu \, D^2}{B_\nu \, (T_{dust}) \, K_\nu} \, , \tag{2.1}$$

where K_ν is the mass absorption coefficient, B_ν the Planck function and D the distance to the nebula (Hildebrand 1983 [51]). K_ν is roughly independent of the grain radius and behaves as ν^β in the FIR. For the cold O-rich silicates of Ossenkopf et al. (1992 [106]), $K_{60} = 50$ cm^{2}g^{-1} at 60 μm and $\beta = 2.1$. By fitting a modified BB with $\beta = 2.1$ to the $\lambda \geqslant 18$ μm photometric data points (Fig. 2.7), we obtain $T_{dust} = 87$ K, not far from the mean value of the temperatures found with 2-Dust. The higher T_{dust} and lower β obtained in Vamvatira-Nakou et al. (2011 [155]) are due to the inclusion in the fit of the data at ~ 10 μm. Using Eq. 2.1 and the color-corrected IRAS flux density $F_{60} = 129$ Jy, we obtain $M_{dust} \simeq 3.5 \times 10^{-2}$ $M_\odot$, which agrees reasonably well with the value derived with 2-Dust, given the large uncertainties. The lower values of M_{dust} reported in Hutsemékers (1994 [59], 1997 [60]) using the same method are essentially due to the use of different values of K_ν and β.

2.5.2 *Properties of the outer nebula*

We now estimate the temperature and the mass of the outer nebula (shown in Fig. 2.3).

After carefully subtracting the background and the bright inner dust shell, we measured $F_{100} = 5.0 \pm 0.5$ Jy at 100 μm where the outer nebula is best seen, and $F_{70} = 6.0 \pm 0.5$ Jy at 70 μm. At 160 μm, we estimated $F_{160} = 5.0 \pm 1.5$ Jy, but this value strongly depends on the reduction procedure and background subtraction.

Assuming the same dust composition for the outer shell as for the inner one, i.e., $\beta \simeq 2$ (silicates), we derived $T_{dust} = 40 \pm 5$ K by fitting a modified BB to the flux densities measured at 70 and 100 μm. Within the uncertainties, the flux density at 160 μm is barely compatible with this temperature, most likely due to background contamination. The temperature of the nebula is higher than the temperature of the nearby background emission measured around $T_{dust} \simeq 20$ K, thus supporting the association of the outer nebula with WRAY 15-751. It is also interesting to note that for silicates, T_{dust} is expected to vary as as $r^{-1/3}$ (e.g. Tielens 2005 [146]), so that the second shell of radius ~ 70″ should have $T_{dust} \simeq 45$ K extrapolating from the average temperature of the inner shell. This is consistent with the measured value.

Using $F_{100} \simeq 5.0 \pm 0.5$ Jy, $K_{100} = 18$ cm^{2}g^{-1} and $T_{dust} = 40 \pm 5$ K in Eq. 2.1, we find $M_{dust} = 5 \pm 2 \times 10^{-2}$ $M_\odot$. Although uncertain, the

mass of dust in the outer shell appears at least as large as the mass in the bright inner shell.

2.6 EMISSION LINE SPECTRUM

2.6.1 *Line flux measurements*

We measured the emission line intensities in each one of the 25 spectra (Fig. 2.5) by fitting a Gaussian to the line profiles using IRAF. The detailed measurements are given in Sect. 2.9. Only at the central spaxel (2,2) are all the lines detected. At this spaxel the intensities of almost all lines reach their highest values. Most of the flux is detected in the 3×3 spaxels central area. In contrast, the outer 16 spaxels contribute significantly less to the line fluxes.

To investigate whether there are differences in the properties of the gas in different parts of the nebula, we also computed for each spaxel the flux ratios of every detected line to the line [NII] λ 122 μm, which is the strongest one. There is some evidence that the ratio [CII] 158 μ m / [NII] 122 μm might be higher in the outer spaxels than in the central ones. However, this trend is not significant given the large errors. Consequently, we cannot conclude that there is any clear trend with the distance to the center.

To measure the total emission line fluxes in the nebula with a reasonable accuracy, in particular to compute diagnostic flux ratios, we used the sum of the spectra that correspond to the 9 (3×3) central spaxels. The 16 outer spaxels are not included in the sum because they bring more noise than signal especially for the faint lines. We again calculated the line flux by fitting a Gaussian profile to each one of the detected forbidden emission lines. The results are given in Table 2.2. This table contains the detected ions, the wavelength of each line, the corresponding spectral waveband in which they were detected, and the fluxes with their errors. The quoted uncertainties are the sum of the line fitting uncertainty plus the uncertainty due to the position of the continuum, to which we quadratically added an error of 20% to account for the uncertainty of the PACS absolute flux calibration. Note that within a given waveband, relative flux uncertainties are smaller, on the order of 10%. There is a good agreement between the fluxes measured in two different bands for a given emission line so that weighted mean values are computed. The line [NII] λ 205 μm had a problematic calibration in PACS. Therefore, to be able to use the corresponding flux values for the following analysis, we calculated a correction factor using objects from the MESS collaboration (Groenewegen et al. 2011 [39]) observed with both PACS and SPIRE. Then, from the SPIRE/PACS cross calibration we found that the measured [NII] λ 205 μm flux should be multiplied by a correction factor of 5.5.

Ion	λ (μm)	Band	F (9 spaxels) (10^{-15} W m^{-2})	F (corrected) (10^{-15} W m^{-2})
[NIII]	57	B2A	1.60 ± 0.38	
		B3A	1.36 ± 0.30	
		Mean	1.45 ± 0.24	1.73 ± 0.29
[OI]	63	B2A	1.06 ± 0.26	
		B3A	0.93 ± 0.21	
		Mean	0.98 ± 0.16	1.18 ± 0.19
[OIII]	88	B2B	0.83 ± 0.18	1.04 ± 0.23
[NII]	122	R1B	4.14 ± 0.82	5.45 ± 1.08
[OI]	146	R1B	0.10 ± 0.03	0.14 ± 0.04
[CII]	158	R1B	0.81 ± 0.16	
		R1A	0.96 ± 0.19	
		Mean	0.87 ± 0.12	1.21 ± 0.17
[NII]	205	R1A	0.97 ± 0.24$^{\alpha}$	1.47 ± 0.36

Notes. $^{(\alpha)}$ Corrected value from PACS/SPIRE cross-calibration

Table 2.2: Line fluxes from the summed spectrum

The error of the final corrected [NII] 205 μm fluxes is assumed to be 25%.

When using the central 3 × 3 spaxel region, some nebular flux is lost, the amount of which depends on the wavelength as the beam size, with consequences on the flux ratios. On the other hand, the spectrum summed over all 25 spaxels encompasses the full ring nebula, as shown in Fig. 2.5 and supported by the agreement with the photometric measurements (Sect. 2.5). Thus, assuming that the spectral lines originate from the same regions as the dust continuum, we used the ratio of the 9-spaxel continuum spectrum to the 25-spaxel continuum spectrum to estimate the correction factor, which varies roughly linearly from 0.85 at 50 μm to 0.65 at 210 μm. Corrected flux values are given in the rightmost column of Table 2.2. For the two lines reasonably detected outside the central area, i.e., [NII] λ 122 μm and [CII] λ 158 μm (Table 2.4), we directly measured the fluxes integrated over the 25 spaxels. We found $F = 5.0 \pm 1.0 \times 10^{-15}$ W m^{-2} for [NII] and $F = 1.31 \pm 0.18 \times 10^{-15}$ W m^{-2} for [CII], in good agreement with the corrected values given in Table 2.2.

2.6.2 *Photoionization region characteristics*

The emission lines associated to the HII region detected in the spectrum of the inner nebula are [NIII] 57 μm, [OIII] 88 μm, and [NII] 122, 205 μm. The other three emission lines originate from a region of transition between ionized and neutral hydrogen, indicating a PDR.

Extensive analysis and discussion of the latter lines is given in the next section.

2.6.2.1 *Hα flux*

The Hα flux from the nebula was estimated by integrating the surface brightness over the whole nebula (Fig. 2.2). Contamination by field stars was corrected for, and emission from the central part extrapolated using the mean surface brightness. The contribution of the strong [NII] lines was removed using the [NII] /Hα ratio measured in Hutsemékers and Van Drom (1991 [61]) and the transmission curve of the Hα+[NII] filter. The conversion to absolute flux was made with the help of spectrophotometric standard stars observed in the same filter. Adopting a color excess E(B−V)=1.8 ± 0.3 based on the available optical studies of the nebula (Hu et al. 1990 [55]; Hutsemékers and Van Drom 1991 [61]; Voors et al. 2000 [164]; Garcia-Lario et al. 1998 [35]), we finally derived $F_0(H\alpha) = 3.1\times 10^{-11}$ ergs cm^{-2} s^{-1} (=3.1×10^{-14} W m^{-2}). The uncertainty of this value amounts to ~20%. It is more accurate than –and agrees with– the value given by Hutsemékers (1994 [59]).

2.6.2.2 *Electron density*

The [NII] 122/205 μm ratio, equal to 3.71 ± 1.17, provides a diagnostics for the electron density, n_e. To calculate it we used the package *nebular* of the IRAF/STSDAS environment (Shaw & Dufour 1995 [125]). This algorithm makes use of the fact that the nebular cooling-rate is dominated by ions, most of which have either p^2, p^3 or p^4 ground-state electron configurations. These configurations have five low-lying levels. The main physical assumption is that only these five levels are considered to calculate the emission line spectrum. For all the following calculations, an electron temperature constant throughout the nebula and equal to $T_e = 10^4$ K was assumed with an uncertainty of 20%. This value is reasonable since we observe higher excitation (i.e., the [NIII] 57 μm and [OIII] 88 μm lines) than in the AG Car nebula, for which Smith et al. (1997 [132]) calculated an electron temperature between 5900 to 7000 K. The electron density, using the [NII] 122/205 μm ratio, is found to be 164 ± 90 cm^{-3}.

The [SII] 6716/6731 Å ratio is also an electron density diagnostics. The value of this ratio measured by Hutsemékers and Van Drom (1991 [61]) is equal to 1.1 ± 0.1, which yields to an electron density of 423 ± 183 cm^{-3}, using the same tool and hypothesis. For the following analysis, we used the average electron density, i.e. n_e = 210 ± 80 cm^{-3}, a typical value for LBV nebulae (Nota et al. 1995 [103]).

2.6.2.3 *Ionizing flux*

It should be noted here that the recombination time in our case is much longer than the timescale of the variability exhibited by the central star of the nebula. More precisely, the recombination time is equal to $\tau_{rec} = 1/n_e\alpha_B = (1.22 \times 10^5/n_e)$ yr (Draine 2011 [27]), where α_B is the recombination coefficient. Using the measured electron density, we estimated that the recombination time is about 440 yr. Consequently, the stellar variations of ~ 10 yr cannot change the photoionization/recombination timescale significantly and an average nonvariable star can be considered.

The rate of emission of hydrogen-ionizing photons, Q_0, and the Strömgren radius of the ionized hydrogen region, R_S, can thus be determined. The nebula was considered to be spherical with an uniform density. Q_0 and R_S were first determined using the estimated Hα flux and second based on the radio flux density, $S_\nu = 24$ mJy at 6 cm (4.9 GHz) which was taken from the study of Duncan and White (2002 [28]), adopting a typical error of 0.5 mJy. It should be mentioned here that the nebula is optically thin at 4.9 GHz, as the optical depth, calculated using Eq. 2.29, is lower than one.

The following equation gives the R_S in pc (see Sect. 2.10)

$$R_S = 3.17 \left(\frac{x_e}{\epsilon}\right)^{1/3} \left(\frac{n_e}{100}\right)^{-2/3} T_4^{(0.272+0.007\ln T_4)} \left(\frac{Q_0}{10^{49}}\right)^{1/3} , \quad (2.2)$$

where, using the Hα flux, Q_0 (in photons s^{-1}) is given by

$$Q_{0(H\alpha)} = 8.59 \times 10^{55} T_4^{(0.126+0.01\ln T_4)} D^2 F_0(H_\alpha) . \quad (2.3)$$

When using the radio flux, Q_0 (in photons s^{-1}) is given by

$$Q_{0(radio)} = 8.72 \times 10^{43} T_4^{(-0.466-0.0208\ln T_4)} \left(\frac{\nu}{4.9}\right)^{0.1} x_e^{-1} D^2 S_\nu . \quad (2.4)$$

In these equations $x_e = n_e/n_p$, i.e. the fraction of the electron density to the proton density, ϵ is the filling factor, $T_4 = T_e/(10^4$ K), ν is the radio frequency (4.9 GHz in this case) and D is the distance of the nebula in kpc. The Hα flux, $F_0(H\alpha)$, is in ergs cm^{-2} s^{-1}, while the radio flux, S_ν, is in mJy.

Using the above equations and assuming $x_e = 1$ (the star is not hot enough to significantly ionize He), $\epsilon = 1$ (the whole volume of the nebula is filled by ionized gas) and $T_4 = 1$, the rate of emission of hydrogen-ionizing photons is found to be $Q_{0(H_\alpha)} = (9.6 \pm 3.7) \times 10^{46}$ photons s^{-1} and $Q_{0(radio)} = (7.5 \pm 2.5) \times 10^{46}$ photons s^{-1}. Within the uncertainties, these two results agree well. This also means that the adopted value of E(B−V) is essentially correct. The mean value is $Q_0 = (8.2 \pm 2.1) \times 10^{46}$ photons s^{-1} and corresponds to an early-B star, T_{eff} ~ 22 000 K (Panagia 1973 [109]), in agreement with the average spectral type of the star (Hu et al. 1990 [55]; Sterken et al. 2008 [142]).

The Strömgren radius calculated from Eq. 2.2 is $R_S = 0.46 \pm 0.17$ pc. By definition, the Strömgren radius is the radius of an ionization bounded nebula. In Sect. 2.3 the radius of the nebula in the optical, which is the radius of the ionized gas region which surrounds the central star, was found to be 0.32 pc. As both radii agree within the errors, we can conclude that the nebula can be ionization bounded, in agreement with the presence of PDR lines in the spectrum.

2.6.2.4 *Abundances*

The N/O abundance ratio can be estimated using the lines [NIII] 57 μm and [OIII] 88 μm and the equation

$$\frac{N}{O} = \frac{\langle N^{++} \rangle}{\langle O^{++} \rangle} = \frac{F_{[NIII]57}/\varepsilon_{[NIII]57}}{F_{[OIII]88}/\varepsilon_{[OIII]88}}, \tag{2.5}$$

where F is the observed line flux and ε is the volume emissivity. Considering $T_e = 10^4$ K and $n_e = 210$ cm^{-3}, we derived the emissivities using the package *nebular*. From the measured line intensities (Table 2.2), the N/O abundance ratio is then found to be 1.00 ± 0.38. The N/O ratio is much higher than the solar value of 0.14 (Grevesse et al. 2010 [37]). Compared with the N/O ratios of other LBVs nebulae (Smith 1997 [130]; Smith et al. 1998 [133]; Lamers et al. 2001 [72]), the value in the WRAY 15-751 nebula is one of the lowest and almost the same as the value found for the Large Magellanic Cloud (LMC) R127 nebula, 0.9 ± 0.4.

An estimate of the N/H abundance number ratio can also be made, based on the observed Hα 6562.8 Å, [NIII] 57 μm, [NII] 122 μm and 205 μm lines, considering that

$$\frac{N}{H} = \frac{\langle N^{+} \rangle + \langle N^{++} \rangle}{\langle H^{+} \rangle}. \tag{2.6}$$

The flux ratios, $F/F_0(H\beta)$ were calculated for the three infrared lines of nitrogen. The observed values of F were taken from Table 2.2. To calculate the Hβ flux, given the dereddened Hα flux, we assumed a case-B recombination with $T_e = 10^4$ K. The ionic abundances N^+/H^+ and N^{++}/H^+ where then derived using again the package *nebular*. Their sum gives the N/H abundance number ratio, calculated to be $(4.3 \pm 2.0) \times 10^{-4}$. This value is equivalent to a logarithmic N/H abundance of $12 + \log(N/H) = 8.63 \pm 0.20$, higher than the solar value of 7.83 (Grevesse et al. 2010 [37]). This value is similar to the N/H abundances of other LBV nebulae (Smith 1997 [130]; Smith et al. 1998 [133]; Lamers et al. 2001 [72]).

2.6.2.5 *Mass of the ionized gas*

The mass of the ionized gas can be estimated based on the Hα and the radio emissions. For this calculation the equations derived in Sect. 2.10 were used.

Since the temperature of the central star is lower than 30 000 K, we can assume that the ionization of He is negligible ($y_+ = 0$). Assuming also $\epsilon = 1$, the mass of the ionized nebula is $M_{i(H\alpha)} = 1.04 \pm 0.53\ M_\odot$ and $M_{i(radio)} = 0.92 \pm 0.46\ M_\odot$. The average value is $M_i = 0.97 \pm 0.35\ M_\odot$. If the nebula is considered to be a shell and not a sphere, with inner radius 7″ (assuming that the Hα shell has the same inner radius as the infrared dust shell) and outer radius 11″, which is the limit of the Hα nebula as described in Sect. 2.3, its ionized mass is $M_i = 0.84 \pm 0.31\ M_\odot$. Considering the errors, the ionized mass in the case of a shell nebula is not significantly different from the spherical case.

2.6.3 *Photodissociation region characteristics*

The fine structure lines [OI] 63, 146 μm and [CII] 158 μm indicate a PDR in the nebula because they are among the important coolants in PDRs (Hollenbach & Tielens 1997 [54]). In this region, which surrounds the ionized region of the nebula, the gas is neutral and the FUV photons (with $h\nu < 13.6$ eV) play a significant role in the chemistry and the heating. The first detection of a PDR in an LBV nebula, through the presence of fine structure lines, was made by Umana et al. (2009 [153]) in their Spitzer study of the nebula that surrounds HR Car. One year later a PDR was found in the nebula around the LBV candidate HD 168625 (Umana et al. 2010 [154]), this time through spectral features indicating the presence of PAHs.

The three infrared fine structure lines mentioned above can be used to determine the physical conditions in the PDR. But before that, any possible contribution of the HII region to the observed line intensities must be determined and subtracted. Neutral oxygen can be found only in neutral regions, because its ionization potential (13.62 eV) is very close to the ionization potential of hydrogen. Consequently, the lines [OI] 63, 146 μm arise exclusively from the PDR (Malhotra et al 2001. [81]). However, carbon is the fourth-most abundant element and has an ionization potential (11.26 eV) lower than that of hydrogen, so that C^+ can be found both in PDRs and HII regions. Therefore, the line [CII] 158 μm may arise from the HII region of the nebula WRAY 15-751 and/or from the associated PDR (Heiles 1994 [50]).

A first estimate of the contribution of the PDR to the flux of the line [CII] 158 μm can be obtained following the empirical method described by Goicoechea et al. (2004 [36]). For each spaxel where the [NII] 122 μm is detected (Sect. 2.9), the [CII] 158 μm emission that comes from the ionized gas should scale with the [NII] 122 μm, since the latter arises exclusively in ionized regions. Fig. 2.9 shows the correlation between the [CII] 158 μm and the [NII] 122 μm flux

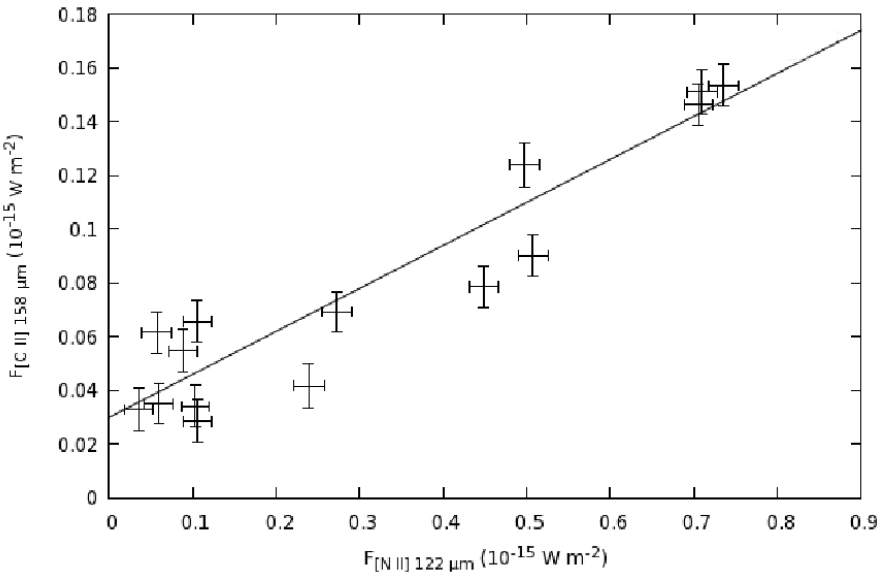

Figure 2.9: Correlation between the [CII] 158 μm and [NII] 122 μm line fluxes for each spaxel where these two lines are detected.

for each spaxel where these two lines are detected. This correlation is described by

$$F_{[CII]158} = (0.16 \pm 0.02)\, F_{[NII]122} + (0.03 \pm 0.01)\,, \tag{2.7}$$

where $F_{[CII]158}$ is the 158 μm line flux and $F_{[NII]122}$ is the 122 μm line flux in units of 10^{-15} W m^{-2}. The constant term of this relation represents the average [CII] 158 μm flux per spaxel that arises in the PDR. Assuming that the PDR extends as the dust nebula, i.e., over 18″ in radius or ∼ 11 spaxels, we then find $F^{PDR}_{[CII]158} \simeq (0.33 \pm 0.11) \times 10^{-15}$ W m^{-2}.

Another estimate of the contribution of the PDR and the HII regions to the flux of [CII] 158 μm line can be also obtained. As the [NII] 122 μm line arises exclusively in the ionized gas regions, measurements of its flux can give an estimate of the contribution of the HII region to the flux of [CII] 158 μm line, $F^{HII}_{[CII]158}$ through a model. We define $F^{HII}_{[CII]158} = \alpha F_{[CII]158}$, where $F_{[CII]158}$ is the total flux of the [CII] 158 μm line from Table 2.2 and α a factor that has to be determined. The ratio of fractional ionization is given, as previously, by

$$\frac{\langle C^+ \rangle}{\langle N^+ \rangle} = \frac{F^{HII}_{[CII]158}/\varepsilon_{[CII]158}}{F_{[NII]122}/\varepsilon_{[NII]122}}\,. \tag{2.8}$$

Malhotra et al. (2001. [81]) provided an estimate for this relation only for the high, $n_e \gg n_{crit}$, and the low, $n_e \ll n_{crit}$, electron density limit, where $n_{crit} = 3.1 \times 10^2 cm^{-3}$ for [NII] 122 μm and $n_{crit} = 50$ cm^{-3} for [CII] 158 μm. As neither of these two limits apply to our case,

the emissivities were calculated using the package *nebular* for the assumed T_e and the measured n_e. Assuming $\langle C^+\rangle/\langle N^+\rangle = C/N$, we find

$$\frac{F^{HII}_{[CII]158}}{F_{[NII]122}} = (0.45 \pm 0.06)\,\frac{C}{N}\,. \tag{2.9}$$

Since N/O has been estimated to be 1, we find that

$$\log\alpha = \log\frac{C}{O} + 0.31\,, \tag{2.10}$$

using the observed ratio $F_{[CII]158}/F_{[NII]122} = 0.222 \pm 0.054$.

To derive the temperature and density of the PDR as well as the C/O abundance ratio, we plot the theoretical $F_{[OI]63}/F_{[OI]146}$ ratio against the $F_{[OI]63}/F^{PDR}_{[CII]158}$ ratio normalized to the solar $(C/O)_\odot = 0.5$ abundance ratio (Fig. 2.10), following a similar study by Liu et al. (2001 [76]). To calculate the populations of the fine-structure levels of C^+ and O^0, we solved the two- and three-level atom equilibrium equations, respectively, considering that collisions with atomic hydrogen dominate in the PDR (Draine 2011 [27]). The radiative transition probabilities, A_{ij}, for the [CII] and [OI] fine-structure lines and the electron collision strengths, Ω_{ij}, were taken from Draine (2011 [27]). The collisional rate coefficients for the fine-structure excitation by hydrogen were taken from Barinovs et al. (2005 [2]) for [CII] and from Abrahamsson et al. (2007 [1]) for [OI]. A simple analytic extrapolation was made for temperatures higher than those given in these two references[2]. Furthermore, if we assume that there is pressure equilibrium between the HII region and the PDR, we have (Tielens 2005 [146])

$$n_{H^0}\,k\,T_{PDR} \simeq 2 n_e k T_e = (4.2 \pm 1.8) \times 10^6\ \mathrm{cm^{-3}K}\,, \tag{2.11}$$

where n_{H^0} is the atomic hydrogen number density and T_{PDR} is the temperature of the PDR. This relation defines a locus of possible values in the diagram of Fig. 2.10.

Given the observed ratio $F_{[OI]63}/F_{[OI]146} = 8.4 \pm 2.8$ and the constraints from Eq. 2.11, we can derive from Fig. 2.10 $\log(F_{[OI]63}\ /\ F^{PDR}_{[CII]158})$ + [C/O] = 0.63, where $[C/O] \equiv \log(C/O) - \log(C/O)_\odot$. Recalling that $F^{PDR}_{[CII]158} = (1-\alpha)F_{[CII]158}$ and considering the above relation between C/O and α (Eq. 2.10), the observed value of the line ratios yields $\alpha = 0.82 \pm 0.07$ and $C/O = 0.40 \pm 0.19$. Considering the errors, the C/O abundance ratio of the nebula has the solar value. C/H is then $(1.7 \pm 1.3) \times 10^{-4}$ from the N/H, C/O and N/O abundance ratios. The contribution of the HII region to [CII] 158 μm is then $F^{HII}_{[CII]158} = (0.99 \pm 0.16) \times 10^{-15}$ W m^{-2} while the contribution of the PDR is $F^{PDR}_{[CII]158} = (0.22 \pm 0.09) \times 10^{-15}$ W m^{-2}. This value agrees with the one obtained using the empirical method.

2 The difference between the diagram of Fig. 2.10 and the one in the study of Liu et al. (2001 [76]) is due to the use of updated collision coefficients.

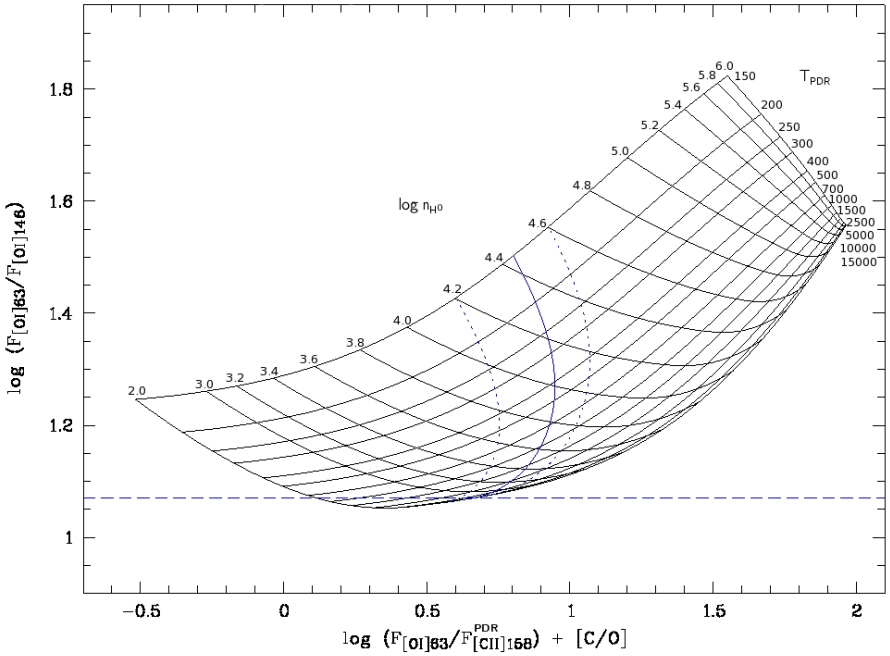

Figure 2.10: Temperature-density PDR diagnostic diagram. The grid of flux ratios $F_{[OI]63}/F_{[OI]146}$ versus $F_{[OI]63}/F^{PDR}_{[CII]158}$ was calculated by solving the level population equations for a range of temperatures and densities. $F_{[OI]63}/F^{PDR}_{[CII]158}$ is normalized to the solar abundance $(C/O)_\odot = 0.5$ so that $[C/O] \equiv \log(C/O) - \log(C/O)_\odot$. The solid line corresponds to the pressure equilibrium between the HII region and the PDR, the two dotted lines on each side accounting for the errors. The horizontal dotted line represents the 1-σ upper limit of the observational $\log(F_{[OI]63}/F_{[OI]146})$ ratio.

The diagram in Fig. 2.10 also provides us with the values of the density and the temperature of the PDR of the nebula, from the observed $F_{[OI]63}/F_{[OI]146}$ ratio: $\log n_{H^0} = 2.38 \pm 0.18$ and $T_{PDR} > 4000$ K. Given the constraints from Eq. 2.11, we estimate that $T_{PDR} \sim 17500$ K but this value is very uncertain, within a factor of 2.

The incident FUV radiation field, G_0, along with the density n_{H^0}, describes the structure of the PDR. Expressed in terms of the average interstellar radiation field, which corresponds to a unidirectional radiation field of 1.6×10^{-3} erg cm^{-2} s^{-1}, it is given by (Tielens 2005 [146])

$$G_0 = 625 \frac{L_\star \chi}{4\pi R^2} \tag{2.12}$$

at the distance R from the star, with $L_\star$ the stellar luminosity and χ the fraction of the luminosity above 6 eV. For an early B star, $\chi \sim 0.7$ (Young Owl et al. 2002 [174]). Considering $L_\star = 10^{5.8} L_\odot$ (Sect. 2.5.1) and the radius of the ionized gas region, which is surrounded by the PDR, $R = 0.32$ pc, the incident FUV radiation field is found to be

$G_0 \simeq 8.5 \times 10^4$ for the PDR of the WRAY 15-751 nebula. This value is consistent with the estimated PDR density, as our results are reasonably compatible with the diagnostic diagrams of the PDR models of Kaufman et al. (1999 [67], Figs. 4 & 5).

The FUV radiation given by G_0 is also absorbed and re-emitted by the dust in the FIR. The radiative equilibrium gives us the dust temperature, T_{dust}, which in case of silicates (i.e., $\beta = 2$) is given by (Tielens 2005 [146])

$$T_{dust} = 50 \left(\frac{1\mu m}{a}\right)^{0.06} \left(\frac{G_0}{10^4}\right)^{1/6} K \quad \text{for } T_{dust} < 250 \text{ K} . \tag{2.13}$$

As the small grains dominate the average cross-section, a typical grain size of $a = 0.1$ μm can be assumed, which leads to a dust temperature of $T_{dust} = 81$ K, in excellent agreement with the results of the 2-Dust model.

The total mass of hydrogen in the PDR, M_H, can be estimated from the [CII] 158 μm line flux derived for the PDR (Tielens 2005 [146]), using the equation given in Sect. 2.11. For the above PDR density, temperature, distance and C/H abundance, the neutral hydrogen mass in the PDR is estimated to be $M_H = 0.43 \pm 0.35\ M_\odot$.

2.6.4 *Total gas mass*

The total gas mass of the nebula is the sum of the mass in the ionized nebula and the mass in the PDR, corrected for the presence of helium, i.e.,

$$M_{gas} = (1 + 4y)\,(M_i + M_H) , \tag{2.14}$$

where $y = n_{He}/n_H$. Assuming a solar abundance for helium of $12 + \log(He/H) = 10.93 \pm 0.01$ (Grevesse et al. 2010 [37]), the gas mass is $M_{gas} = 1.7 \pm 0.6\ M_\odot$. Considering the calculated dust mass (Sect. 2.5.1), the dust-to-gas mass ratio for the inner nebula is $M_{dust}/M_{gas} = 0.026 \pm 0.010$, i.e., $\sim 3\%$. If the He abundance is higher, as expected for an evolved star, the total gas mass will be higher, typically 20% for a He/H abundance ratio corresponding to the observed N/O abundance ratio.

2.7 DISCUSSION

A summary of the measurements obtained in the previous sections is given in Table 2.3. The luminosity, effective temperature and distance of the central star are given first (from Hu et al. 1990 [55]; Sterken and al. 2008 [142], and this work), followed by the parameters of the inner and the outer dust shells, i.e., the radius, the expansion velocity (from Hutsemékers and Van Drom 1991 [61]; assumed to be identical for both shells), the kinematic age, the electron density and the assumed

Star	$\log L/L_\odot$	5.7 ± 0.2
	T_{eff} (K)	$30\,000 \leftrightarrow 9000$
	D (kpc)	6.0 ± 1.0
Inner Shell	r (pc)	0.5
	v_{exp} (km s^{-1})	26
	t_{kin} (10^4 yr)	1.9
	n_e (cm^{-3})	210 ± 80
	T_e (K)	10 000
	N/O	1.00 ± 0.38
	C/O	0.40 ± 0.19
	12+log N/H	8.63 ± 0.20
	M_{dust} (10^{-2} $M_\odot$)	4.5 ± 0.5
	M_{gas} ($M_\odot$)	1.7 ± 0.6
Outer Shell	r (pc)	2.0
	t_{kin} (10^4 yr)	7.5
	M_{dust} (10^{-2} $M_\odot$)	5.0 ± 2.0

Table 2.3: Parameters of WRAY 15-751

temperature of the ionized gas, the abundance ratios, and the dust and gas masses.

The *Herschel*-PACS FIR images of WRAY 15-751 reveal the dust nebula as a shell of radius 0.5 pc and width 0.35 pc. These observations also unveiled a second dust nebula, four times bigger, lying in an empty cavity. As in the case of WR stars (Marston 1996 [84]), the empty cavity probably corresponds to the interior of O-star wind bubble formed when the star was on the main sequence.

Our study consistently shows that the main nebula is illuminated by an average early-B star and consists of a shell of ionized gas surrounded by a thin photodissociation region. Both these regions are mixed with dust. The mass of this nebula amounts to $\sim 2\ M_\odot$ ejected $\sim 2 \times 10^4$ years ago. The second, larger and older nebula contains a similar amount of mass if we assume a similar dust-to-gas ratio so that, in total, $\sim 4\ M_\odot$ of gas have been ejected within $\sim 6 \times 10^4$ years. This also indicates that the star had multiple episodes of intense mass-loss. Moreover, it is possible that the very inner dense nebula spectroscopically detected by Hutsemékers and Van Drom (1991 [61]) and resolved by Duncan and White (2002 [28]) constitutes a third ejection some 10^3 years ago, assuming an angular radius of 1″ (Duncan and White 2002 [28]) and an expansion velocity of 26 km s^{-1}, the same as for the main ring nebula.

The N/O abundance ratio appears to be enhanced by a factor 8 with respect to the solar abundances given in Ekström et al. (2012 [29]). This confirms the presence of processed material in the nebula. The C/O ratio, measured for the first time in a LBV nebula, is solar within the uncertainties. These ratios correspond to an enhancement

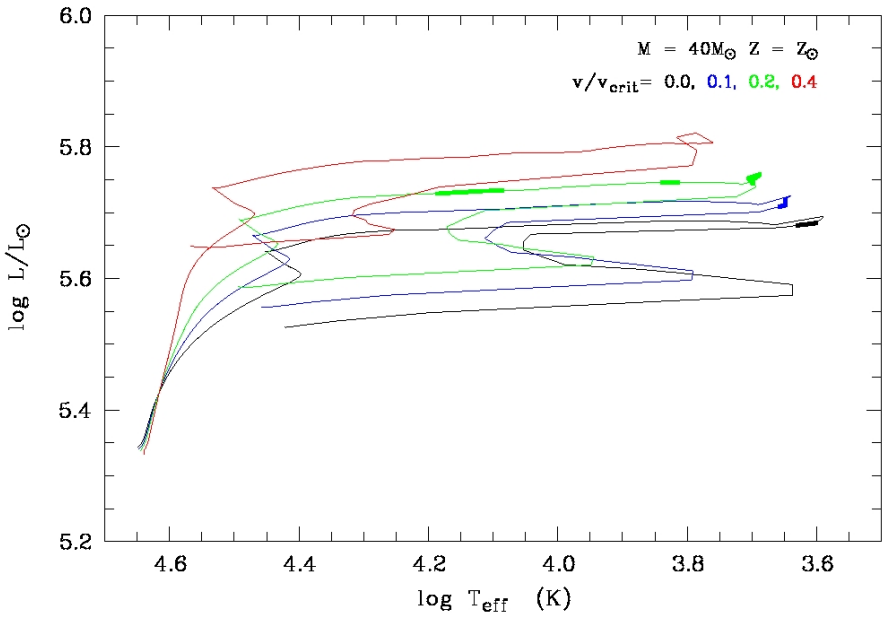

Figure 2.11: Evolutionary path in the HR diagram of a 40 $M_\odot$ star of solar metallicity and for initial rotation rates v/v_{crit} from 0 to 0.4, using the models of Ekström et al. (2012 [29]). The thicker lines emphasize the part of the tracks compatible with the measurements (cf. Fig. 2.12 and Fig. 2.13). For clarity, the tracks are stopped at the beginning of the blue loop (data point n° 210 in Ekström et al. 2012 [29]).

in N/H by a factor 6 and a depletion in C/H and O/H by a factor 1.4 with respect to the solar abundances.

The N/O ratio of 1.00 ± 0.38 is quite similar to the ratio measured in the nebula around the LMC LBV R127 (Smith et al. 1998 [133]). The 12+log(N/H) abundance of 8.63 ± 0.20 is between the values for the LBVs AG Car and η Car (Smith et al. 1998 [133]). The conclusion of Smith et al. (1997 [132], 1998 [133]) that LBV nebulae contain only mildly enriched material with respect to CNO equilibrium values and thus were ejected during a previous RSG or Yellow Super Giant (YSG) phase therefore applies to WRAY 15-751, especially as the star is less luminous, $\log L/L_\odot = 5.7 \pm 0.2$, i.e., just at or below the Humphreys-Davidson limit. In addition, the nebula has a relatively low expansion velocity of 26 km/s, more compatible with RSG outflows than the higher velocities measured in more luminous LBVs such as AG Car. The ejection of the WRAY 15-751 nebula during an RSG phase was also proposed by Voors et al. (2000 [164]) on the basis on its dust composition.

Our observations can be used to constrain the evolutionary path of the star and the epoch of ejection of the nebula. Given its luminosity, WRAY 15-751 is expected to result from the evolution of a star of initial mass in the range $40 - 60$ $M_\odot$. Figs. 2.11, 2.12, and 2.13 show the

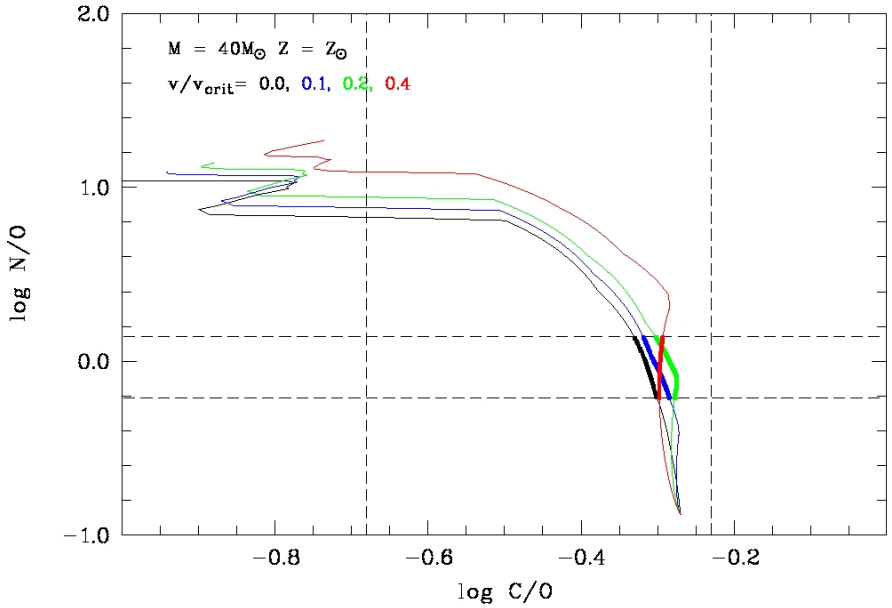

Figure 2.12: Evolution of the N/O versus the C/O surface abundance ratios for a 40 $M_\odot$ star of solar metallicity and for initial rotation rates v/v_{crit} from 0 to 0.4, using the models of Ekström et al. (2012 [29]). The dashed lines correspond to the values measured for the inner shell around WRAY 15-751, with their errors. The thicker lines emphasize the part of the tracks compatible with the measurements. For clarity, the tracks are stopped at the beginning of the blue loop (data point n° 210 in Ekström et al. 2012 [29]).

evolution of some properties of a 40 $M_\odot$ star using the models of Ekström et al. (2012 [29]). Four different cases of stellar rotation are considered, from no rotation to a rotation rate of v/v_{crit}=0.4. The tracks are first compared with the observed N/O and C/O abundance ratio to identify the part of the tracks where the computed surface abundances match the observed nebular abundances (Fig. 2.12). Possible tracks were additionally constrained when compared with the observed mass-loss rate (Fig. 2.13). The mass-loss rate is estimated from the mass of the inner nebula divided by the duration of the enhanced mass-loss episode (estimated from the kinematic age), i.e., the time needed to cover the ring width: $\log \dot{M} = -3.8 \pm 0.2$, accounting for an increase of the mass of 20% due to the higher He/H abundance at that time. These constraints are finally reported in the HR diagram (Fig. 2.11) to identify the locus of the ejection of the inner nebula. The model appears to remarkably agree with the observations, supporting the scenario of an ejection of the nebula during the RSG phase[3]. The N/H enhancement factor as well as the C/H and O/H depletion factors predicted by the model also agree with the observed values.

3 We loosely use the term RSG for the reddest part of the tracks in the HR diagram, while strictly speaking RSG have $\log T_{eff} < 3.65$.

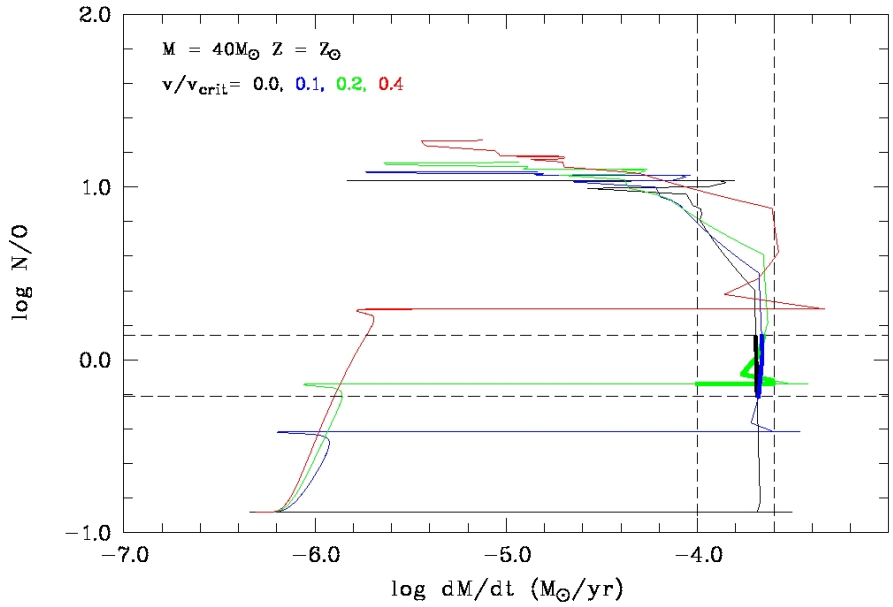

Figure 2.13: Evolution of the N/O surface abundance ratio as a function of the mass-loss rate for a 40 $M_\odot$ star of solar metallicity and for initial rotation rates v/v_{crit} from 0 to 0.4, using the models of Ekström et al. (2012 [29]). The dashed lines correspond to the values measured for the inner shell around WRAY 15-751, with their errors. The thicker lines emphasize the part of the tracks compatible with the measurements. For clarity, the tracks are stopped at the beginning of the blue loop (data point n° 210 in Ekström et al. 2012 [29]).

The mild N/O enrichment indicates that the star cannot be a fast rotator, the v/v_{crit}=0.4 track being clearly excluded. A similar result is obtained for a 45 $M_\odot$ star except that the only possible tracks have v/v_{crit}= 0.0 and 0.1. For a 50 $M_\odot$ star, no track satisfies the observational constraints.

The time between the ejections of the outer and the inner nebulae, about 6×10^4 years, is compatible with the duration of the RSG phase of a 40 $M_\odot$ star, as computed by the model. Thus, the outer nebula could also have been ejected during this phase, especially in the models with $v/v_{crit} < 0.2$ for which the inner, younger nebula is ejected closer to the end of the RSG phase than to the beginning (Fig. 2.11). The total mass lost during the RSG phase amounts to $8-9$ $M_\odot$ in the model. Although higher, this is compatible with our value of 4 ± 2 $M_\odot$, recalling that the value for the outer nebula is particularly uncertain due to the unknown dust-to-gas ratio and He abundance.

Our results suggest that the ejection of the nebula does not occur because the star is rotating close to the critical velocity, as proposed by Meynet et al. (2011 [92]). Moreover, the existence of multiple nebular shells points to an instability mechanism at work during the RSG evolutionary stage and not to a continuous wind. In particular, models

by Stothers and Chin (1996 [143]) suggest that LBV nebulae can result from strong, closely spaced mass-loss episodes in the RSG phase and not from a continuous wind. For a 45 $M_\odot$ star, they found that about 4 $M_\odot$ can be ejected, in agreement with our measurements.

While our results support the scenario of an ejection of LBV in the RSG phase, the study of Lamers et al. (2001 [72]) reached the conclusion that LBV nebulae were ejected during the Blue Super Giant (BSG) phase with high rotational velocities, and not during the RSG stage. However, Lamers et al. (2001 [72]) only considered very luminous LBVs ($\log L/L_\odot > 5.8$), while WRAY 15-751 is a lower luminosity LBV. Moreover, the nebula around WRAY 15-751 is only weakly bipolar compared with other LBV nebulae such as those around AG Car or HR Car, in qualitative agreement with little effect of rotation. Finally, the discovery of a dusty LBV-like ring nebula around the YSG Hen3-1379, which is very similar to WRAY 15-751, also supports the ejection of nebulae during the RSG phase (Hutsemékers et al. 2013 [62]). Therefore, high-luminosity and low-luminosity LBVs probably follow different evolutionary paths.

Our results are compatible with the evolutionary model of an $\sim$ 40 $M_\odot$ star and the O–BSG–RSG–YSG–LBV filiation. According to Toalá and Arthur (2011 [148]), an $\sim$ 40 $M_\odot$ star creates a bubble of radius $\sim$ 25 pc as a main- sequence O star, in agreement with the structure tentatively observed in Fig. 2.4. Then, when an RSG, the star ejects several solar masses of material in the cavity previously created, forming the observed dusty nebulae. It is interesting to note that in this scenario, the age of WRAY 15-751 since the ejection of the last nebula is only $\sim 2 \times 10^4$ years, which corresponds in the computed tracks of Fig. 2.11 to the loop at $\log T_{\rm eff} \sim 4.1$. Higher temperatures are only reached $\sim 10^5$ years later. It is not clear whether a star at that location in the HR diagram, which corresponds to a hot YSG, can have the LBV-like instability properties currently displayed by WRAY 15-751. This might indicate that the LBV phenomenon could occur at different evolutionary stages. Determining the surface abundances of WRAY 15-751 in its present stage might help to constrain this scenario more closely.

2.8 CONCLUSIONS

We have presented the analysis of *Hershel* PACS imaging and spectroscopic data of the nebula around the LBV Wray 15-751, together with new optical-imaging data. The FIR images clearly show that the main, dusty nebula is a shell extending outside the well-known Hα nebula. Furthermore, these images reveal a second, bigger and fainter dust nebula that is observed for the first time. The two nebulae lie in an empty cavity, very likely the remnant of the O-star wind bubble formed when the star was on the main sequence.

The dust parameters of the main nebula were determined based on dust modeling. This model shows that the FIR emission did not significantly change during the different phases of the S Dor cycle. This stability points to a stellar variation under essentially constant luminosity. We also found that Fe-rich dust is needed to reproduce the data. This is not unexpected in LBV nebulae as a consequence of depletion of C and O with respect to heavier elements (Gail et al. 2005 [33]).

The FIR spectrum of the main nebula contains forbidden emission lines coming from an ionized region and from a photodissociation region, from which we derived the gas parameters, such as the C, N, O abundances and the ejected gas mass, with the C/O ratio measured for the first time in an LBV nebula. As a result of this study, the main shell nebula consists of an ionized gas region which is surrounded by a thin PDR, both regions being mixed with the dust. As expected for such an evolved star, the nebula shows N enrichment and C, O depletion.

The measured abundances, masses and kinematic ages of the nebulae were used to constrain the evolution of the star and the epoch at which the nebulae were ejected. Our results point to an ejection of the nebulae during the RSG evolutionary phase of an $\sim 40\ M_{\odot}$ star. The multiple shells around the star suggest that the mechanism of mass-loss is not a continuous wind but instead a series of short episodes of extreme mass-loss.

This scenario is compatible with the recent evolutionary tracks computed for an $\sim 40\ M_{\odot}$ star with little rotation, in particular the O–BSG–RSG–YSG–LBV filiation although it should be stressed that post-main-sequence evolutionary tracks of massive stars are still very uncertain, in particular since they rely on poorly known mass-loss mechanisms and rates. If the evolutionary tracks are correct, our results support the idea that high-luminosity and low-luminosity LBVs follow different evolutionary paths. The forthcoming analysis of similar data for higher luminosity LBVs (e.g., AG Car) and for LBVs known to be fast rotators (e.g., HR Car) should allow us to constrain this scenario more closely.

Acknowledgements. We thank Xiaowei Liu, Daniel Pequignot and Evelyne Roueff for help with the PDR diagnostic diagram construction. CVN, PR, DH, YN, KE and MATG acknowledge support from the Belgian Federal Science Policy Office via the PRODEX Programme of ESA. The Liège team acknowledges also support from the FRS-FNRS (Comm. Franç. de Belgique). PACS has been developed by a consortium of institutes led by MPE (Germany) and including UVIE (Austria); KU Leuven, CSL, IMEC (Belgium); CEA, LAM (France); MPIA (Germany); INAF-IFSI/OAA/OAP/OAT, LENS, SISSA (Italy); IAC (Spain). This development has been supported by the funding agencies BMVIT (Austria), ESA-PRODEX (Belgium), CEA/CNES (France), DLR (Germany), ASI/INAF (Italy), and CICYT/MCYT (Spain).

Data presented in this paper were analyzed using "HIPE", a joint development by the Herschel Science Ground Segment Consortium, consisting of ESA, the NASA Herschel Science Center, and the HIFI, PACS and SPIRE consortia. This research has made use of the NASA/IPAC Infrared Science Archive, which is operated by the Jet Propulsion Laboratory, California Institute of Technology.

2.9 APPENDIX A: EMISSION LINE FLUXES FOR EACH SPAXEL

Table 2.4 gives the results of the emission line flux measurements for each spaxel. The first column contains the detected ions along with the spectral band in which the corresponding line was measured. The following columns contain the line fluxes, expressed in W/m^2, along with their errors. The spaxel numbers (Fig. 2.5) are mentioned in every cell of the table. No spectral lines were detected in the western column of the spectrometric camera (spaxels [0,0] to [4,0]), and these spaxels were hence not included in the table. The quoted uncertainties are the sum of the line-fitting uncertainty plus the uncertainty due to the position of the continuum.

2.10 APPENDIX B: IONIZED NEBULA

The formulae needed to estimate the nebular mass and the ionizing flux from both Hα and radio emissions are re-derived here for consistency of hypotheses and notations.

2.10.1 Hα *emission*

The luminosity in the Hα recombination line, integrated over the volume V of the nebula, is given by (Osterbrock & Ferland 2006 [107])

$$L(H\alpha) = \int_V 4\pi j_{H\alpha} \epsilon dV \,, \tag{2.15}$$

where ϵ is the filling factor that gives the fraction of the volume of the nebula that is filled by ionized gas, and $j_{H\alpha}$ is the Hα line emission coefficient. The flux received by the observer is

$$F_0(H\alpha) = \frac{L(H\alpha)}{4\pi D^2} \,, \tag{2.16}$$

where D is the distance to the nebula. By integrating over the volume, assuming a spherical uniform nebula of radius R and considering the effective recombination coefficient $\alpha^{eff} = (4\pi j)/(n_e n_p h\nu)$, we have

$$F_0(H\alpha) = \left(\frac{R^3}{3D^2}\right) \epsilon h\nu_{H_\alpha} n_e n_p \alpha^{eff}_{H_\alpha} \,, \tag{2.17}$$

where n_e is the electron density, n_p is the proton density, h is the Plank's constant and ν_{H_α} is the frequency of the Hα line.

The mass of the ionized nebula, M_i, is equal to

$$M_i = \frac{4\pi}{3} R^3 \mu_+ n_p m_H \epsilon \,, \tag{2.18}$$

with m_H being the H atomic mass and μ_+ the mean ionic mass per H ion. By replacing n_e in the Eq. 2.17 with $n_e = x_e n_p$ and combining it with Eq. 2.18, the ionized mass can be written as

$$M_{i(H\alpha)} = \frac{4\pi\mu_+ m_H}{\sqrt{3h\nu_{H_a} x_e \alpha^{eff}_{H_a}}} \epsilon^{1/2} \theta^{3/2} D^{5/2} F_0^{1/2}(H\alpha) \,, \tag{2.19}$$

where θ is the angular radius of the nebula ($R = \theta D$) in Hα. By replacing the effective recombination coefficient with the following formula, taken from Draine (2011 [27]),

$$\alpha^{eff}_{H\alpha} = 1.17 \times 10^{-13} T_4^{(-0.942 - 0.031 \ln T_4)} \ cm^3 s^{-1} \,, \tag{2.20}$$

where $T_4 = T_e/(10^4\ K)$ and T_e is the electron temperature, we obtain the following expression for the ionized mass of the nebula in solar masses

$$M_{i(H\alpha)} = 57.9 \frac{1 + 4y_+}{\sqrt{1 + y_+}} T_4^{(0.471 + 0.015 \ln T_4)} \epsilon^{1/2} \theta^{3/2} D^{5/2} F_0^{1/2}(H\alpha) \,, \tag{2.21}$$

where θ is in arcsec, D is in kpc and $F_0(H\alpha)$ is in ergs cm^{-2} s^{-1}. With $n_{H^+} = n_p$, n_{He^+} and $n_{He^{++}}$ the ionized hydrogen, ionized helium and doubly ionized helium number densities, respectively, $x_e = n_e/n_p \simeq 1 + n_{He^+}/n_{H^+} = 1 + y_+$ and $\mu_+ \simeq 1 + 4\, n_{He^+}/n_{H^+} = 1 + 4y_+$ assuming $n_{He^{++}} = 0$ and denoting $y_+ = n_{He^+}/n_{H^+}$.

The number of hydrogen ionizing photons per unit time, $Q(H^0)$, emitted by a nebula in equilibrium is given by (Osterbrock and Ferland 2006 [107])

$$Q(H^0) = \epsilon n_e n_p \alpha_B V \,, \tag{2.22}$$

where α_B is the recombination coefficient given by the following equation, taken from Draine (2011 [27]),

$$\alpha_B = 2.54 \times 10^{-13} T_4^{(-0.8163 - 0.0208 \ln T_4)} \ cm^3 s^{-1} \,. \tag{2.23}$$

The combination of the two previous equations gives us the radius, R_S, which is the radius of the Strömgren sphere

$$R_S = 3.17 \left(\frac{x_e}{\epsilon}\right)^{1/3} \left(\frac{n_e}{100}\right)^{-2/3} T_4^{(0.272 + 0.007 \ln T_4)} \left(\frac{Q(H^0)}{10^{49}}\right)^{1/3} \tag{2.24}$$

in units of pc. By combining this equation with the Eq. 2.17, with $R = R_S$ (ionization bounded nebula), the rate of emission of hydrogen-ionizing photons for a given Hα flux, in photons per second is

$$Q_{0(H\alpha)} = 8.59 \times 10^{55} T_4^{(0.126 + 0.01 \ln T_4)} D^2 F_0(H_\alpha) \,. \tag{2.25}$$

2.10.2 *Continuum radio emission*

In the radio frequency region, where $h\nu \ll kT$, the Plank law can be written as

$$B_\nu = \frac{2\nu^2 kT}{c^2} \, , \tag{2.26}$$

where $B_\nu = j_\nu/\kappa_\nu$, with j_ν and κ_ν the emission and absorption coefficients at a given frequency ν, respectively.

The radio flux density at a distance D from the nebula is given by

$$S_\nu = \frac{L_\nu}{4\pi D^2} \, , \tag{2.27}$$

with $L_\nu = \int_V 4\pi j_\nu \epsilon dV$. Assuming that the nebula is an optically thin sphere of radius R, the radio flux density can then be written

$$S_\nu = \left(\frac{4\pi R^3}{3D^2}\right) \epsilon B_\nu \kappa_\nu \, . \tag{2.28}$$

The continuum free-free effective absorption coefficient at radio frequencies is given by (Osterbrock and Ferland 2006 [107])

$$\kappa_\nu = 8.24 \times 10^{-2} T_e^{-1.35} \nu^{-2.1} n_+ n_e \, , \tag{2.29}$$

where the temperature T_e is in K and the frequency ν is in GHz. The ion density is equal to $n_+ = n_{H^+} + n_{He^+} = n_e$.

The ionized mass of the nebula is defined by Eq. 2.18. By adopting the same formalism as in the first part of this Appendix, the ionized mass in solar masses is finally found to be

$$M_{i(radio)} = 5.82 \times 10^{-5} \frac{1 + 4y_+}{1 + y_+} T_4^{0.175} \left(\frac{\nu}{4.9}\right)^{0.05} \epsilon^{1/2} \theta^{3/2} D^{5/2} S_\nu^{1/2} \, , \tag{2.30}$$

where ν is the radio frequency in GHz, θ is the angular radius of the ionized nebula in arcsec, D is the distance to the nebula in kpc and S_ν is the radio flux density in mJy.

The rate of emission of hydrogen-ionizing photons, for a given radio flux density, can be found by combining Eq. 2.24 and 2.28:

$$Q_{0(radio)} = 8.72 \times 10^{43} T_4^{(-0.466 - 0.0208 \ln T_4)} \left(\frac{\nu}{4.9}\right)^{0.1} x_e^{-1} D^2 S_\nu \, . \tag{2.31}$$

2.11 APPENDIX C: PHOTODISSOCIATION REGION

According to Tielens (2005 [146]), the total mass of hydrogen in the PDR is given by

$$M_H = \frac{4\pi D^2 m_H}{X_C A_{ul} E_{lu}} \left(\frac{g_l}{g_u} \exp[E_{lu}/kT_{PDR}] + 1\right) F_{[CII]} \, , \tag{2.32}$$

where X_C is the C/H abundance in number, T_{PDR} the temperature of the gas, g_l, g_{lu}, A_{ul} and E_{lu} the statistical weights, transition probability and energy difference of the levels involved to this transition, D the distance to the star and $F_{[CII]}$ the observed [CII] 158 μm flux. From the cooling law, we have that (Tielens 2005 [146])

$$n_u A_{ul} h\nu_{ul} = \frac{(g_u/g_l)\exp[-h\nu_{ul}/kT_{PDR}]}{1 + n_{crit}/n_{H^0} + (g_u/g_l)\exp[-h\nu_{ul}/kT_{PDR}] + 1} , \quad (2.33)$$

where n_{H^0} is the number density of atomic hydrogen and the n_{crit} the critical density, given by $n_{crit} = 3.2 \times 10^3 T_2^{-0.1281-0.0087 \ln T_2}$ cm^{-3} where $T_2 = T_{PDR}/(10^2$ K) (Draine 2011 [27]). By replacing the known parameters with their values and by considering that $T_{PDR} \gg E_{ul}/k = 92$K, we finally have

$$M_H(M_\odot) = 4.93 \times 10^9 \left(1 + \frac{n_{crit}/n_{H^0}}{3}\right) D^2 \left(\frac{F_{[CII]}}{X_C}\right) , \quad (2.34)$$

where D is in kpc and $F_{[CII]}$ is in W m^{-2}.

Ion	λ (band) (μm)	F ± ΔF (10^{-15} W m^{-2})	F ± ΔF (10^{-15} W m^{-2})	F ± ΔF (10^{-15} W m^{-2})	F ± ΔF (10^{-15} W m^{-2})
		spaxel 4,4	spaxel 4,3	spaxel 4,2	spaxel 4,1
[NIII]	57 (B2A)	-	-	-	-
[OI]	63 (B2A)	-	-	-	-
[NIII]	57 (B3A)	-	-	-	-
[OI]	63 (B3A)	-	-	-	-
[OIII]	88 (B2B)	-	-	0.13 ± 0.03	-
[NII]	122 (R1B)	-	0.09 ± 0.02	0.10 ± 0.02	-
[OI]	146 (R1B)	-	-	-	-
[CII]	158 (R1B)	0.04 ± 0.01	0.06 ± 0.01	0.03 ± 0.01	0.04 ± 0.01
[CII]	158 (R1A)	0.05 ± 0.01	0.05 ± 0.01	0.04 ± 0.01	-
[NII]	205 (R1A)	-	-	-	-
		spaxel 3,4	spaxel 3,3	spaxel 3,2	spaxel 3,1
[NIII]	57 (B2A)	-	0.29 ± 0.08	0.24 ± 0.09	-
[OI]	63 (B2A)	-	0.15 ± 0.06	0.26 ± 0.06	-
[NIII]	57 (B3A)	-	0.16 ± 0.08	0.18 ± 0.07	-
[OI]	63 (B3A)	-	0.11 ± 0.07	0.13 ± 0.06	-
[OIII]	88 (B2B)	-	0.10 ± 0.04	0.10 ± 0.03	0.10 ± 0.04
[NII]	122 (R1B)	0.06 ± 0.02	0.50 ± 0.02	0.71 ± 0.02	0.04 ± 0.02
[OI]	146 (R1B)	-	-	-	-
[CII]	158 (R1B)	0.07 ± 0.01	0.11 ± 0.01	0.14 ± 0.01	0.02 ± 0.01
[CII]	158 (R1A)	0.05 ± 0.01	0.14 ± 0.01	0.16 ± 0.01	0.04 ± 0.01
[NII]	205 (R1A)	-	-	-	-
		spaxel 2,4	spaxel 2,3	spaxel 2,2	spaxel 2,1
[NIII]	57 (B2A)	-	0.18 ± 0.08	0.25 ± 0.08	0.23 ± 0.08
[OI]	63 (B2A)	-	0.17 ± 0.06	0.40 ± 0.06	-
[NIII]	57 (B3A)	-	0.27 ± 0.08	0.25 ± 0.07	-
[OI]	63 (B3A)	-	0.14 ± 0.06	0.35 ± 0.06	-
[OIII]	88 (B2B)	0.12 ± 0.04	0.08 ± 0.04	0.14 ± 0.04	0.11 ± 0.04
[NII]	122 (R1B)	0.11 ± 0.02	0.74 ± 0.02	0.71 ± 0.02	0.27 ± 0.02
[OI]	146 (R1B)	-	-	0.02 ± 0.01	-
[CII]	158 (R1B)	0.06 ± 0.01	0.15 ± 0.01	0.15 ± 0.01	0.06 ± 0.01
[CII]	158 (R1A)	0.07 ± 0.01	0.16± 0.01	0.16 ± 0.01	0.07 ± 0.01
[NII]	205 (R1A)	-	0.17 ± 0.03	0.26 ± 0.04	-
		spaxel 1,4	spaxel 1,3	spaxel 1,2	spaxel 1,1
[NIII]	57 (B2A)	-	0.12 ± 0.08	0.23 ± 0.08	0.17 ± 0.08
[OI]	63 (B2A)	-	0.07 ± 0.06	-	-
[NIII]	57 (B3A)	-	-	0.19 ± 0.07	-
[OI]	63 (B3A)	-	-	0.18 ± 0.06	-
[OIII]	88 (B2B)	0.08 ± 0.04	-	0.11 ± 0.03	0.07 ± 0.02
[NII]	122 (R1B)	0.06 ± 0.02	0.45 ± 0.02	0.51 ±0.02	0.24 ± 0.02
[OI]	146 (R1B)	-	-	-	-
[CII]	158 (R1B)	0.03 ± 0.01	0.07 ± 0.01	0.09 ± 0.01	0.03 ± 0.01
[CII]	158 (R1A)	0.04 ± 0.01	0.09 ± 0.01	0.09 ± 0.01	0.05 ± 0.01
[NII]	205 (R1A)	-	-	-	-
		spaxel 0,4	spaxel 0,3	spaxel 0,2	spaxel 0,1
[NIII]	57 (B2A)	-	0.17 ± 0.08	-	-
[OI]	63 (B2A)	-	-	-	-
[NIII]	57 (B3A)	-	-	-	-
[OI]	63 (B3A)	-	-	-	-
[OIII]	88 (B2B)	-	-	-	-
[NII]	122 (R1B)	-	0.11 ± 0.02	0.13 ± 0.02	-
[OI]	146 (R1B)	-	-	-	-
[CII]	158 (R1B)	-	0.02 ± 0.01	-	-
[CII]	158 (R1A)	-	0.04 ± 0.01	-	-
[NII]	205 (R1A)	-	-	-	-

Table 2.4: Line fluxes in each spaxel. A dash indicates a poor S/N or a non-detection. The spatial configuration corresponds to the footprint of the PACS-spectrometer as it is displayed in Fig. 2.5.

3

THE NEBULA AROUND THE LBV STAR AG CAR

The second object of this study is the nebula around the well known LBV star AG Car. Despite that numerous studies of this nebula exist, it was chosen to be part of this thesis because its central star has a higher luminosity than the LBV WRAY 15-751, so it is very interesting to compare the results for these two targets in terms of the massive star evolution. For this purpose, an analysis of the *Herschel* imaging and spectroscopic data of this nebula that is similar to the analysis of the WRAY 15-751 data was performed. The initial aim was to see whether or not LBV with different luminosity and consequently different initial stellar mass can eject material through episodes of extreme mass-loss during different evolutionary stages.

This analysis was published in *Astronomy & Astrophysics* (2015 A&A, 578, A108). The paper is reproduced in the next pages. It is organized as follows. An introduction to the study of this nebula is first given, including important results of previous studies. The description of the observations is given immediately after. The morphology of the nebula is then described, considering the *Herschel* infrared and the optical imaging data. The analysis of the infrared spectrum follows, where the dust continuum emission is analyzed and the emission line spectrum is discussed. The properties of the dust and the gas are estimated and a discussion on the evolution of the central star is performed.

The analysis of the infrared data in combination to the optical imaging data revealed a dusty ring nebula with non-uniform brightness that coincides with the ionized gas nebula but extends further out. A PDR surrounds the ionized gas region as was also the case for WRAY 15-751 nebula. The nebula around AG Car is also composed of enriched material. Our observational data are in agreement with a nebular ejection during a LBV phase of the central star of about 55 $M_{\odot}$ with little rotation, considering the available theoretical models of stellar evolution. The comparison to the results for the lower luminosity LBV WRAY 15-751 indicates that LBV nebulae can be ejected at different evolutionary phases of their central star, depending on its luminosity.

THE HERSCHEL VIEW OF THE NEBULA AROUND THE LUMINOUS BLUE VARIABLE STAR AG CARINAE

Vamvatira-Nakou, C., Hutsemékers, D., Royer, P., Cox, N. L. J., Nazé, Y., Rauw, G., Waelkens, C., and Groenewegen, M. A. T.

Abstract

Far-infrared *Herschel* PACS imaging and spectroscopic observations of the nebula around the luminous blue variable (LBV) star AG Car have been obtained along with optical imaging in the Hα+[NII] filter. In the infrared light, the nebula appears as a clumpy ring shell that extends up to 1.2 pc with an inner radius of 0.4 pc. It coincides with the Hα nebula, but extends further out. Dust modeling of the nebula was performed and indicates the presence of large grains. The dust mass is estimated to be $\sim 0.2\ M_\odot$. The infrared spectrum of the nebula consists of forbidden emission lines over a dust continuum. Apart from ionized gas, these lines also indicate the existence of neutral gas in a photodissociation region that surrounds the ionized region. The abundance ratios point towards enrichment by processed material. The total mass of the nebula ejected from the central star amounts to $\sim 15\ M_\odot$, assuming a dust-to-gas ratio typical of LBVs. The abundances and the mass-loss rate were used to constrain the evolutionary path of the central star and the epoch at which the nebula was ejected, with the help of available evolutionary models. This suggests an ejection during a cool LBV phase for a star of $\sim 55\ M_\odot$ with little rotation.

3.1 INTRODUCTION

The term "luminous blue variable" LBV was used by Conti (1984 [19]) for the first time and referred to hot luminous massive variable stars that are evolved, but are not WR stars. Nowadays, LBVs, also known as S Doradus variables, are considered to be massive evolved stars mainly characterized by a) high luminosity, $\sim 10^6\ L_\odot$; b) photometric variability with amplitudes from $\sim$ 0.1 mag (small oscillations) up to $\geqslant$ 2 mag (giant eruptions); and c) high mass-loss rates $\sim 10^{-5} - 10^{-4}\ M_\odot\ yr^{-1}$ (Humphreys & Davidson 1994 [117]). Their location on the HR diagram is in the upper left part although some of them undergo occasional excursions to the right.

An early-type O star with initial mass $\geqslant 30\ M_\odot$ evolves to a WR star by losing a significant fraction of its initial mass. LBVs represent a short stage ($\sim 10^4 - 10^5$ yr) in this evolutionary path according to current evolutionary scenarios (Maeder & Meynet 2010 [79]). Although stellar winds can be responsible for stellar mass-loss, the mass-loss

rates of O stars have been revised downward in the past few years (Bouret et al. 2005 [8]; Fullerton et al. 2006 [32]; Puls et al. 2008 [116]). Consequently, episodes of extreme mass-loss during an intermediate evolutionary phase, like a LBV or a RSG phase, are now thought to play a key role, which is why the study of the LBVs and their circumstellar environments is crucial for understanding massive star evolution.

Such extreme mass-loss leads to the formation of ejected nebulae, which have been observed around many LBVs (Hutsemékers 1994 [59]; Nota et al. 1995 [103]). They are classified into three categories according to their morphology: shell nebulae, filamentary nebulae and peculiar morphologies (Nota et al. 1995 [103]). The study of these circumstellar environments can reveal the mass-loss history of the central star since they are formed by the material that has been ejected from the central star in a previous evolutionary phase. Dust and molecular gas (CO) have been revealed by infrared and millimeter studies of LBV nebulae (McGregor et al. 1988 [88]; Hutsemékers 1997 [60]; Nota et al. 2002 [105]).

Some LBVs are surrounded by more than one nebulae. This is the case of the LBV G79.29+0.46. Near-infrared and millimeter data analyzed by Jiménez-Esteban et al. (2010 [65]) revealed multiple shells around this star. Infrared observations by the *Herschel* Space Observatory (Pilbratt et al. 2010 [113]) revealed a second nebula around the LBV WRAY 15-751 (Vamvatira-Nakou et al. 2013 [156])

AG Car (=HD 94910 =IRAS 10541-6011) is a well-studied prototypical LBV. Its variability was first discovered by Wood (1914 [172]). It was first classified as a P Cygni star by Cannon (1916 [9]) and finally classified as a LBV by Humphreys (1989 [56]). Numerous studies show that this star exhibits photometric and spectroscopic variability. In the optical V-band, the photometric changes during the S Dor cycle are about 2 mag on a timescale of $5-10$ years (Stahl 1986 [138]; van Genderen et al. 1988 [160]; Leitherer et al. 1992 [74]; Sterken et al. 1996 [141]). In addition, smaller variations of $0.1-0.5$ mag on a timescale of about 1 year were discovered (van Genderen et al. 1997 [162]). During the periods of visual minimum, AG Car has a spectrum of a WR star, with Ofpe/WN9 spectral type according to Stahl (1986 [138]) and with WN11 according to a more recent study of Smith et al. (1994 [131]). During the periods of visual maximum, AG Car's spectrum corresponds to that of an early-A hypergiant (Wolf & Stahl 1982 [169]; Stahl et al. 2001 [140]).

Humphreys et al. (1989 [58]) concluded that the distance to AG Car is 6 ± 1 kpc, based on the calculated kinematic distance and on the observed variation of the interstellar extinction with distance. This result was confirmed by Hoekzema et al. (1992 [52]), based again on the extinction versus distance relation. Stahl et al. (2001 [140]) suggested a slightly lower distance of $5-6$ kpc based on their calculations of the heliocentric systemic velocity of AG Car (10 ± 5 km s^{-1}),

which is compatible with the value of Humphreys et al. (1989 [58]) considering the errors. Groh et al. (2009 [41]) calculated a similar systemic velocity. Consequently, the value of 6 ± 1 kpc that encompasses all measurements is adopted for all calculations in this study.

Lamers et al. (1989 [71]) calculated $\log L/L_{\odot} = 6.2 \pm 0.2$ for the luminosity of AG Car and showed that it remains constant during the light variations of the star, as was also found for other LBVs (R71: Wolf et al. 1981 [170]; R127: Stahl and Wolf 1986 [139]). Later on, Leitherer et al. (1994 [75]), in their study of the stellar wind of AG Car, found a slightly lower bolometric luminosity of 6.0 ± 0.2 based on ultraviolet observations combined with visual and near-infrared photometry. They also confirmed the nonvariability of the bolometric luminosity during the S Dor cycle. Given such a high value of bolometric luminosity, AG Car is well above the Humphreys-Davidson limit (Humphreys and Davidson 1979 [57]), the limit above which a massive star becomes unstable and high mass loss episodes take place. However, in a recent study of the fundamental parameters of AG Car during visual minima, Groh et al. (2009 [41]) concluded that the bolometric luminosity of AG Car does change during the S Dor cycle. They obtained a maximum value of the bolometric luminosity during minimum phase of $\log L/L_{\odot} = 6.18$, with a variation amplitude of $\Delta(\log L/L_{\odot}) \sim 0.17$ dex. This luminosity variation lies inside the limits of the previously calculated values considering the errors. In all these studies, the distance 6 ± 1 kpc was used.

Thackeray (1950 [145]) discovered that AG Car is surrounded by a nebulous shell that has the shape of an elliptical ring with nonuniform intensity. He measured the size of the nebula to be $39'' \times 30''$ and the width of the ring to be about $5''$. Stahl (1987 [137]) studied direct CCD imaging data of AG Car and suggested that very likely the nebula around this star is the result of a heavy mass-loss episode that took place during an S Dor outburst and not the result of interstellar material that was swept up by the stellar wind. Smith (1991 [129]) studied the dynamics of AG Car nebula based on spectroscopic observations in the optical waveband. She measured an average nebular expansion velocity of 70 km s^{-1} and concluded that the shell expansion is roughly symmetrical. She also reported the presence of a jet-like bipolar mass outflow, expanding with a velocity of 83 km s^{-1} and distorting the northeastern edge of the shell. Nota et al. (1992 [101]) studied the nebula around AG Car using high-resolution coronographic imaging and spectroscopic data so as to constrain its geometry. They confirmed the value of the expansion velocity of Smith (1991 [129]) and concluded that this nebular shell shows a deviation from spherical symmetry, based on the observed radial velocity variations and on the gas distribution observed in the images.

Voors et al. (2000 [164]) studied AG Car in the infrared waveband by modeling ground-based infrared images taken at about 10 μm and

ISO spectroscopic observations, from which they derived the properties of the circumstellar dust. The dust shell is detached and slightly elongated. The ionized gas appears co-spatial with the dust. PAHs are present. The dust shell contains mostly large grains, although very large grains are present and also a population of small, warm, out of thermal equilibrium grains that produce continuum and PAH bands emission.

Duncan and White (2002 [28]) observed the AG Car nebula at the radio wavelengths (3 and 6 cm). Their 3 cm wavelength radio image revealed a nebula with a detached ring shape, very similar to the morphology in the Hα+[NII] filter (see Sect. 3.3).

Nota et al. (2002 [105]) detected ^{12}CO $J = 1 \rightarrow 0$ and $J = 2 \rightarrow 1$ emission from AG Car for the first time. The CO line profiles indicate a region of molecular gas that is close to the star, expanding slowly and not originating from the gaseous nebula. They argued that the most plausible scenario to explain the observed profile is the presence of a circumstellar disk.

Weis (2008 [167]), using deep Hα imaging, reported the presence of diffuse emission in the form of a cone-like extension to the north of the AG Car nebula and concluded that it is clearly part of the nebula. It extends up to 28″ outside the nebula, increasing its size by about two times. It has a higher radial velocity than the ring.

In this study we present an analysis and discussion of the images and the spectrum of the AG Car nebula taken by PACS (Poglitsch et al. 2010 [115]), which is one of the three instruments on board the *Herschel* Space Observatory. The paper is organized as follows. In Sect. 3.2 the observations and the data reduction procedure are presented. A description of the nebular morphology based on these observations is given in Sect. 3.3. The dust continuum emission is modeled in Sect. 3.4, while the emission line spectrum is analyzed in Sect. 3.5. In Sect. 3.6 a general discussion is presented and in Sect. 3.7 conclusions are drawn.

3.2 OBSERVATIONS AND DATA REDUCTION

3.2.1 *Infrared observations*

The infrared observations include imaging and spectroscopy of the AG Car nebula and were carried out using PACS in the framework of the MESS Guaranteed Time Key Program (Groenewegen et al. 2011 [39]).

The PACS imaging observations were carried out on August 12, 2010, which corresponds to *Herschel*'s OD 456. The observing mode was the scan map in which the telescope slews at constant speed (in our case the "medium" speed of 20″/s) along parallel lines in order to cover the required area of the sky. Two orthogonal scan maps were

obtained for each filter. Our final data set consists of maps at 70, 100 and 160 μm. The obsIDs of the four scans are 1342202927, 1342202928, 1342202929, and 1342202930; each scan has a duration of 157 s.

To perform the data reduction we used HIPE (Ott 2010 [108]) up to level 1. Subsequently, the data were reduced and combined using the Scanamorphos software (Roussel 2013 [119]). The pixel size in the final maps is 2″ in the blue channel (70, 100 μm) and 3″ in the red channel (160 μm). It should be mentioned that the *Herschel* PACS PSF FWHMs are 5.2″, 7.7″, and 12″ at 70 μm, 100 μm and 160 μm, respectively.

The spectrum of the AG Car nebula was taken on June 5, 2010 (OD 387), with the PACS integral-field spectrometer that covers the wavelength range from 52 μm to 220 μm in two channels that operate simultaneously in the blue 52-98 μm band (second order: B2A 52-73 μm and B2B 70-105 μm), and the red 102-220 μm band (first order: R1A 133-220 μm and R1B 102-203 μm). Simultaneous imaging of a $47'' \times 47''$ field of view is provided that is resolved in 5×5 square spatial pixels (i.e., spaxels). The two-dimensional field of view is then rearranged along a 1×25 pixel entrance slit for the grating via an image slicer employing reflective optics. Its resolving power is $\lambda/\delta\lambda \sim 940 - 5500$ depending on the wavelength. The observing template was the SED that provides a complete coverage between 52 and 220 μm. The two obsIDs are 1342197792 and 1342197793. HIPE was also used for the data reduction. The standard reduction steps were followed and in particular the subtraction of the background spectrum obtained through chopping and nodding.

3.2.2 *Visible observations*

The optical images of the AG Car nebulae were obtained on April 6, 1995, with the 3.6 m telescope at the ESO, La Silla, Chile. A series of short (1s-10s) and longer (30s-60s) exposures were secured in a Hα+[NII] filter (λ_c = 6560.5Å ; FWHM =62.2Å) and in a continuum filter just redwards (λ_c = 6644.7Å; FWHM = 61.0Å). The EFOSC1 camera was used in its coronographic mode: for the longer exposures, the 8″ circular coronographic mask was inserted in the aperture wheel and positioned on the central star while the Lyot stop was inserted in the grism wheel (Melnick et al. 1988 [64]). The frames were bias-corrected and flat-fielded. The CCD pixel size was 0.605″ on the sky. The night was photometric and the seeing around 1.2″. In order to properly calibrate the images, three spectrophotometric standard stars and three planetary nebulae with known Hα flux were observed in the Hα+[NII] filter.

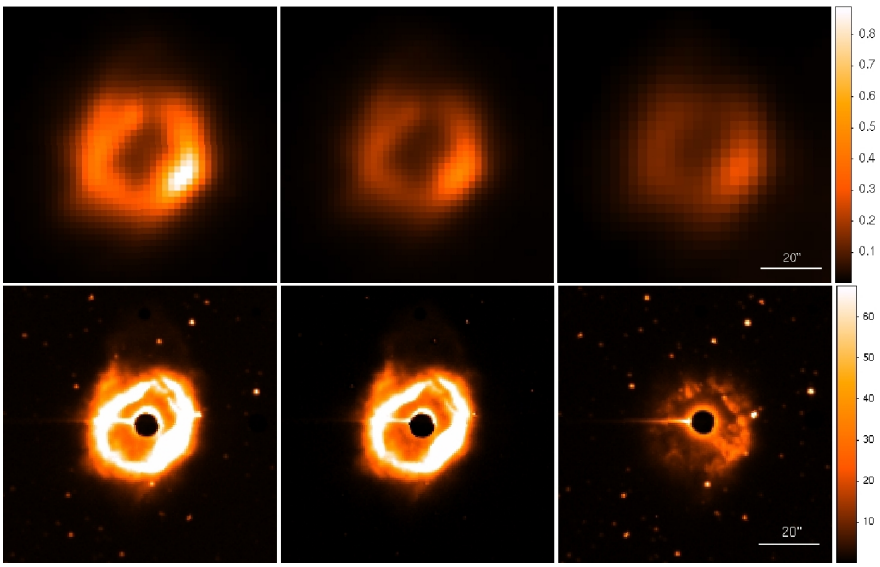

Figure 3.1: Images of the nebula around AG Car. *Top*: PACS images at 70 μm, 100 μm, and 160 μm from left to right. *Bottom*: the Hα+[NII] image (left), the continuum image (right) and the image resulting from the subtraction of the continuum image from the Hα+[NII] image after correcting for the position offsets and for the different filter transmissions using field stars (middle). The size of each image is 1.5′ × 1.5′. The scale on the right corresponds to the surface brightness (arbitrary units). North is up and east is to the left.

3.3 MORPHOLOGY OF THE NEBULA

The three PACS infrared images of the nebula around the LBV AG Car at 70 μm, 100 μm, and 160 μm along with images taken at optical wavelengths are shown in Figs. 3.1 and 3.2.

The infrared images reveal a dusty shell nebula with a clumpy ring morphology that is clearly detached from the central star (not visible at these wavelengths). The brightness of the nebula is not uniform, with the southwestern part being the brightest one. This agrees with the nonuniform brightness of the images at 12.5 μm and 12.78 μm analyzed by Voors et al. (2000 [164]). An axis at PA ~ 160° can be defined (North: PA = 0°; East: PA = 90°). Cuts of the 70 μm PACS image through PA ~ 160° and PA ~ 70° (Fig. 3.4) show peaks at a radius of about 14″, although with different intensities. The ring extends up to ~ 42″. These values correspond to 0.4 pc and 1.2 pc, respectively, at a distance of 6 kpc. On top of this central circular nebula, there is a northern faint extension. No other more extended nebula associated with the star can be detected. A three-color infrared image of the nebula and its environment is illustrated in Fig. 3.3, which shows best this faint northern extension first reported by Weis (2008 [167]), although the resolution is not good enough to reveal its detailed structure. The

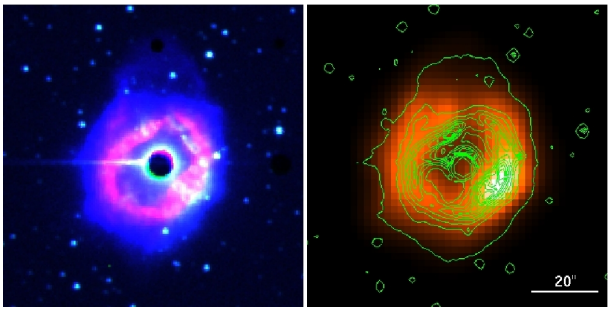

Figure 3.2: *Left*: View of the nebula in the optical. The bright Hα+[NII] ring nebula is illustrated in red (also shown in Fig. 3.1 at the same scale) while the fainter Hα+[NII] emission is shown in blue, differently scaled in surface brightness, revealing the northern extension (Weis 2008 [167]). The continuum image that outlines the dust scattered nebula is presented in green. *Right*: Contour image of the optical emission from the nebula (green lines) superposed on the infrared image of the nebula at 70 μm (also shown in Fig. 3.1 at the same scale). The size of each image is 1.5′ × 1.5′. North is up and east is to the left.

LBV nebula seems to be located in a cavity in the interstellar medium, probably excavated by the star in a previous evolutionary phase. The radius of this empty cavity is about 2.5′, which corresponds to 4.4 pc at a distance of 6 kpc.

The Hα+[NII] image (Fig. 3.1) shows that the gas nebula around AG Car forms an elliptical shell with an average outer radius of ∼ 20″ and an inner radius of ∼ 11″. To more accurately investigate the morphology of the nebula in the optical, a three-color image is presented in Fig. 3.2. The fainter nebular optical emission reveals the northern extension described in Weis (2008 [167]). The nebula that surrounds the bright ring extends up to ∼ 23″, while the north extension goes up to ∼ 36″ from the center of the nebula. These numbers correspond to 0.7 pc and 1 pc, respectively, at a distance of 6 kpc, in agreement with the size of the nebula given in Weis (2008 [167], 2011 [168]).

In the Hα light, the dynamics points to a spherically expanding shell distorted by a more extended bipolar nebula (Smith 1991 [129]; Nota et al. 1992 [101]). In projection on the sky, the shell appears as an elliptical ring with PA ∼ 131°, different from the infrared shell PA. Nevertheless, the contour image of the optical emission (both bright and faint) superimposed on the infrared image of the nebula at 70 μm as illustrated in the right panel of Fig. 3.2 shows that the overall morphology of the gas nebula is similar to the infrared dust morphology, although the Hα+[NII] ring nebula appears slightly smaller and more elliptical than the infrared nebula. The bright region at the southwestern part of the gas nebula coincides with the bright region of the infrared dust nebula. The northern faint extended structure, which appears both in the infrared and in the optical, is likely a lobe

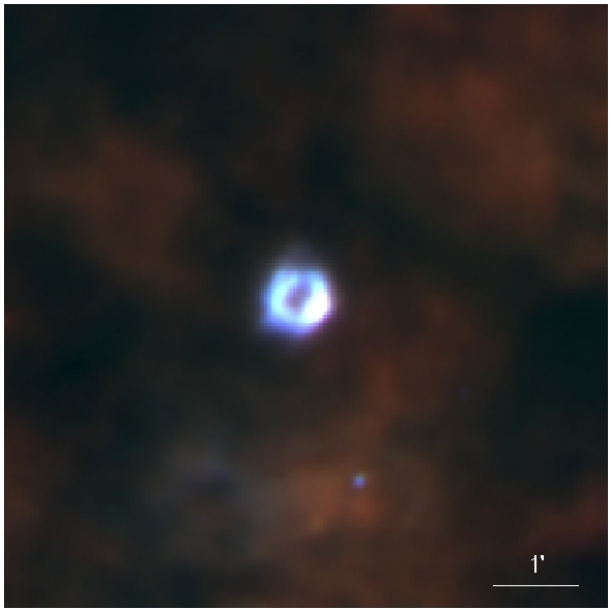

Figure 3.3: Three-color image (70 μm in blue, 100 μm in green and 160 μm in red) of the AG Car nebula. The LBV nebula appears located inside a cavity in the interstellar medium. The size of the image is $7' \times 7'$. North is up and east is to the left.

of the bipolar nebula. The extension seen to the south in the Hα+[NII] map and in the velocity maps of Smith (1991 [129]) could constitute a part of a second fainter lobe. The system may thus consist of a typical bipolar nebula seen roughly through the poles (i.e., at inclination $\lesssim$ 30°), with two faint lobes and a bright waist.

The nebula is also clearly detected in the optical continuum filter (Fig. 3.1), indicating significant dust scattering. The morphology of the dust reflection nebula appears somewhat different from the morphology of the Hα+[NII] emission. This reflection nebula around AG Car was first described in Paresce and Nota (1989 [110]) and its stunning structure resolved with the Hubble Space Telescope (HST) (Nota et al. 1995 [103], 1996 [104]). More specifically, in the optical continuum image (Figs. 3.1 and 3.2) the ring appears circular and very clumpy with a jet-like feature that starts from the central part of the nebula and extends towards the southwestern part, which is the brightest region of the dust and gas emission. The northern extension of the nebula is not detected in the optical continuum. As does the Hα+[NII] ring nebula, the optical continuum emission appears slightly inside the infrared continuum emission, although a detailed comparison is difficult given the lower spatial resolution of the PACS images. The difference in morphology between the optical continuum and the Hα+[NII] nebulae may arise from anisotropic illumination and thus ionization of different parts of the nebula owing to its clumpy structure.

Considering the nebular expansion velocity, v_{exp}, of 70 km s^{-1} measured by Smith (1991 [129]), the kinematic age, t_{kin}, of the nebula can be estimated. As mentioned above, the nebula in the infrared extends to 1.2 pc in radius, *r*, so it has a kinematic age of $t_{kin} = r/v_{exp}$ = 1.7×10^4 years. The temporal difference between the inner and the outer radius of the nebula is 1.1×10^4 years.

3.4 DUST CONTINUUM EMISSION

Integrated flux densities were derived for the nebular shell at the three PACS wavelengths by performing aperture photometry on the PACS images. We also used imaging data taken from the archives of the IRAS mission (Neugebauer et al. 1984 [99]) and the Infrared Astronomical Mission AKARI (Murakami et al. 2007 [98]). In these archival data we did not include the IRAS observation at 12 µm because it is only an upper limit or at 100 µm because it is not of high quality. We note that the beam size of the IRAS and AKARI observations is large enough to fully encompass the ring nebula around AG Car. Images from the SPIRE (Griffin et al. 2010 [38]) instrument on board the *Herschel* Space Observatory were also included. They were taken from the observations of the *Herschel* Infrared Galactic Plane survey (Hi-GAL, Molinari et al. 2010 [96]) made immediately public for legacy. The Hi-GAL observations of the field around AG Car were retrieved from the archive processed up to level 2. Only the maps at 250 µm and at 350 µm were used, because at 500 µm the nebula is very faint so that flux determination is highly uncertain. Integrated flux densities were derived for the nebular shell at these two SPIRE wavelengths by performing aperture photometry on the images.

We applied photometric color correction to all flux densities derived from the observations of these three space missions. With this correction, the monochromatic flux densities that refer to a constant energy spectrum are converted to the true object SED flux densities at the photometric reference wavelengths of each instrument. We used the flux density ratio to derive the color temperature for the color correction of the IRAS data and then we chose the corresponding color-correction factor (Beichman et al. 1988 [4]). The ratio R (25,60) corresponds to a temperature of 140 K, so the correction factors for this temperature were used. To color correct the AKARI FIS and IRC data we fitted a blackbody to the two data sets independently using the 25 µm IRAS observation because we needed a measurement near the maximum of the curve. These fits led us to adopt the color-correction factors that correspond to a temperature of 150 K for FIS (Yamamura et al. 2010 [173]) and 220 K for IRC data (Lorente et al. 2008 [77]). To estimate the color correction of the *Herschel*-PACS data, we fitted a blackbody, considering again the 25 µm IRAS observation. This fit gave a temperature of 150 K, for which we adopted the correspond-

Spacecraft-Instrument	Date	λ (μm)	F_ν (Jy)	Error (Jy)
IRAS [α]	1983	25	187.5	9.4
		60	177.7	28.4
AKARI-IRC [b]	2007	9	9.04	0.14
		18	119.2	0.24
AKARI-FIS [c]	2007	65	229.3	6.53
		90	81.0	3.9
		140	45.5	5.2
		160	35.1	4.6
Herschel-PACS [d]	2010	70	173	2
		100	103	3
		160	42	3
Herschel-SPIRE [e]	2010	250	8.1	2
		350	3.0	1

Notes. Data from: [(α)] IRAS Point Source Catalog (Beichman et al. 1988 [4]) [(b)] Akari / IRC Point Source Catalogue (Ishihara et al. 2010 [63]) [(c)] Akari / FIS Bright Source Catalogue (Yamamura et al. 2010 [173]) [(d)] This work [(e)] Observations of Hi-GAL (Molinari et al. 2010 [96]) retrieved from the *Herschel* archive

Table 3.1: Color-corrected nebular flux densities.

ing correction factor (Müller et al. 2011 [144]). For the SPIRE data, the instructions for color correction given in the SPIRE Handbook[1], were followed.

The corrected measurements are presented in Table 3.1. They enabled us to construct the infrared SED of the nebula, along with the archived spectrum that was part of the observations carried out by the ISO mission (Kessler et al. 1996 [68]). A detailed discussion on this ISO-LWS spectrum can be found in Voors et al. (2000 [164]).

The infrared SED of the nebula around AG Car obtained at different epochs with the various instruments is shown in Fig. 3.5. All these measurements agree very well within the uncertainties except the one at 90 μm. This is likely due to the uncertainty on the color correction that was stronger for the 90 μm (AKARI-FIS) data point.

A model of the dust nebula around the LBV AG Car has been carried out in the past by Voors et al. (2000 [164]). They used a one-dimensional radiative transfer code to fit both imaging and spectroscopic infrared data. To further constrain the dust properties, we use the AKARI archive imaging data and the new PACS and SPIRE imaging data in addition to the IRAS imaging data and the ISO infrared spectrum. The PACS imaging allows us to measure the nebular radius at the wavelengths of the bulk of dust emission. To model the dust shell we only considered the spectrum at $\lambda > 20$ μm. The spectrum at $\lambda < 12$ μm comes from the central star that Voors et al. (2000 [164]) fitted with a spherical non-LTE model atmosphere. For the spectrum

1 http://herschel.esac.esa.int/Docs/SPIRE/spire_handbook.pdf

between $\lambda \sim 14$ and 20 μm they argued that it too likely comes from the central star and not from some extended source.

The two - dimensional radiative transfer code 2-Dust (Ueta and Meixner 2003 [152]) was used to model and interpret the dust emission spectrum and the FIR images. This is a publicly available versatile code that can be supplied with various grain size distributions and optical properties as well as complex axisymmetric density distributions.

It should be mentioned here that since the PACS spectral field of view is smaller than the nebular size, the PACS spectrum was not taken into consideration for the dust model as this spectrum is indeed fainter than the PACS photometric points that contain the total flux of the nebula.

To model the PACS ring of dust with the code 2-Dust, it is necessary to consider the morphology of the nebula revealed through the infrared PACS and the optical images so as to choose the best geometric parameters for the axisymmetric dust density distribution model. The 2-Dust code uses a normalized density distribution function (Meixner et al. 2002 [89]) that is based on a layered shell model,

$$\rho(R,\theta) = \left(\frac{R}{R_{min}}\right)^{-B\left\{1+C\sin^F\theta\left[e^{-(R/R_{sw})^D}/e^{-(R_{min}/R_{sw})^D}\right]\right\}} \times \left\{1+A(1-\cos\theta)^F\left[e^{-(R/R_{sw})^E}/e^{-(R_{min}/R_{sw})^E}\right]\right\}, \quad (3.1)$$

where $\rho(R,\theta)$ is the dust mass density at radius R and latitude θ, R_{min} is the inner radius of the shell, and R_{sw} is the superwind radius that defines the boundary between the spherical wind and the axisymmetric superwind. The first term represents the radial profile of the spherical wind; the parameters A-F define the density profile; the radial factor B can also be a function of the latitude through the elongation parameter C; A is the equatorial enhancement parameter; the parameter F defines the flatness of the shell; and D and E are the symmetry transition parameters that describe the abruptness of the geometrical transition in the shell.

It should be specified that we only consider the bright ring-nebula for this model. No attempt has been made to model the nebular northern extension since it is faint in the infrared and not clearly resolved.

A purely spherical model cannot reproduce the observed morphology of the dust shell because there would be too much emission at the center of the ring with respect to the observations. A sphere with equatorial enhancement may be considered to reproduce the difference in intensity between the two cuts on the infrared image. To appear nearly circular with a clear central hole in projection, a spherical shell with equatorial enhancement must be seen at small inclination $\lesssim 30°$, roughly through the poles. This scheme is in agreement with the observed global morphology. At very low inclination

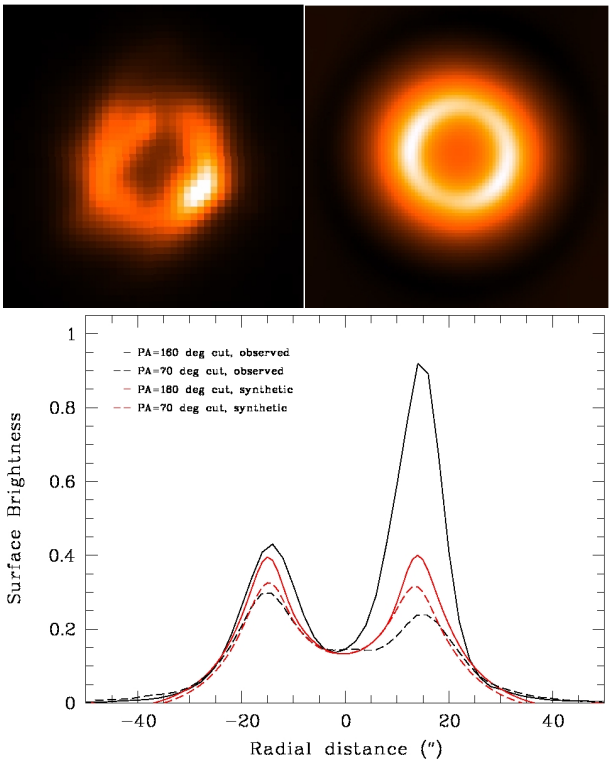

Figure 3.4: *Top left*: the $1.5' \times 1.5'$ image of the nebula around AG Car observed with PACS at 70 μm. North is up and east to the left. *Top right*: the synthetic image computed with 2-Dust using $r_{in} = 14''$ and $r_{out} = 42''$ and convolved with the PACS PSF. *Bottom*: Cuts with PA=160° and 70° through the central part of the nebula at 70 μm, observed (black) and synthetic (red) ones.

it is difficult to reproduce the large difference in intensity between the two cuts in an axisymmetric model like this one. On the other hand, by increasing the inclination too much a strongly elliptical ring would be seen, which is not observed. In addition to the equatorial enhancement, the structure appears clumpy. These inhomogeneities cannot be reproduced by the present model. The best approximate axisymmetric model for the observed ring is a sphere with equatorial enhancement ($A \sim 5$) that is seen at small inclination ($\sim 30°$). The values for the other five geometric parameters of Eq. 3.1 are B=3, C=0, D=0, E=0, F=1 to keep the model simple and limit the number of free parameters.

The synthetic image produced by 2-Dust and convolved with the PACS PSF is given in the top right panel of Fig. 3.4. By comparing the PACS image to the synthetic one, we determined the inner, $r_{in} = 14''$, and the outer, $r_{out} = 42''$, radii of the dust ring. In the bottom panel of Fig. 3.4, cuts with PA=160° and 70° through the central part of the observed and the simulated nebula are illustrated. Although the basic morphology (radii, thickness and axisymmetry of the shell) reproduced by the model agrees with the observed one, the intensity

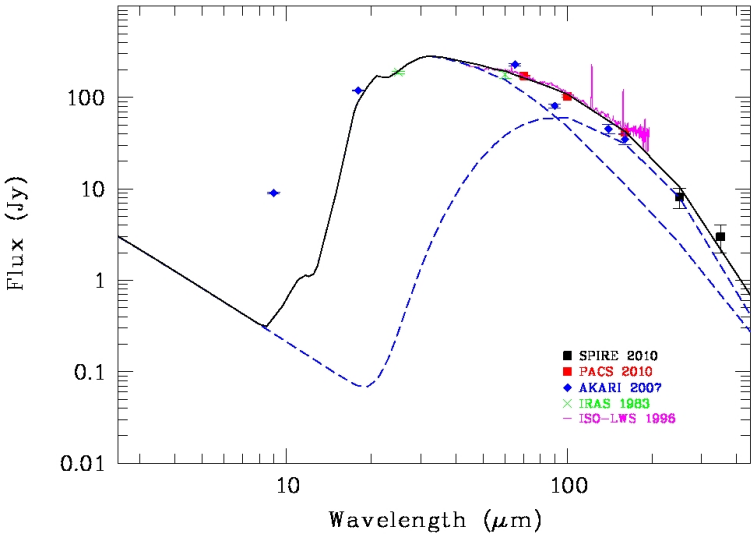

Figure 3.5: Infrared SED of the nebula around the LBV AG Car from data collected at different epochs: the ISO-LWS spectrum and color-corrected photometric measurements from IRAS, AKARI and *Herschel* (PACS and SPIRE) space observatories. Results of the 2-Dust model fitting are illustrated. Data at $\lambda < 20$ μm are not considered in the fit. The best fit (solid line) is achieved considering two populations of dust grains (dashed lines).

of the peaks does not because no attempt was made to fit the clumps, as mentioned earlier.

After constraining the nebular geometry we can proceed with the model of the dust SED. For the stellar parameters we adopted the distance D = 6 kpc, the luminosity $\log L/L_{\odot} = 6.1$, and the temperature $T_{\rm eff} = 20000$ K (Voors et al. 2000 [164]; Groh et al. 2009 [41]). The infrared SED of AG Car (Fig. 3.5) is too broad to be reproduced with only one population of dust grains, so we considered two populations of grains with the same composition but different sizes. Voors et al. (2000 [164]) showed that the dust in this nebula contains large grains, up to 40 μm in radius, and is dominated by amorphous silicates with little contribution from crystalline species, and more specifically pyroxenes with a 50/50 Fe to Mg abundance. We therefore adopted a similar dust composition. The optical constants of silicates given by Dorschner et al. (1995 [26]) were used for both populations, extrapolated to a constant refraction index in the FUV. The size distribution for the dust grains of Mathis et al. (1977 [86], hereafter MRN) was assumed, for each of the two populations: $n(a) \propto a^{-3.5}$ with $a_{\rm min} < a < a_{\rm max}$, where a is the grain radius. The model can be adjusted to the data by varying $a_{\rm max}$ (or $a_{\rm min}$), which controls the 20μm / 100μm flux density ratio, and the opacity, which controls the strength of the emission.

The best fit (Fig. 3.5) was achieved with the use of the following populations of dust grains. The first is a population of small grains

with radii from 0.005 to 1 μm, which is responsible for the emission at $\lambda < 40$ μm. The second is a population of large grains with radii from 1 to 50 μm, which is responsible for the slope of the SED at $\lambda > 70$ μm. It should be pointed out that the large grains are necessary to reproduce the observed infrared SED. Several attempts were made to fit the SED using different grain sizes. They showed that a_{max} cannot be very different from 50 μm for the population of large grains. More details are given in Sect. 3.8.

The total mass of dust derived from the modeling is $M_{dust} \sim 0.21$ $M_\odot$ (0.05 $M_\odot$ from the small dust grains and 0.16 $M_\odot$ from the large ones), with an uncertainty of ~ 20%. This result is in agreement with the total dust mass found by Voors et al. (2000 [164]). The small grains have temperatures from 88 K at r_{in} to 62 K at r_{out}, while the large grains have temperatures from 43 K at r_{in} to 29 K at r_{out}. Similar results are obtained when fitting modified BB curves to the SED (see Sect. 3.9 for details).

As described in the introduction, AG Car is a variable star with photometric and spectroscopic variations. Although the data used for the dust model are obtained at different epochs, the visual magnitude of the star is approximately the same at the epochs of the IRAS, ISO, AKARI, and *Herschel* observations. In addition, AG Car varies under a roughly constant bolometric luminosity (Sect. 3.1). By keeping the luminosity constant and changing the radius and the temperature of the star within reasonable limits, we do not see significant changes in the model results.

3.5 EMISSION LINE SPECTRUM

3.5.1 *Spectrum overview*

Figure 3.6 illustrates the footprint of the PACS spectral field of view on the image of the nebula at 70 μm. This field of view is composed of 25 (5×5) spaxels, each corresponding to a different part of the nebula, but it is not large enough to cover the whole nebula.

The integrated spectrum of the nebula over the 25 spaxels is shown in Fig. 3.7. Below 55 μm the shape of the continuum results from a spectral response correction in this range that has not yet been perfected, while above 190 μm it results from a light leak from the second diffraction order of the grating to the first one.

The following forbidden emission spectral lines are detected on the dust continuum: [OI] λλ 63, 146 μm, [NII] λλ 122, 205 μm, and [CII] λ 158 μm. The absence of higher ionization lines indicates that the ionization state of the gas in the nebula around AG Car is not as high as in the case of the nebulae around other LBVs, for example WRAY 15-751 (Vamvatira-Nakou et al. 2013 [156]). This implies that the gas temperature is lower.

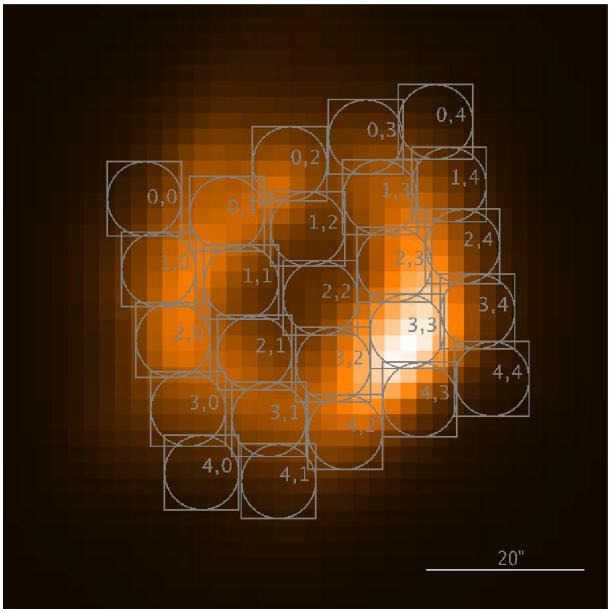

Figure 3.6: Footprint of the PACS spectral field of view on the image of the AG Car nebula at 70 μm. Each number pair is the label of a specific spaxel. North is up and east is to the left.

3.5.2 *Line flux measurements*

A Gaussian fit was performed on the line profiles to measure the emission line intensities in each of the 25 spectra (Fig. 3.6) using the IRAF (Tody 1986 [149], 1993 [150]). The table with these measurements is given in Sect. 3.10. We note that not all the lines are detected in the outer spaxels and that all fluxes reach their highest values at the spaxel (3,3). This spaxel corresponds to the southwestern part of the nebula, which is the brightest part (see Sect. 3.3).

Maps of the line intensities were created for each of the five detected lines in an effort to investigate whether there are differences in the gas properties for distinct parts of the nebula. There are only 25 spaxels, and the coverage of the nebula is not complete, so we cannot really see the full nebula in these "spectroscopic images". The only wavelength at which we barely see the nebular ring is that of 122 μm. Furthermore, maps of line intensity ratios of every detected line to the [NII] 122 μm line were created. The differences between distinct nebular regions are not significant or convincing. Since these maps are difficult to interpret given the large uncertainties on the fluxes and the wavelength-dependent PSF, they were not considered in the present study.

To measure the total flux of the nebula in each line we need to use the integrated spectrum over the 25 spaxels, but as already mentioned above the beam size of the PACS spectrometer is smaller than the size of the nebula. Consequently, the fluxes measured using the

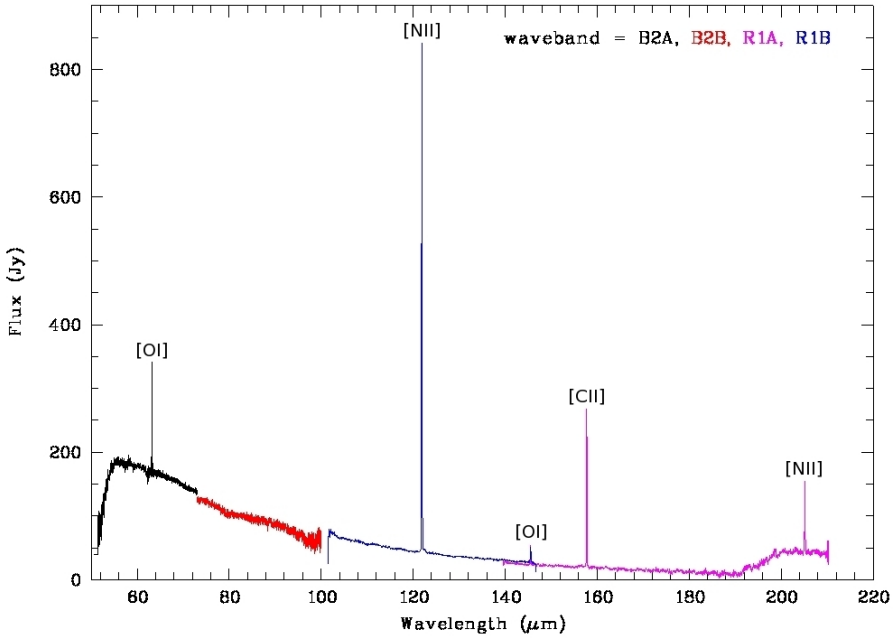

Figure 3.7: PACS spectrum of the nebula around AG Car, integrated over the 25 spaxels. Indicated are the lines [OI], [NII], and [CII]. Below 55 μm the shape of the continuum results from a spectral response function correction that has not yet been perfected. Above 190 μm the shape results from a light leak from the second diffraction order of the grating in the first one. The different observing bands are indicated with different colors. We note that the spectral resolution depends on the waveband.

sum of the 25 spaxels do not correspond to the real nebular fluxes. For this reason, the PACS spectrum was corrected using the three PACS photometric observations. A modified BB was fitted to these data and another one to the continuum of the PACS spectrum, for wavelengths smaller than 190 μm. The ratio of the two curves gives the correction factor. In other words, the spectrum was scaled to the photometry. This factor linearly depends on the wavelength and goes from 1.11 at 55 μm to 2.12 at 185 μm. This correction assumes a constant line-to-continuum ratio and is analogous to the point source correction applied in the pipeline to correct the effect of flux lost for a point source.

The [NII] 205 μm line has a problematic calibration in PACS. Consequently, its flux needs to be corrected before being used in the following analysis. More precisely, the flux in [NII] 205 μm is incorrect for all PACS measurements owing to a light leak, superimposing a lot of flux from 102.5 μm at that wavelength. The Relative Spectral Response Function (RSRF) used to reduce the data suffers from the same light leak. Consequently, when this RSRF is applied during the data reduction, the signal at wavelengths $\gtrsim$ 190 μm is divided by a number that is too high. The continuum at these wavelengths is irremediably

Ion	λ (μm)	F (25 spaxels) (10^{-15} W m^{-2})	c. f.	F (corrected) (10^{-15} W m^{-2})
[OI]	63	7.7	1.17	9.0 ± 1.8
[NII]	122	23.6	1.64	38.7 ± 7.7
[OI]	146	0.6	1.83	1.1 ± 0.3
[CII]	158	4.1	1.92	7.9 ± 1.6
[NII]	205	1.1	$2.26^{\alpha} \times 4.2^{b}$	10.3 ± 2.6

Notes. $^{(\alpha)}$ Missing flux correction $^{(b)}$ PACS / SPIRE cross-calibration factor

Table 3.2: Line fluxes of the nebula around AG Car.

lost, but provided one can "scale-back up" with the right number to compensate for the exaggerated RSRF, one can recover the line-flux.

Using instrument test data obtained on the ground with calibration light sources set at different and known temperatures, one can invert the problem and reconstruct the "clean" RSRF, i.e., in the absence of light leak. This suffers from some defects and a large uncertainty due to the propagation of errors and to the very low response of the instrument at these wavelengths. A correction factor could nevertheless be derived from it, and confirmed within a certain margin by comparison of the line fluxes obtained for a few sources by both PACS and SPIRE at that wavelength. We finally found that the measured [NII] 205 μm flux should be multiplied by a correction factor of 4.2. An error of 25 % was assumed for the final corrected [NII] 205 μm flux[2].

The emission line measurements of the nebula integrated over the 25 spaxels, before and after the correction for the missing flux, are given in Table 3.2 along with the correction factor (c.f.) at each wavelength. It should be mentioned that the flux measurements of the three lines present in the ISO-LWS spectrum of AG Car ([OI] λ 63 μm, [NII] λ 122 μm and [CII] λ 158 μm) do agree with the corrected values from the PACS spectrum within the errors, showing that the correction for the missing flux is essentially correct.

3.5.3 *Photoionization region characteristics*

The detected emission lines [NII] 122, 205 μm are associated with the HII region of the nebula around AG Car. The other three detected emission lines originate from a region of transition between ionized

2 This part of the infrared spectrum of AG Car has also been observed with SPIRE as part of the MESS program. Unfortunately, these data cannot be used so as to have a more precise flux for the line [NII] 205 μm because the whole ring nebula is outside of the detector coverage owing to the geometry of the detector array and because the observing mode was a single pointing and not a raster map. Consequently, any attempt to recover the nebular flux has huge uncertainty and we decided not to include the SPIRE spectroscopic data in our study.

and neutral hydrogen and may indicate the presence of a PDR. Their analysis is given in the next subsection.

3.5.3.1 *Hα flux*

The Hα+[NII] flux from the nebula was estimated by integrating the surface brightness over the whole nebula. Contamination by field stars and the background was corrected and the emission from the occulted central part extrapolated. The continuum flux from the reflection nebula was measured in the adjacent filter, accounting for the difference in filter transmissions. However since AG Car is a strong emission-line star, the reflected stellar Hα must also be subtracted. Considering the Hα equivalent widths measured by Schulte-Ladbeck et al. (1994 [123]) and Stahl et al. (2001 [140]) for AG Car in 1993-1994 (i.e., accounting for ~ 1.5 years of time-delay) we estimate the final contamination due to the reflection nebula to be 20%. The contribution of the strong [NII] lines was then subtracted using the [NII] /Hα ratios from available spectroscopic data and the transmission curve of the Hα+[NII] filter. The conversion to absolute flux was done with the help of the three spectrophotometric standard stars and three planetary nebulae observed in the same filter; the conversion factors derived from these six objects show excellent internal agreement.

We measured $F_0(H\alpha) = 1.1 \times 10^{-10}$ ergs cm^{-2} s^{-1} uncorrected for reddening. The uncertainty amounts to ~ 20%. Adopting E(B−V) = 0.59 ± 0.03 (de Freitas Pacheco et al. 1992 [22]), we derived $F_0(H\alpha) = 4.2 \pm 0.9 \times 10^{-10}$ ergs cm^{-2} s^{-1} for the AG Car nebula. This flux is higher by a factor of 2 than the fluxes measured by Stahl (1987 [137]), Nota et al. (1992 [101]) and de Freitas Pacheco et al. (1992 [22]) in 1986, 1989, and 1991, but is compatible with the Hβ flux measured by Perek (1971 [112]) in 1969 (i.e., $F_0(H\alpha) \simeq 3 \times 10^{-10}$ ergs cm^{-2} s^{-1} with $H\alpha/H\beta = 6$ and E(B−V) = 0.59). The flux density from the reflection nebula is $F_\lambda = 3.9 \times 10^{-13}$ ergs cm^{-2} s^{-1} Å^{-1} at 6650 Å (the central wavelength of the continuum filter). The high value of $F_0(H\alpha)$ we find is in agreement with the radio flux, also observed in 1994-1995 (Duncan and White 2002 [28]), and E(B−V) = 0.59.

3.5.3.2 *Electron density*

Smith et al. (1997 [132]) found a non-constant nebular electron density, n_e, that varies from 600 to 1050 cm^{-3} using the optical [SII] 6731/6717 ratio as an electron density diagnostic. Their result is in agreement with those of Mitra and Dufour (1990 [95]) and Nota et al. (1992 [101]) who used the same ratio as a diagnostic.

In the infrared waveband, the [NII] 122/205 μm ratio is a diagnostic for the electron density of the nebula at low density, $1 \text{ cm}^{-3} \leqslant n_e \leqslant 10^3 \text{ cm}^{-3}$ (Rubin et al. 1994 [121]). Considering the values of Table 3.2, this ratio is equal to 3.8 ± 1.2 for the whole nebula. The package *nebular* of the IRAF/STSDAS environment (Shaw & Dufour

1995 [125]) was used for the calculation of the electron density. An electron temperature, T_e, constant throughout the nebula and equal to 6350 ± 400 K was used for all of the following calculations. This is the average temperature calculated by Smith et al. (1997 [132]). The electron density is then found to be 160 ± 90 cm^{-3}.

The calculated electron density based on the infrared data is much lower than the density based on the optical data. This discrepancy is usual and has also been observed in planetary nebulae (Liu et al. 2001 [76]; Tsamis et al. 2003 [151]). When the density of a nebula is spatially inhomogeneous, different line ratios used as density diagnostics lead to different values of the density. This is related to the difference in the critical density between the lines taken into consideration for the density calculation (Rubin 1989 [120]; Liu et al. 2001 [76]). The lines [NII] 122, 205 μm have lower critical densities than the lines [SII] 6731, 6717 Å, which means that the calculated density using the first pair of lines is smaller than the density using the second pair (Rubin 1989 [120]).

In the following calculations we will use our estimate of the electron density based on infrared data because the electron density is best determined when it is similar to the critical density of the lines whose ratio is used as a diagnostic (Rubin et al. 1994 [121]). Otherwise, any attempt to calculate ionic abundances will give incorrect results (Rubin 1989 [120], Liu et al. 2001 [76]).

3.5.3.3 *Ionizing flux*

To calculate the radius of the Strömgren sphere, R_S, and the rate of emission of hydrogen-ionizing photons, Q_0, a steady nonvariable star must be considered. Such an analysis can be done in the case of a variable star like AG Car if the recombination time is longer than the variability timescale of the ionizing star. The recombination time is given by $\tau_{rec} = 1/n_e \alpha_B$ yr (Draine 2011 [27]), where α_B is the recombination coefficient. Using the adopted value for the electron density and the assumed electron temperature, the recombination time was estimated to be about 520 yr. It is much longer than the timescale of the variability ($5 - 10$ yr) exhibited by the central star of the nebula, and this conclusion still holds if the higher electron density derived in the optical is considered. Therefore, an average nonvariable star is a valid approximation in our case.

The values of Q_0 and R_S can be determined first by using the estimated Hα flux and second by using the radio flux density, S_ν = 268.7 mJy at 6 cm (4.9 GHz) that was measured by Duncan and White (2002 [28]), adopting a typical error of 0.5 mJy. At 4.9 GHz the nebula is optically thin and it is assumed to be spherical with a uniform density.

The R_S in pc is given by (Vamvatira-Nakou et al. 2013 [156])

$$R_S = 3.17 \left(\frac{x_e}{\epsilon}\right)^{1/3} \left(\frac{n_e}{100}\right)^{-2/3} T_4^{(0.272+0.007\ln T_4)} \left(\frac{Q_0}{10^{49}}\right)^{1/3} , \quad (3.2)$$

where Q_0 (in photons s^{-1}) using the Hα flux is given by

$$Q_{0(H\alpha)} = 8.59 \times 10^{55} T_4^{(0.126+0.01\ln T_4)} D^2 F_0(H_\alpha) ; \quad (3.3)$$

when using the radio flux it is given by

$$Q_{0(radio)} = 8.72 \times 10^{43} T_4^{(-0.466-0.0208\ln T_4)} \left(\frac{\nu}{4.9}\right)^{0.1} x_e^{-1} D^2 S_\nu , \quad (3.4)$$

where $x_e = n_e/n_p$ is the ratio of the electron to the proton density, ϵ is the filling factor, $T_4 = T_e/(10^4$ K), ν is the radio frequency in GHz, D is the distance of the nebula in kpc, $F_0(H\alpha)$ is the Hα flux in ergs cm^{-2} s^{-1}, and S_ν is the radio flux in mJy.

Assuming $x_e = 1$ because the star is not hot enough to significantly ionize He and $T_4 = 0.635$, we found that the rate of emission of hydrogen-ionizing photons is $Q_{0(H\alpha)} = (1.2 \pm 0.5) \times 10^{48}$ photons s^{-1} and $Q_{0(radio)} = (1.0 \pm 0.4) \times 10^{48}$ photons s^{-1}. There is a good agreement between these two results within the uncertainties implying that the value of E(B−V) adopted for the calculations is essentially correct. The mean value $Q_0 = (1.1 \pm 0.3) \times 10^{48}$ photons s^{-1} corresponds to an early-B star with $T_{eff} \sim 26000$ K (Panagia 1973 [109]), which can be considered as the average spectral type of the star.

We also derived $R_S = 1.1 \pm 0.4$ pc assuming $\epsilon = 1$, i.e., that the ionized gas fills the whole volume of the nebula. The fact that the nebula is a shell and not a sphere, with inner radius of about $R_{in} = 11'' = 0.3$ pc in Hα, does not change this result because in that case the new Strömgren radius is $R_S' = (R_S^3 + R_{in}^3)^{1/3} = 1.1$ pc. The Strömgren radius is the radius of an ionization bounded nebula by definition. In Sect. 3.3, it was observed that the faint part of the nebula in Hα extends up to 0.7 pc from the central star. Moreover, the northern faint extension discussed in that section extends up to 1 pc. The comparison of these numbers with the estimated value of the Strömgren radius, considering the uncertainties, leads to the conclusion that the Hα nebula may be ionization bounded. The presence of PDR signatures in the spectrum supports this conclusion. This value of the Strömgren radius is only an average value which can vary locally depending on the density inhomogeneities. In particular, according to the adopted morphological model, the electron density of the shell could be higher along the equator and smaller along the poles so that the ionizing radiation can reach the faint extensions or bipolar lobes.

3.5.3.4 *Abundance ratio N/H*

Given the detected emission lines in the spectrum and the lack of [NIII] 57 μm and [OIII] 88 μm, only an estimate of the N/H abun-

dance number ratio can be made based on the observed Hα 6562.8 Å, [NII] 122 μm and 205 μm lines and considering that

$$\frac{N}{H} = \frac{\langle N^+ \rangle}{\langle H^+ \rangle} \, . \tag{3.5}$$

The flux ratios $F/F_0(H\beta)$ were calculated for the two infrared lines of [NII] with the observed values of F from Table 3.2. Using the dereddened Hα flux, a case-B recombination with $T_e = 6350$ K was assumed to calculate the Hβ flux, adopting the effective recombination coefficient equations of Draine (2011 [27]). The ionic abundances N^+/H^+ were then derived using the package *nebular*. The N/H abundance number ratio was calculated to be $(2.6 \pm 1.2) \times 10^{-4}$, which is equivalent to a logarithmic value of $12 + \log(N/H) = 8.41 \pm 0.20$. Considering the errors, this value is entirely compatible with that of Smith et al. (1997 [132]), which is 8.27 ± 0.05. It is significantly higher than the solar value (7.83, Grevesse et al. 2010 [37]).

3.5.3.5 *Mass of the ionized gas*

An estimate of the ionized gas mass can be made from the Hα and the radio emissions. The equations that are analytically derived in Vamvatira-Nakou et al. (2013 [156]) are used for this calculation.

For a spherical nebula the ionized mass in solar masses, taking into account the Hα emission, is given by

$$M^{\rm sphere}_{i(H\alpha)} = 57.9 \frac{1+4y_+}{\sqrt{1+y_+}} T_4^{(0.471+0.015\ln T_4)} \epsilon^{1/2} \theta^{3/2} D^{5/2} F_0^{1/2}(H\alpha) \, , \tag{3.6}$$

where θ is the angular radius of the nebula ($R = \theta D$) in arcsec and $n_{H^+} = n_p$, n_{He^+}, and $n_{He^{++}}$ are the number densities of the ionized hydrogen, ionized helium, and doubly ionized helium, respectively. Assuming $n_{He^{++}} = 0$ and denoting $y_+ = n_{He^+}/n_{H^+}$, we have $x_e = n_e/n_p \simeq 1 + n_{He^+}/n_{H^+} = 1 + y_+$ and $\mu_+ \simeq 1 + 4\, n_{He^+}/n_{H^+} = 1 + 4y_+$.

Considering now the radio flux and using the same formalism as above, the mass of a spherical nebula in solar masses is given by

$$M^{\rm sphere}_{i(\rm radio)} = 5.82 \times 10^{-5} \frac{1+4y_+}{1+y_+} T_4^{0.175} \left(\frac{\nu}{4.9}\right)^{0.05} \epsilon^{1/2} \theta^{3/2} D^{5/2} S_\nu^{1/2} \, . \tag{3.7}$$

In Hα the nebula around AG Car is a shell with inner radius $\theta_{in} = 11''$ and an average outer radius $\theta_{out} = 20''$. In the radio the nebula has approximately the same radii (Duncan and White 2002 [28]). In this case the mass of the ionized shell nebula is given by

$$M_i^{\rm shell} = (\theta_{out}^3 - \theta_{in}^3)^{1/2} \theta_{out}^{-3/2} M_i^{\rm sphere} \, . \tag{3.8}$$

The mass of the ionized shell nebula is thus $M^{shell}_{i(H\alpha)} = 6.9 \pm 2.8\ M_\odot$ and $M^{shell}_{i(radio)} = 6.4 \pm 2.5\ M_\odot$, with an average value of $M^{shell}_i = 6.6 \pm 1.9\ M_\odot$, assuming $\epsilon = 1$. The assumption that the ionization of He is negligible ($y_+ = 0$) was made because the central star has a temperature lower than 30 000 K. This result is slightly higher, considering the uncertainties, than the mass of 4.2 $M_\odot$ estimated by Nota et al. (1992 [101], 1995 [103]).

3.5.4 *Photodissociation region characteristics*

The fine structure emission lines [OI] 63, 146 μm and [CII] 158 μm are among the most important coolants in PDRs (Hollenbach & Tielens 1997 [54]). Their detection in our spectrum may indicate the presence of a PDR in the nebula. On the other hand, a shock, which is the result of the interaction between the fast stellar wind and the slow expanding remnant of a previous evolutionary phase, could also photodissociate molecules and result in [OI] and [CII] emission. However, the values of the calculated ratios of [OI] 63 μm/[OI] 146 μm and [OI] 63 μm/[CII] 158 μm are in agreement with the PDR models of Kaufman et al. (1999 [67]) and not with the shock models of Hollenbach and McKee (1989 [53]). In particular, the ratio [OI] 63 μm/[CII] 158 μm is a diagnostic between PDR and shock as it is < 10 in PDRs (Tielens and Hollenbach 1985 [147]). Consequently, based on these ratios, we can conclude that a PDR and not a shock is present in the nebula around the LBV AG Car and that it is responsible for the [OI] and [CII] emission. Photodissociation regions were detected in the nebula that surrounds the LBV HR Car (Umana et al. 2009 [153]) and in the nebula around the LBV candidate HD 168625 (Umana et al. 2010 [154]). Later on, the infrared study of the LBV WRAY 15-751 also revealed the presence of a PDR in the nebula that surrounds this star (Vamvatira-Nakou et al. 2013 [156]).

The physical conditions in the PDR can be determined using these three infrared lines, but because of the vicinity of the bright Carina nebula, we have to check if these lines come entirely from the LBV nebula or if there is a significant contribution to the measured fluxes from the background. We therefore checked the spectra of the background taken at two different positions on the sky and found that the lines [OI] 63 μm, 146 μm come entirely from the nebula. However, the flux of the line [CII] 158 μm is contaminated by the [CII] foreground/background emission. For the nebular spectrum discussed and analyzed in this section, the background has been subtracted, as mentioned in Sect. 3.2. Nevertheless, careful examination of the two off-source spectra shows that the background is strong and not uniform. The difference between the spectra of the two off positions induces an uncertainty of at least a factor of 2 on the [CII] 158 μm line flux. Hence, the measured [CII] 158 μm flux is unreliable and

the mass of hydrogen in the PDR based on the [CII] flux cannot be estimated. We note that the previous conclusion about the presence of a PDR in the nebula is still valid when background contamination is taken into account.

The structure of the PDR is described by the density of the atomic hydrogen, n_{H^0}, and the incident FUV radiation field, G_0, which can be calculated using the following equation (Tielens 2005 [146]), where it is expressed in terms of the average interstellar radiation field that corresponds to an unidirectional radiation field of 1.6×10^{-3} erg cm^{-2} s^{-1},

$$G_0 = 625 \frac{L_\star \chi}{4\pi R^2} \, , \tag{3.9}$$

where $L_\star$ is the stellar luminosity, χ is the fraction of this luminosity above 6 eV, which is ~ 0.7 for an early-B star (Young Owl et al. 2002 [174]), and R is the distance from the star. For the PDR of the AG Car nebula, the incident FUV radiation field is then $G_0 \simeq 3.7 \times 10^4$, considering that $L_\star = 10^{6.1} L_\odot$ (Sect. 3.4) and $R = 0.7$ pc, which is the radius of the ionized gas region surrounded by the PDR. This result can be used to constrain the density of the PDR. The diagnostic diagram of the PDR models of Kaufman et al. (1999 [67], Figs. 4 and 5) give the ratios of the fluxes $F_{[OI]63}/F_{[CII]158}$ and $F_{[OI]145}/F_{[OI]63}$ as a function of the density and the incident FUV radiation field. By using only the latter ratio and the calculated G_0 and considering the uncertainties, we can estimate the density of the PDR to be $\log n_{H^0} \simeq 3$, with a large uncertainty.

To verify the consistency of the PDR analysis with the results of the dust nebula analysis, the dust temperature, T_{dust}, can be estimated based on the radiative equilibrium, since the dust absorbs and re-emits the FUV radiation in the FIR. In case of silicates (i.e., $\beta = 2$) the dust temperature is given by (Tielens 2005 [146])

$$T_{dust} = 50 \left(\frac{1\,\mu m}{a} \right)^{0.06} \left(\frac{G_0}{10^4} \right)^{1/6} \text{K} \quad \text{for } T_{dust} < 250 \text{ K} \, . \tag{3.10}$$

We obtain a dust temperature of $T_{dust} = 71$ K, assuming a typical grain size of $a = 0.1$ μm because the average cross-section is dominated by small grains. This result is in agreement with the results of the 2-Dust model (Sect. 3.4).

3.6 DISCUSSION

The parameters of the LBV AG Car given in Table 3.3 summarize the measurements obtained in this work along with results taken from previous studies. The stellar parameters of luminosity, effective temperature, and distance are from Voors et al. (2000 [164]), Groh et al. (2009 [41]), Humphreys et al. (1989 [58]), and this work. The parameters for the shell include the radii, the expansion velocity (Smith

Star	log $L/L_\odot$	6.1 ± 0.2
	T_{eff} (K)	$20\,000 \pm 3000$
	D (kpc)	6.0 ± 1.0
Shell	r_{in} (pc)	0.4
	r_{out} (pc)	1.2
	v_{exp} (km s^{-1})	70
	t_{kin} (10^4 yr)	1.7
	n_e (cm^{-3})	160 ± 90
	T_e (K)	6350 ± 400
	N/O	5.7 ± 2.2
	12+log N/H	8.41 ± 0.20
	M_{dust} ($M_\odot$)	0.20 ± 0.05
	$M_{ion.gas}$ ($M_\odot$)	6.6 ± 1.9

Table 3.3: Parameters of the LBV AG Car and its shell nebula.

1991 [129]), the kinematic age, the ionized gas electron density and the adopted electron temperature, the abundance ratios (N/O from Smith et al. 1997 [132] and N/H from our study), and the measured masses of dust and gas.

The *Herschel*-PACS infrared images of the LBV AG Car reveal a dusty shell nebula that surrounds the central star. It is a clumpy ring with an inner radius of 0.4 pc and an outer radius of 1.2 pc. The Hα+[NII] images show a gas shell nebula that coincides with the dust nebula, but seems to be slightly smaller and more elliptical. The nebula has bipolar morphology, a common feature among LBV nebulae (Weis 2001 [166]; Lamers et al. 2001 [72]).

The nebula around AG Car lies in an empty cavity (Fig. 3.3). If associated with the star, the cavity may correspond to a previous mass-loss event when the wind of the O-type progenitor formed a bubble, as in the case of WR stars (Marston 1996 [84]). A similar case is the cavity observed around the LBV WRAY 15-751 (Vamvatira-Nakou et al. 2013 [156]), though the latter is much larger. Velocity mapping of the surrounding interstellar gas would be needed to confirm this hypothesis and derive constraints on the O-star evolutionary phase.

The results of our study point to a shell nebula of ionized gas and dust, surrounded by a thin photodissociation region that is heated by an average early-B star. The dust mass-loss rate is about $(1.8 \pm 0.5) \times 10^{-5}$ $M_\odot$ yr^{-1}, considering the duration of the enhanced mass-loss episode that was estimated from the kinematic age of the inner and outer radii of the nebula. Because we do not know the total gas mass as we cannot calculate the neutral gas mass, we must assume a gas-to-dust mass ratio in order to estimate the total mass-loss rate. A typical value for this ratio is 100 and so the gas mass will be ~ 20 $M_\odot$. In the study of the nebula around the LBV WRAY 15-751 (Vamvatira-Nakou et al. 2013 [156]), this ratio was calculated to be about 40. If

we assume a similar value, the gas mass will be about 10 $M_\odot$, higher than but comparable to the mass of the ionized gas. Adopting the average value, the gas mass of the nebula around AG Car is about 15 $M_\odot$ with an uncertainty of about 30%. The total mass-loss rate is then estimated to be $(1.4 \pm 0.5) \times 10^{-3}$ $M_\odot$ yr^{-1}.

It is interesting to compare this mass-loss rate that corresponds to the period during which the ejection took place with recent mass-loss rates. Leitherer et al. (1994 [75]) found $\dot{M}(H) = 0.6 \times 10^{-5}$ to 4.0×10^{-5} $M_\odot$ yr^{-1} in 1990-1992 when the star luminosity was rising, showing no significant dependence on the luminosity phase. Groh et al. (2009 [41]) studied the fundamental parameters of AG Car during the last two periods of minimum, 1985-1990 and 2000-2003, and calculated a mass-loss rate from 1.5×10^{-5} to 6.0×10^{-5} $M_\odot$ yr^{-1}. The mass-loss rate during the nebula ejection phase thus appears roughly 50 times higher than in the present evolutionary phase.

The N/O ratio of 5.7 ± 2.2 calculated by Smith et al. (1997 [132]) points to the presence of highly processed material because it is much higher than the solar abundances. It is the highest value of N/O among the known LBVs, except the case of η Car (Smith et al. 1998 [133]). The 12+log N/H abundance of 8.41 ± 0.20, calculated on the basis of our observations, is enhanced by a factor of 4.3 with respect to the solar abundance. It is lower than the value for the LBV η Car and higher than the values reported for all other LBVs (Smith et al. 1998 [133]).

Groh et al. (2009 [41]) calculated the surface abundances of several chemical elements at the surface of the star. The comparison of the nebular abundances with the surface ones shows that the N/O abundance ratio of the nebula is much lower than the surface value of 39^{+28}_{-18}. As the authors mention, this is compatible with the idea that the nebulae around massive stars contain material that is less processed than the material of the stellar photosphere.

Smith et al. (1997 [132]), based on a detailed abundances study, argued that the AG Car nebula was formed from material ejected during a RSG phase. This was also the suggestion of Voors et al. (2000 [164]) based on their analysis of the dusty nebula, but Lamers et al. (2001 [72]), in their study of the chemical composition of LBVs, concluded that the ejection occurred in a BSG phase as this can better explain the high expansion velocity. Moreover, the problem with an ejection during a RSG phase is the lack of luminous RSGs in the HR diagram.

Based on our observations as well as on evolutionary models (Ekström et al. 2012 [29]), we can constrain the evolutionary path of the central star and the epoch at which the nebula was ejected, using the abundance ratios, the measured mass-loss rate, and the timescale of the ejection as constraints. The only available abundance ratio that can be used is the N/O ratio. The N/H abundance ratio is indeed

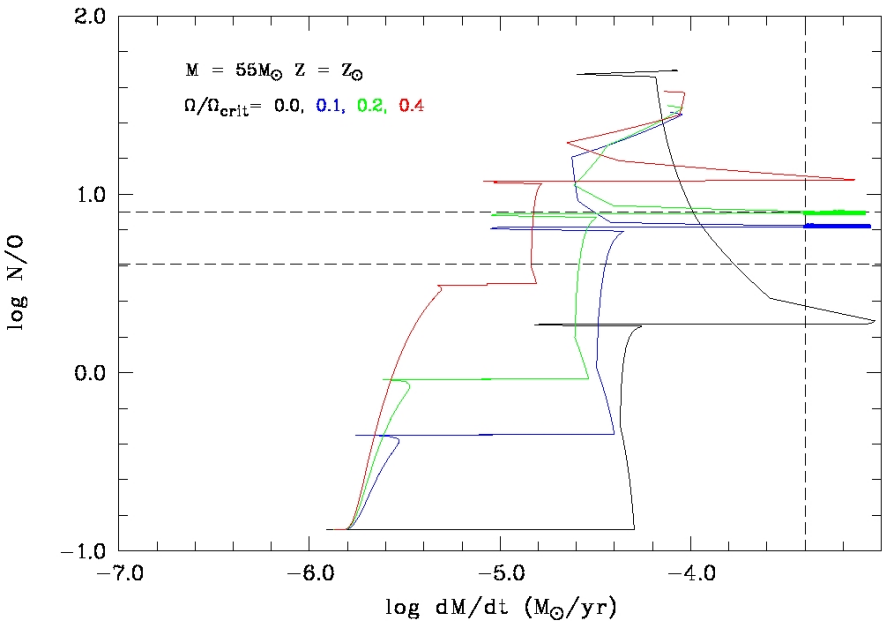

Figure 3.8: Evolution of the N/O surface abundance ratio as a function of the mass-loss rate for a 55 $M_\odot$ star of solar metallicity and for initial rotation rates Ω/Ω_{crit} from 0 to 0.4, using the models of Ekström et al. (2012 [29]). The dashed lines correspond to the adopted value of N/O, with its errors, and the lower limit for the mass-loss rate. The thicker lines emphasize the part of the tracks compatible with the measurements. For clarity, the tracks are stopped during the He burning phase (data point n^o 195 in Ekström et al. 2012 [29]).

sensitive to inhomogeneities of the nebula (Lamers et al. 2001 [72]). It should also be stressed that the evolutionary models for massive stars are very uncertain at the post-main-sequence phases as they do not include any eruptive event, which means that the mass-loss rate recipes are poorly known (Smith 2014 [134]).

A constraint on the initial rotational velocity of AG Car can be imposed, based on the results of Groh et al. (2011 [42]). In their study of AG Car during two periods of visual minimum, they concluded that the progenitor did not have a high initial rotational velocity, although they measured the current projected rotational velocity to be 220 km s^{-1}. Their conclusions were based on the comparison with the evolutionary paths of Meynet and Maeder (2003 [91]). The luminosity and effective temperature of the star were found to be compatible with the evolutionary tracks of a nonrotating star with initial mass between 40 and 60 $M_\odot$.

The total mass-loss rate, estimated during the nebular ejection, is quite high but uncertain. A lower limit of the mass-loss rate can be considered, based on the sum of the dust mass and the ionized gas mass that are well determined in the nebula ring. Considering the er-

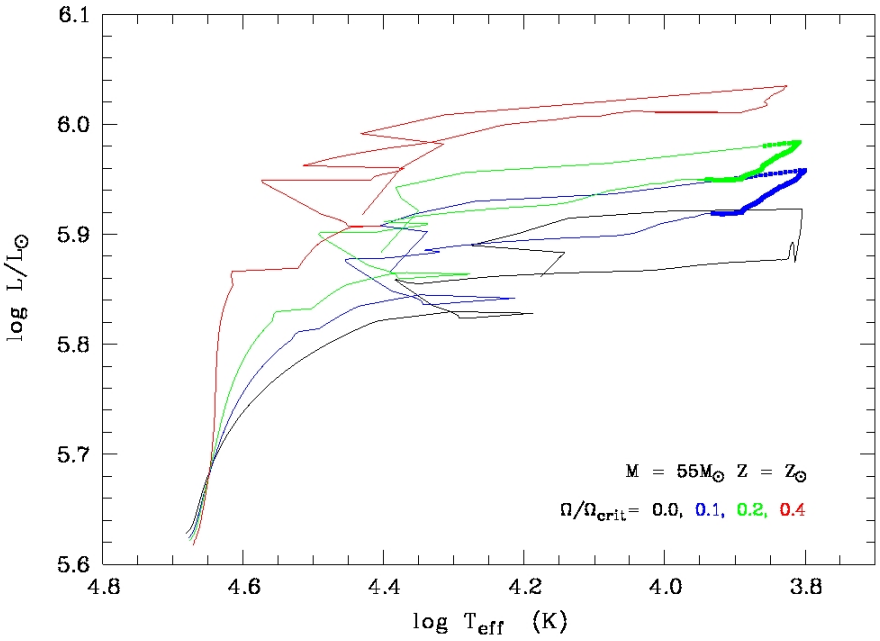

Figure 3.9: Evolutionary path in the HR diagram of a 55 $M_\odot$ star of solar metallicity and for initial rotation rates Ω/Ω_{crit} from 0 to 0.4, using the models of Ekström et al. (2012 [29]). The thicker lines emphasize the part of the tracks compatible with the N/O abundance ratio and the mass-loss rate. For clarity, the tracks are stopped during the He burning phase (data point n° 195 in Ekström et al. 2012 [29]).

rors, this lower limit is $\log \dot{M} = -3.4$, where $\dot{M}$ is in $M_\odot$ yr^{-1}. This result along with the nebular N/O abundance ratio, which is assumed to be the surface abundance ratio at the time of the ejection, were compared to the computed evolution of the mass-loss rate versus this abundance ratio using the models of Ekström et al. (2012 [29]) for stars of initial masses that correspond to the high stellar luminosity of AG Car, considering four different cases of stellar rotation from no rotation to a rotation rate of $\Omega/\Omega_{crit} = 0.4$. In Fig. 3.8, the evolution of the mass-loss ratio versus the N/O abundance ratio is illustrated for a 55 $M_\odot$ star from the models of Ekström et al. (2012 [29]). The measured N/O value, with its errors, and the measured lower limit of the mass-loss rate are plotted with dashed lines. The part of these tracks compatible with the measurements is emphasized with thicker lines. To identify at which evolutionary phase of the star this corresponds, the same parts of the tracks are reported in the HR diagram (Fig. 3.9).

Our results are compatible with the evolutionary tracks of the models of Ekström et al. (2012 [29]) for a star of 55 $M_\odot$ with solar metallicity and medium rotational velocity. In this case, the ejection of the nebula occurs in a post-main-sequence short-lived episode of high mass loss in agreement with the observations. We note that in

such short-lived episodes, the mass-loss rate could be higher than computed from the model since the model does not account for eruptive events. For a star of 57 $M_\odot$ the only compatible evolutionary track is the nonrotating one. Consequently, we can conclude that the star may have a low initial rotational velocity as suggested by Groh et al. (2011 [42]). For a mass of 50 $M_\odot$, the only compatible evolutionary track is the one rotating at $\Omega/\Omega_{\rm crit} = 0.4$. For a mass of 60 $M_\odot$, the N/O ratio is reached on the main sequence where the mass-loss rate is much smaller than our lower limit, such that no track is compatible with both the observed N/O ratio and a short-lived ($\lesssim 2 \times 10^4$ yr) high mass-loss event.

A star with initial mass between 40 and 60 $M_\odot$ immediately evolves to a BSG without passing through the RSG phase. It then evolves towards the LBV and the WR phase (Meynet et al. 2011 [92]). Groh et al. (2014 [44]) performed a detailed study on the evolutionary stages of a nonrotating star of 60 $M_\odot$ with solar metallicity, combining the evolutionary models of Ekström et al. (2012 [29]) with atmospheric models. Before the WR phase, the evolutionary tracks of a 55 $M_\odot$ star (Fig. 3.9) with little rotation are very similar to the track of Groh et al. (2014 [44]) for a 60 $M_\odot$ without rotation in terms of effective temperature and luminosity. Making use of this result points to an ejection of the nebula during the LBV evolutionary phase of AG Car and more precisely during a cool LBV phase. Compared to the results obtained for WRAY 15-751, a lower luminosity LBV that passed through a RSG phase where the ejection of its nebula took place (Vamvatira-Nakou et al. 2013 [156]), this indicates that depending on their luminosity, LBV nebulae can be ejected at different evolutionary stages. It should be mentioned that de Freitas Pacheco et al. (1992 [22]) compared the AG Car nebular properties, based on their spectroscopic observations, with the evolutionary models available at that time, and concluded that they were consistent with the properties of a star of 60 $M_\odot$ at the beginning of the LBV phase.

The model of the dust nebula in Sect. 3.4 showed that large dust grains are necessary to reproduce the observed infrared SED, in agreement with the results of Voors et al. (2000 [164]). This was also the case for the dust nebulae around the LBV WRAY 15-751 (Vamvatira-Nakou et al. 2013 [156]) and the yellow hypergiant Hen 3-1379, a possible pre-LBV (Hutsemékers et al. 2013 [62]). Large grains ($a > 5\mu$m) have also been detected in SNe (Gall et al. 2014 [34]). In the case of LBVs, the stellar temperature is most often too high for dust formation to take place so that dust production can only happen during large eruptions, when a pseudo-photosphere with a sufficiently low temperature is formed. As shown by Kochanek (2011 [69], 2014 [70]), large dust grains can be produced during LBV eruptions and other transients when the conditions of high mass-loss rate and low pseudo-photosphere temperature are encountered. According to these mod-

els, to produce grains larger than 10 μm, the central star should have gone through a great outburst, with a pseudo-photosphere temperature as low as 4000 K, i.e., much lower than during normal eruptions. During this event, the mass-loss rate is expected to be as high as 10^{-2} $M_\odot yr^{-1}$. For AG Car, this would require a duration of the event shorter than estimated from the shell thickness, which is possible if the shell thickness is mostly due to a spread in velocity (Kochanek 2011 [69]).

3.7 CONCLUSIONS

The analysis of *Herschel* PACS imaging and spectroscopic observations of the nebula around the LBV AG Car, along with optical imaging data have been presented. The PACS images show that the dust nebula appears as a clumpy ring. It coincides with the Hα nebula, but extends farther out.

The determination of the dust parameters of the nebula was performed by dust modeling with the help of a two-dimensional radiative transfer code. This model points to the presence of both a small and a large grain population of pyroxenes with a 50/50 Fe to Mg abundance. Large grains ($a \gtrsim 10$ μm) are needed to reproduce the observational data.

The infrared spectrum of the nebula consists of forbidden emission lines over a dust continuum, without the presence of any other dust feature. These lines reveal the presence of ionized and photodissociation regions that are mixed with the dust. The derived gas abundances show a strong N/O and N/H enhancement as well as a O/H depletion, which is expected for massive evolved stars enriched with CNO-cycle processed material.

The evolutionary path of the star and the epoch at which the nebula was ejected were constrained using the abundances, mass-loss rate and available evolutionary models. The results point to a nebular ejection during a cool LBV evolutionary phase of a star with initial mass of about 55 $M_\odot$ and with little rotation.

Acknowledgements. We thank the referee, Rens Waters, for his careful reading and his constructive suggestions that greatly improved the manuscript. C.V.N., D.H., P.R., N.L.J.C., Y.N. and M.A.T.G. acknowledge support from the Belgian Federal Science Policy Office via the PRODEX Programme of ESA. The Liège team also acknowledges support from the FRS-FNRS (Comm. Franç. de Belgique). PACS has been developed by a consortium of institutes led by MPE (Germany) and including UVIE (Austria); KU Leuven, CSL, IMEC (Belgium); CEA, LAM (France); MPIA (Germany); INAF-IFSI/OAA/OAP/OAT, LENS, SISSA (Italy); IAC (Spain). This development has been supported by the funding agencies BMVIT (Austria), ESA-PRODEX (Belgium), CEA/CNES (France), DLR (Germany), ASI/INAF (Italy), and CICYT/MCYT (Spain). Data presented in this paper were analyzed using "HIPE", a joint devel-

opment by the Herschel Science Ground Segment Consortium, consisting of ESA, the NASA Herschel Science Center, and the HIFI, PACS and SPIRE consortia. This research has made use of the NASA/IPAC Infrared Science Archive, which is operated by the Jet Propulsion Laboratory, California Institute of Technology, as well as NASA/ADS and SIMBAD (CDS/Strasbourg) databases.

3.8 APPENDIX A: TESTS OF THE DUST MODEL

In Sect. 3.4 the model of the dust nebula is presented and the necessity of a population of large dust grains is stressed. Several tests have been performed using the 2-Dust code in an effort to reproduce the observed data with different populations of dust grains from those adopted in Sect. 3.4. Our main concern was to investigate the influence of the dust grain size and composition on the model SED. For this reason, we calculated many models by changing one parameter and keeping the other ones constant. Keeping in mind that two different populations of grains were used to reproduce the broad observed SED in Sect. 3.4, we consider one population of small grains with radii $a_{min} < a < a_{cen}$ and one population of large grains with radii $a_{cen} < a < a_{max}$. For the dust composition, we used the optical constants given by Dorschner et al. (1995 [26]) for three different abundances of Mg to Fe, 0.5/0.5 (the model presented in Sect. 3.4), 0.4/0.6, and 0.8/0.2. For the dust grain sizes, the values of 20, 50, and 80 μm were considered for a_{max} and the values of 0.1, 0.3, 1, and 3 μm were considered for a_{cen}, with the value of a_{min} being kept constant and equal to 0.005 μm.

The comparison of these tests shows that large grains are necessary to reproduce the data. The influence of the change of a_{cen} on the fit of the observed SED is almost negligible. Furthermore, the fit depends little on the dust abundance of Mg to Fe. This is illustrated in Figs. 3.10 - 3.12. In Fig. 3.10 three dust models are illustrated. The dust composition is the same (optical constants of silicates with a 50/50 Mg-to-Fe abundance given by Dorschner et al. 1995 [26]) and the only parameter that changes is a_{max}. We see that better fits to the data are achieved when large grains are considered, in particular when a_{max} = 50 μm. In all cases, when adjusting the observed flux at 250 μm, a value for a_{max} that is too small (< 20 μm) gives too much flux at 60-100 μm. In Fig. 3.11 the comparison of three models with the same a_{max} and dust composition but with different a_{cen} is illustrated. The model SED depends little on a_{cen}. In Fig. 3.12 the comparison of three models with the same grain sizes but different dust composition (in terms of the abundance Mg to Fe) is illustrated. Again, the model SED depends little on this dust abundance ratio, with a slightly better adjustment for Mg/Fe = 50/50. We finally note that changing the power law index of the grain size distribution does not significantly affect these results.

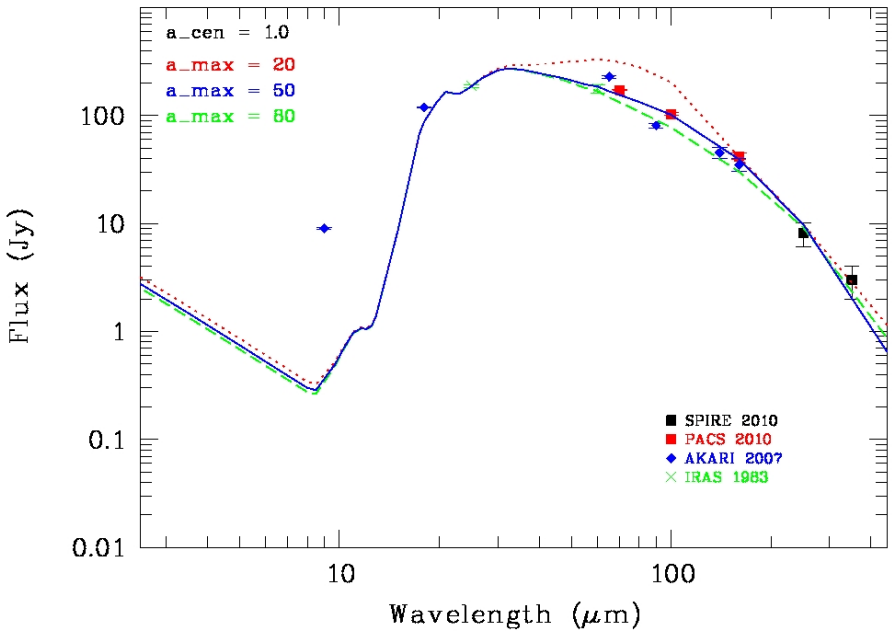

Figure 3.10: Fits of the far-infrared ($\lambda > 20\mu m$) SED of the nebula around AG Car. The dust composition (optical constants of silicates with a 50/50 Mg-to-Fe abundance given by Dorschner et al. 1995 [26]) and a_{cen} are kept constant while the value of a_{max} changes.

3.9 APPENDIX B: MODIFIED BLACKBODY FIT ON THE SED

The observed SED (Fig. 3.5) can also be reproduced with a simpler model that is the sum of two modified BB curves $F_\nu \propto B_\nu(T_d)\nu^\beta$. Only the photometric points were considered for making the fit illustrated in Fig. 3.13. The mass of the dust can then be derived using the equation

$$M_{dust} = \frac{F_\nu \, D^2}{B_\nu \, (T_d) \, \kappa_\nu} \, , \tag{3.11}$$

where κ_ν is the mass absorption coefficient, i.e. the absorption cross section per unit mass, B_ν the Planck function and D the distance to the nebula (Hildebrand 1983 [51]). For this calculation, the two populations of dust grains are considered independently. The fluxes measured at 25 μm and 250 μm are used, i.e., at those wavelengths where the contribution of each population dominates (Fig. 3.13). At 25 μm, $\kappa_\nu = 483$ cm^{2}g^{-1} for the silicates of Dorschner et al. (1995 [26]). For grains of radii smaller than the wavelengths at which dust radiates, κ_ν is roughly independent of the radius and behaves as ν^β in the FIR. However the second population of dust grains involves large grains (up to 50 μm) so that this hypothesis is no longer valid. The value of κ_ν is then taken from the 2-Dust results where it is explicitly computed for the adopted grain population. At 250 μm,

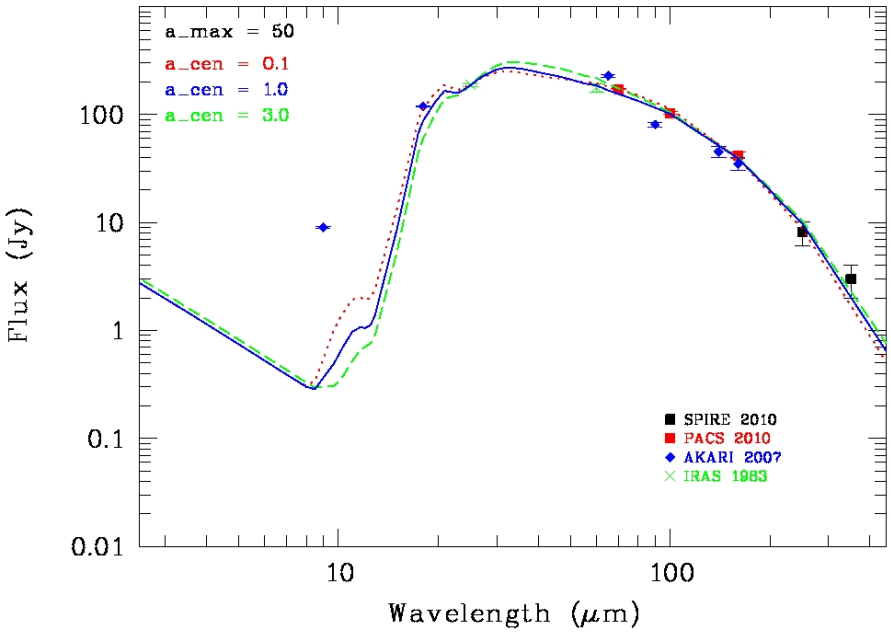

Figure 3.11: Fits of the far-infrared ($\lambda > 20\mu$m) SED of the nebula around AG Car. The dust composition (optical constants of silicates with a 50/50 Mg-to-Fe abundance given by Dorschner et al. 1995 [26]) and a_{max} are kept constant while the value of a_{cen} changes.

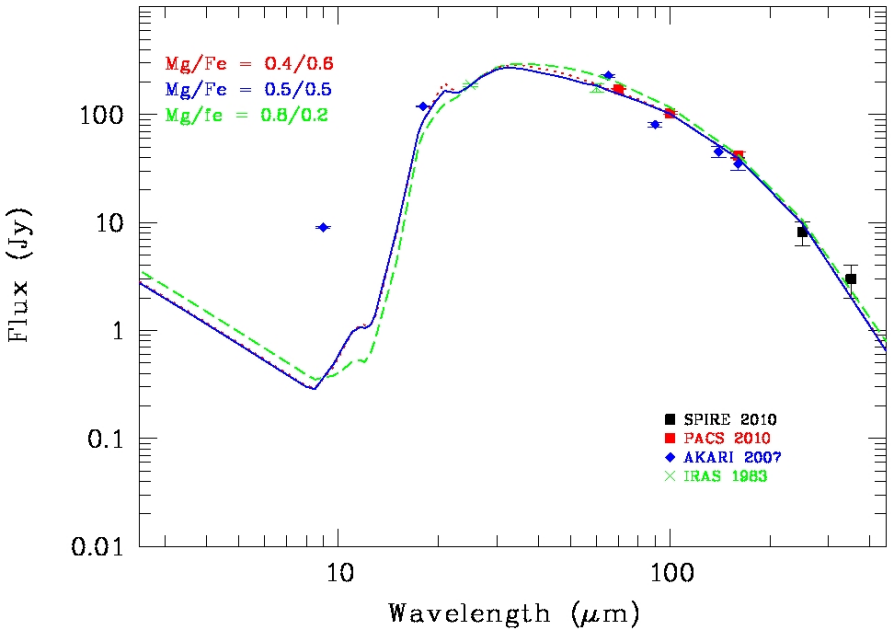

Figure 3.12: Fits of the far-infrared ($\lambda > 20\mu$m) SED of the nebula around AG Car. $a_{max} = 50$ μm and $a_{cen} = 1$ μm are kept constant while the dust composition changes. The optical constants of silicates given by Dorschner et al. (1995 [26]) are used for different Mg-to-Fe abundances.

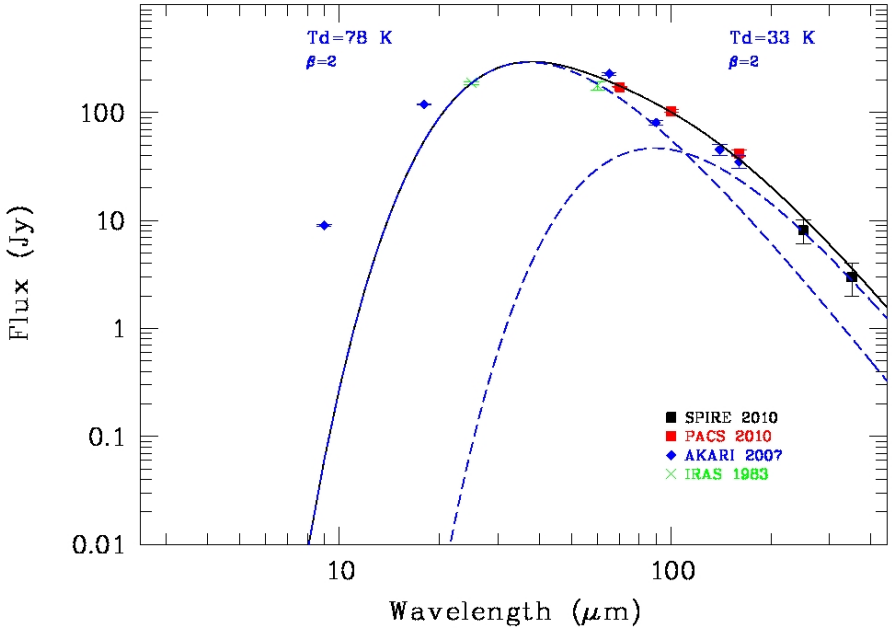

Figure 3.13: Same as Fig. 3.5 but the infrared SED of the nebula around the LBV AG Car is fitted by the sum of two modified blackbody curves.

$\kappa_\nu = 13.6$ cm^{2}g^{-1}, which is significantly higher than expected under the small-grain approximation. With such large grains the frequency dependence of κ_ν also differs from the ν^2 law, being closer to ν^1 below 100 μm. A fit with such a composite modified BB gives $T_{dust,1} = 76$ K and $T_{dust,2} = 31$ K (which is only slightly different from the values obtained with ν^2 only). Using $T_{dust,1} = 76 - 78$ K and $T_{dust,2} = 31 - 33$ K in Eq. 3.11, we then derive $M_{dust,1} = 0.05 - 0.04$ $M_\odot$ and $M_{dust,2} = 0.22 - 0.19$ $M_\odot$ for the small and the large grains respectively, in very good agreement with the 2-Dust results.

3.10 APPENDIX C: EMISSION LINE FLUXES FOR EACH SPAXEL

The results of the emission line flux measurements for each spaxel are given in Table 3.4. The first column contains the detected ions along with the spectral band in which the corresponding line was measured. The following columns contain the line fluxes, expressed in W/m^2, along with their errors. The spaxel numbers (Fig. 3.6) are mentioned in every cell of the table. The quoted uncertainties are the sum of the line-fitting uncertainty plus the uncertainty due to the position of the continuum.

Ion	λ (band) (μm)	F ± ΔF (10^{-15} W m^{-2})	F ± ΔF (10^{-15} W m^{-2})	F ± ΔF (10^{-15} W m^{-2})	F ± ΔF (10^{-15} W m^{-2})	F ± ΔF (10^{-15} W m^{-2})
		spaxel 0,0	spaxel 0,1	spaxel 0,2	spaxel 0,3	spaxel 0,4
[OI]	63 (B2A)	-	0.40 ± 0.05	0.14 ± 0.05	-	-
[NII]	122 (R1B)	0.15 ± 0.02	1.15 ± 0.01	0.85 ± 0.02	0.56 ± 0.02	0.26 ± 0.02
[OI]	146 (R1B)	-	0.03 ± 0.01	-	-	-
[OI]	146 (R1A)	-	0.03 ± 0.01	-	-	-
[CII]	158 (R1A)	-	0.21 ± 0.01	0.13 ± 0.01	0.05 ± 0.01	-
[NII]	205 (R1A)	-	0.21 ± 0.05	0.11 ± 0.03	-	-
		spaxel 1,0	spaxel 1,1	spaxel 1,2	spaxel 1,3	spaxel 1,4
[OI]	63 (B2A)	0.22 ± 0.05	0.65 ± 0.05	0.47 ± 0.05	0.29 ± 0.05	-
[NII]	122 (R1B)	0.64 ± 0.01	1.86 ± 0.02	1.49 ± 0.02	1.38 ± 0.01	0.61 ± 0.03
[OI]	146 (R1B)	0.02 ± 0.01	0.04 ± 0.01	0.04 ± 0.01	0.02 ± 0.01	-
[OI]	146 (R1A)	0.02 ± 0.01	0.04 ± 0.01	0.04 ± 0.01	0.03 ± 0.01	-
[CII]	158 (R1A)	0.09 ± 0.01	0.25 ± 0.01	0.24 ± 0.01	0.19 ± 0.01	0.06 ± 0.01
[NII]	205 (R1A)	0.10 ± 0.02	0.27 ± 0.07	0.29 ± 0.07	0.24 ± 0.06	0.14 ± 0.04
		spaxel 2,0	spaxel 2,1	spaxel 2,2	spaxel 2,3	spaxel 2.4
[OI]	63 (B2A)	0.41 ± 0.05	0.26 ± 0.05	0.15 ± 0.05	0.65 ± 0.05	0.19 ± 0.05
[NII]	122 (R1B)	1.18 ± 0.02	1.43 ± 0.02	1.01 ± 0.02	1.63 ± 0.02	0.75 ± 0.01
[OI]	146 (R1B)	0.03 ± 0.01	0.02 ± 0.01	0.02 ± 0.01	0.04 ± 0.01	0.02 ± 0.01
[OI]	146 (R1A)	0.03 ± 0.01	0.02 ± 0.01	0.01 ± 0.01	0.05 ± 0.01	0.02 ± 0.01
[CII]	158 (R1A)	0.20 ± 0.01	0.24 ± 0.01	0.17 ± 0.01	0.30 ± 0.01	0.14 ± 0.01
[NII]	205 (R1A)	0.17 ± 0.04	0.35 ± 0.09	0.28 ± 0.07	0.33 ± 0.08	0.15 ± 0.04
		spaxel 3,0	spaxel 3,1	spaxel 3,2	spaxel 3,3	spaxel 3,4
[OI]	63 (B2A)	0.25 ± 0.05	0.36 ± 0.05	0.60 ± 0.05	1.35 ± 0.06	-
[NII]	122 (R1B)	1.04 ± 0.02	1.56 ± 0.02	1.46 ± 0.02	1.68 ± 0.02	0.40 ± 0.01
[OI]	146 (R1B)	0.03 ± 0.01	0.02 ± 0.01	0.05 ± 0.01	0.07 ± 0.01	-
[OI]	146 (R1A)	0.02 ± 0.01	0.03 ± 0.01	0.04 ± 0.01	0.09 ± 0.01	0.02 ± 0.01
[CII]	158 (R1A)	0.16 ± 0.01	0.26 ± 0.01	0.32 ± 0.01	0.43 ± 0.01	0.13 ± 0.01
[NII]	205 (R1A)	0.16 ± 0.04	0.22 ± 0.06	0.23 ± 0.06	0.35 ± 0.09	-
		spaxel 4,0	spaxel 4,1	spaxel 4,2	spaxel 4,3	spaxel 4,4
[OI]	63 (B2A)	-	-	0.58 ± 0.05	0.58 ± 0.06	-
[NII]	122 (R1B)	0.43 ± 0.02	0.66 ± 0.02	1.06 ± 0.02	0.49 ± 0.02	0.11 ± 0.02
[OI]	146 (R1B)	-	-	0.04 ± 0.01	0.03 ± 0.01	-
[OI]	146 (R1A)	-	-	0.04 ± 0.01	0.04 ± 0.01	-
[CII]	158 (R1A)	0.04 ± 0.01	0.09 ± 0.01	0.26 ± 0.01	0.22 ± 0.01	0.04 ± 0.01
[NII]	205 (R1A)	0.09 ± 0.02	-	0.17 ± 0.04	-	-

Table 3.4: Line fluxes in each spaxel. A dash indicates a poor S/N or a non-detection. The spatial configuration corresponds to the footprint of the PACS-spectrometer as displayed in Fig. 3.6.

4

THE NEBULA M1-67 AROUND THE STAR WR 124

The third object studied in this thesis is the nebula M1-67 around the Wolf-Rayet star WR 124. This target has been chosen to be part of this study because it is a nebula around a Wolf-Rayet star in contrast to the previous two ones that are located around a LBV star. The comparison of the results for M1-67 to the results for the other two nebulae can give us constraints on the evolution of massive stars, since the LBV phase is thought to be a previous evolutionary phase of a WR star. The *Herschel* infrared imaging, along with the optical imaging data, allows us to investigate the morphology of this nebula and its environment. Together with the infrared spectroscopic data, they help us to constrain the evolutionary tracks of the central star and define the stage where the nebular ejection took place.

This analysis is ready for submission to *Astronomy & Astrophysics*. The draft paper is reproduced in the next pages, and it is organized as follows. An introduction to this star and its nebula is first given where a selection of results of previous studies that are related to our study is presented, followed by the description of our observations, the *Herschel* infrared imaging and spectroscopy and the optical imaging. The morphology of the nebula in the infrared and the optical light is the discussed. After, the analysis of the dust continuum emission is performed to estimated the dust properties. The nebular spectrum is then presented with the corresponding forbidden emission lines analysis to determine the ionized and neutral gas properties.

Our *Herschel* observations of the nebula M1-67 along with the optical imaging data revealed a clumpy nebula with a complex structure where the dust is mixed with the gas. The ionized gas nebula is surrounded by a PDR, as was the case of the nebula around the LBV stars WRAY 15-751 and AG Car. The material that forms the nebula is mildly enriched, as found also in the other two nebulae. Using the available theoretical models of stellar evolution, our observations are compatible with a nebular ejection during a LBV phase of a star of about 60 $M_{\odot}$ with little rotation.

HERSCHEL OBSERVATIONS OF THE NEBULA M1-67 AROUND THE WOLF-RAYET STAR WR 124

Vamvatira-Nakou, C., Hutsemékers, D., Royer, P., Waelkens, C., Groenewegen, M. A. T., and Barlow, M. J.

Abstract

Infrared *Herschel* imaging and spectroscopic observations of the nebula M1-67 around the Wolf-Rayet star WR 124 have been obtained along with optical imaging observations. The infrared images revealed a clumpy dusty nebula that extends up to 1 pc. The comparison with the optical images shows that the ionized gas nebula coincides with the dust nebula, with the dust and the gas being mixed together. The ionized gas region is surrounded by a photodissociation region as revealed from the infrared spectroscopic analysis. The analysis of the infrared spectrum of the nebula, where forbidden emission lines of highly ionized elements were detected, showed that the nebula consists of mildly processed material with the calculated abundance number ratios being N/O = 1.0 ± 0.5 and C/O = 0.46 ± 0.27. Based on a radiative transfer model, the dust mass of the nebula was estimated to be 0.22 $M_\odot$ with a large grain population being necessary to reproduce the observations. The total mass of the material ejected from WR 124 that composes the nebula M1-67 was estimated to be about 16 $M_\odot$, assuming typical dust to gas ratio. The comparison of the mass-loss rate and the abundance ratios to theoretical models of the stellar evolution led to the conclusion that the nebular ejection took place during a LBV evolutionary phase of the central star with an initial mass of 60 $M_\odot$ with little rotation.

4.1 INTRODUCTION

WR stars represent an intermediate phase in the late evolution of O-type massive stars with an initial mass $\geqslant$ 30 $M_\odot$ (Maeder & Meynet 2010 [79]). Progressively, the star loses a significant fraction of its mass through the stellar wind and/or through episodes of extreme mass-loss during a RSG or LBV evolutionary phase and the outer layer are removed leaving a bare core that becomes a WR. If the WR is in a close binary system the lower limit for the initial mass is not as robust (Crowther 2007 [21]) and in this case the H-rich envelope is lost through a Roche lobe overflow. These objects are characterized by strong broad emission lines in the optical region due to stellar winds. They are divided into two groups: the WN subtypes that show strong

lines of He and N and the WC and WO subtypes that shows strong He, C, and O in their spectra (Crowther 2007 [21]).

One third of the galactic WR stars are observed having an associated nebula at optical wavelengths (Marston 1997 [85]). Different types of morphologies have been observed around Galactic WR stars (Chu et al. 1983 [15]) and around WR stars in the Magellanic Clouds (Dopita et al. 1994 [25]). The ring nebulae around WR stars are thought to contain material that has been ejected in a previous evolutionary phase of the star, a LBV or a RSG phase (Crowther 2007 [21]). Besides, ejected nebula have been observed around LBV stars (Hutsemékers 1994 [59]; Nota et al. 1995 [103]). Consequently, the study of the nebulae around WR stars and in general around evolved massive stars is crucial for understanding the evolution of these stars, in particular through the study of their mass-loss history.

The nebula M1-67 surrounds the galactic WR 124 star (209 BAC, also known as Merrill's star), which has a WN 8 spectral type (Smith and Aller 1969 [128]). It was discovered by Minkowski (1946 [94]) who suggested that it might be a PN. Then, Sharpless (1959 [124]) classified it as an HII region. Merrill (1938 [90]) measured a high heliocentric velocity of $+200$ km s^{-1} for WR 124 that was confirmed by Bertola (1964 [5]). The nebula M1-67 was later found to have similar heliocentric velocity (Perek and Kohoutek 1971 [112]; Cohen and Barlow 1975 [17]; Pismis and Recillas-Cruz 1979 [114]) and continued to appear in PN catalogs. It was first suggested to be a WR ring nebula in the study of Cohen and Barlow (1975 [17]) based on infrared observations.

Solf and Carsenty (1982 [136]), based on their analysis of high-resolution spectra of the nebula M1-67, argued that the nebular material originates from the central WR star. This material may have been lost in an earlier evolutionary stage of the central star and was swept-up by the strong stellar wind. The study of Esteban et al. (1991 [30]) confirmed the stellar origin of the nebular material. They drew this conclusion based on the abundances of N (enhanced by a factor of 4-7.5), O (depleted by a factor of 5-7.5) and S (normal HII region abundance), and concluded that M1-67 is a WR ring nebula. Though the nebula is spatially non-uniform and has a clumpy appearance with knots of emission, they also found that there is an homogeneity in excitation conditions throughout the nebula since the knots have similar spectra.

Nota et al. (1995 [102]), analyzing optical coronagraphic data, reported for the first time the observation of an axisymmetrical outflow in M1-67. Sirianni et al. (1998 [126]) performed similar observations but with higher resolution. Their radial velocity data revealed two different motions in the circumstellar environment of WR 124; the expansion of a spherical shell and a bipolar outflow that both may have been formed during the post-main sequence evolution of the central star, when it was a LBV. Deep HST imaging (Grosdidier et al.

1998 [45]) revealed details of the fragmentation of the nebula M1-67, which appeared composed of filamentary structures that extend around the central star and many, mostly unresolved, clumps. These data showed no clear evidence for a bipolar or axisymmetrical structure. The authors argued that M1-67 could be the result of a material ejection through a clumpy wind during a LBV evolutionary phase of the central star.

Van der Sluys and Lamers (2003 [158]) studied the dynamics of the M1-67 nebula. They showed that it interacts with the interstellar medium so that a parabolic-like bow shock is formed. Because the star is moving away from us with a velocity of about 180 km s^{-1}, we see the hollow bow shock from behind. They concluded that the M1-67 nebula is due to multiple outbursts during a previous LBV phase of the central star. Cichowolski et al. (2008 [16]) analyzed high resolution radio data of the circumstellar environment of WR 124. They reported the presence of two HI cavities that are parts of the same bow shock structure. The radio morphology of the nebula at 8.5 GHz is very similar to the optical one.

Marchenko et al. (2010 [82]) analyzed HST images of the WR 124 and its surrounding nebula M1-67 taken in two different epochs. They retrieved the physical and wind properties of this star confirming its runaway status. Fernández-Martín et al. (2013 [31]), based on integral field spectroscopic data and considering theoretical evolutionary models, proposed that the central star has recently entered the WR phase and that there are no signs of interaction between the WR wind and the interstellar medium. The nebula is then essentially composed of material that was ejected during a LBV phase of the star.

Concerning the distance to M1-67, several studies tried to determine it but, given the peculiar velocity of the nebula, they had to assume the nature of the central star and its nebula. Cohen and Barlow (1975 [17]) calculated a distance of 4.33 kpc, arguing that the central star is a Population I WN8 star and using the absolute magnitude calibration of Smith (1973 [127]), a value that was consistent with the observed extinction. Pismis and Recillas-Cruz (1979 [114]) estimated a distance of about 4.5 kpc, also assuming a Population I WR star of spectral type WN8 but using a different and more recent absolute magnitude calibration. Later on, Crawford and Barlow (1991 [20]) analyzed the interstellar Na I D_2 absorption spectrum of the star and found a distance of $4-5$ kpc that excluded a PN nature. Recently, Marchenko et al. (2010 [82]) calculated a distance of 3.35 kpc with an estimated uncertainty of 20%. Since this is the latest distance calculation, assumption-free as stressed by the authors, we adopt this distance for our study as well as the properties of the star and the wind that were derived based on it and are given in Marchenko et al. (2010 [82]).

In the present paper we analyze and discuss the infrared images and the spectrum of the nebula M1-67 taken with the PACS (Poglitsch et al. 2010 [115]), and SPIRE (Griffin et al. 2010 [38]) instruments onboard the *Herschel* Space Observatory (Pilbratt et al. 2010 [113]). We present these observations and the data reduction procedure in Sect. 4.2. Based on these observations, we then describe the nebular morphology in Sect. 4.3. In Sect. 4.4 we perform the dust continuum emission model, while the analysis of the emission line spectrum follows in Sect. 4.5. In Sect. 4.6 a general discussion is presented and finally in Sect. 4.7 the conclusions of this work are given.

4.2 OBSERVATIONS AND DATA REDUCTION

4.2.1 *Infrared observations*

The infrared observations of the M1-67 nebula were carried out in the framework of the *Mass-loss of Evolved StarS (MESS)* Guaranteed Time Key Program (Groenewegen et al. 2011 [39]), including PACS and SPIRE imaging and PACS spectroscopy.

The PACS imaging observations were carried out on April 8, 2010, which corresponds to *Herschel*'s OD 329. The scan map observing mode was used, in which the telescope slews at constant speed (20″/s) along parallel lines so as to cover the required area of the sky. Two orthogonal scan maps were obtained for each filter and finally our data set consists of maps at 70, 100, and 160 μm. The obsIDs of the four scans are 1342194080, 1342194081, 1342194082, and 1342194083 with a duration of 2622 s each. The HIPE package (Ott 2010 [108]) was used for the data reduction up to level 1. Subsequently, the Scanamorphos software (Roussel 2013 [119]) was used to further reduce and combine the data. In the final maps, the pixel size is 2″ in the blue (70, 100 μm) channel and 3″ in the red (160 μm) channel. The *Herschel* PACS PSF FWHMs are 5.2″, 7.7″, and 12″ at 70 μm, 100 μm, and 160 μm, respectively.

The SPIRE imaging observations were carried out on September 21, 2010 (OD 495). The large map observing mode was used. In this mode the telescope slews at constant speed (nominal speed: 30″/s) along parallel lines so as to scan the required sky area. The cross scan pointing mode was selected so as to obtain two orthogonal scans during a single observation. Our dataset consists of maps at 250, 350, and 500 μm. The obsID is 1342204949 with a duration of 911 s. The data were retrieved from the archive, processed up to level 2. The surface brightness of the three maps was transformed from Jy/sr to Jy/pixel with the help of HIPE. The pixel size is 6″, 10″, and 14″ at 250 μm, 350 μm, and 500 μm, respectively.

The PACS spectroscopic observations of the M1-67 nebula were carried out on May 4, 2011 (OD 720). The PACS integral-field spectrometer

covers the wavelength range from 52 μm to 220 μm in two channels that operate simultaneously in the blue band, 52-98 μm, and the red band, 102-220 μm with a resolving power of $\lambda/\delta\lambda \sim 940 - 5500$ depending on the wavelength. Simultaneous imaging of a $47'' \times 47''$ field of view is provided, resolved in 5×5 square spatial pixels (i.e., spaxels). Then, the two-dimensional field-of-view is re-arranged via an image slicer along a 1×25 pixels entrance slit for the grating. The chopped line scan observing mode was use for these observations. In this mode, instead of having a complete coverage between 52 μm and 220 μm, the observations are done in specific, previously chosen, short wavebands where it is possible to detect a nebular emission line. The background spectrum was obtained through chopping and nodding. The two obsIDs are 1342220598 and 1342220599. For the spectroscopic data reduction we followed the standard steps using HIPE.

4.2.2 *Visible observations*

The optical images of the M1-67 nebulae were obtained on April 6, 1995, with the 3.6-m telescope at the ESO, La Silla, Chile. A series of short (1 s - 10 s) and long (30 s - 60 s) exposures were secured in a Hα+[NII] filter (λ_c = 6560.5 Å; FWHM = 62.2 Å) and in a continuum filter just redwards (λ_c = 6644.7 Å; FWHM = 61.0 Å). The frames were bias-corrected and flat-fielded. The night was photometric and the seeing around 1.2″. The CCD pixel size was 0.605″ on the sky. To properly calibrate the images, three spectrophotometric standard stars and three PN with known Hα flux were observed.

4.3 MORPHOLOGY OF THE NEBULA

The PACS images of the nebula M1-67 around the WR 124 star at the three infrared filters, 70 μm, 100 μm, and 160 μm, are shown in Fig. 4.1[1]. The optical Hα+[NII] image of the nebula M1-67 is illustrated in Fig. 4.2. To emphasize the Hα+[NII] ionized gas emission, the redward continuum image has been subtracted, after correcting for the position offsets and for the different filter transmissions, using field stars. It should be mentioned that the nebula is clearly detected in the λ_c6644.7 Å continuum filter, indicating significant dust scattering. In the right panel of Fig. 4.2, the contour image of the Hα+[NII] emission is illustrated, superimposed on the infrared image of the nebula at 70 μm. A three color image of the nebula M1-67 and its environment is shown in Fig. 4.3.

The infrared images reveal a dust nebula with a non-uniform brightness. It appears to be clumpy but the clumps are not resolved in these observations. Although the brightest points of the nebula

1 The SPIRE images are not presented here because they have low resolution so that the nebula is barely resolved.

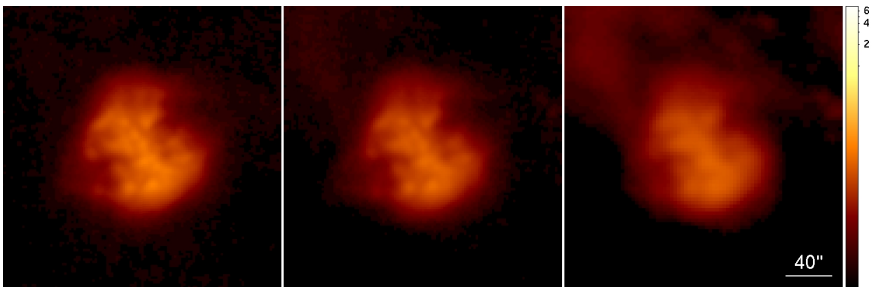

Figure 4.1: PACS images of the nebula M1-67 at 70 μm, 100 μm, and 160 μm, from left to right. The size of each image is 4′×4′. The scale on the right corresponds to the surface brightness (arbitrary units) and is logarithmic to better show the faint emission. North is up and east is to the left.

appear distributed along an elongated structure, there is no clear evidence from the infrared images that the nebula is bipolar as it was suggested by Fernández-Martín et al. (2013 [31]). Moreover, a fainter structure, with a more spherical shape, seems to surround the bright nebulosities. It is better detected in the three color infrared image (Fig. 4.3). This faint spherical structure was also observed in the Spitzer MIPS 24 μm image (Gvaramadze et al. 2010 [48]) discussed in Fernández-Martín et al. (2013 [31]). The global infrared morphology of the M1-67 is thus essentially spherical, with an average radius of about 60″ that corresponds to 1 pc at the adopted distance of 3.35 kpc. The nebula seems to be located inside an empty cavity (Fig. 4.3) that may have been formed in a previous evolutionary phase of the central star.

The Hα+[NII] view of the nebula is very similar to the infrared one. Its general morphology is the same, but with more details because optical images have a higher resolution (Fig. 4.2). The dust nebula extends slightly further out the gas nebula. The ionized gas nebula is also clumpy with a very complex structure of filaments. The contour image of the optical emission superimposed on the 70 μm image shows that the brightest regions (clumps) of the ionized gas nebula coincide with the bright regions of the dust nebula. An average angular radius of ~ 55″, which corresponds to 0.9 pc at a distance of 3.35 kpc, can be defined for the ionized gas nebula, in agreement with the previous measurements of Grosdidier et al. (1998 [45]) who detected a fainter diffused component of the optical nebula. Solf & Carsenty (1982 [136]) and Sirianni et al. (1998 [126]) had measured a smaller radius of about 45″, without detecting the faint component. The similarity between the optical and the infrared view implies that the gas is mixed with the dust in the nebula M1-67.

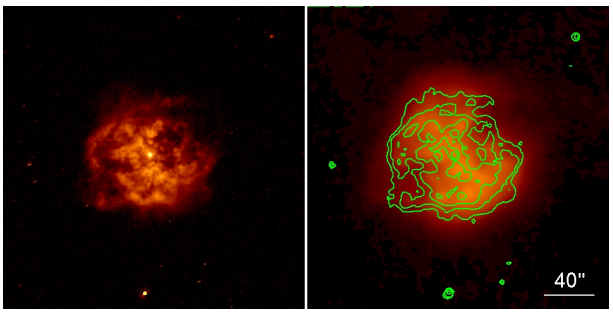

Figure 4.2: *Left*:View of the nebula M1-67 in the optical Hα+[NII] filter. The continuum image has been subtracted to emphasize the ionized gas emission. *Right*: Contour image of the optical Hα+[NII] emission from the nebula (green lines) superposed on the PACS infrared image of the nebula at 70 μm (shown also in Fig. 4.1 at the same scale). The size of each image is 4′×4′. North is up and east is to the left.

4.4 DUST CONTINUUM EMISSION

By performing aperture photometry on the PACS and SPIRE images, we derived integrated flux densities for the nebula M1-67. Imaging data taken from the archive of the IRAS mission (Neugebauer et al. 1984 [99]) were also used to extend the SED to smaller wavelengths. To all the flux densities derived from the data of these space missions we applied photometric color correction in order to make the conversion of the monochromatic flux densities, which refer to a constant energy spectrum, to the true object SED flux densities at the photometric reference wavelengths of each instrument.

For the IRAS data, the flux density ratios were used to derive the color temperature and then the corresponding correction factor was chosen to correct the flux densities (Beichman et al. 1988 [4]). The ratio R (12,25) corresponds to a temperature of 140 K, while the ratios R (25,60) and R (60,100) correspond to a temperature of 100 K. Consequently, we decided to calculate the correction for the flux densities at 12 μm and 25 μm using both temperatures and then consider the average of the two corrected flux densities for each wavelength and accounting the difference between them in the error. The flux densities at 60 μm and 100 μm were corrected using the correction factors that correspond to a temperature of 100 K. For the *Herschel*-PACS data color correction, we fitted a BB, using also the 25 μm IRAS observation to have a point before the maximum of the curve needed for the fitting. The color correction factors that correspond to a temperature of 100 K derived from this fit were then used to correct the flux densities (Müller et al. 2011 [144]). For the *Herschel*-SPIRE data color correction, we followed the instructions given in SPIRE Handbook [2].

2 http://herschel.esac.esa.int/Docs /SPIRE/spire_handbook.pdf

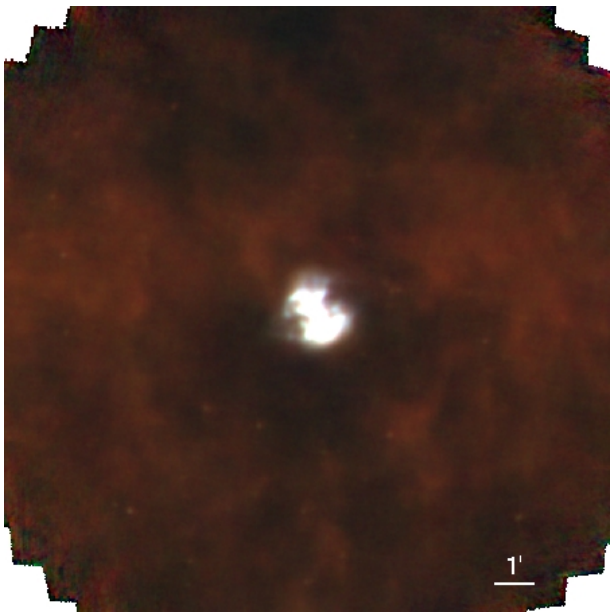

Figure 4.3: Three-color (70 μm in blue, 100 μm in green, and 160 μm in red) image of the nebula M1-67. The size of the image is 15′×15′. North is up and east is to the left.

Table 4.1 presents the corrected flux density measurements from IRAS and *Herschel* space missions. These data are used to construct the infrared SED of the nebula M1-67 shown in Fig. 4.4.

To model the dust nebula around WR 124 and calculate the temperature and the mass of the dust we used the 2-Dust code (Ueta and Meixner 2003 [152]), a publicly available two-dimensional radiative transfer code that can be supplied with complex axisymmetric density distributions as well as with various dust grain density distributions and optical properties. The photometric points previously discussed are used for the dust model.

The first step for the dust modeling is to constrain the nebular geometry revealed through the optical and the infrared images. As mentioned in Sect. 4.1, according to previous studies there are two different scenarios for the nebula M1-67: a) a bipolar morphology that was suggested by Sirianni et al. (1998 [126]), firstly reported by Nota et al. (1995 [102]), but that was not confirmed by Grosdidier et al. (1998 [45], 2001 [47]); and b) a bow shock model that was suggested by Van der Sluys and Lamers (2003 [158]) after a detailed analysis of radial velocities, firstly mentioned by Grosdidier et al. (1999 [46]), and that was confirmed by Cichowolski et al. (2008 [16]) and Marchenko et al. (2010 [82]).

The bow shock scenario is the most plausible because the nebula M1-67 surrounds a massive runway star that moves with a velocity much higher than the velocity of the interstellar medium (Van der Sluys and Lamers 2003 [158]). Also, the optical and infrared view of

Spacecraft-Instrument	Date	λ (μm)	F_ν (Jy)	Error (Jy)
IRAS [α]	1983	12	1.4	0.2
		25	17.4	0.9
		60	48.5	4.4
		100	31.6	4.4
Herschel-PACS [b]	2010	70	54.2	0.5
		100	39.1	2.4
		160	17.9	3.1
Herschel-SPIRE [b]	2010	250	6.2	0.6
		350	2.2	0.3
		500	0.8	0.1

Notes. Data from: [(α)] IRAS Faint Source Reject Catalog (Moshir et al. 1992 [97]) [b] This work

Table 4.1: Color-corrected flux densities of the nebula M1-67.

the nebula does not show clear evidence for a bipolar morphology (Sect. 4.3). In this case, the standoff distance of the bow shock, d_s, is about 0.65 pc using the parameters given in Marchenko et al. (2010 [82]) and the stellar velocity of 200 km/s determined by Cichowolski et al. (2008 [16]). This distance is equivalent to 40″ at 3.35 kpc. It is smaller than the measured radius of the nebula in the infrared, which is 60″ or 1 pc (Sect. 4.3), so the star is decentered in respect to the nebula but not much. Consequently, to model the dust, we make the approximation that the nebula is spherical with $r_{in} = 40''$ and $r_{out} = 60''$.

For the parameters of the central star WR 124 we adopted the distance D = 3.4 kpc, the luminosity $\log L/L_\odot = 5.18$, and the temperature $T_{eff} = 35\,800$ K that were estimated by Marchenko et al. (2010 [82]). We considered two populations of dust grains that have same composition but different sizes, because the infrared SED of M1-67 (Fig. 4.4) is too broad to be reproduced with only one population as this was the case for the nebula around the LBV AG Car (Vamvatira-Nakou et al. 2015 [157]). For each of the two populations of dust grains, we assumed the size distribution of Mathis et al. (1997 [86]): $n(a) \propto a^{-3.5}$ with $a_{min} < a < a_{max}$, a being the grain radius. By varying a_{min} (or a_{max}), which controls the 20μm/100μm flux density ratio and the opacity, which controls the strength of the emission, we can adjust the model to the data. The fit is done for data points at $\lambda >$ 20 μm.

The best fit (Fig. 4.4) was achieved using the following populations of dust grains with the optical constants of olivines with a 50/50 Fe to Mg abundance given by Dorschner et al. (1995 [26]), extrapolated to a constant refraction index in the FUV. The first is a population of small grains with radii from 0.005 to 0.1 μm, which is responsible for the emission at $\lambda < 40$μm. The second is a population of large

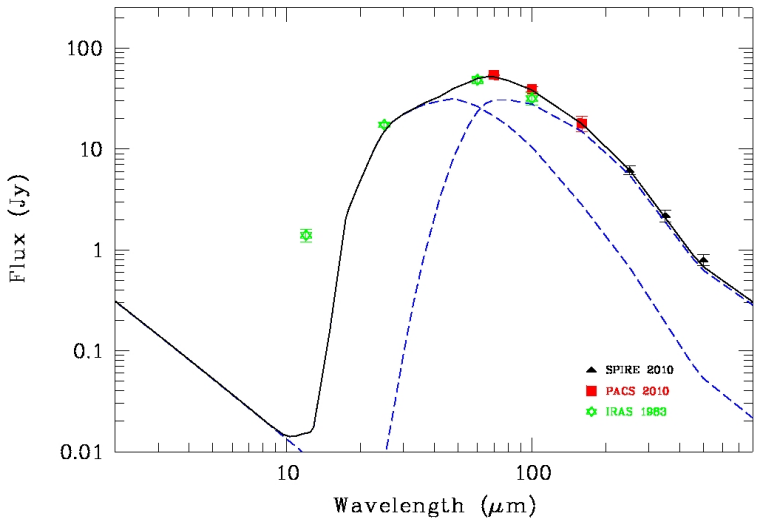

Figure 4.4: Infrared SED of the nebula M1-67 around the Wolf-Rayet star WR 124 from data collected at different epochs: color-corrected photometric measurements from IRAS and *Herschel* (PACS and SPIRE) space missions. The best result of the 2-Dust model fitting is illustrated (solid line). It was achieved considering two populations of dust grains (dashed lines). Data at $\lambda < 20$ μm are not considered in the fit.

grains with radii from 2 to 10 μm, which is responsible for the slope of the infrared SED at $\lambda > 70$μm. Such large grains were also found in our analysis of the AG Car nebula (Vamvatira-Nakou et al. 2015 [157]).

According to the model results, the total mass of dust is $M_{dust} \sim 0.22\ M_\odot$ ($0.006\ M_\odot$ from the small dust grains and $0.21\ M_\odot$ from the large dust grains). The uncertainty is $\sim$ 20%. The temperature of small grains goes from 65 K at r_{in} to 58 K at r_{out}, while the temperatures of large grains goes from 29 K at r_{in} to 26 K at r_{out}. Cichowolski et al. (2008 [16]) found a dust temperature of 70-100 K mentioning that they are in agreement with previous bow shocks observations. There is a difference between these results and our results because we used two populations of dust grains for the fit.

4.5 EMISSION LINE SPECTRUM

Fig. 4.5 illustrates the footprint of the PACS spectral field-of-view, which is composed of 25 (5×5) spaxels, on the image of the M1-67 nebula at 70 μm. Each spaxel corresponds to a different part of the nebula, and we have a spectrum for each one of them. Nevertheless, a big part of the nebula is outside of the spectral field-of-view, which is not large enough to cover the entire nebula.

The integrated spectrum of the nebula over the 25 spaxels is shown in Fig. 4.6 and Fig. 4.7, recalling that the spectroscopic observational

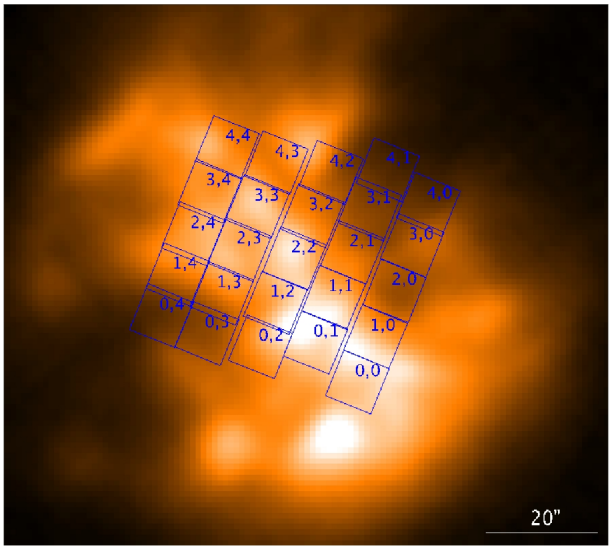

Figure 4.5: Footprint of the PACS spectral field-of-view on the image of the nebula M1-67 at 70 μm. This field is composed of 5×5 spaxels, each one of them labeled with a number pair. North is up and east is to the left.

mode provides us only with some preselected areas of the PACS waveband and not a complete coverage. The forbidden emission lines that have been detected are the following: [OI] λλ 63, 146 μm, [NII] λλ 122, 205 μm, [CII] λ 158 μm, [NIII] λ 57 μm, and [OIII] λ 88 μm. The presence of the latter lines indicates that the nebula M1-67 is highly ionized.

4.5.1 *Line flux measurements*

To measure the emission line intensities in each one of the 25 spectra we performed a Gaussian fit to the line profiles using the IRAF package (Tody 1986 [149], 1993 [150]). These measurements are presented in the Table 4.4 of Sect. 4.8. Not all the lines are detected in each spaxel. The [OI] 146 μm line seems to be the most difficult to detect. On the contrary, the [NII] 122 μm line, detected everywhere, has the highest flux among the detected lines in every spaxel.

To increase the S/N ratio, we then measured the flux of the emission lines that are present on the summed spectrum over the 25 spaxels (Fig. 4.6 and Fig. 4.7). We note that the [NIII] 57 μm and [OIII] 88 μm lines are detected only in the summed spectrum. The [NII] 205 μm line is known to have a problematic calibration in PACS. As a result, we need to correct its flux before using it in the following analysis. Using objects from the MESS collaboration (Groenewegen et al. 2011 [39]) that were observed with both PACS and SPIRE, we calculated a correction factor. With the help of the SPIRE/PACS cross calibration, we then found that the measured [NII] 205 μm flux should

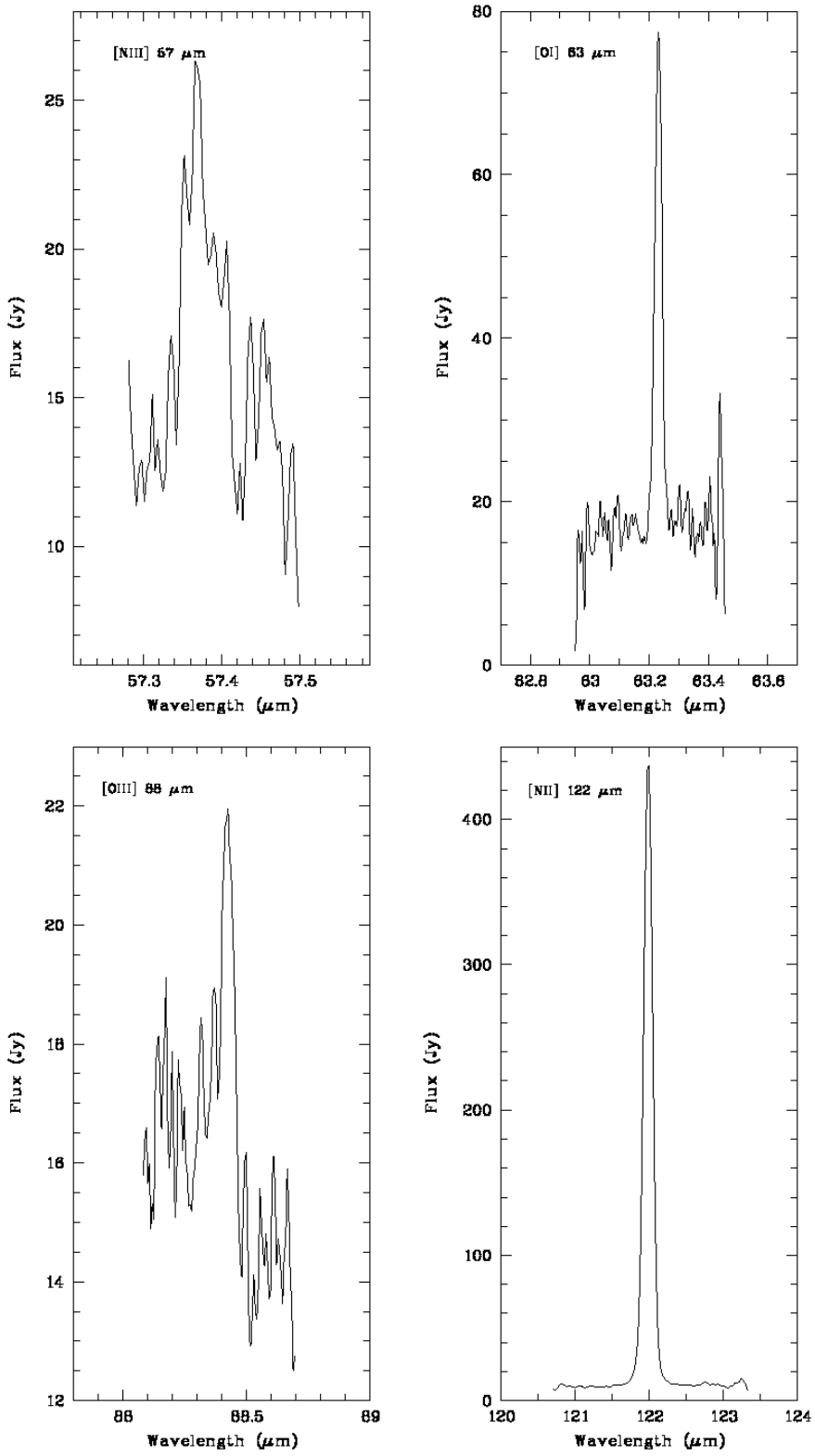

Figure 4.6: Integrated PACS spectra of the nebula M1-67 around the WR 124 star over the 25 spaxels. The detected forbidden emission lines are: [NIII] 57 μm, [OI] 63 μm, [OIII] 88 μm, [NII] 122 μm.

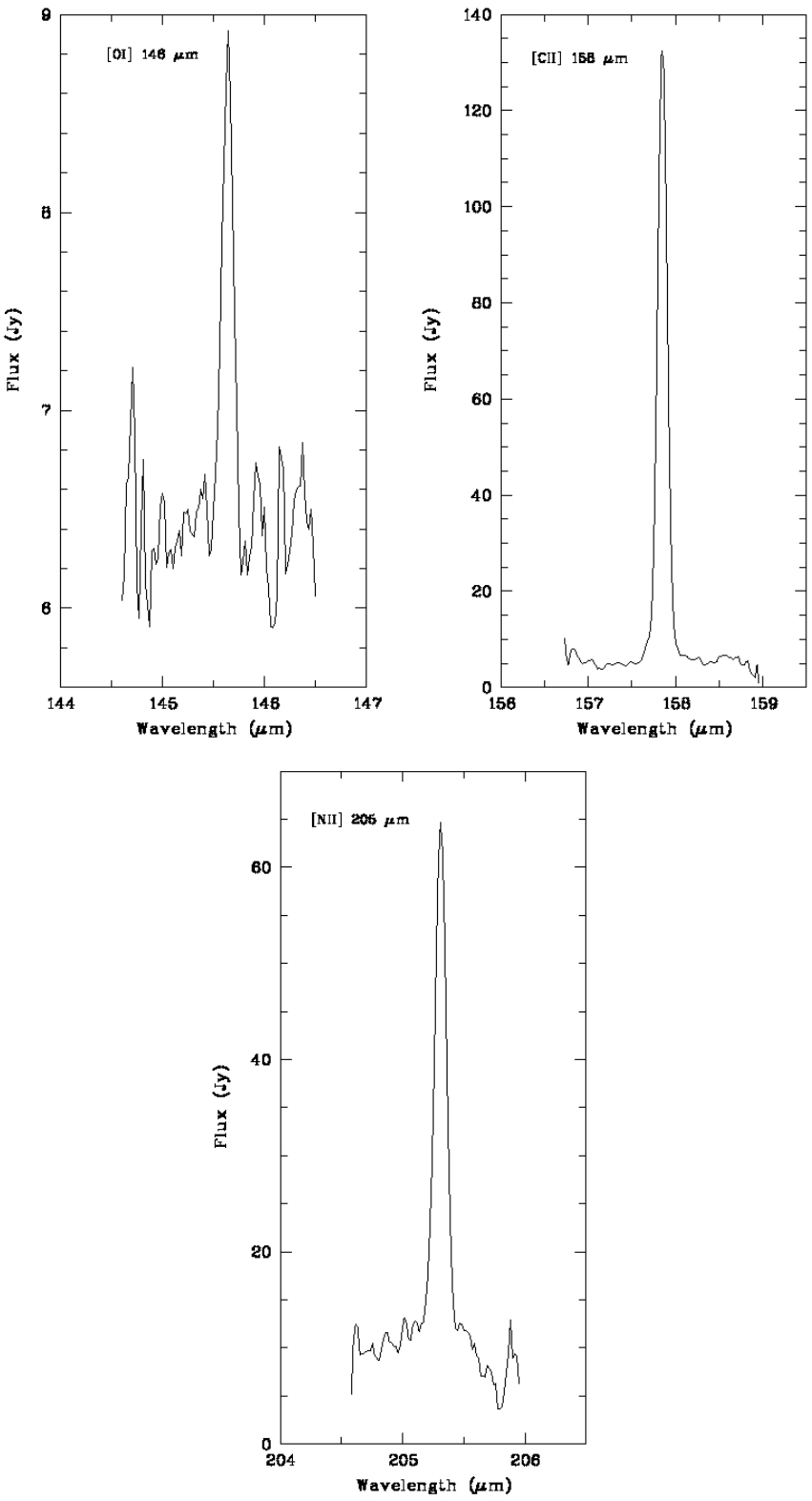

Figure 4.7: Integrated PACS spectra of the nebula M1-67 around the WR 124 star over the 25 spaxels. The detected forbidden emission lines are:[OI] 146 μm, [CII] 158 μm and [NII] 205 μm.

Ion	λ (μm)	F ± ΔF (10^{-15} W m^{-2})
[NIII]	57	0.29 ± 0.10
[OI]	63	1.34 ± 0.29
[OIII]	88	0.14 ± 0.04
[NII]	122	13.05 ± 2.70
[OI]	146	0.05 ± 0.01
[CII]	158	2.13 ± 0.44
[NII]	205	$1.89 \pm 0.47^{\alpha}$

Notes. $^{(\alpha)}$ Corrected value from PACS/ SPIRE cross-calibration

Table 4.2: Line fluxes from the summed spectrum (25 spaxels) of the nebula M1-67.

be multiplied by a correction factor of 4.2, assuming an error of 25% for the final corrected [NII] 205 μm flux. [3]

The emission line flux measurements from the summed spectrum over the 25 spaxels are given in Table 4.2, taking into account the correction on the [NII] 205 μm line flux.

In the following spectral analysis, we use only ratios of the line fluxes from the spectrum summed over the 25 spaxels to determine nebular properties assuming that they represent the whole nebula. We do not use the line fluxes themselves because they are only coming from a part of the nebula that corresponds to the area covered by the 25 spaxels.

4.5.2 *Photoionization region characteristics*

The following four detected emission lines: [NII] 122, 205 μm, [NIII] 67 μm, and [OIII] 88 μm are associated to the photoionization region (i.e., HII region) of the M1-67 nebula. The other forbidden emission lines, detected in the nebular spectrum, originate from a region of transition between ionized and neutral hydrogen. They may indicate the presence of a PDR. We analyze and discuss them in the next subsection.

3 Although there are also SPIRE observations of the spectrum of the nebula M1-67, taken in the framework of the MESS program, they cannot be used to have a more precise flux for the line [NII] 205 μm. That is due to the combination of the geometry of the detector array and the geometry of the nebula and due to the fact that the observing mode was a single pointing and not a raster map, in a way that any attempt to recover the nebular flux is highly uncertain. As a result, we decided not to include the SPIRE spectroscopic data in this study.

4.5.2.1 *Hα flux*

To estimate the Hα+[NII] flux from the M1-67 nebula we integrated the surface brightness over the whole nebula. We then corrected the contamination by field stars and the background and we extrapolated the emission from the occulted central part using the mean surface brightness. We measured the continuum flux from the reflection nebula in the adjacent filter, accounting for the difference in filter transmissions. Since WR 124 is a strong emission-line star, the reflected stellar Hα flux must also be subtracted. The final contamination due to the reflection nebula was estimated to be 13%, considering the Hα equivalent widths measured by Hamann et al. (1993 [49]) for WR 124 in 1992 (i.e., accounting for ~ 3 years of time-delay). We then subtracted the contribution of the strong [NII] lines using the [NII] /Hα ratios from available spectroscopic data and from the transmission curve of the Hα+[NII] filter. With the help of the three PN and the three spectrophotometric standard stars observed in the same filter, we did the conversion to absolute flux. The conversion factors derived from all these six objects are in excellent internal agreement.

The Hα flux was measured to be $F(H\alpha) = 2.4 \times 10^{-11}$ ergs cm^{-2} s^{-1} uncorrected for reddening and with an uncertainty of ~ 20%. Adopting $E(B-V) = 0.93 \pm 0.10$ (Esteban et al. 1991 [30]), we derived $F_0(H\alpha) = (2.0 \pm 0.6) \times 10^{-10}$ ergs cm^{-2} s^{-1} for the M1-67 nebula. Within the uncertainties, this flux is in agreement with the flux measured by Grosdidier et al. (1998 [45]), i.e., $F_0(H\alpha) = 2.3 \times 10^{-10}$ ergs cm^{-2} s^{-1} using the same reddening. The flux density from the reflection nebula is $F_\lambda = 2.9 \times 10^{-14}$ ergs cm^{-2} s^{-1} Å^{-1} at 6650 Å (the central wavelength of the continuum filter).

4.5.2.2 *Electron density*

The [SII] 6717/6731 ratio is an electron density diagnostic in the optical. Several electron density estimate were made based on this ratio. Solf and Carsenty (1982 [136]) calculated an electron density of 1000 ± 300 cm^{-3}. Later on, Esteban et al. (1991 [30]) calculated the electron density at different parts of the nebula (four different slit positions). Their results for the central parts agree with the value of Solf and Carsenty (1982 [136]), while at the outer parts the electron density is about 200 cm^{-3}. The results of Sirianni et al. (1998 [126]), who presented a detailed electron density distribution versus the distance from the star, confirmed the previous two studies. Fernández-Martín et al. (2013 [31]) calculated a density range from ~ 1500 cm^{-3}, near the star, to ~ 650 cm^{-3} towards the nebular edge, results that are consistent with their electron density maps and the previous studies.

Grosdidier et al. (1998 [45]) estimated the electron density to be 825 ± 115 cm^{-3} based on the analysis of Hα observations of the nebula and adopting a distance of 4.5 kpc. Cichowolski et al. (2008 [16]) found a value of $630 - 360$ cm^{-3} based on radio continuum data at

3.6 cm and adopting a distance of 5 kpc. Considering the uncertainties, these estimations agree with the previously mentioned ones that were based on the [SII] 6717/6731 ratio.

The [NII] 122/205 μm ratio is a diagnostic for the electron density of the nebula in the infrared waveband. Using the package *nebular* of the IRAF/STSDAS environment (Shaw & Dufour 1995 [125]), assuming an electron temperature, T_e, equal to 7000 K (mean value of the estimation of Barker 1978 [3] and Esteban et al. 1991 [30]), also adopted by Fernández-Martín et al. (2013 [31]) with an uncertainty of 20% and constant throughout the nebula, and considering the values given in Table 4.2, the electron density of the nebula M1-67 was estimated to be 600 ± 180 cm^{-3}. Given the uncertainties, this estimate of the average nebular electron density is in agreement with the previous studies. Furthermore, when a nebula has a spatially inhomogeneous electron density, the use of different line ratios as density diagnostic lead to different results because of the difference in critical density between the lines used for the density calculation (Rubin 1989 [120], Liu et al. 2001 [76]). This has been observed in PN (Liu et al. 2001 [76], Tsamis et al. 2003 [151]) and in a LBV nebula (Vamvatira-Nakou et al. 2015 [157]).

Our estimate of the electron density based on infrared data will be used in the following calculations, because the best determination of the electron density is done when it is similar to the critical density of the lines used for the calculation (Rubin et al. 1994 [121]). Otherwise, the further calculation of ionic abundances will not give correct results (Rubin 1989 [120], Liu et al. 2001 [76]).

4.5.2.3 *Ionizing flux*

Using the estimated Hα flux, the rate of emission of hydrogen-ionizing photons, Q_0, in photons s^{-1}, and the radius of the Strömgren sphere, R_S, in pc, can be estimated with the help of the following equations (Vamvatira-Nakou et al. 2013 [156])

$$Q_{0(H_\alpha)} = 8.59 \times 10^{55} T_4^{(0.126+0.01 \ln T_4)} D^2 F_0(H_\alpha) \, , \tag{4.1}$$

$$R_S = 3.17 \left(\frac{x_e}{\epsilon}\right)^{1/3} \left(\frac{n_e}{100}\right)^{-2/3} T_4^{(0.272+0.007 \ln T_4)} \left(\frac{Q_0}{10^{49}}\right)^{1/3} \, , \tag{4.2}$$

$x_e = n_e/n_p \simeq 1 + n_{He^+}/n_{H^+} = 1 + y_+$, with $n_{H^+} = n_p$, n_{He^+} being the number densities of the ionized hydrogen and ionized helium respectively, assuming that the number density of the doubly ionized helium is $n_{He^{++}} = 0$, ϵ is the filling factor, $T_4 = T_e/(10^4$ K), D is the distance of the nebula in kpc and $F_0(H\alpha)$ is the Hα flux in ergs cm^{-2} s^{-1}.

Assuming that $\epsilon = 0.05$, which is also the value used by Grosdidier et al. (1998 [45]), and using the abundance ratio $n_{He^+}/n_{H^+} =$

0.013 from Esteban et al. (1991 [30]) we calculated a rate of emission of hydrogen-ionizing photons of about 1.8×10^{47} photons s^{-1} and a Strömgren radius of 0.7 pc. For a higher filling factor of 0.15 (Cichowolski et al. 2008 [16]) the Strömgren radius is 1.0 pc. Considering the uncertainties of the nebular parameters, our estimation for the Strömgren radius is in agreement with the radio measurements of 1.3 pc of Cichowolski et al. (2008 [16]) given that they used a higher distance (5 kpc).

The ionized gas nebula extends up to about 0.9 pc from the central star (Sect. 4.3). This value is comparable, considering the uncertainties, to the estimated Strömgren radius that is the radius of an ionization bounded nebula by definition. Consequently, the nebula M1-67 around the WR 124 may be ionization bounded.

4.5.2.4 *Abundance ratio N/O*

Using the emission lines [NIII] 57 μm and [OIII] 88 μm, the N/O abundance number ratio can be estimated by the equation

$$\frac{N}{O} = \frac{\langle N^{++} \rangle}{\langle O^{++} \rangle} = \frac{F_{[NIII]57}/\varepsilon_{[NIII]57}}{F_{[OIII]88}/\varepsilon_{[OIII]88}}, \tag{4.3}$$

where F is the flux and ε is the volume emissivity of a given line. The emissivities were calculated with the package *nebular*, using the adopted value for the electron temperature and the previously calculated electron density. From the measured line fluxes (Table 4.2), the N/O abundance ratio is 1.0 ± 0.5, a value that is much higher than the Solar one of 0.14 (Grevesse et al. 2010 [37]). Given the uncertainties, it is in agreement with the estimated value of Esteban et al. (1991 [30]) and similar to the values for other nebulae around WR stars (Smith 1997 [132]).

4.5.2.5 *Mass of the ionized gas*

Based on the Hα emission we can estimate the ionized gas mass. Assuming a spherical nebula, the ionized mass in solar masses is given by (Vamvatira-Nakou et al. 2013 [156])

$$M_{i(H\alpha)} = 57.9 \frac{1 + 4y_+}{\sqrt{1 + y_+}} T_4^{(0.471 + 0.015 \ln T_4)} \epsilon^{1/2} \theta^{3/2} D^{5/2} F_0^{1/2} (H\alpha), \tag{4.4}$$

where θ is the angular radius of the nebula ($R = \theta D$) in arcsec and $y_+ = n_{He^+}/n_{H^+}$.

Using the previous assumptions for the filling factor and the abundance ratio, we estimated the mass of the ionized gas to be 1.3 ± 0.7 $M_\odot$. For a higher filling factor, $\epsilon = 0.15$, the ionized gas mass is about 2.3 ± 1.1 $M_\odot$. On average, the mass of the ionized gas is estimated to be between 0.5 and 3.4 $M_\odot$.

Previous studies gave various results for the mass of ionized gas of the nebula that are not always in agreement with each other because different assumptions are made and different parameters are used. Cohen and Barlow (1975 [17]) found an ionized mass of 9 $M_\odot$. Solf and Carsenty (1982 [136]) estimated a mass of about 0.8 $M_\odot$, which, as they reported, is in agreement with the value of Johnson (1980 [66]) and Chu and Treffers (1981 [14]). Later on, Grosdidier et al. (1998 [45]) estimated that the total mass of the ionized shell could be as low as about 1.33 $M_\odot$. More recently, Cichowolski et al. (2008 [16]) calculated a mass of $5-9$ $M_\odot$, depending on the filling factor used ($0.05-0.15$).

If we consider the geometry of the nebula as described in Sect. 4.4 the shell has an inner radius of $\theta_{in} = 40''$ and an outer radius $\theta_{out} = 60''$. The mass of the ionized shell nebula is then given by

$$M_i^{shell} = (\theta_{out}^3 - \theta_{in}^3)^{1/2} \theta_{out}^{-3/2} M_i^{sphere}. \tag{4.5}$$

The mass of the ionized shell nebula is thus $M_{i(H\alpha)}^{shell} = 0.6-3.0$ $M_\odot$ depending on the filling factor.

4.5.3 *Photodissociation region characteristics*

The detection of the other three emission lines, [OI] 63, 146 μm, and [CII] 158 μm, may indicate the presence of a PDR in the nebula, because these fine structure lines are among the most important coolants in PDRs (Hollenbach & Tielens 1997 [54]). Nevertheless, a possible shock, resulting from the fast stellar wind that interacts with the slow expanding remnant formed in a previous stage of the stellar evolution, could also be the cause of molecules photodissociation and consequently the cause of the observed [OI] and [CII] emission. In any case, the ratio [OI] 63 μm/[CII] 158 μm can be used to exclude one of these two possible scenarios. This ratio is $\gtrsim 10$ in shocks (Hollenbach and McKee 1989 [53], Castro-Carrizo et al. 2001 [12]), which is not our case since for the nebula M1-67 this ratio is equal to 0.6. Consequently, we can conclude that a PDR is likely responsible for the [OI] and [CII] emission detected in the nebula M1-67.

In the past, PDRs were detected in some nebula that surround LBV stars. Firstly, Umana et al. (2009 [153]) discovered a PDR in the nebula around the LBV HR Car. Later on, Umana et al. (2010 [154]) observed a PDR in the nebula associated with the LBV candidate HD 168625. The analysis of *Herschel* data revealed the presence of a PDR in the nebula around the LBV WRAY 15-751 (Vamvatira-Nakou et al. 2013 [156]) and around the LBV AG Car (Vamvatira-Nakou et al. 2015 [157]).

It should be stressed here that the data were checked for possible background contamination and that there is no contribution from the background to none of the observed emission lines. The measured line fluxes come entirely from the nebula M1-67.

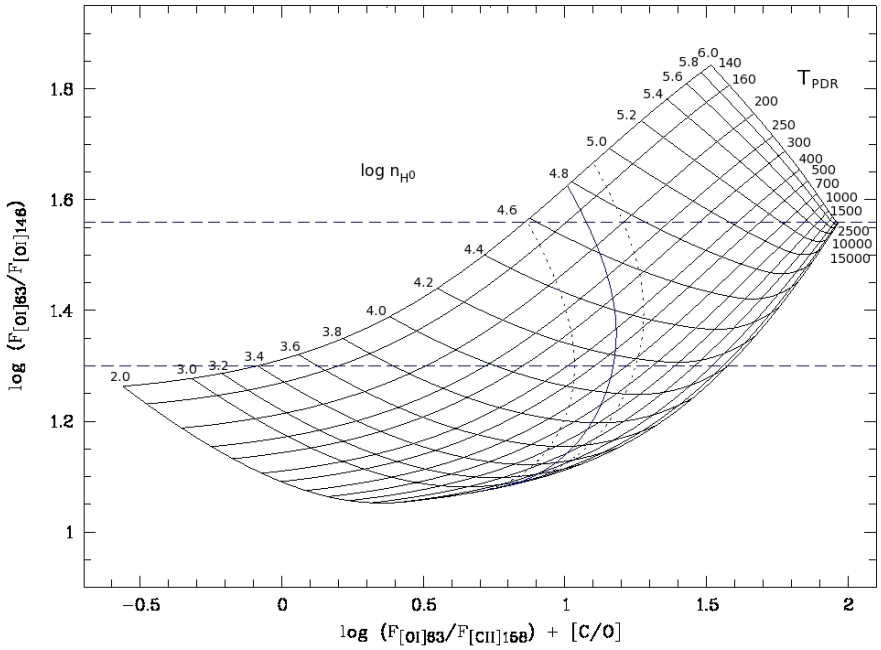

Figure 4.8: Temperature-density PDR diagnostic diagram. The grid of flux ratios $F_{[OI]63}/F_{[OI]146}$ versus $F_{[OI]63}/F^{PDR}_{[CII]158}$ was calculated by solving the level population equations for a range of temperatures and densities. $F_{[OI]63}/F^{PDR}_{[CII]158}$ is normalized to the solar abundance $(C/O)_\odot = 0.5$ so that $[C/O] \equiv \log(C/O) - \log(C/O)_\odot$. The solid line corresponds to the pressure equilibrium between the HII region and the PDR, the two dotted lines on each side accounting for the errors. The horizontal dotted lines correspond to the observational $\log(F_{[OI]63}/F_{[OI]146})$ ratio with its error.

The C/O abundance ratio can be estimated based on the PDR line fluxes and following the method described in Vamvatira-Nakou et al. (2013 [156]) that was used to disentangle the contribution of the PDR and the HII region to the flux of [CII] 158 μm. In the ionized gas region, the ratio of fractional ionization is given, as previously (see Eq. 4.3) by

$$\frac{\langle C^+ \rangle}{\langle N^+ \rangle} = \frac{F^{HII}_{[CII]158}/\varepsilon_{[CII]158}}{F_{[NII]122}/\varepsilon_{[NII]122}}\,, \tag{4.6}$$

where we define $F^{HII}_{[CII]158} = \alpha F_{[CII]158}$, with $F_{[CII]158}$ being the total flux of the [CII] 158 μm line from Table 4.2 and α a factor to be determined. Assuming that $\langle C^+ \rangle / \langle N^+ \rangle = C/N$ and calculating the emissivities using the package *nebular*, we end up with the following equation

$$\frac{F^{HII}_{[CII]158}}{F_{[NII]122}} = (0.34 \pm 0.02)\,\frac{C}{N}\,. \tag{4.7}$$

Since N/O has been estimated to be ~ 1, we have

$$\log \alpha = \log \frac{C}{O} + 0.32 \,, \tag{4.8}$$

using the observed ratio $F_{[CII]158}/F_{[NII]122} = 0.163 \pm 0.048$.

The theoretical $F_{[OI]63}/F_{[OI]146}$ ratio against the $F_{[OI]63}/F^{PDR}_{[CII]158}$ ratio normalized to the solar $(C/O)_\odot = 0.5$ abundance ratio is plotted in Fig. 4.8 so as to derive the C/O abundance ratio, as well as the temperature, T_{PDR}, and the density, n_{H^0}, of the PDR (for details see Vamvatira-Nakou et al. 2013 [156]). Assuming that there is pressure equilibrium between the ionized gas region and the PDR, we have the following relation (Tielens 2005 [146])

$$n_{H^0} k T_{PDR} \simeq 2 n_e k T_e = (8.4 \pm 3.0) \times 10^6 \text{ cm}^{-3}\text{K} \,, \tag{4.9}$$

that is used to define a locus of possible values in the diagram of Fig. 4.8.

From Fig. 4.8 we derive $\log(F_{[OI]63}/\ F^{PDR}_{[CII]158})$ + [C/O] = 1.1, where by definition [C/O] ≡ log(C/O) - $\log(C/O)_\odot$, using the constraints from Eq. 4.9 and the observed ratio $F_{[OI]63}/F_{[OI]146} = 26.8 \pm 7.9$. Finally, using also Eq. 4.8, we calculate $\alpha = 0.95 \pm 0.03$ and C/O = 0.46 ± 0.27, which is a solar abundance considering the errors. From the calculated C/O and N/O abundance ratios and considering the N/H abundance ratio of Esteban et al. (1991 [30]), the C/H abundance ratio is then $(1.3 \pm 0.9) \times 10^{-4}$. The contribution of the HII region to the [CII] 158 μm line flux is then $F^{HII}_{[CII]158} = (2.02 \pm 0.42) \times 10^{-15}$ W m^{-2} while the contribution of the PDR is $F^{PDR}_{[CII]158} = (0.11 \pm 0.07) \times 10^{-15}$ W m^{-2}, reminding that these are the fluxes of the integration on the 25 spaxels and not the fluxes of the whole nebula.

The values of the density and the temperature of the PDR of the nebula are also provided by the diagram in Fig. 4.8. Using the observed $F_{[OI]63}/F_{[OI]146}$ ratio we find $\log n_{H^0} = 4.43 \pm 0.33$ and $T_{PDR} \simeq 470 \pm 330$ K.

The total mass of hydrogen in the part of the PDR that corresponds to the 25 spaxels, M_H, can be estimated from the [CII] 158 μm line flux derived for the PDR (Tielens 2005 [146]), using the equation given in Vamvatira-Nakou et al. (2013 [156]). For the above PDR density, temperature, distance and C/H abundance, the neutral hydrogen mass is estimated to be $M_H = 0.05 \pm 0.02\ M_\odot$, which is a low limit.

4.6 DISCUSSION

In Table 4.3 the parameters of WR 124 and its nebula M1-67 are summarized. The stellar luminosity, effective temperature and distance are from the study of Marchenko et al. (2010 [82]). For the shell nebula that surrounds the star, the radii, the expansion velocity, the kinematic age, the electron density of the ionized gas, the adopted value

Star	log $L/L_\odot$	5.18 ± 0.2
	T_{eff} (K)	35800 ± 2000
	D (kpc)	3.35 ± 0.67
Shell	r_{in} (pc)	0.65
	r_{out} (pc)	1.00
	v_{exp} (km s^{-1})	50 - 150
	t_{kin} (10^3yr)	2.3 - 7.0
	n_e (cm^{-3})	600 ± 180
	T_e (K)	7000 ± 1400
	N/O	1.0 ± 0.5
	C/O	0.46 ± 0.27
	M_{dust} ($M_\odot$)	0.22 ± 0.04
	$M_{ion.gas}$ ($M_\odot$)	0.5 - 3.0

Table 4.3: Parameters of WR 124 and its nebula M1-67.

of the electron temperature, the measured abundances and masses of dust and gas are given.

Concerning the expansion velocity of the nebula, Sirianni et al. (1998 [126]) discovered a bipolar outflow with an expansion velocity of 88 km s^{-1}, apart from a spherical shell that expands with a velocity of 46 km s^{-1}. Van der Sluys and Lamers (2003 [158]) found an expansion velocity of 150 km s^{-1} for the structure of the nebula that expands freely and it is not located on the surface of the bow shock.

Consequently, considering an expansion velocity that can be between 50 and 150 km s^{-1}, the kinematic age, t_{kin}, of the nebula M1-67 can be estimated. Since the nebula extends up to 1 pc from its central star, its kinematic age is $t_{kin} = r/v_{exp}$ = (6.5×10^3) - (2.0×10^4) years. The temporal difference between the inner and the outer radius of the nebula is $(2.3 - 7.0) \times 10^4$ years.

The *Herschel* infrared images of M1-67 show a dusty clumpy shell nebula that has a radius of about 1 pc. The Hα+[NII] view of the nebula is very similar to the infrared view. The ionized gas nebula is clumpy and appears to be slightly smaller. The bright regions coincide in the optical and the infrared images. The nebula of ionized gas and dust is surrounded by a thin region of neutral gas (PDR), according to the *Herschel* spectra analysis. The nebula seems to lie in a cavity that may be the result of a mass-loss event in a previous evolutionary stage of the central star, i.e. a wind-blown bubble from the O-type progenitor (Marston 1996 [84]). Cavities have also been observed by *Herschel* around LBV stars (WRAY 15-751: Vamvatira-Nakou et al. 2013 [156], AG Car : Vamvatira-Nakou et al. 2015 [157]).

The abundance ratios calculations show that the nebula is composed of processed material. The N/O ratio, calculated in this study, is the same as the ratio measured in the nebula around the LBV WRAY 15-751 (Vamvatira-Nakou et al. 2013 [156]) and similar to the ratio of

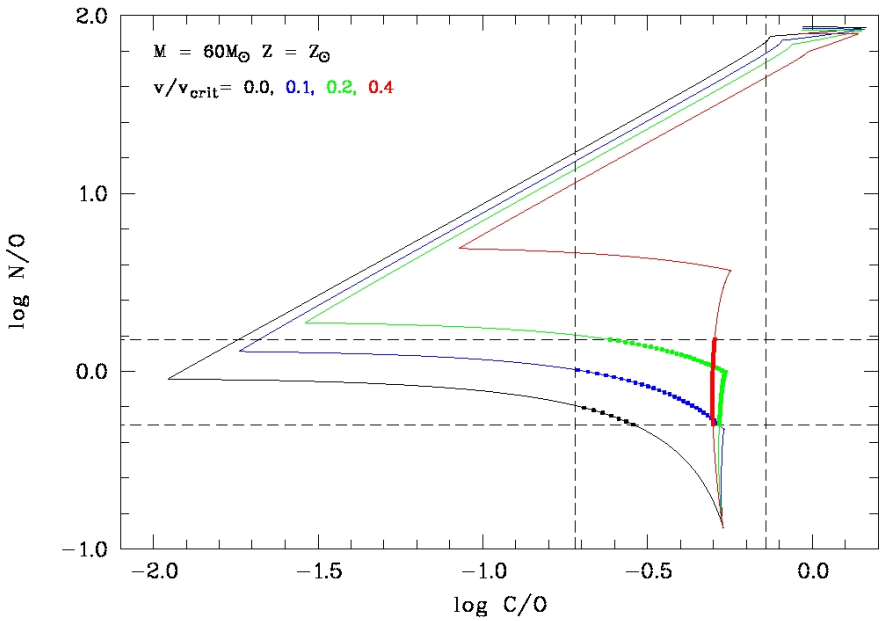

Figure 4.9: Evolution of the N/O versus the C/O surface abundance ratios for a 60 $M_\odot$ star of solar metallicity and for initial rotation rates v/v_{crit} from 0 to 0.4, using the models of Ekström et al. (2012 [29]). The dashed lines correspond to the values measured for the nebula M1-67, with their errors. The thicker lines emphasize the part of the tracks compatible with the measurements. For clarity, the tracks are stopped during the He burning phase (data point nº 195 in Ekström et al. 2012 [29]).

the nebula around the LMC LBV R127 (Smith et al. 1998 [133]). In respect to the solar N/O abundance ratio (Ekström et al. 2012 [29]), it is enhanced by a factor of 8. The 12+log(N/H) abundance of 8.45 (Esteban et al. 1991 [30]) is enhanced by a factor of about 4.5 in respect to the solar abundance. These abundance ratios are typical for LBV and WR nebulae (Smith 1997 [130]) that are known to be composed by processed material. The calculated C/O abundance ratio is essentially solar, despite its high uncertainty.

Apart from the study of Van der Sluys and Lamers (2003 [158]), other studies in the past, which are mentioned in Sect. 4.1 also concluded that the progenitor of WR 124, from which the nebula M1-67 was ejected, was a LBV star and not a RSG, even if some are based in a bipolar model. Sirianni et al. (1998 [126]) explained the two different motions found around WR 124 as two outbursts from a LBV. Grosdidier et al. (1998 [45]) concluded that this nebula is an ejection nebula resulting from a LBV phase wind. Fernández-Martín et al. (2013 [31]), to explain their findings, proposed that this nebula was ejected during a LBV phase of the central star with an initial mass between 60 and 80 $M_\odot$.

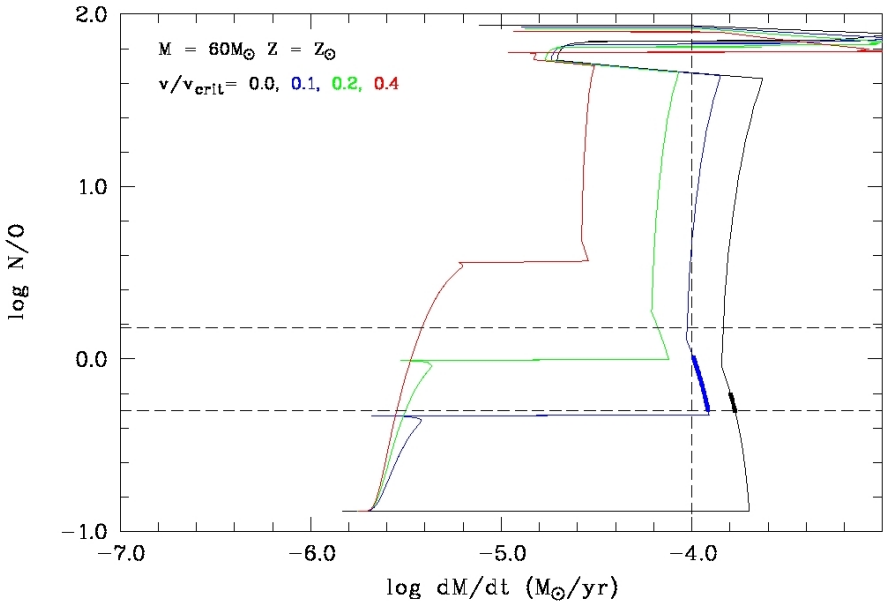

Figure 4.10: Evolution of the N/O surface abundance ratio as a function of the mass-loss rate for a 60 $M_\odot$ star of solar metallicity and for initial rotation rates Ω/Ω_{crit} from 0 to 0.4, using the models of Ekström et al. (2012 [29]). The dashed lines correspond to the calculated value of N/O for the nebula M1-67, with its errors, and the lower limit for the mass-loss rate. The thicker lines emphasize the part of the tracks compatible with the measurements. For clarity, the tracks are stopped during the He burning phase (data point n° 195 in Ekström et al. 2012 [29]).

The results of our observations analysis can be used to constrain the evolutionary phase of the central star at which the nebula was ejected with the help of the evolutionary models of Ekström et al. (2012 [29]). Even though it should be mentioned that the models of the massive stars evolution are very uncertain at the post-main-sequence evolutionary phases because they do not include any eruptive event, so that the mass-loss rate recipes are not well known (Smith 2014 [134]).

Since our integrated spectra cover only the area of the nebula that corresponds to the 25 spaxels (Fig. 4.5), we cannot estimate the total mass of the neutral gas based on the [CII] 158 μm line flux, neither the total gas mass and the corresponding mass-loss rate during the ejection without making assumptions. A typical value for the dust to gas ratio is 100 in such stellar environments. With this assumption, the total nebular mass is about 22 $M_\odot$, using the calculated dust mass. But if this ratio is lower, as in the case of the LBV WRAY 15-751 (Vamvatira-Nakou et al. 2013 [156]) were it was calculated to be 40, then we can adopt an average value for the dust to gas ratio and estimate the total mass of the nebula M1-67 to be ~ 15 $M_\odot$, with an uncertainty of about 40%.

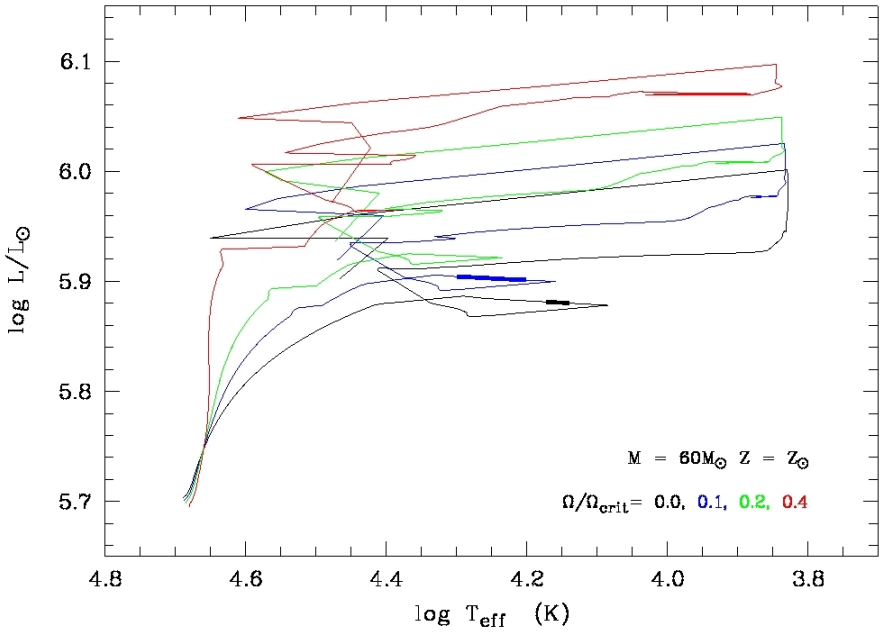

Figure 4.11: Evolutionary path in the HR diagram of a 60 $M_\odot$ star of solar metallicity and for initial rotation rates Ω/Ω_{crit} from 0 to 0.4, using the models of Ekström et al. (2012 [29]). The thicker lines emphasize the part of the tracks compatible with the N/O and C/O abundance ratios and the mass-loss rate for the nebula M1-67. For clarity, the tracks are stopped during the He burning phase (data point n^o 195 in Ekström et al. 2012 [29]).

We can consider a lower limit of the total mass-loss rate using the sum of the dust mass and the ionized gas mass. Since the latter varies with respect to the filling factor used for its calculation (Sect. 4.5), we consider the lower value (see Table 4.3). The lower limit of the mass-loss rate at the time of the nebular ejection is then calculated to be $\log \dot{M} = -4.0$, where $\dot{M}$ is in $M_\odot$ yr^{-1}, considering the higher value of the previously estimated temporal difference between the inner and the outer radius of the nebula, which corresponds to the lower expansion velocity.

This limit of the mass-loss rate along with the calculated nebular abundance ratios of N/O and C/O that are assumed to be the surface abundance ratios at the time of the nebular ejection were compared to the theoretical evolution of these parameters according to the models of Ekström et al. (2012 [29]). The stellar initial mass was chosen from the known stellar luminosity of WR 124. Models with rotation rates $\Omega/\Omega_{crit} = 0.0 - 0.4$ and solar metallicities were considered. The evolution of the C/O abundance ratio versus the N/O abundance ratio for a star of initial mass 60 $M_\odot$ is illustrated in Fig. 4.9. The calculated values for these two parameters with their errors are plotted with dashed lines, while the part of these tracks that is compatible with our results is emphasized with thicker lines. In Fig. 4.10 the evolu-

tion of the mass-loss rate versus the N/O abundance ratio is plotted. The constraints from these two diagrams are then reported to the HR diagram for a star of 60 $M_\odot$ to identify at which stage of the stellar evolution correspond our measurements (Fig. 4.11).

The results of our data analysis are compatible with the evolutionary tracks of the models of Ekström et al. (2012 [29]) for a star with an initial mass of 60 $M_\odot$, solar metallicity and low rotational velocity. For a star of 65 $M_\odot$ only the track with no rotation is compatible. For stellar masses < 60 and $\geqq 70$ no tracks that satisfy the constrains from our calculations are found.

According to the current evolutionary models, a star with initial mass of $60 - 70$ $M_\odot$ evolves towards a WR by passing only through a LBV phase, there is no RSG phase for this star (Maeder & Meynet 2010 [79]; Meynet et al. 2011 [92]). Based on the study of Groh et al. (2014 [44]) that presents a detailed analysis of the evolution of a non-rotating star with initial mass of 60 $M_\odot$, we can conclude that the nebula M1-67 was ejected from WR 124 during a LBV evolutionary phase.

Large dust grains are necessary in the dust model to reproduce the infrared SED. Large grains were also found in the dust nebula around the LBV WRAY 15-751 (Vamvatira-Nakou et al. 2013 [156]), the LBV AG Car (Vamvatira-Nakou et al. 2015 [157]) and the yellow hypergiant Hen 3-1379, which is a possible pre-LBV (Hutsemékers et al. 2013 [62]). Kochanek (2011 [69], 2014 [70]) showed in his models that during a LBV eruption, large dust grains can be produced.

4.7 CONCLUSIONS

The *Herschel* photometric and spectroscopic data analysis of the nebula M1-67 around the Wolf-Rayet star WR 124 have been presented, together with optical imaging data. The images show a clumpy dusty nebula that coincides with the gas nebula, which has a very complex structure but a global spherical morphology. The dust and the gas are mixed together and they are surrounded by a thin photodissociation region that was revealed from the infrared spectroscopic data analysis.

The dust nebula model was performed using a two-dimensional radiative transfer code. Two populations of dust grains with different grain size but with the same composition, olivines with 50/50 Fe to Mg abundance, were needed to reproduce the infrared SED. The presence of large grains is necessary for this model. Large grains were also found in circumstellar environments of other evolved massive stars.

The analysis of the emission line infrared spectrum points towards a nebula composed of enriched material, which is a common feature in the nebulae of WR and LBV that show the CNO-cycle imprints.

The calculated mass-loss rate and the abundance ratios were used to constrain the evolutionary stage of the star when the nebular ejection took place, with the help of theoretical stellar evolution models. The results of this study suggest that the ejection of the material that forms the nebula M1-67 around the Wolf-Rayet star WR 124 occured during a LBV phase of the star with intital mass of 60 $M_{\odot}$ and little rotation.

Acknowledgements. We thank Dr. Nick Cox for providing us the scanamorphos images and Prof. Gregor Rauw for his valuable comments on the manuscript. C.V.N., D.H., P.R., N.L.J.C., Y.N. and M.A.T.G. acknowledge support from the Belgian Federal Science Policy Office via the PRODEX Programme of ESA. The Liège team acknowledges also support from the FRS-FNRS (Comm. Franç. de Belgique). PACS has been developed by a consortium of institutes led by MPE (Germany) and including UVIE (Austria); KU Leuven, CSL, IMEC (Belgium); CEA, LAM (France); MPIA (Germany); INAF-IFSI/OAA/OAP/OAT, LENS, SISSA (Italy); IAC (Spain). This development has been supported by the funding agencies BMVIT (Austria), ESA-PRODEX (Belgium), CEA/CNES (France), DLR (Germany), ASI/INAF (Italy), and CICYT/MCYT (Spain). Data presented in this paper were analyzed using "HIPE", a joint development by the Herschel Science Ground Segment Consortium, consisting of ESA, the NASA Herschel Science Center, and the HIFI, PACS and SPIRE consortia. This research has made use of the NASA/IPAC Infrared Science Archive, which is operated by the Jet Propulsion Laboratory, California Institute of Technology.

4.8 APPENDIX A: EMISSION LINE FLUXES FOR EACH SPAXEL

In Table 4.4, the results of the emission line flux measurements for each spaxel are given. The first column contains the detected ions along with its wavelenght. The following columns contain the line fluxes, expressed in W/m^2, along with their errors. In every cell of the table, the spaxel numbers are mentioned (Fig. 4.5). The quoted uncertainties are the sum of the line-fitting uncertainty plus the uncertainty due to the position of the continuum.

Ion	λ (μm)	F ± ΔF (10^{-15} W m^{-2})	F ± ΔF (10^{-15} W m^{-2})	F ± ΔF (10^{-15} W m^{-2})	F ± ΔF (10^{-15} W m^{-2})	F ± ΔF (10^{-15} W m^{-2})
		spaxel 4,4	spaxel 4,3	spaxel 4,2	spaxel 4,1	spaxel 4,0
[OI]	63	-	0.047 ± 0.008	0.067 ± 0.008	-	-
[NII]	122	0.470 ± 0.026	0.551 ± 0.031	0.420 ± 0.025	0.124 ± 0.010	0.170 ± 0.012
[OI]	146	-	-	-	-	-
[CII]	158	0.068 ± 0.005	0.094 ± 0.006	0.066 ± 0.006	0.020 ± 0.003	0.028 ± 0.003
[NII]	205	0.010 ± 0.002	0.020 ± 0.003	0.020 ± 0.003	0.005 ± 0.002	-
		spaxel 3,4	spaxel 3,3	spaxel 3,2	spaxel 3,1	spaxel 3,0
[OI]	63	-	0.160 ± 0.016	0.070 ± 0.009	-	0.010 ± 0.007
[NII]	122	0.599 ± 0.032	0.764 ± 0.040	0.451 ± 0.025	0.195 ± 0.011	0.297 ± 0.018
[OI]	146	-	0.004 ± 0.001	-	-	-
[CII]	158	0.105 ± 0.008	0.128 ± 0.008	0.081 ± 0.006	0.037 ± 0.003	0.050 ± 0.004
[NII]	205	0.019 ± 0.003	0.025 ± 0.003	0.018 ± 0.002	0.006 ± 0.001	0.012 ± 0.003
		spaxel 2,4	spaxel 2,3	spaxel 2,2	spaxel 2,1	spaxel 2,0
[OI]	63	0.063 ± 0.010	0.089 ± 0.008	0.148 ± 0.011	0.012 ± 0.005	0.008 ± 0.005
[NII]	122	0.710 ± 0.038	0.769 ± 0.040	0.624 ± 0.033	0.315 ± 0.018	0.316 ± 0.018
[OI]	146	0.004 ± 0.001	-	0.007 ± 0.001	-	-
[CII]	158	0.115 ± 0.007	0.139 ± 0.009	0.110 ± 0.008	0.062 ± 0.005	0.062 ± 0.005
[NII]	205	0.024 ± 0.003	0.031 ± 0.004	0.026 ± 0.003	0.018 ± 0.002	0.019 ± 0.003
		spaxel 1,4	spaxel 1,3	spaxel 1,2	spaxel 1,1	spaxel 1,0
[OI]	63	0.031 ± 0.010	0.048 ± 0.007	0.076 ± 0.009	0.084 ± 0.010	0.052 ± 0.007
[NII]	122	0.547 ± 0.031	0.613 ± 0.034	0.740 ± 0.040	0.642 ± 0.035	0.745 ± 0.040
[OI]	146	-	-	0.004 ± 0.002	0.005 ± 0.002	0.003 ± 0.001
[CII]	158	0.084 ± 0.006	0.104 ± 0.007	0.118 ± 0.008	0.091 ± 0.006	0.112 ± 0.007
[NII]	205	0.021 ± 0.004	0.023 ± 0.003	0.029 ± 0.003	0.023 ± 0.003	0.020 ± 0.002
		spaxel 0,4	spaxel 0,3	spaxel 0,2	spaxel 0,1	spaxel 0,0
[OI]	63	-	-	0.075 ± 0.008	0.180 ± 0.015	0.063 ± 0.014
[NII]	122	0.279 ± 0.018	0.394 ± 0.023	0.751 ± 0.041	0.848 ± 0.045	0.719 ± 0.038
[OI]	146	-	-	-	0.006 ± 0.001	0.006 ± 0.001
[CII]	158	0.042 ± 0.004	0.069 ± 0.004	0.122 ± 0.009	0.139 ± 0.008	0.104 ± 0.007
[NII]	205	-	0.019 ± 0.003	0.016 ± 0.002	0.021 ± 0.002	0.018 ± 0.003

Table 4.4: Line fluxes in each spaxel. A dash indicates a poor S/N or a non-detection. The spatial configuration corresponds to the footprint of the PACS spectral field-of-view as it is displayed in Fig. 4.5.

5

CONCLUSIONS

In this thesis, the studies of the nebulae ejected by three massive evolved stars have been presented. These are the LBV stars WRAY 15-751 and AG Car and the Wolf-Rayet star WR 124. All the studies were based on new high-resolution infrared photometric and spectroscopic data taken by the *Herschel* Space Observatory. They contain calculations of the dust and the gas parameters in the nebulae aiming to shed light on the mass-loss history of the central stars. Their main results are summarized in this chapter, along with a discussion on important common aspects that have been found. Finally, future work and perspectives are briefly mentioned.

The infrared images and spectra of the circumstellar environment of the LBV WRAY 15-751, along with images in the optical, revealed a dust shell nebula, of radius 0.5 pc and width 0.35 pc, that extends outside the Hα nebula and the presence of a thin photodissociation region that surrounds the ionized gas region. Both regions are mixed with dust. Apart from this well known inner nebula, a second fainter and bigger dusty nebula, of radius 2 pc, was observed in the infrared *Herschel* images for the first time. The presence of multiple shells points to a series of episodes of extreme mass-loss. Both nebulae are lying in an empty cavity. The dust modeling of the inner nebula required Fe-rich dust to reproduce the data. Modeling of observations at different epochs showed that the infrared emission remained stable during the S Dor cycle of the central star pointing at stellar variations under constant luminosity. Each one of the nebulae contains about 0.05 $M_\odot$ of dust. The calculated abundance ratios show N enrichment and C, O depletion indicating mild N/O enrichment. In total the estimated mass ejected from the star amounts to 4 ± 2 $M_\odot$. Our measurements were used to constrain the time of the nebular ejection, considering available evolutionary models. The results suggest an ejection during the RSG evolutionary stage of a $\sim 40 M_\odot$ star with little rotation.

The infrared and optical images of the nebula around the LBV AG Car show a clumpy dusty ring nebula extending up to 1.2 pc with an inner radius of 0.4 pc. It coincides with the Hα nebula but extends further out. The nebula seems to lie in an empty cavity. The dust modeling indicates the presence of a population of small and large

dust grains. The dust mass is about 0.2 $M_\odot$. The spectroscopic analysis showed that there is neutral gas in a photodissociation region that surrounds the ionized gas region. Gas and dust are mixed together. The calculated abundance ratios point towards enrichment by processed material. Assuming a dust-to-gas ratio typical of LBV, the total mass ejected from the central star is $\sim 15 M_\odot$. The evolutionary stage of the star at the time of the nebular ejection was constrained with the help of the abundance ratios and the mass-loss rate using available evolutionary models. The conclusion is that this nebula was ejected during the cool LBV phase of a star of $\sim 55 M_\odot$ with little rotation.

The infrared images of the nebula M1-67 around the Wolf-Rayet star WR 124 revealed a clumpy dusty nebula that extends up to 1 pc. The comparison with the optical images shows that it coincides with the ionized gas nebula that has a global spherical morphology. Again the nebula is lying in an empty cavity. A thin photodissociation region surrounds the ionized gas region, as revealed from the infrared spectroscopic analysis. The dust nebula model indicated the presence of large dust grains also in this case. The nebula contains about 0.22 $M_\odot$ of dust. The calculated abundance ratios points once more towards a nebula composed of enriched material. The total ejected mass that forms the nebula is about 15 $M_\odot$, assuming a typical dust-to-gas mass ratio. The measurements used as constraints for the ejection time along with evolutionary models point to an ejection during a LBV phase of a star with initial mass of 60 $M_\odot$ and little rotation.

Overall the infrared *Herschel* imaging data allowed us to map the detailed structure of the nebulae around these massive evolved stars at the peak wavelengths at which the dust radiates. The photometry complemented the infrared SED of these objects to far-infrared wavelengths ($\lambda > 300$ μm) allowing us to study the coldest dust. The infrared *Herschel* spectroscopic data allowed us to study the gas in these circumstellar environments and calculate abundance ratios. In particular the C/O abundance ratio was calculated for the first time. The derived abundances allowed us to constrain the evolutionary path of the central star at the time of the nebula ejection.

The infrared *Herschel* images allowed us to search for multiple shells around the stars. Indeed, around the well known shell nebula around the LBV WRAY 15-751, a second bigger and fainter dusty shell was discovered. A well known example of multiple shells around a massive evolved star is the case of the LBV G79.29+0.46 after the study by Jiménez-Esteban et al. (2010 [65]) based on near-infrared and millimeter data. The presence of multiple shells indicates that the mass-loss from the central star occured in a series of episodes of extreme mass-loss rather that from a continuous stellar wind. Consequently, the detection or not of such multiplicity can help to understand the mass-loss mechanism at the origin of the nebulae.

The infrared *Herschel* images revealed that all the three nebula are lying in empty cavities that may have been formed during a previous evolutionary phase of their central star. If they are associated to the star, these cavities may correspond to a previous mass-loss event when the wind of the O-type progenitor formed a circumstellar bubble, like in the case of large WR nebulae observed by Marston (1996 [84]). To confirm this hypothesis, velocity mapping of the surrounding interstellar gas would be needed to verify that the cavity is due to the star and it is not a foreground/background structure. This would further help constrain the O star evolutionary phase.

In all the three nebulae, the spectroscopic analysis revealed the presence of neutral gas in a photodissociation region that surrounds the ionized gas region. This is in agreement with the calculations of the Strömgren radius based on the Hα and the radio flux, when available, that indicate ionization bounded nebulae. The central star of each nebulae does not ionize all the gas so that around the ionized region there is a transition region of neutral gas.

The dust models of the nebulae performed using a two - dimensional radiative transfer code indicate that large grains are necessary to reproduce the infrared SEDs. This is due to the fact that the SED is too wide to be reproduced with a single population of grains. This is also the case for the dust nebula around the yellow hypergiant Hen 3-1379 (Hutsemékers et al. 2013 [62]). Large grains ($a > 5$ μm) have also been detected in supernovae remnants (Gall et al. 2014 [34]). In the case of LBV stars, the dust production can only happen during large eruptions when the formation of a pseudo-photosphere with sufficiently low temperature takes place. Otherwise, the stellar temperature is most often too high for dust formation to happen. Kochanek (2011 [69], 2014 [70]) showed that large grains can be produced during LBV eruptions when the conditions of low pseudo-photosphere temperature and high mass-loss rate are encountered.

Concerning the epoch of the nebular ejection, this study showed that for the LBV WRAY 15-751, with an initial mass of 40 $M_\odot$, the ejection took place during a RSG phase, while for the LBV AG Car, with an initial stellar mass of 55 $M_\odot$, the ejection happened during a LBV phase. For the nebula M1-67 around the star WR 124 with an initial mass of 60 $M_\odot$, the ejection also took place during a LBV phase. In particular we rule out ejection during a BSG phase. These results are in agreement with current evolutionary scenarios in which the more massive LBVs did not have a RSG stage. Consequently, our study shows that nebular ejection can take place at different evolutionary stages of the central star depending on its initial stellar mass.

The results of the analysis for all the three nebulae points to an ejection from a central star with little rotation. Models with high rotation are not compatible with the calculated abundances and mass-loss rates. The rotation is a very important parameter that influences the

evolution of massive stars (Meynet and Maeder 2003 [91]) through the mixing of the chemical elements. Our results suggest that the ejection of the nebula does not occur because the star is rotating close to the critical velocity, as proposed by Meynet et al. (2011 [92]).

Obviously a detailed analysis of the other objects of the target list presented in the introduction, following similar methods as presented in this thesis, should be carried out. As this is a small but representative sample of nebulae around LBV and WR stars with various morphologies and stellar parameters, the comparison of the results should allow us to better understand what is the dependence of the mass-loss history as a function of the stellar parameters and how this influences the observed structure of the nebulae. In particular, is the existence of multiple shells or a single one related to the ejection of the nebula during a RSG or a cool LBV phase, or not?

Part III

APPENDIX

A

APPENDIX

A.1 Hα EMISSION

The integrated luminosity over the volume V of the nebula in the Hα recombination line is given by (Osterbrock & Ferland 2006 [107])

$$L(H\alpha) = \int_V 4\pi j_{H\alpha} \epsilon dV \, , \tag{A.1}$$

where ϵ is the filling factor that gives the fraction of the volume of the nebula filled by ionized gas. The flux received by the observer is

$$F_0(H\alpha) = \frac{L(H\alpha)}{4\pi D^2} \, , \tag{A.2}$$

where D is the distance to the nebula. By integrating over the volume, assuming a spherical uniform nebula of radius R and considering the previously given expression for the effective recombination coefficient the flux received by the observed is rewrited as

$$F_0(H\alpha) = \left(\frac{R^3}{3D^2}\right) \epsilon h\nu_{H_\alpha} n_e n_p \alpha^{eff}_{H_\alpha} \, . \tag{A.3}$$

The mass of the ionized nebula, M_i, is given by

$$M_i = (4\pi/3) R^3 \mu_+ n_p m_H \epsilon \, , \tag{A.4}$$

with m_H being the H atomic mass and μ_+ the mean ionic mass per H ion. By replacing n_e in the Eq. A.3 with $n_e = x_e n_p$ and combining it with Eq. A.4, the ionized mass can be written as

$$M_{i(H\alpha)} = \frac{4\pi\mu_+ m_H}{\sqrt{3h\nu_{H_\alpha} x_e \alpha^{eff}_{H_\alpha}}} \epsilon^{1/2} \theta^{3/2} D^{5/2} F_0^{1/2}(H\alpha) \, , \tag{A.5}$$

where θ is the angular radius of the nebula ($R = \theta D$) in Hα. By replacing the effective recombination coefficient from Eq. 1.8, the ionized mass of the nebula in solar masses is finally given by

$$M_{i(H\alpha)} = 57.9 \frac{1+4y_+}{\sqrt{1+y_+}} T_4^{(0.471+0.015\ln T_4)} \epsilon^{1/2} \theta^{3/2} D^{5/2} F_0^{1/2}(H\alpha), \tag{A.6}$$

where θ is in arcsec, D is in kpc and $F_0(H\alpha)$ is in ergs cm^{-2} s^{-1}. With $n_{H^+} = n_p$, n_{He^+} and $n_{He^{++}}$ the ionized hydrogen, ionized helium and doubly ionized helium number densities, respectively, $x_e =$

$n_e/n_p \simeq 1 + n_{He^+}/n_{H^+} = 1 + y_+$ and $\mu_+ \simeq 1 + 4\, n_{He^+}/n_{H^+} = 1 + 4y_+$ assuming $n_{He^{++}} = 0$ and denoting $y_+ = n_{He^+}/n_{H^+}$.

The number of hydrogen ionizing photons per unit time, $Q(H^0)$ that is emitted by a nebula in equilibrium is given by (Osterbrock and Ferland 2006 [107])

$$Q(H^0) = \epsilon n_e n_p \alpha_B V, \tag{A.7}$$

where α_B is the recombination coefficient given by the following equation (Draine 2011 [27]),

$$\alpha_B = 2.54 \times 10^{-13} T_4^{(-0.8163 - 0.0208 \ln T_4)}\ \mathrm{cm^3 s^{-1}}\ . \tag{A.8}$$

By combining the two previous equations, the radius, R_S that is the radius of the Strömgren sphere is given by

$$R_S = 3.17 \left(\frac{x_e}{\epsilon}\right)^{1/3} \left(\frac{n_e}{100}\right)^{-2/3} T_4^{(0.272 + 0.007 \ln T_4)} \left(\frac{Q(H^0)}{10^{49}}\right)^{1/3} \tag{A.9}$$

in units of pc. The combination of this equation with the Eq. A.3, using $R = R_S$ (ionization bounded nebula), gives the rate of emission of hydrogen-ionizing photons for a given Hα flux, in photons per second

$$Q_{0(H\alpha)} = 8.59 \times 10^{55} T_4^{(0.126 + 0.01 \ln T_4)} D^2 F_0(H_\alpha)\ . \tag{A.10}$$

Since optical Hα observations are available for all the nebulae, the ionized gas mass, the number of hydrogen ionizing photons per unit time and the Strömgren radius are calculated for each one of them, using Eq. A.6, A.10 and A.9 respectively.

A.2 RADIO EMISSION

The Plank law in the radio frequency region ($h\nu \ll kT$) can be written as

$$B_\nu = \frac{2\nu^2 kT}{c^2}\ , \tag{A.11}$$

where $B_\nu = j_\nu/\kappa_\nu$, with j_ν and κ_ν being the emission and absorption coefficients at a given frequency ν, respectively.

The radio flux density at a distance D from the nebula is

$$S_\nu = \frac{L_\nu}{4\pi D^2}\ , \tag{A.12}$$

with $L_\nu = \int_V 4\pi j_\nu \epsilon dV$. Assuming that the nebula is an optically thin sphere of radius R, the radio flux density can then be written as

$$S_\nu = \left(\frac{4\pi R^3}{3D^2}\right) \epsilon B_\nu \kappa_\nu\ . \tag{A.13}$$

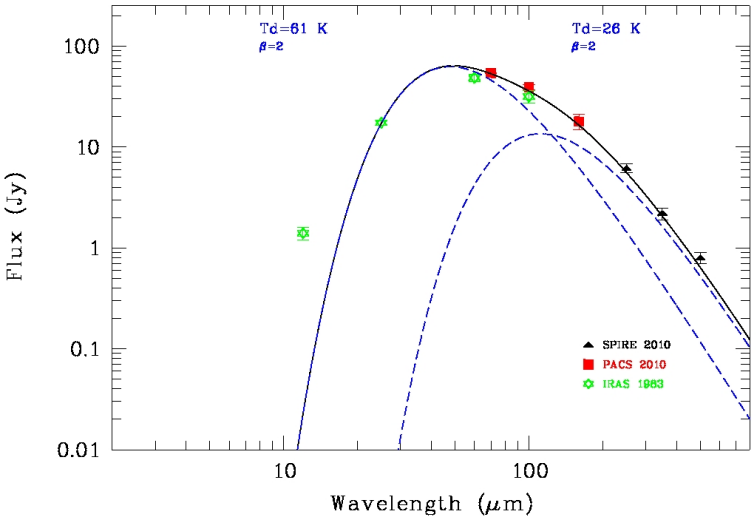

Figure A.1: Same as Fig. 4.4 but the infrared SED of the nebula M1-67 is fitted by the sum of two modified BB curves.

The continuum free-free effective absorption coefficient at radio frequencies is given by (Osterbrock and Ferland 2006 [107])

$$\kappa_\nu = 8.24 \times 10^{-2} T_e^{-1.35} \nu^{-2.1} n_+ n_e \, , \tag{A.14}$$

where the temperature T_e is in K and the frequency ν is in GHz and the ion density is equal to $n_+ = n_{H^+} + n_{He^+} = n_e$.

Considering the Eq. A.4, the ionized mass in solar masses can be expressed as

$$M_{i(radio)} = 5.82 \times 10^{-5} \frac{1+4y_+}{1+y_+} T_4^{0.175} \left(\frac{\nu}{4.9}\right)^{0.05} \epsilon^{1/2} \theta^{3/2} D^{5/2} S_\nu^{1/2} \, , \tag{A.15}$$

where ν is the radio frequency in GHz, θ is the angular radius of the ionized nebula in arcsec, D is the distance to the nebula in kpc and S_ν is the radio flux density in mJy.

By combining Eq. A.9 and A.13, the rate of emission of hydrogen-ionizing photons, for a given radio flux density is then expressed as

$$Q_{0(radio)} = 8.72 \times 10^{43} T_4^{(-0.466-0.0208 \ln T_4)} \left(\frac{\nu}{4.9}\right)^{0.1} x_e^{-1} D^2 S_\nu \, . \tag{A.16}$$

For the nebulae with radio observations available in the literature, the ionized gas mass and the number of hydrogen-ionizing photons can be calculated using Eq. A.15 and A.16 and compared to the results derived from the Hα emission analysis.

A.3 BLACK BODY FIT ON THE SED OF THE NEBULA M1-67

For the nebula M1-67, a simpler model can also be used to reproduce the infrared SED and that is the sum of two modified BB curves $F_\nu \propto$

$B_\nu(T_d)\nu^\beta$, given that the SED is considerably broad and cannot be reproduced with only one dust grain population. This fit is illustrated in Fig. A.1 and gives $T_{dust,1} = 61$ K for the first dust grain population and $T_{dust,2} = 26$ K for the second one, results that are in agreement with the results of the 2-dust fit (Sect. 4.4).

PUBLICATIONS

A. PAPERS IN REFERRED JOURNALS

Vamvatira-Nakou, C., Hutsemékers, D., Royer, P., Waelkens, C., Groenewegen, M. A. T., and Barlow, M. J.
Herschel observations of the nebula M1-67 around the Wolf-Rayet star WR 124. to be submitted to A&A, 2015

Vamvatira-Nakou, C., Hutsemékers, D., Royer, P., Cox, N. L. J., Nazé, Y., Rauw, G., Waelkens, C., and Groenewegen, M. A. T.
The Herschel view of the nebula around the luminous blue variable star AG Carinae. A&A, 578:A108, 2015

Vamvatira-Nakou, C., Hutsemékers, D., Royer, P., Nazé, Y., Magain, P., Exter, K., Waelkens, C., and Groenewegen, M. A. T.
Herschel imaging and spectroscopy of the nebula around the luminous blue variable star WRAY 15-751. A&A, 557:A20, 2013

Hutsemékers, D., Cox, N. L. J., and Vamvatira-Nakou, C.
A massive parsec-scale dust ring nebula around the yellow hypergiant Hen 3-1379. A&A, 552:L6, 2013

Groenewegen, M. A. T., Waelkens, C., Barlow, M. J., Kerschbaum, F., Garcia-Lario, P., Cernicharo, J., Blommaert, J. A. D. L., Bouwman, J., Cohen, M., Cox, N., Decin, L., Exter, K., Gear, W. K., Gomez, H. L., Hargrave, P. C., Henning, Th., Hutsemékers, D., Ivison, R. J., Jorissen, A., Krause, O., Ladjal, D., Leeks, S. J., Lim, T. L., Matsuura, M., Nazé, Y., Olofsson, G., Ottensamer, R., Polehampton, E., Posch, T., Rauw, G., Royer, P., Sibthorpe, B., Swinyard, B. M., Ueta, T., Vamvatira-Nakou, C., Vandenbussche, B., van de Steene, G. C., van Eck, S., van Hoof, P. A. M., van Winckel, H., Verdugo, E., and Wesson, R.
MESS (Mass-loss of Evolved StarS), a Herschel key program. A&A, 526:162, 2011

B. PROCEEDINGS, TALKS AND POSTERS

Vamvatira-Nakou, C., Hutsemékers, D., Royer, P., Nazé, Y., Cox, N. L. J., Exter, K., Groenewegen, M. A. T., Magain, P., and Waelkens, C.
Herschel observations of nebulae ejected by massive evolved stars (poster). "The Universe Explored by Herschel", 15-18 October 2013, ESTEC, Noordwijk, The Netherlands
Online at http://www.cosmos.esa.int/web/herschel/the-universe-explored-by-herschel

Cox, N. L. J., Hutsemékers, D., and Vamvatira-Nakou, C.
Yellow Hypergiant /Luminous Blue Variable (poster). "The Universe Explored by Herschel", 15-18 October 2013, ESTEC, Noordwijk, The Netherlands

Vamvatira-Nakou, C., Hutsemékers, D., Royer, P., Nazé, Y., Magain, P., Exter, K., Waelkens, C., and Groenewegen, M. A. T.
The Nebula around the Luminous Blue Variable WRAY 15-751 as seen by Herschel (poster). "Massive Stars: From α to Ω", 10-14 June 2013, Rhodes, Greece
Online at http://a2omega-conference.net

Vamvatira-Nakou, C., Nazé, Y., Hutsemékers, D., and Royer, P.
Massive stars' nebulae, as seen through Herschel's eyes (poster). "IAU XXVIII General Assembly, Session: The IR view of massive stars: the main sequence and beyond", 23-24 August 2012, Beijing, China

Vamvatira-Nakou, C., Hutsemékers, D., Royer, P., Nazé, Y., Magain, P., Rauw, G., Exter, K., Groenewegen, M. A. T., and Waelkens C.
Ejecta Around Evolved Massive Stars Observed with Herschel (oral contribution). "The Mass Loss Return form Stars to Galaxies" workshop, 28-30 March 2012, STScI, Baltimore, USA

Groenewegen, M. A. T., Waelkens, C., Barlow, M. J., Kerschbaum, F., Garcia-Lario, P., Cernicharo, J., Blommaert, J. A. D. L., Bouwman, J., Cohen, M., Cox, N., Decin, L., Exter, K., Gear, W. K., Gomez, H. L., Hargrave, P. C., Henning, Th., Hutsemékers, D., Ivison, R. J., Jorissen, A., Krause, O., Ladjal, D., Leeks, S. J., Lim, T. L., Matsuura, M., Nazé, Y., Olofsson, G., Ottensamer, R., Polehampton, E., Posch, T., Rauw, G., Royer, P., Sibthorpe, B., Swinyard, B. M., Ueta, T., Vamvatira-Nakou, C., Vandenbussche, B., van de Steene, G. C., van Eck, S., van Hoof, P. A. M., van Winckel, H., Verdugo, E., and Wesson, R.
Results from the Herschel Key Program MESS. in Proceedings of the conference "Why Galaxies Care about AGB Stars II: Shining Examples and Common Inhabitants", Viena, Austria, 16-20 August 2010. ASPC, 445:567, 2011

Vamvatira-Nakou, C., Royer, P., Hutsemékers, D., Nazé, Y., Rauw, G., Exter, K., Waelkens, C., and Groenewegen, M.
The Herschel view of nebulae around evolved massive stars (oral contribution). "10th Hellenic Astronomical Conference", 5-8 September 2011, Ioannina, Greece.
Online at http://www.helas.gr/conf/2011/

Vamvatira-Nakou, C., Royer, P., Hutsemékers, D., Rauw, G., Nazé, Y., Exter, K., Waelkens, C., and Groenewegen, M.
Herschel-PACS observations of Nebulae Ejected by Massive Stars. in Proceedings of the 39th Liège Astrophysical Colloquium "The multi-wavelength view of Hot, Massive Stars", Liège, Belgium, July 12-16 July 2010. BSRSL, 80:435, 2011

Vamvatira-Nakou, C., Royer, P., Hutsemékers, D., Rauw, G., Nazé, Y., Exter, K., and Waelkens, C.
Observations of Nebulae Ejected by Massive Stars with PACS (poster). "Herschel First Results Symposium (aka ESLAB 2010)", 4-7 May 2010, ESTEC, Noordwijk, The Netherlands.
Online at http://herschel.esac.esa.int/FirstResultsSymposium.shtml

BIBLIOGRAPHY

[1] E. Abrahamsson, R. V. Krems, and A. Dalgarno. *Fine–Structure Excitation of O I and C I by Impact with Atomic Hydrogen*. *ApJ*, 654: 1171–1174, January 2007.

[2] Ğ. Barinovs, M. C. van Hemert, R. Krems, and A. Dalgarno. *Fine-Structure Excitation of C^+ and Si^+ by Atomic Hydrogen*. *ApJ*, 620:537–541, February 2005.

[3] T. Barker. *Spectrophotometry of planetary nebulae. I – Physical conditions*. *ApJ*, 219:914–930, February 1978.

[4] C. A. Beichman, G. Neugebauer, H. J. Habing, P. E. Clegg, and T. J. Chester. *Infrared Astronomical Satellite (IRAS) Catalogs and Atlases, vol. 1, Explanatory Supplement*. 1988.

[5] F. Bertola. *A Planetary Nebula with WN Nucleus*. *PASP*, 76:241, August 1964.

[6] J. Blommaert, R. Siebenmorgen, A. Coulais, L. Metcalfe, M.-A. Miville-Deschênes, K. Okumura, S. Ott, A. Pollack, M. Sauvage, and J.-L. Starck. *The ISO Handbook Volume II: CAM - The ISO Camera (v 2.0)*. November 2003.

[7] M. F. Bode and A. Evans. *Infrared emission by dust grains near variable primary sources*. *A&A*, 73:113–120, March 1979.

[8] J.-C. Bouret, T. Lanz, and D. J. Hillier. *Lower mass loss rates in O–type stars: Spectral signatures of dense clumps in the wind of two Galactic O4 stars*. *A&A*, 438:301–316, Jully 2005.

[9] A. J. Cannon. *Spectra having bright lines*. *Annals of the Astron. Obs. of Harvard College*, 76:19–42, 1916.

[10] C. M. Cantalupo, J. D. Borrill, A. H. Jaffe, T. S. Kisner, and R. Stompor. *MADmap: A Massively Parallel Maximum Likelihood Cosmic Microwave Background Map–maker*. *ApJS*, 187:212–227, March 2010.

[11] E. D. Carlson and K. G. Henize. *Twenty southern peculiar emission–line stars*. *VA*, 23:213–263, 1979.

[12] A. Castro-Carrizo, V. Bujarrabal, D. Fong, M. Meixner, A. G. G. M. Tielens, W. B. Latter, and M. J. Barlow. *Low-excitation atomic gas around evolved stars. II. ISO observations of O-rich nebulae*. *A&A*, 367:674–693, February 2001.

[13] G. Chabrier. *Galactic Stellar and Substellar Initial Mass Function*. *PASP*, 809:763–795, Jully 2003.

[14] Y.-H. Chu and R. R. Treffers. *Galactic ring nebulae associated with Wolf-Rayet stars. II - M1-67: A nebula braked by the interstellar medium*. *ApJ*, 249:586–591, Octobre 1981.

[15] Y.-H. Chu, R. R. Treffers, and K. B. Kwitter. *Galactic ring nebulae associated with Wolf-Rayet stars. VIII Summary and atlas*. *ApJ*, 53: 937–944, December 1983.

[16] S. Cichowolski, S. Pineault, E. M. Arnal, and C. E. Cappa. *VLA and Effelsberg observations of the interstellar medium around the run-away star WR 124*. *A&A*, 478:443–452, February 2008.

[17] M. Cohen and M. J. Barlow. *Infrared observations of three unusual nebulae*. *ApJ*, 16:165–171, February 1975.

[18] A. J. Collison and J. D. Fix. *Axisymmetric models of circumstellar dust shells*. *ApJ*, 368:545–557, February 1991.

[19] P. S. Conti. *Basic Observational Constraints on the Evolution of Massive Stars*. *IAUs*, 105:233, 1984.

[20] I. A. Crawford and M. J. Barlow. *On the distance to M1 - 67*. *A&A*, 249:518–520, September 1991.

[21] P. A. Crowther. *Physical Properties of Wolf-Rayet Stars*. *ARA&A*, 45:177–219, September 2007.

[22] J. A. de Freitas Pacheco, A. Damineli Neto, R. D. D. Costa, and R. Viotti. *The AG Carinae nebula revisited*. *A&A*, 266:360–364, Dcember 1992.

[23] Th. de Graauw, F. P. Helmich, T. G. Phillips, J. Stutzki, E. Caux, et al. *The Herschel-Heterodyne Instrument for the Far-Infrared (HIFI)*. *A&A*, 518:L6, Jully 2010.

[24] D. de Winter, M. R. Perez, J. Y. Hu, and P. S. The. *A study of the optical and ultraviolet spectral characteristics and of the circumstellar material around the new luminous blue variable WRA 751*. *A&A*, 257:632–640, April 1992.

[25] M. A. Dopita, J. F. Bell, Y.-H. Chu, and T. A. Lozinskaya. *An atlas of the interstellar environment of Wolf-Rayet stars in the Magellanic clouds*. *ApJS*, 93:455–463, August 1994.

[26] J. Dorschner, B. Begemann, T. Henning, C. Jaeger, and H. Mutschke. *Steps toward interstellar silicate mineralogy. II. Study of Mg–Fe–silicate glasses of variable composition*. *A&A*, 300:503–520, August 1995.

[27] B. T. Draine. *Physics of the Interstellar and Intergalactic Medium*. Princeton University Press, Princeton, New Jersey, USA, 2011.

[28] R. A. Duncan and S. M. White. *Radio images of four luminous blue variable stars*. *MNRAS*, 330:63–68, February 2002.

[29] S. Ekström, C. Georgy, P. Eggenberger, G. Meynet, N. Mowlavi, A. Wyttenbach, A. Granada, T. Decressin, R. Hirschi, U. Frischknecht, C. Charbonnel, and A. Maeder. *Grids of stellar models with rotation. I. Models from 0.8 to 120 $M_\odot$ at solar metallicity (Z = 0.014)*. *A&A*, 537:A146, January 2012.

[30] C. Esteban, J. M. Vilchez, A. Manchado, and L. J. Smith. *Spatially resolved spectroscopy of WR ring nebulae. II - M1-67*. *A&A*, 244:205–216, April 1991.

[31] A. Fernández-Martín, J. M. Vílchez, E. Pérez-Montero, A. Candian, S. F. Sánchez, D. Martín-Gordón, and A. Riera. *Integral field spectroscopy of M1-67. A Wolf-Rayet nebula with luminous blue variable nebula appearance*. *A&A*, 554:A104, June 2013.

[32] A. W. Fullerton, D. L. Massa, and R. K. Prinja. *The Discordance of Mass–Loss Estimates for Galactic O–Type Stars*. *ApJ*, 637:1025–1039, February 2006.

[33] H.-P. Gail, W. J. Duschl, A. S. Ferrarotti, and K. Weis. *Dust formation in LBV envelopes*. *ASPC*, 332:317–319, September 2005.

[34] C. Gall, J. Hjorth, D. Watson, E. Dwek, J. R. Maund, O. Fox, G. Leloudas, Malesani D., and A. C. Day-Jones. *Rapid formation of large dust grains in the luminous supernova 2010jl*. *Nature*, 511: 326–329, Jully 2014.

[35] P. Garcia-Lario, A. Riera, and A. Manchado. *A spectroscopic analysis of the Luminous Blue Variable candidate WRA 751*. *A&A*, 334: 1007–1015, June 1998.

[36] J. R. Goicoechea, N. J. RodrÃguez-FernÃ¡ndez, and J. Cernicharo. *The Far-Infrared Spectrum of the Sagittarius B2 Region: Extended Molecular Absorption, Photodissociation, and Photoionization*. *ApJ*, 600:214–233, January 2004.

[37] N. Grevesse, M. Asplund, A. J. Sauval, and P. Scott. *The chemical composition of the Sun*. *Ap&SS*, 328:179–183, Jully 2010.

[38] M. J. Griffin, A. Abergel, A. Abreu, P. A. R. Ade, P. André, and J.-L. Augueres. *The Herschel-SPIRE instrument and its in-flight performance*. *A&A*, 518:L3, Jully 2010.

[39] M. A. T. Groenewegen, C. Waelkens, M. J. Barlow, F. Kerschbaum, P. Garcia-Lario, J. Cernicharo, J. A. D. L. Blommaert,

J. Bouwman, M. Cohen, N. Cox, L. Decin, K. Exter, W. K. Gear, H. L. Gomez, P. C. Hargrave, Th. Henning, D. Hutsemékers, R. J. Ivison, A. Jorissen, O. Krause, D. Ladjal, S. J. Leeks, T. L. Lim, M. Matsuura, Y. Nazé, G. Olofsson, R. Ottensamer, E. Polehampton, T. Posch, G. Rauw, P. Royer, B. Sibthorpe, B. M. Swinyard, T. Ueta, C. Vamvatira-Nakou, B. Vandenbussche, G. C. van de Steene, S. van Eck, P. A. M. van Hoof, H. van Winckel, E. Verdugo, and R. Wesson. *MESS (Mass-loss of Evolved StarS), a Herschel key program*. *A&A*, 526:162, February 2011.

[40] M. A. T. Groenewegen, C. Waelkens, M. J. Barlow, F. Kerschbaum, P. Garcia-Lario, J. Cernicharo, J. A. D. L. Blommaert, J. Bouwman, M. Cohen, N. Cox, L. Decin, K. Exter, W. K. Gear, H. L. Gomez, P. C. Hargrave, Th. Henning, D. Hutsemékers, R. J. Ivison, A. Jorissen, O. Krause, D. Ladjal, S. J. Leeks, T. L. Lim, M. Matsuura, Y. Nazé, G. Olofsson, R. Ottensamer, E. Polehampton, T. Posch, G. Rauw, P. Royer, B. Sibthorpe, B. M. Swinyard, T. Ueta, C. Vamvatira-Nakou, B. Vandenbussche, G. C. van de Steene, S. van Eck, P. A. M. van Hoof, H. van Winckel, E. Verdugo, and R. Wesson. *Results from the Herschel Key Program MESS*. *ASPC*, 445:567, September 2011.

[41] J. H. Groh, D. J. Hillier, A. Damineli, P. A. Whitelock, F. Marang, and C. Rossi. *On the Nature of the Prototype Luminous Blue Variable Ag Carinae. I. Fundamental Parameters During Visual Minimum Phases and Changes in the Bolometric Luminosity During the S-Dor Cycle*. *ApJ*, 698:1698–1720, June 2009.

[42] J. H. Groh, D. J. Hillier, and A. Damineli. *On the Nature of the Prototype Luminous Blue Variable AG Carinae. II. Witnessing a Massive Star Evolving Close to the Eddington and Bistability Limits*. *ApJ*, 736:46, Jully 2011.

[43] J. H. Groh, G. Meynet, C. Georgy, and S. Ekström. *Fundamental properties of core-collapse supernova and GRB progenitors: predicting the look of massive stars before death*. *A&A*, 558:A131, October 2013.

[44] J. H. Groh, G. Meynet, S. Ekström, and C. Georgy. *The evolution of massive stars and their spectra. I. A non-rotating 60 $M_{\odot}$ star from the zero-age main sequence to the pre-supernova stage*. *ApJ*, 564:30, April 2014.

[45] Y. Grosdidier, A. F. J. Moffat, G. Joncas, and A. Acker. *HST WFPC2/Hα Imagery of the Nebula M1-67: A Clumpy LBV Wind Imprinting Itself on the Nebular Structure?* *ApJ*, 506:L127–L131, October 1998.

[46] Y. Grosdidier, A. F. J. Moffat, G. Joncas, and A. Acker. *The Ejected Nebula M1-67: Interface Between Clumpy Stellar Winds and the Clumpy Interstellar Medium*. *ASPC*, 168:453, 1999.

[47] Y. Grosdidier, A. F. J. Moffat, S. Blais-Ouellette, G. Joncas, and A. Acker. *Hubble Space Telescope Imagery and Canada-France-Hawaii Telescope Fabry-Perot Two-dimensional Spectroscopy in Hα of the Ejected Nebula M1-67: Turbulent Status*. *ApJ*, 562:753–769, December 2001.

[48] V. V. Gvaramadze, A. Y. Kniazev, and S. Fabrika. *Revealing evolved massive stars with Spitzer*. *MNRAS*, 405:1047–1060, December 2010.

[49] W. R. Hamann, L. Koesterke, and U. Wessolowski. *Spectra Analysis of the Galactic Wolf-Rayet Stars - a Comprehensive Study of the WN Class*. *A&A*, 274:397, Jully 1993.

[50] C. Heiles. *On the origin of the diffuse C(+) 158 micron line emission*. *ApJ*, 436:720–727, December 1994.

[51] R. H. Hildebrand. *The Determination of Cloud Masses and Dust Characteristics from Submillimetre Thermal Emission*. *QJRAS*, 24: 267, September 1983.

[52] N. M. Hoekzema, H. J. G. L. M. Lamers, and A. M. van Genderen. *The distance and reddening of stars near the Luminous Blue Variable AG Carinae*. *A&A*, 257:118–127, April 1992.

[53] D. Hollenbach and C. F. McKee. *Molecule formation and infrared emission in fast interstellar shocks. III - Results for J shocks in molecular clouds*. *ApJ*, 342:306–336, Jully 1989.

[54] D. J. Hollenbach and A. G. G. M. Tielens. *Dense Photodissociation Regions (PDRs)*. *ARA&A*, 35:179–216, 1997.

[55] J. Y. Hu, D. de Winter, P. S. The, and M. R. Perez. *WRA 751, a candidate for a new luminous blue variable*. *A&A*, 227:17–20, January 1990.

[56] R. M. Humphreys. *What are LBVs? - Their characteristics and role in the upper H-R diagram*. *in Physics of luminous blue variables, Proceedings of the 113th IAU Colloquium, Val Morin, Canada*, pages 3–12, 1989.

[57] R. M. Humphreys and K. Davidson. *Studies of luminous stars in nearby galaxies. III - Comments on the evolution of the most massive stars in the Milky Way and the Large Magellanic Cloud*. *ApJ*, 232: 409–420, September 1979.

[58] R. M. Humphreys, H. J. G. L. M. Lamers, N. Hoekzema, and A Cassatella. *The distance and evolutionary phase of the luminous blue variable AG CAR*. *A&A*, 218:17–19, Jully 1989.

[59] D. Hutsemékers. *Evidence for violent ejection of nebulae from massive stars*. *A&A*, 281:L81–L84, January 1994.

[60] D. Hutsemékers. *Dust in LBV-type Nebulae*. *ASPC*, 120:316, 1997.

[61] D. Hutsemékers and E. van Drom. *The nature of the nebula associated with the luminous blue variable star WRA 751*. *A&A*, 251: 620–624, November 1991.

[62] D. Hutsemékers, N. L. J. Cox, and C. Vamvatira-Nakou. *A massive parsec-scale dust ring nebula around the yellow hypergiant Hen 3-1379*. *A&A*, 552:L6, April 2013.

[63] D. Ishihara, T. Onaka, H. Kataza, A. Salama, C. Alfageme, and A. Cassatella. *The AKARI/IRC mid-infrared all-sky survey*. *A&A*, 514:A1, Mai 2010.

[64] Melnick J., Dekker H., and D'Odorico S. *EFOSC, ESO operating manual 4*. 1989.

[65] F. M. Jiménez-Esteban, J. R. Rizzo, and A. Palau. *Multiple Shells Around G79.29+0.46 Revealed from Near-IR to Millimeter Data*. *ApJ*, 713:429–439, April 2010.

[66] H. M. Johnson. *IUE low-dispersion spectra of four luminous stars in symmetric nebulae*. *ApJ*, 235:66–75, January 1980.

[67] M. J. Kaufman, M. G. Wolfire, D. J. Hollenbach, and M. L. Luhman. *Far-Infrared and Submillimeter Emission from Galactic and Extragalactic Photodissociation Regions*. *ApJ*, 527:795–813, December 1999.

[68] M. F. Kessler, J. A. Steinz, M. E. Anderegg, J. Clavel, G. Drechsel, P. Estaria, J. Faelker, J. R. Riedinger, A. Robson, B. G. Taylor, and S. Ximénez de Ferrán. *The Infrared Space Observatory (ISO) mission*. *A&A*, 315:27–31, November 1996.

[69] C. S. Kochanek. *The Astrophysical Implications of Dust Formation during the Eruptions of Hot, Massive Stars*. *ApJ*, 743:73, December 2011.

[70] C. S. Kochanek. *Dust Formation in the Presence of Photons I: Evaporation Rates for Small Dust Grains*. *arXiv:1407.7856*, 2014.

[71] H. J. G. L. M. Lamers, N. Hoekzema, N. R. Trams, A. Cassatella, and M. Barylak. *AG Carinae : Variability, Extinction, Distance and Luminosity*. *in Physics of luminous blue variables, Proceedings of the 113th IAU Colloquium, Val Morin, Canada*, page 271, 1989.

[72] H. J. G. L. M. Lamers, A. Nota, N. Panagia, L. J. Smith, and N. Langer. *Chemical Composition and Origin of Nebulae around Luminous Blue Variables*. *ApJ*, 551:764–780, April 2001.

[73] Laureijs, R. J., U. Klaas, P. J. Richards, B. Schulz, and P. Ábrahám. *The ISO Handbook, Volume IV - PHT - The Imaging Photo-Polarimeter*. European Space Agency, 2003.

[74] C. Leitherer, A. Damineli Neto, and W. Schmutz. *AG Carinae and the LBV Phenomenon*. *ASPC*, 22:366, 1992.

[75] C. Leitherer, R. Allen, B. Altner, A. Damineli, L. Drissen, T. Idiart, O. Lupie, A. Nota, C. Robert, W. Schmutz, and S. N. Shore. *Geometry and physical conditions in the stellar wind of AG Carinae*. *ApJ*, 428:292–318, June 1994.

[76] X.-W. Liu, M. J. Barlow, M. Cohen, I. J. Danziger, S.-G. Luo, J. P. Baluteau, P. Cox, R. J. Emery, T. Lim, and D. Péquignot. *ISO LWS observations of planetary nebula fine-structure lines*. *MNRAS*, 323:343–361, Mai 2001.

[77] R. Lorente, T. Onaka, Y. Ita, T. Ohyama, Y. amd Tanabe, and C. Pearson. *AKARI IRC Data User Manual Version 1.4*. 2008.

[78] A. Maeder and P. S. Conti. *Massive Star Populations in Nearby Galaxies*. *ARA&A*, 32:227–275, 1994.

[79] A. Maeder and G. Meynet. *Evolution of massive stars with mass loss and rotation*. *New Astron. Rev.*, 54:32–38, Mars 2010.

[80] P. Magain, F. Courbin, and S. Sohy. *Deconvolution with Correct Sampling*. *ApJ*, 494:472–477, February 1998.

[81] S. Malhotra, M. J. Kaufman, D. Hollenbach, G. Helou, R. H. Rubin, J. Brauher, D. Dale, N. Y. Lu, S. Lord, G. Stacey, A. Contursi, D. A. Hunter, and H. Dinerstein. *Far-Infrared Spectroscopy of Normal Galaxies: Physical Conditions in the Interstellar Medium*. *ApJ*, 561:766–786, November 2001.

[82] S. V. Marchenko, A. F. J. Moffat, and P. A. Crowther. *Population I Wolf-Rayet Runaway Stars: The Case of WR124 and its Expanding Nebula M1-67*. *ApJ*, 724:L90–L94, November 2010.

[83] A. P. Marston. *Far-infrared observations and the structure of Wolf-Rayet ring nebulae*. *ApJ*, 366:181–191, January 1991.

[84] A. P. Marston. *Large IRAS Shells Around Galactic Wolf-Rayet Stars and the O Star Phase of Wolf-Rayet Evolution*. *AJ*, 112:2828, December 1996.

[85] A. P. Marston. *A Survey of Nebulae around Galactic Wolf-Rayet Stars in the Southern Sky. III. Survey Completion and Conclusions*. *ApJ*, 475:188–193, January 1997.

[86] J. S. Mathis, W. Rumpl, and K. H. Nordsieck. *The size distribution of interstellar grains*. *ApJ*, 217:425–433, October 1977.

[87] J. S. Mathis, J. P. Cassinelli, K. A. van der Hucht, T. Prusti, P. R. Wesselius, and P. M. Williams. *An infrared study of three Wolf-Rayet ring nebulae*. *ApJ*, 384:197–211, January 1992.

[88] Hyland A. R. McGregor P. J. and Hillier D. J. *Atomic and molecular line emission from early-type high-luminosity stars*. *ApJ*, 324: 1071–1098, January 1988.

[89] M. Meixner, T. Ueta, M. Bobrowsky, and A. Speck. *Two Subclasses of Proto-Planetary Nebulae: Model Calculations*. *ApJ*, 571: 936–946, June 2002.

[90] P. W. Merrill. *A Wolf-Rayet Star with High Velocity*. *PASP*, 50:350, December 1938.

[91] G. Meynet and A. Maeder. *Stellar evolution with rotation. X. Wolf-Rayet star populations at solar metallicity*. *A&A*, 404:975–990, June 2003.

[92] G. Meynet, C. Georgy, R. Hirschi, A. Maeder, P. Massey, N. Przybilla, and M.-F. Nieva. *Red Supergiants, Luminous Blue Variables and Wolf-Rayet stars: the single massive star perspective*. *BSRSL*, 80: 266–278, January 2011.

[93] G. E. Miller and J. M. Scalo. *The initial mass function and stellar birthrate in the solar neighborhood*. *ApJS*, 41:513–547, November 1979.

[94] R. Minkowski. *New Emission Nebulae*. *PASP*, 58:305, October 1946.

[95] P. M. Mitra and R. J. Dufour. *Spectrophotometry of the shell around AG Carinae*. *MNRAS*, 242:98–108, January 1990.

[96] S. Molinari, B. Swinyard, J. Bally, M. Barlow, J.-P. Bernard, et al. *Hi-GAL: The Herschel Infrared Galactic Plane Survey*. *PASP*, 122: 314–325, March 2010.

[97] M. Moshir, G. Kopman, and T. A. O. Conrow. *IRAS Faint Source Survey, Explanatory supplement version 2*. 1992.

[98] H. Murakami, H. Baba, P. Barthel, D. L. Clements, M. Cohen, et al. *The Infrared Astronomical Mission AKARI*. *PASJ*, 59:369, October 2007.

[99] G. Neugebauer, H. J. Habing, R. van Duinen, H. H. Aumann, B. Baud, et al. *The Infrared Astronomical Satellite (IRAS) mission*. *ApJ*, 278:1–6, March 1984.

[100] A. Nota. *Variable and Non-spherical Stellar Winds in Luminous Hot Stars*. *IAU Colloq. No 169, Lecture Notes in Physics*, 523:62–70, 1999.

[101] A. Nota, C. Leitherer, M. Clampin, P. Greenfield, and D. A. Golimowski. *Mapping AG Carinae - Long-slit spectroscopy and coronographic imaging of the nebula and jet*. *ApJ*, 398:621–631, October 1992.

[102] A. Nota, M. Clampin, M. Sirianni, P. Greenfield, and D. A. Golimowski. *The inner M1-67 nebula: coronagraphic imaging and echelle observations*. *IAU Symp.*, 163:78, 1995.

[103] A. Nota, M. Livio, M. Clampin, and R. Schulte-Ladbeck. *Nebulae around Luminous Blue Variables: A Unified Picture*. *ApJ*, 448: 788, August 1995.

[104] A. Nota, M. Clampin, G. GarcÃa-Segura, C. Leitherer, and N. Langer. *Large and Small Scale Structures in the AG Carinae Nebula from WFPC2/HST Observations*. *in Science with the Hubble Space Telescope - II. Proceedings, Paris, France*, page 398, 1996.

[105] A. Nota, A. Pasquali, A. P. Marston, H. J. G. L. M. Lamers, M. Clampin, and R. E. Schulte-Ladbeck. *Detection of* ^{1}2*CO J=1–>o and J=2–>1 Emission from the Luminous Blue Variable AG Carinae: Circumstellar Envelope or Disk?* *AJ*, 124:2920–2930, November 2002.

[106] V. Ossenkopf, T. Henning, and J. S. Mathis. *Constraints on cosmic silicates*. *A&A*, 261:567–578, August 1992.

[107] D. E. Osterbrock and G. J. Ferland. *Astrophysics of Gaseous Nebulae and Active Galactic Nuclei*. University Sciences Books, Mill Valley, California, USA, 2006.

[108] S. Ott. *The Herschel Data Processing System - HIPE and Pipelines - Up and Running Since the Start of the Mission*. *ASPC*, 434:139, December 2010.

[109] N. Panagia. *Some Physical parameters of early-type stars*. *AJ*, 78: 929–934, November 1973.

[110] F. Paresce and A. Nota. *Dust in the circumstellar environment of AG Carinae - Evidence for a bipolar and helical structure*. *ApJ*, 341: 83–85, June 1989.

[111] A. Pasquali, F. Comerón, and A. Nota. *The birth-cluster of the galactic luminous blue variable WRA 751*. *A&A*, 448:589, March 2006.

[112] L. Perek. *Photometry of southern planetary nebulae*. *Bull. of the Astron. Inst. of Czechoslovakia*, 22:103, 1971.

[113] G. L. Pilbratt, J. R. Riedinger, T. Passvogel, G. Crone, D. Doyle, U. Gageur, A. M. Heras, C. Jewell, L. Metcalfe, S. Ott, and M. Schmidt. *Herschel Space Observatory. An ESA facility for far-infrared and submillimetre astronomy*. *A&A*, 518:L1, Jully 2010.

[114] P. Pismis and E. Recillas-Cruz. *Internal motions in H II regions. V - The planetary nebula M1-67, possibly an H II region*. *Rev. Mex. de Astron. y Astrof.*, 4:271–277, January 1979.

[115] A. Poglitsch, C. Waelkens, N. Geis, H. Feuchtgruber, B. Vandenbussche, et al. *The Photodetector Array Camera and Spectrometer (PACS) on the Herschel Space Observatory*. *A&A*, 518:L2, Jully 2010.

[116] J. Puls, N. Markova, and S. Scuderi. *Stellar Winds from Massive Stars - What are the REAL Mass-Loss Rates?* *ASPC*, 388:101, June 2008.

[117] Humphreys R.M. and Davidson K. *The luminous blue variables: Astrophysical geysers*. *PASP*, 106:1025–1051, October 1994.

[118] M. S. Roberts. *The galactic distribution of the Wolf-Rayet stars*. *AJ*, 67:79–85, February 1962.

[119] H. Roussel. *Scanamorphos: A Map-making Software for Herschel and Similar Scanning Bolometer Arrays*. *PASP*, 125:1126–1163, September 2013.

[120] R. H. Rubin. *The effect of density variations on elemental abundance ratios in gaseous nebulae*. *ApJS*, 69:897–910, April 1989.

[121] R. H. Rubin, J. P. Simpson, S. D. Lord, S. W. J. Colgan, E. F. Erickson, and M. R. Haas. *Nebular properties from far-infrared spectrosopy*. *ApJ*, 420:772–782, January 1994.

[122] E. E. Salpeter. *The Luminosity Function and Stellar Evolution*. *ApJ*, 121:161, January 1955.

[123] R. E. Schulte-Ladbeck, G. C. Clayton, D. J. Hillier, T. J. Harries, and I. D. Howarth. *The axisymmetric stellar wind of AG Carinae*. *ApJ*, 429:846–856, July 1994.

[124] S. Sharpless. *A Catalogue of H II Regions*. *ApJS*, 4:257, December 1959.

[125] R. A. Shaw and R. J. Dufour. *Software for the Analysis of Emission Line Nebulae*. *PASP*, 107:896, September 1995.

[126] M. Sirianni, A. Nota, A. Pasquali, and M. Clampin. *A bipolar outflow in the M 1-67 nebula around the Wolf-Rayet star WR 124*. *A&A*, 335:1029–1039, Jully 1998.

[127] L. F. Smith. *Classification and Distribution of WR Stars and an Interpretation of the WN Sequence. in IAU Symposium No. 49, ed. M. K. V. Bappu, J. Sahade (Dordrecht: Reidel)*, page 15, 1973.

[128] L. F. Smith and L. H. Aller. *On the Classification of Emission-Line Spectra of Planetary Nuclei*. *ApJ*, 157:1245, September 1969.

[129] L. J. Smith. *The Dynamics of the AG CAR Ring Nebula*. *IAUS*, 143: 385, 1991.

[130] L. J. Smith. *Abundance Determinations in LBV Nebulae*. *ASPC*, 120:310, 1997.

[131] L. J. Smith, P. A. Crowther, and R. K. Prinja. *A study of the luminous blue variable candidate He 3-519 and its surrounding nebula*. *A&A*, 281:833–854, January 1994.

[132] L. J. Smith, M. P. Stroud, C. Esteban, and J. M. Vilchez. *The AG Carinae nebula: abundant evidence for a red supergiant progenitor? MNRAS*, 290:265–275, September 1997.

[133] L. J. Smith, A. Nota, A. Pasquali, C. Leitherer, M. Clampin, and P. A. Crowther. *Ejected Nebulae as Probes of the Evolution of Massive Stars in the Large Magellanic Cloud*. *ApJ*, 503:278–296, August 1998.

[134] N. Smith. *Mass Loss: Its Effect on the Evolution and Fate of High-Mass Stars*. *ARA&A*, 52:487–528, August 2014.

[135] N. Smith, J. S. Vink, and A. de Koter. *The Missing Luminous Blue Variables and the Bistability Jump*. *ApJ*, 615:475–484, November 2004.

[136] J. Solf and U. Carsenty. *M1-67 - A wind-blown bubble carried along by the high-velocity WR star 209 BAC*. *A&A*, 116:54–59, December 1982.

[137] O. Stahl. *Direct imagery of circumstellar shells around Ofpe/WN9 stars in the galaxy and in the LMC*. *A&A*, 182:229–236, August 1987.

[138] O. Stahl. *The relationship of the variable stars AG CAR and HDE 269852 to the Ofpe/WN9 objects*. *A&A*, 164:321–327, August 1986.

[139] O. Stahl and B. Wolf. *New observational results of the LMC-S DOR variable R 127 during outburst*. *A&A*, 154:243–248, January 1986.

[140] O. Stahl, I. Jankovics, J. Kovács, B. Wolf, W. Schmutz, A. Kaufer, Th. Rivinius, and Th. Szeifert. *Long-term spectroscopic monitoring of the Luminous Blue Variable AG Carinae*. *A&A*, 375:54–69, August 2001.

[141] C. Sterken, A. Jones, B. Vos, I. Zegelaar, A. M. van Genderen, and M. de Groot. *On the Cyclicity of the S Dor Phases in AG Carinae*. *IBVS*, 4401:1, November 1996.

[142] C. Sterken, A. M. van Genderen, A. Plummer, and A. F. Jones. *Wra 751, a luminous blue variable developing an S Doradus cycle*. *A&A*, 484:463–467, June 2008.

[143] R. B. Stothers and C.-W. Chin. *Evolution of Massive Stars into Luminous Blue Variables and Wolf-Rayet Stars for a Range of Metallicities: Theory versus Observation*. *ApJ*, 468:842, September 1996.

[144] Müller T., Okumura K., and Klaas U. *PACS Photometer Passbands and Colour Correction Factors for Various Source SEDs*. 2011.

[145] A. D. Thackeray. *Some southern stars involved in nebulosity*. *MNRAS*, 110:524, 1950.

[146] A. G. G. M. Tielens. *The Physics and Chemistry of the Interstellar Medium*. Cambridge University Press, New York, USA, 2005.

[147] A. G. G. M. Tielens and D. Hollenbach. *Photodissociation regions. I - Basic model. II - A model for the Orion photodissociation region*. *ApJ*, 291:722–754, April 1985.

[148] J.A. Toalá and S.J. Arthur. *Radiation-hydrodynamic Models of the Evolving Circumstellar Medium around Massive Stars*. *ApJ*, 737:100, August 2011.

[149] D. Tody. *The IRAF Data Reduction and Analysis System*. *in Instrumentation in Astronomy VI - Proceedings, Tucson, AZ,*, 627:733, January 1986.

[150] D. Tody. *IRAF in the Nineties*. *ASPC*, 52:173, January 1993.

[151] Y. G. Tsamis, M. J. Barlow, X.-W. Liu, I. J. Danziger, and P. J. Storey. *A deep survey of heavy element lines in planetary nebulae - I. Observations and forbidden-line densities, temperatures and abundances*. *MNRAS*, 345:186, January 2003.

[152] T. Ueta and M. Meixner. *2-DUST: A Dust Radiative Transfer Code for an Axisymmetric System*. *ApJ*, 586:1338–1355, April 2003.

[153] G. Umana, C. S. Buemi, C. Trigilio, J. L. Hora, G. G. Fazio, and P. Leto. *The Dusty Nebula Surrounding HR Car: A Spitzer View*. *ApJ*, 694:697–703, March 2009.

[154] G. Umana, C. S. Buemi, C. Trigilio, P. Leto, and J. L. Hora. *Spitzer, Very Large Telescope, and Very Large Array Observations of the Galactic Luminous Blue Variable Candidate HD 168625*. *ApJ*, 718:1036–1045, August 2010.

[155] C. Vamvatira-Nakou, P. Royer, D. Hutsemékers, G. Rauw, Y. Nazé, K. Exter, C. Waelkens, and M. Groenewegen. *Herschel-PACS observations of Nebulae Ejected by Massive Stars*. *BSRSL*, 80: 435–439, January 2011.

[156] C. Vamvatira-Nakou, Hutsemékers, P. Royer, Y. Nazé, P. Magain, K. Exter, C. Waelkens, and M. A. T. Groenewegen. *Herschel imaging and spectroscopy of the nebula around the luminous blue variable star WRAY 15-751*. *A&A*, 557:A20, September 2013.

[157] C. Vamvatira-Nakou, Hutsemékers, P. Royer, N. L. J. Cox, Y. Nazé, G. Rauw, C. Waelkens, and M. A. T. Groenewegen. *The Herschel view of the nebula around the luminous blue variable star AG Carinae*. *A&A*, 578:A108, June 2015.

[158] M. V. van der Sluys and H. J. G. L. M. Lamers. *The dynamics of the nebula M1-67 around the run-away Wolf-Rayet star WR 124*. *A&A*, 398:181–194, January 2003.

[159] A. M. van Genderen. *S Doradus variables in the Galaxy and the Magellanic Clouds*. *A&A*, 366:508–531, February 2001.

[160] A. M. van Genderen, P. S. The, T. Augusteijn, E. C. Engelsman, E. W. van der Grift, J. J. Prein, R. L. Remijn, F. W. M. Steeman, and N. van Weeren. *An investigation of the micro-variations of highly luminous OBA stars (Alpha CYG variables). VI - The characteristics of the S DOR type stars R71 and AG CAR*. *A&AS*, 74: 453–466, September 1988.

[161] A. M. van Genderen, P. S. The, D. de Winter, A. Hollander, P. J. de Jong, F. C. van den Bosch, O. M. Kolkman, and M. A. W. Verheijen. *On the distance to the new luminous blue variable WRA 751 and its variability*. *A&A*, 258:316–322, Mai 1992.

[162] A. M. van Genderen, C. Sterken, and M. de Groot. *New discoveries on the S DOR phenomenon based on an investigation of the photometric history of the variables AG Car, S DOR and Eta Car*. *A&A*, 318:81–98, February 1997.

[163] R. H. M. Voors. *Infrared Studies of Hot Stars with Dust*. Ph.D. Thesis, Universiteit Utrecht, The Netherlands, 1999.

[164] R. H. M. Voors, L. B. F. M. Waters, A. de Koter, J. Bouwman, P. W. Morris, M. J. Barlow, R. J. Sylvester, N. R. Trams, and H. J. G. L. M. Lamers. *Infrared imaging and spectroscopy of the Luminous Blue Variables Wra 751 and AG Car*. *A&A*, 356:501–516, April 2000.

[165] K. Weis. *A kinematic and morphological investigation of the asymmetric nebula around the LBV candidate WRA 751*. *A&A*, 357:938–944, Mai 2000.

[166] K. Weis. *LBV Nebulae: The Mass Lost from the Most Massive Stars*. *Reviews in Modern Astronomy*, 14:261, 2001.

[167] K. Weis. *The AG Carinae Nebula – Bigger than ever?* *ASPC*, 388: 231, June 2008.

[168] K. Weis. *Nebulae around Luminous Blue Variables - large bipolar variety*. *IAUS*, 272:372–377, Jully 2011.

[169] B. Wolf and O. Stahl. *AG CAR - A galactic S DOR variable*. *A&A*, 112:111–115, August 1982.

[170] B. Wolf, I. Appenzeller, and O. Stahl. *IUE and ground-based spectroscopic observations of the S Dor-type LMC variable R 71 during minimum state*. *A&A*, 103:94–102, November 1981.

[171] C. Wolf and G. Rayet. *Spectroscopie stellaire*. *Comptes rendus de l'Académie des sciences*, 65:292–293, 1867.

[172] H. E. Wood. *Discovery of a variable star in Carina*. *MNRAS*, 74: 689, June 1914.

[173] I. Yamamura, S. Makiuti, N. Ikeda, Y. Fukuda, S. Oyabu, T. Koga, and G. J. White. *AKARI/FIS All-Sky Survey Bright Source Catalogue, Version 1.0*. 2010.

[174] R. C. Young Owl, M. M. Meixner, D. Fong, M. R. Haas, A. L. Rudolph, and A. G. G. M. Tielens. *Testing Models of Low-Excitation Photodissociation Regions with Far-Infrared Observations of Reflection Nebulae*. *ApJ*, 578:885–896, October 2002.